INFORMATION TO USERS

This manuscript has been reproduced from the microfilm master. UMI films the text directly from the original or copy submitted. Thus, some thesis and dissertation copies are in typewriter face, while others may be from any type of computer printer.

The quality of this reproduction is dependent upon the quality of the copy submitted. Broken or indistinct print, colored or poor quality illustrations and photographs, print bleedthrough, substandard margins, and improper alignment can adversely affect reproduction.

In the unlikely event that the author did not send UMI a complete manuscript and there are missing pages, these will be noted. Also, if unauthorized copyright material had to be removed, a note will indicate the deletion.

Oversize materials (e.g., maps, drawings, charts) are reproduced by sectioning the original, beginning at the upper left-hand corner and continuing from left to right in equal sections with small overlaps. Each original is also photographed in one exposure and is included in reduced form at the back of the book.

Photographs included in the original manuscript have been reproduced xerographically in this copy. Higher quality 6" x 9" black and white photographic prints are available for any photographs or illustrations appearing in this copy for an additional charge. Contact UMI directly to order.

UMI

A Bell & Howell Information Company
300 North Zeeb Road, Ann Arbor MI 48106-1346 USA
313/761-4700 800/521-0600

SPACE ELECTRIC PROPULSION PLASMA CHARACTERIZATION USING MICROWAVE AND ION ACOUSTIC WAVE PROPAGATION

by

Shawn Garrick Ohler

A dissertation submitted in partial fulfillment
of the requirements for the degree of
Doctor of Philosophy
(Electrical Engineering)
in The University of Michigan
1996

Doctoral Committee:

Assistant Professor Brian Gilchrist, Chair
Assistant Professor Alec Gallimore
Professor Ward Getty
Professor Fawwaz Ulaby

ACKNOWLEDGMENTS

This research would not have been possible without help and assistance of the many individuals and groups that I have been in contact with throughout my graduate career. Within the University I have received never ending help and advice from many people within three primary laboratories: the Radiation Laboratory, the Plasmadynamic and Electric Propulsion Laboratory, and the Space Physics Laboratory.

There are several individuals who I would like to extend special acknowledgment. In particular, I would like to thank Professor Brian Gilchrist for providing support, guidance, and vision throughout my graduate career. He provided a high standard to follow both personally and professionally. I would also like to thank Professor Alec Gallimore who has also provided unending assistance throughout my graduate career. I thank Sven Bilén for numerous stimulating conversations, reviewing my work, and never ending assistance with practical details. I would also like to thank all of the students at PEPL, a laboratory where team effort is essential to a successful experiment. In particular, I would like to thank Matt Domonokos, John Foster, James Haas, Sang-Wook Kim, Brad King, and Colleen Marrese.

I would also like to acknowledge individuals who provided support in specific areas of my research. Thanks goes to Professor Valdis Liepa and Professor Kamal Sarabandi for their advice and generous use of equipment related to the microwave measurements. I wish to thank Matthew Holladay and Christopher Nelson for their work on the ray tracing simulations. I thank Stephen F. Stewart for his help with Langmuir

probe measurements, and Dr. Larry Brace for the use of the Langmuir probe system. I thank Tom Budka for help with design and implementation of the microwave filter.

The thrusters used in this research were generously loaned to PEPL. I acknowledge Dr. Frank Curran of NASA Lewis Research Center for loan of the 1 kW arcjet and PPU. I also acknowledge Mike Day of Space Systems/ Loral for the loan of the Fakel SPT-100. Lastly, I acknowledge Dr. Sergey Khartov of the Moscow Aviation Institute for the loan of the lab-model SPT.

On a personal level, I wish to thank my parents, Larry and Bonnie Ohler, for their never ending support and guidance throughout my life and whose encouragement lead me to this accomplishment. I would also like to thank Dan and Micki McCormick who have provided much appreciated support throughout my graduate career. Lastly, I would like to give heartfelt thanks to my wife, Kimberly, for her support, encouragement, and understanding during my graduate career.

This research was funded in part by University of Michigan start-up research funding from the office of the Vice-President for Research, the College of Engineering, and AFOSR grant #F49620-95-1-0331 (contract monitor: Dr. M. Birkan).

TABLE OF CONTENTS

LIST OF FIGURES

Figure

LIST OF TABLES

Table

LIST OF APPENDICES

APPENDIX

NOTATION

A	Area (m^2)
B_o	Magnetic flux vector (T)
c	Speed of light ($3x10^8$ m/s)
D	Plasma dispersion function (unitless)
e	Unit charge ($1.6\ 10^{-19}$ C)
$\hat{e}$	Electric field unit vector (unitless)
E	Electric field (V/m)
E_o	Amplitude of the electric field (V/m)
f	Test frequency (Hz)
FN	Antenna pattern distribution function (unitless)
j	$\sqrt{-1}$
k	Wave number (m^{-1})
k_r, k_i	Real and imaginary part of the wavenumber (m^{-1})
k_{noise}	Wave number of plume oscillations (m^{-1})
K	Boltzmann's constant (J/K)
I_e	Electron current (A)
I_{oe}	Electron saturation current (A)
I_{sp}	Specific impulse (s^{-1})
J_o0	Bessel function (unitless)
l_{tot}, l_{tot_0}	Length of ray tube with and with out a plasma present for ray N (m)
m_e,m_i	Mass of electron and ion (kg)
m_i	Mass of ion (kg)
m_n	Mass of neutral particles (kg)
m_{amp}, m_{freq},	Modulation Factors for amplitude (unitless), frequency (rad/s),
m_{phase}, m_{noise}	phase (rad), and density noise or oscillations (unitless)
N	Index of ray (unitless)
n_C	$(f/8.98)^2$, Critical or cutoff density (m^{-3})
n_e, n_i	Electron number density (m^{-3})
n_{IR}	Index of refraction (unitless)

n_n	Neutral density (m^{-3})
N_{max}	Number of rays (unitless)
n_0 m, p	Coefficients in static plume model (m^{-3},unitless, unitless)
n_{stat}	Static electron density model (m^{-3})
n_{temp}	Temporal component of electron density (unitless)
P	Pressure (Pa)
P_{rel}	Relative antenna power (to free space) (dB or W)
P_e, P_i	Pressure due to electrons and ions (Pa)
q_e, q_i	Charge of electrons and ions (C)
r	Radial position from thruster axis (m)
R	Maximum radial extent of the plume (m)
s	Position of ray (m)
s_1, s_2	Points along a ray path (m)
S	Intensity or power density (W/m^2)
t	Time (s)
T_e,T_i	Electron and ion temperatures (eV or K)
v_A	Alfén velocity (m/s)
υ_c	Total effective collision frequency (Hz)
v_{cei}, v_{cen}	Electron-ion and electron-neutral collision frequency (Hz)
v_e, v_i	Directed flow velocity of electrons and ions (m/s)
V_{flow}	Directed plasma flow velocity, same as v_e, v_i when v_e=v_i (m/s)
V_{iaw}	Ion acoustic wave velocity
V_{the}, V_{thi}	Electron and ion thermal velocity
w	Width of ray tube (m)
x	Position coordinate orthogonal to plume axis and orthogonal to microwave transmission direction (m)
x_{rel}, x_{nopl}	Position of rays relative to center of antenna (m)
z	Position coordinate along plume axis (m)
$\Delta\phi$	Phase shift (radians or degrees)
ε_o	Free space permittivity (8.854×10^{-12} F/m)
ε_r	Relative permittivity (unitless)
ϕ_{rel}	Phase shift of antenna (relative to free space) (rad)
$\phi(s)$	Phase of wave at position s (radians or degrees)
ϕ_{nopl}	Phase of wave without a plasma (radians or degrees)

γ_e, γ_i	Thermal compression equilibrium factor, 1-isothermal, 2-one dimensional compression
λ	Wavelength of wave in plasma (m)
λ_D	Debye length (m)
λ_0	Wavelength in free space(m)
Λ	The plasma parameter (unitless)
μ_0	Permeability of free space ($4\pi x10^{-7}$ H/m)
θ	Angle from thruster axis (radians or degrees)
ρ	Radial distance from thruster (m)
σ	Standard deviation used in the antenna calibration function (m)
ω	Radial frequency (rad/sec)
ω_{ce}, ω_{ci}	Electron and ion cyclotron frequencies (rad/s)
ω_h	Upper hybrid frequency (rad/sec)
ω_l	Lower hybrid frequency (rad/s)
ω_{noise}	Frequency spectrum of plume oscillations (rad/s)
ω_{oscil}	Dominant frequency of density oscillations (rad/s)
ω_{pe},ω_{pi}	Radial plasma frequency of electron and ions(rad/s)

CHAPTER 1
INTRODUCTION

1.0 Overview of Chapter

The use of satellite technology for a wide range of application is pervasive in modern society. Applications range from communications, navigation, remote sensing, and space environment exploration; to manned exploration and even commercial opportunities such as materials and pharmaceuticals processing in a low-gravity environment. In any spacecraft, the control of attitude and position are essential capabilities. The performance of subsystems responsible for attitude and position can be important constraints on overall performance. Electric propulsion technology offers a more efficient method with often optimal operating parameters when compared to traditional chemical propulsion.

In an electric propulsion thruster, considerable performance information can be learned from measurements in the plasma plume of the thruster as well as determining what impact the plume will have when applied to satellite systems. Plasma plume measurements are needed which are more accurate and complete than previously reported in terms of spatial resolution. Ideally these measurements are obtained using techniques that are simple to implement. Additionally, the impact of next-generation thrusters to space-craft systems is of near-term importance. In this research, diagnostics are studied and developed for three parameters: electron density, flow velocity, and ion temperature. Further, the impact to electromagnetic propagation is studied for a typical next generation thruster, the 100 mm

stationary plasma thruster (SPT-100). This work also supports the flight qualification of SPT-100 thrusters for U.S. communication satellite applications.

This research develops methods and measurements for both, plasma parameter characterization and plume impact assessment for satellite radiative electromagnetic systems. The two primary directions of this research address these issues, and the work is divided by measurement technique (Chapters 2 through 4 and Chapters 5 through 7). The first study encompasses microwave propagation through the plasma plume to determine both electron density and electromagnetic signal impact. The second part of the research is an investigation of a diagnostic technique to estimate flow velocity and ion temperature by generating ion acoustic waves and measuring propagation characteristics.

As motivation for the research, previous knowledge is summarized in this chapter, gaps are indicated, and opportunity for advancement is suggested. Appendix A contains a detailed outline of the motivation progression leading to this research. The background and motivation are broken into three areas: the progression of thruster technological challenges emphasizing questions relevant to this work; electron density measurement techniques and the radiative electromagnetic system impact of electric propulsion, as these are intrinsically related; and finally, techniques to measure flow velocity and ion temperature. This research capitalizes on many of the opportunities for advancement which are listed in this chapter, and an overview is given which summarizes the contributions of this research.

1.1 Electric Propulsion: Background and Motivation

Electric propulsion is ideal for some space missions due to the high exhaust velocities and nearly optimal thrust characteristics, both producing high efficiency systems [Myers, *et al.* 1993]. Electric propulsion originated in the 1950's and 1960's with the desire for a more efficient and reliable propulsion system than traditional chemical systems which rely on chemical reactions to produce heating and thrust. It has surpassed other alternative propulsion systems such as fusion, anti-matter, and solar wind in practicality

primarily due to its cost, efficiency, size, and ease of integration with present spacecraft systems. Recently, electric propulsion has been developed into a feasible technology for low thrust applications such as station-keeping and orbit raising of satellites or propulsion for inter-planetary missions [Spores, *et al.* 1995; Stone, 1986]. Studies currently focus on a number of implementation issues including: identification of mission scenarios, integration into present spacecraft systems, and improvements in performance and operation.

Electric propulsion is divided into three classes according to the method of thrust: electrothermal, electrostatic, and electromagnetic. All of these classes utilize electrical energy to energize and accelerate a propellant. Some examples of electric thrusters include gridded ion engines, magnetoplasmadynamic (MPD) thrusters, pulsed plasma thrusters, arcjets, and Hall effect thrusters where each type comprises a number of individual versions of thrusters. Two thrusters have been utilized in this research: a 1 kW arcjet and a Hall effect thruster known as the stationary plasma thruster (SPT-100).

The 1 kW arcjet (see Appendix B for greater detail and references) is a simple electrothermal device that ionizes a gas through an electric discharge and accelerates the plasma through a traditional expansion nozzle [Sankovic, *et al.* 1991]. The arcjet is presently in use aboard spacecraft primarily due to its simplicity, reliability, reduced propellant requirements, and ease of integration into present spacecraft systems; however, other electric propulsion thruster types appear to offer even higher efficiencies with similar velocity and ease of installation.

Constant improvement of the thruster is necessary to keep pace with increasing expectations of propulsion systems. In order to improve thruster efficiency and operation, computer models are used to predict how changes to thruster geometry and operation will affect performance. Computer models require or predict a number of thruster and plasma parameters such as, thrust, ion energy, bulk flow velocity, electron temperature, electron

density, and ion temperature. The arcjet electron density is characterized in this work in Chapters 2 through 4.

The SPT-100 (see Appendix B for greater detail and references) is an electrostatic device significantly more complex than the arcjet, but also more efficient, thus more appropriate for use in some space flight missions [Kaufman, 1985; Sankovic, *et al.* 1993; Garner, *et al.* 1993]. This device utilizes a radial magnetic field to trap electrons, which ionize the gas propellant (xenon). A potential gradient between the cathode and anode electrostatically accelerates the ionized gas. This device is currently being prepared and tested for use aboard modern satellites due to its high efficiency and applicability to certain satellite missions. In order to incorporate the thruster onto a spacecraft, not only do the electrical, mechanical and thermal characteristics need to be properly accounted for, but the thruster's impact on spacecraft systems needs to be evaluated. Additionally, computer modeling can describe the thruster performance through the thruster and plume parameters similar to the arcjet [Rhee, *et al.* 1995; Oh, *et al.* 1995]. In this work, the SPT-100's effect on spacecraft radiative electromagnetic systems are investigated through direct experiment and through computer modeling, and the plasma plume is characterized through the measurement of electron density, ion temperature, and bulk flow velocity.

1.2 Characterization of Electron Density and its Impact on Electromagnetic Propagation

1.2.1 Alternate Methods to Characterize Electron Number Density Measurement

Thus far, measurements of electron density for electric propulsion have been made using intrusive methods with limited accuracy and spatial mapping. For the arcjet [Carney ,*et al.* 1989a; Carney, *et al.* 1989b; Hoskins, *et al.* 1992] and the SPT-100 [Sankovic, *et al.* 1993; Myers, *et al.* 1993; Patterson, *et al.* 1985; Absalamov, *et al.* 1992] a number of

experiments have been reported which primarily characterize the electron density by utilizing a Langmuir probe.

A number of techniques exist to measure electron number density. Microwave reflectometry [Simonet, 1985; Baang, *et al.* 1990; TFR Group, 1985; Hugenholtz, *et al.* 1990; Sips, 1991] is a simple and effective method; however, the resolution is limited by the plasma frequency of the plasma (which, in the cases of interest, the corresponding wavelength is greater than 0.1 m). The resonance probing technique [Stenzel, 1976; Jensen, *et al.* 1992; Swenson, 1989] is very precise and the Langmuir probe [Hutchinson, 1987; Hopkins, *et al.* 1986; Tilley, *et al.* 1990] is generally accepted as an effective measure of electron density, however they both have problems in probe heating and local plasma perturbations inherent in *in situ* techniques. Various spectroscopic techniques are inherently non-intrusive and have excellent spatial resolution, but the techniques rely on detailed finite rate chemistry and energy level models that are not well understood (except for hydrogenic propellants) [Hutchinson, 1987; Manzella, 1993].

1.2.2 Present State of Microwave Interferometry Diagnostic Technique

A viable alternative to these techniques is microwave interferometry which is non-intrusive and relies on the direct relationship between a propagating wave and the electron number density (see Figure 1.1). Non-intrusive radio frequency diagnostics of plasma density and temperature are well recognized for their accuracy and speed of measurement in numerous fields such as fusion research, plasma processing, and studies of planetary ionospheres [Heald, *et al.* 1969; Ginzburg, 1970; Sheffield, 1975; Soltwick, 1994]. Interest has also recently been shown in using microwave interferometric measurement techniques of plasma plumes generated by high energy electric propulsion (EP) thrusters [Birkner, *et al.* 1990; Dickens, 1995; Ohler, *et al.* 1995].

Experimentally, characterizing the interaction of a microwave signal with an EP thruster plume can provide a direct measure of line-integrated electron number density

through microwave interferometry which is a well established technique [Heald, *et al.* 1969] . It is inherently nonintrusive and hence, avoids the issues of probe heating and local plasma perturbations of *in-situ* techniques in dense energetic plasmas. Most present systems provide highly accurate single channel (measurement point) measurements of line integrated density but must assume a spatial distribution in order to estimate local density from a single line integrated measurement [Krall, *et al.* 1993; Lehecka, *et al.* 1988; Kelly, 1965; Overzet, *et al.* 1993; Neumann, *et al.* 1993; Kumar, *et al.* 1979; Kinderdijk, *et al.* 1972; Wharton, *et al.* 1960; Fessey, *et al.* 1987; Efthimion, *et al.* 1985; Doane, *et al.* 1981; Tsang, *et al.* 1975; Domier, *et al.* 1988; Bora, *et al.* 1983, 1988]. The results are sometimes used for calibration of Langmuir probes [Cecchi, 1984], and a number of comparisons exist between the more common Langmuir probe and microwave interferometry [Overzet, *et al.* 1993; Neumann, *et al.* 1993; Kumar, *et al.* 1979; Kinderdijk, *et al.* 1972]. A few systems provide spatial mapping in one plane of the plasma and use Abel inversion in that plane to find local density [Janson, 1993, 1994a, 1994b; Okada, *et al.* 1989; Okazaki, *et al.* 1990; Howard, 1990; Howard, *et al.* 1988; Hattori, *et al.* 1991]. It would be desirable to provide spatial mapping in two planes of the plasma for more complete characterization of the local plasma density. Additionally, present systems are limited when compensating for vacuum chamber effects such as chamber resonances or multipath since most use single frequencies and traditional phase detector circuits for the interferometric phase comparison. A partial solution to assessing and/or limiting chamber effects is through the use of a network analyzer as suggested by Birkner [*et al.* 1990], although it apparently has not been implemented.

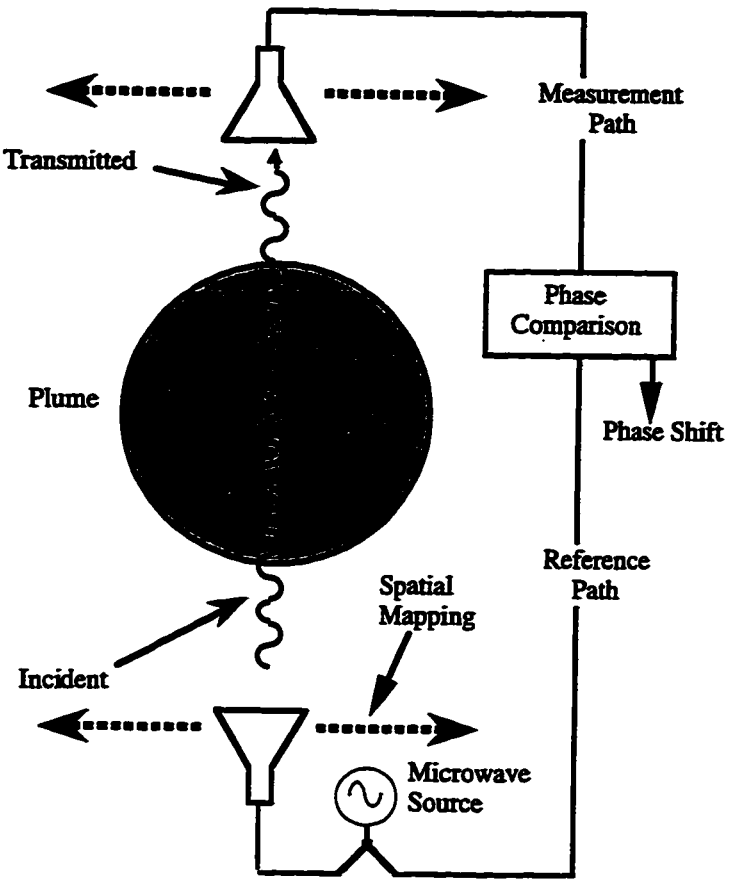

Figure 1.1. Illustration of microwave interferometry technique.

1.2.3 Past Research of Electromagnetic Propagation Through Electric Thruster Plasma Plume

The plasma-microwave interaction is a well known effect where a propagating electromagnetic signal is altered in a number of ways including signal attenuation, phase shift, added phase or amplitude noise, and refraction of signal direction. Some studies have used ray tracing simulations to predict propagation impact [Carney, 1988; Birkner, *et al.* 1990, Ling, *et al.* 1991a, 1991b; Kim, *et al.* 1991; Dickens, 1995, *et al.* 1995a, *et al.* 1995b]. For the SPT the modeling has focused on phase shift and phase modulation [Dickens, 1995, *et al.* 1995a, *et al.* 1995b]; however, experiments have demonstrated significant amplitude effects also [Ohler, *et al.* 1995]. Quantifying the impact on communications due to electric thrusters has received only minimal attention in ground or

space-based experimental simulations. The modeling of phase shift and noise has been compared with measurements only in the range from 2.6 to 10 GHz. Additional investigation is necessary to more completely model plume effects through attenuation and amplitude modulation as well as additional experimental validation of computer models.

1.2.4 Advancement Produced by this Research

In this work an innovative microwave system is developed to quantify both the electron density and the communications impact of an electric thruster plasma plume. This microwave measurement tool, which is new for EP generated plasmas, provides spatially resolved measurements in various orientations, quantifies both magnitude and phase modification, and addresses signal multipath and resonance effects in the enclosed vacuum test facility. Additionally, for studies assessing impact to propagated electromagnetic systems, this novel diagnostic tool is capable of covering a wide frequency band and operates in a sufficiently large vacuum facility such that plasma boundary effects are minimized.

The research utilizes a microwave network analyzer (quadrature heterodyne receiver) which can accurately measure signal phase and magnitude with respect to a reference signal. It operates in the Ku frequency band to maintain adequate phase sensitivity (peak plasma frequency in the 1-3 GHz range. It utilizes a unique up-down frequency converter circuit to minimize measurement errors otherwise induced by operation in the Ku-band frequency range, while still allowing broadband frequency operation required for communications impact studies. Because of a unique time-gating feature of the network analyzer, it is also possible to compensate for signal multipath and resonances inside the vacuum chamber. Finally, a highly accurate probe positioning system allows detailed mapping through the plume.

1.3 Bulk Flow Velocity, Ion Temperature and Ion Acoustic Wave

Flow velocity and ion temperature are two key parameters in plasmas in general and in electric propulsion thruster plumes in particular. Bulk flow velocity is a direct measure of the kinetic energy that the ions possess and, hence, it is a measure of the thrust. The ion temperature is an indication of the ionization processes and the particle interaction in the plasma. A diagnostic to measure flow velocity and ion temperature should be accurate and flexible, have a simple and robust implementation, and provide spatially resolved measurements. Within electric propulsion, these two quantities have been characterized in a number of experiments. The experiments and research of flow velocity and ion temperature within electric propulsion is reviewed along with relevant work in other fields. An alternative method to find the two quantities is proposed here which utilizes ion acoustic wave propagation; hence, past work in ion acoustic wave research is also summarized.

1.3.1 Alternate Flow Velocity Diagnostics

Bulk flow velocity can be measured through a number of methods [Hutchinson, 1987]. One method uses a retarding potential analyzer to find the ion energy distribution. In general, this is a relatively intrusive technique that requires grids which accelerate and decelerate the ions. The ion energy distribution is related to the average flow velocity through interpretation of the energy distribution. One implementation of this technique has been applied to the SPT [Marrese, *et al.* 1995] where the ion energy distribution implies the average velocity. A second method utilizes the Doppler shift of an electromagnetic signal in the plasma. This method is very flexible because the frequency can range from optical to microwave; however, the small magnitude of the optical or microwave signal can be a problem which often requires high densities. Additionally the geometry of the experiment precludes direct measurement of the velocity along the flow direction. Total flow velocity

can be found by measuring two vector components of the flow so the total flow velocity can be found. A common implementation uses the method of laser induced florescence (LIF) to find the Doppler shift of an absorption peak in the plume of arcjet [Erwin, *et al.* 1991, Storm, *et al.* 1995] and SPT [Manzella, 1994]. LIF offers the possibility of excellent spatial resolution without a probe but depends on knowledge of the complex energy level structure of the plasma constituents to find flow velocity. Yet another, technique utilizes a quadruple probe or crossed electrostatic probes to measure flow velocity. The velocity is found through measuring the ratio of current to one probe compared to another probe relative to the angle with respect to the flow direction. Two reported implementations measure the velocity profile of an MPD thruster [Bufton, *et al.* 1995; Burton, *et al.* 1993] and an argon plasma jet [Poissant, *et al.* 1985; Johnson, 1969]. This method while offering excellent spatial resolution and flexibility for simultaneously measuring other quantities requires a complex probe-plasma coupling model and is greatly dependent on the accurate knowledge of the effective area of probes. Two final techniques are similar to the technique presented here using ion acoustic waves. The first uses the frequency domain of lower hybrid waves injected into the plasma to find the flow velocity [Diamant, *et al.* 1991]. This technique requires difficult spectral interpretation due to a poor signal to noise ratio and requires a magnetic field to excite the lower hybrid waves. The second technique, referred to as Time of Flight [Boyle, 1974] uses the total velocity of an injected wave as an approximation to the flow velocity; this technique is only useful when the flow velocity is much greater than the wave velocity (see Chapter 7 for an example of this method).

1.3.2 Alternate Ion Temperature Diagnostics

Measurement of ion temperature is generally difficult and is accomplished through various methods. The choice of method is dependent on plasma parameter ranges in a given instance. In the plumes of electric thrusters, Thompson scattering and Rutherford

scattering are both incoherent scattering techniques which require the wavelength to be much smaller than the Debye length. These techniques are difficult to apply to electric thrusters due to extremely low level of scattered energy from the relatively low electron density and the high frequencies required (visible) [Hutchinson, 1987, van Blokland, *et al.* 1992; Haddad, *et al.* 1991]. Another scattering technique which requires the wavelength be larger than the Debye length (hence sometimes referred to as coherent scattering) scatters from the natural fluctuations in the plasma density due to the electron and ion temperatures [Vickrey, 1980, Sheffield, 1975]. This technique is also extremely difficult to implement due to the small scattered signal, but it has been studied as a possibility in electric thrusters (Appendix F). Laser-induced-florescence (LIF) has been utilized to find the ion temperature in the SPT plume, but this technique depends on an elaborate theoretical model based on ionization energy levels. All of the present techniques depend on small levels of scattered power or elaborate models to determine the ion temperature.

1.3.3 Summary of Past Ion Acoustic Wave Research

The diagnostic technique presented here utilizes ion acoustic wave propagation (see Figure 1.2). It is based on the knowledge acquired through studies on general wave propagation in a plasma, probe-plasma coupling in a stationary and flowing plasma, ion acoustic wave excitation and detection, and ion acoustic wave propagation where general references are also available covering many of the relevant issues in this study [Season, *et al.* 1989; Jones, *et al.* 1985]. Early reviews of the wave propagation processes in plasmas provide the basis for understanding the excitation and propagation of ion acoustic waves [Chen, 1964; Birmingham, *et al.* 1965; Ohnuma, 1978]. Probe-plasma coupling has been explored primarily with reference to Langmuir probes and the voltage current characteristics of a probe [Chung, *et al.* 1975; Godard, 1975; Godard, *et al.* 1989; Chung, *et al.* 1988, Wang, *et al.* 1986; Segall, *et al.* 1973; Crawford, *et al.* 1964; Buckley, 1967; De Boer, *et al.* 1994; Bruce, *et al.* 1975]. Another area of work relevant to this research is the effect on

a moving plasma from probe insertion which creates a wake downstream of the probe. Most research in this area investigates the wake produced by a DC-biased object which is still relevant to this research as discussed in Chapter 6. Both theoretical [Koneman, et al. 1978; Coggiola, *et al.* 1991; Taylor, 1967; Senebetu, *et al.* 1989] and experimental [Chan, *et al.* 1986; Biasca, *et al.* 1994; Stone, *et al.* 1972, *et al.* 1973, *et al.* 1980; Morgan, *et al.* 1989; Fournier, *et al.* 1975] approaches have investigated wakes behind small metallic objects such as cylinders, spheres, or discs. This work is helpful in understanding the propagation pattern of the ion acoustic wave. Excitation and detection of ion acoustic waves has been implemented not only through spherical, cylindrical, or planar probes [Chen, 1977; Ikezi, *et al.* 1973], but also through gridded structures [Nakamura, *et al.* 1993; Gould, 1964; Schott, 1992]. In addition, theoretical investigations have modeled the sheath coupling and production of the ion acoustic wave [Hong, *et al.* 1993; Widner, *et al.* 1970]. Recent studies of ion acoustic wave propagation has focused on damping mechanisms such as collisional, Landau, and fluid dynamic damping [Dum, 1975; Schott, 1975; Randall, 1982; Tsang, *et al.* 1975; Epperlein, 1994; Epperlein, *et al.* 1992; Bychenkov, *et al.* 1994; Basu, *et al.* 1988; Huang, *et al.* 1974]. Additional studies of interest include investigation on the spatial decay of ion acoustic waves [Hirshfield, *et al.* 1971] and the near field pattern of ion acoustic wave [Christiansen, *et al.* 1977; Nakamura, *et al.* 1979]. The existing work is helpful in developing a diagnostic to utilize the ion acoustic wave propagation information although minimal published information directly addresses ion acoustic waves in a flowing plasma [Drake, *et al.* 1994; Srivastava, *et al.* *1994*]. Although not directly applicable, increased understanding of this research has been attained through investigation of ion acoustic wave reflection at boundaries [Schott, *et al.* 1986; Popa, *et al.* 1983, Ito, *et al.* 1994, Nakamura, *et al.* 1989], ion acoustic wave grid interaction [Doucet, *et al.* 1970; Stefant, 1971; Schott, 1991, 1992; Nakamura, *et al.* 1993; Bernstein, *et al.* 1971; Gabl, *et al.* 1984; Jahns, *et al.* 1972; Longren, *et al.* 1982], and nonlinear processes of ion acoustic waves [Alexeff, *et al.* 1968; Bingham, *et al.* 1984;

Andrews, *et al.* 1972; Rizzato, *et al.* 1992; Raychaudhuri, *et al.* 1985; Weibel, *et al.* 1976; Watanabe, *et al.* 1975; Hershkowitz, *et al.* 1978; Murakami, *et al.* 1993].

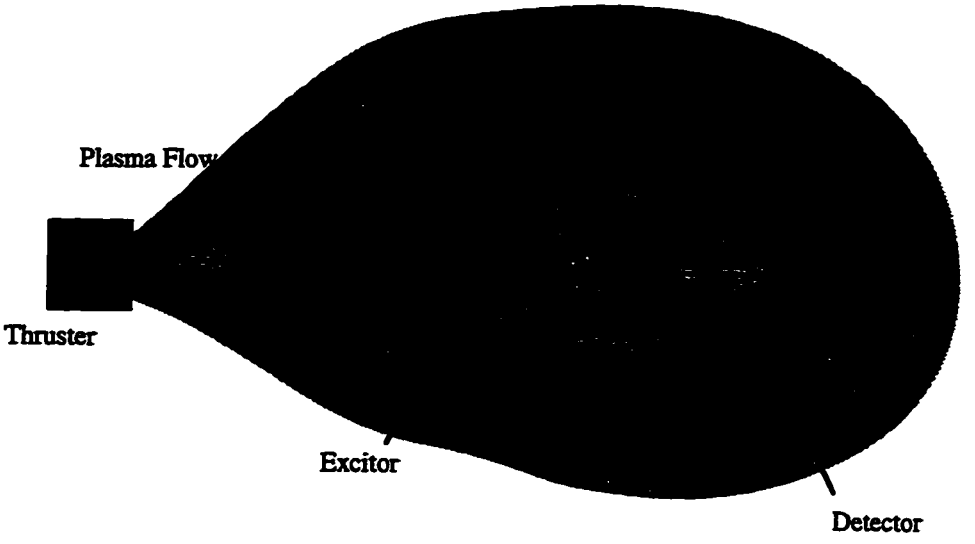

Figure 1.2. Schematic description of generating an ion acoustic wave; its propagation and detection characterization in a flowing plasma. In these studies the transmitted ion acoustic wave amplitude and phase are characterized.

1.3.4 Advancement Produced by this Research

Each of the mentioned diagnostic techniques have advantages and disadvantages. This research develops a novel diagnostic technique to measure flow velocity and ion temperature that uses ion acoustic wave propagation characteristics. Utilization of the ion acoustic wave propagation does not depend on an elaborate model and is independent of exact probe size, thereby offering a simple measurement. The spatial resolution is not as good as some previous methods but it is still relatively non-intrusive since the probe is small, being on the order of the scale length of the plasma (the Debye length).

The work presented here is based on previous information from ion acoustic waves in a static inhomogeneous plasma, ion acoustic wave probe coupling in a static plasma, probe coupling to flowing plasma for a DC bias, and general wave propagation in a moving

media. The research presented extends previous knowledge of ion acoustic wave propagation by characterizing ion acoustic waves in a flowing inhomogeneous plasma produced by a thin cylindrical probe and received by a separate probe (Figure 1.2). A new diagnostic technique is developed and demonstrated to characterize flow velocity and ion temperature utilizing ion acoustic wave propagation. The methodology, results, and analysis of the ion acoustic wave study are presented in Chapters 5 through 7.

1.4 Contributions of this Research

The previous sections presented background on electric propulsion, microwave diagnostic, ion acoustic waves, and diagnostics to measure electron density, flow velocity, and ion temperature. Advancement produced by this work in these areas was also outlined in those sections. This research expands the understanding and knowledge in a number of areas. The main contributions of this work are summarized below.

- Development of an innovative microwave measurement system for interferometry and electromagnetic transmission impact studies for electric propulsion.
- Novel functional model of electron density based on nonintrusive microwave interferometry mapping of near- to far- zone region of SPT-100
- First demonstration of electromagnetic attenuation by electric propulsion plumes through experimental measurements and first validation of ray tracing simulation to model attenuation of a microwave signal.
- First demonstration of electromagnetic amplitude modulation through ray tracing simulation and comparison to power spectral density measurements.
- Quantitatively demonstrated effect on microwave propagation through the plasma plume by simulating amplitude and phase modulation for a range of microwave frequencies.
- Extend knowledge of ion acoustic wave propagation by characterizing ion acoustic wave excitation and propagation in a flowing plasma.

- Novel use of ion acoustic waves to measure directed flow velocity and obtain an upper bound for ion temperature in the plume of a stationary plasma thruster.

CHAPTER 2

METHODOLOGY OF MICROWAVE MEASUREMENTS

2.0 Overview of Chapter

Electromagnetic propagation through plasma plumes is highly probable for satellite systems, hence, defining the thruster effect on microwave propagation is critical. Furthermore, controlled microwave propagation through plasmas can help to characterize electron number density, an intrinsic plasma parameter. Wave propagation in plasmas is given at least a chapter in most general plasma texts, and complete books have been written on the interaction of an electromagnetic wave with plasmas [Ginzburg, 1970; Sheffield, 1975]. Additionally, microwave measurements of plasmas is also discussed in detail in many texts [Hutchinson, 1987; Heald, *et al.* 1969].

The starting point for predicting the characteristics of propagating waves is a set of well known dispersion relations which are essential for predicting the variation of wave propagation properties and for interpreting the measurements [Ginzburg, 1970; Sheffield, 1975]. These equations are used to develop predictive models correlated to measurement test conditions. Given the predictive model, one diagnostic technique, microwave interferometry, is applicable to measuring plasma electron number density [Heald, *et al.* 1969]. In order to verify conclusions of the predictive model and to characterize the electron density of a high speed plasma, a new measurement system is introduced to characterize amplitude, phase, and spectral content of a propagating wave. Chapter 2 will review the fundamental equations, predictive model, electron density diagnostic technique,

and the measurement system as applied to wave propagation through the high speed plasma plume of an arcjet and SPT-100 electric thruster.

2.1 Electromagnetic Wave Propagation in a Plasma

Electromagnetic wave propagation is governed by a general dispersion relation that includes all field and plasma characteristics. The dispersion relation utilized in this analysis is based on cold fluid theory which is readily applicable to this case. This general dispersion relation can be separated into various modes, each with its own simplified dispersion relation that predicts propagation as well as attenuation. These electromagnetic mode dispersion relations are primarily defined by the magnetic field and the densities, temperatures, and masses of the constitutive particles [Chen, 1984; Sheffield, 1975; Ginzburg, 1970].

In this study, the mode dispersion relations are identified for the undamped electromagnetic modes. Then each modal dispersion relation is evaluated and addressed given the parameter estimations for the cases of interest. Attenuation is then evaluated for the primary damping mechanism, collisional damping. Lastly, using the evaluation of the modes and collisional damping, a simple dispersion relation is used to define the constraints of wave propagation in an inhomogeneous time-varying plasma.

2.1.1 Electromagnetic Propagation Modes and Characteristic Parameters

The dispersion relations for the electromagnetic modes are summarized in Table 2.1 [Chen, 1984] where wave damping has been ignored. The modes of electromagnetic electron and ion waves are as follows: O wave (ordinary wave), X wave (extraordinary wave), R wave (right hand circularly polarized wave), L wave (left hand circularly polarized wave), Alfvén wave, and magnetosonic wave.

The mode dispersion relations are evaluated based on estimates of characteristic parameters for the arcjet [Boyd, *et al.* 1993; Carney, *et al.* 1989; Hoskins, *et al.* 1992;

Zana, 1987; Pencil, *et al.* 1993] and the SPT-100 [Myers, *et al.* 1993; Absalamov, *et al.* 1992; Manzella, 1993, 1994, *et al.* 1995; Patterson, *et al.* 1985; Pencil, 1993] thrusters summarized in Table 2.2 and the experimental system described in Section 2.4. The parameter responsible for multiple modes is the magnetic field. No magnetic field is produced by the arcjet, therefore the only magnetic field of significance is due to the Earth's geomagnetic field. This magnetic field in the vacuum facility is oriented mostly along the axis of the chamber (same as the thruster), and hence, it is typically orthogonal to the direction of propagation. On the other hand, a magnetic fringing field is produced by magnetic coils of the SPT-100 thruster that is 10^{-3} T at the closest measurement point of 0.09 m [Oh, *et al.* 1995]. This field can have components parallel and perpendicular to the propagation direction.

Electron Electromagnetic Waves		Dispersion Relations	
O wave	$B_o = 0$ or $k \perp B_o, E \parallel B_o$	$\frac{c^2k^2}{\omega^2} = 1 - \frac{\omega_{pe}^2}{\omega^2}$	• 2-1
X wave	$k \perp B_o$, $E \perp B_o$	$\frac{c^2k^2}{\omega^2} = 1 - \frac{\omega_{pe}^2}{\omega^2}\frac{\omega^2 - \omega_{pe}^2}{\omega^2 - \omega_h^2}$	• 2-2
R wave	$k \parallel B_o$	$\frac{c^2k^2}{\omega^2} = 1 - \frac{\omega_{pe}^2/\omega^2}{1 - \omega_{ce}/\omega}$	• 2-3
L wave	$k \parallel B_o$	$\frac{c^2k^2}{\omega^2} = 1 - \frac{\omega_{pe}^2/\omega^2}{1 + \omega_{ce}/\omega}$	• 2-4
Ion Electromagnetic Waves			
none	$B_o = 0$		
Alfvén wave	$k \parallel B_o$	$\frac{k^2}{\omega^2} = \frac{1}{v_A^2}$	• 2-5
Magneto-sonic wave	$k \perp B_o$	$\frac{c^2k^2}{\omega^2} = \frac{c^2 + v_A^2}{V_{iaw}^2 + v_A^2}$	• 2-6

Table 2.1. Dispersion relations for electromagnetic waves in plasmas.

	Arcjet	SPT-100
Plasma Density, n_o (m^{-3})	10^{15}	10^{17}
Electron Temperature, T_e (eV)	0.3 (3500 K)	3 (35000 K)
Ion Temperature, T_i (eV)	0.3 (3500 K)	0.1 (1160 K)
Ion Mass, m_i (kg)	$1.67x10^{-27}$ (H)	$2.2x10^{-25}$ (Xe)
Magnetic Flux, B (T)	$5x10^{-5}$	$<10^{-3}$
Pressure, P (Pa)	$2.8x10^{-3}$	$7x10^{-4}$

Table 2.2. Estimate of physical parameter for arcjet and SPT-100 approximately 0.5 m downstream on the thruster axis.

Based on general physical characteristics, evaluation of the various mode dispersion relations are summarized for both the arcjet and SPT-100 where the O wave will stand out as the dominant mode through a process of elimination. For the arcjet , the R wave, L wave, and Alfvén wave will not be induced to any significant degree because they propagate along the magnetic field lines and the magnetic field is orthogonal to the propagation direction. Additionally, the R and L waves degenerate into an O wave since $\omega >> \omega_{ce}$. The dispersion relation for the X wave degenerates into the O wave dispersion function since the upper hybrid frequency, ω_h, is the same as the plasma frequency, ω_p, within the accuracy of the parameter estimations. Finally, the Alfvén wave and magnetosonic waves will not be excited while trying to excite an O wave due to the extremely small wavelength compared to the scale length of the system (10^6 wavelengths compared to the O wave).

The dispersion relations are evaluated again for the SPT-100 since it induces an additional magnetic field. Even with the increased magnetic field in comparison to the arcjet, the X wave, R wave, and L wave all degenerate into the form of the O wave since the upper hybrid frequency is very close to the plasma frequency and the ratio of the cyclotron frequency to the propagation frequency is very small ($2x10^{-3}$). The Alfvén wave and the magnetosonic wave again are not be excited while trying to excite an O wave due to

the extremely small wavelength compared to the scale length of the system. Therefore, propagation is limited to the O mode (f=17 GHz, k=1.8 cm^{-1}) in the plumes of the arcjet and SPT-100 even though a magnetic field exists. The propagation is evaluated based on single mode propagation.

2.1.2 Attenuation of O Wave Through Collisional Damping

The damping of an electron electromagnetic wave occurs primarily through electron-ion and electron-neutral collisions which are both momentum transferring collisions. Electron-electron collisions are lossless, and the ions are taken to be stationary (eliminating ion-neutral collisions) for the frequency range of interest (17 GHz). The damping term is included in the dispersion relation through the collision frequency as in Equation 2-7 [Ginzburg, Section 3, 1970]. The collision frequencies are given in Equations 2-9 to 2-10 [Sheffield, Chapter 2, 1975] where the total collision frequency (ν_c) in Equation 2-7 in the sum of the electron-ion and electron-neutral collision frequencies. The neutral density is found through Equation 2-11 where ambient temperature (290 K) is used with a pressure of 2.8x10^{-3} Pa and 7x10^{-4} Pa for the arcjet and SPT-100, respectively.

$$\frac{c^2k^2}{\omega^2} = 1 - \frac{\omega_{pe}^2/\omega^2}{(1 - j\,\nu_c/\omega)} \qquad \bullet 2\text{-}7$$

$$\Lambda \equiv \frac{12\pi\varepsilon_o KT_e}{q_e q_i}\left(\frac{\varepsilon_o KT_e}{q_e^2 n_e}\right)^{1/2} \qquad \bullet 2\text{-}8$$

$$\nu_{cei} = \frac{m_e + m_i}{3\pi^{3/2} m_e^2 m_i}\frac{q_e^2 q_i^2}{\varepsilon_o^2} n_i \left(\frac{2KT_e}{m_e} + \frac{2KT_i}{m_i}\right)^{-3/2} \ln\Lambda \qquad \bullet 2\text{-}9$$

$$\nu_{cen} = \frac{8\pi^{1/2}}{3}\frac{m_n}{m_e + m_n} n_n \sigma^2 \left(\frac{2KT_e}{m_e} + \frac{2KT_n}{m_n}\right)^{1/2} \qquad \bullet 2\text{-}10$$

$$P = n_n KT_n \qquad \bullet 2\text{-}11$$

The total effective radius, σ, in the electron-neutral collisions (Equation 2-10) is taken to be that of the background neutral particles which is estimated to be 10^{-10} m [Sheffield, 1975]. The collision frequencies are summarized in Table 2.3 for the parameters in Table 2.2. All of the collision frequencies are much smaller than the propagation frequency; therefore, given Equation 2-7, the attenuation of the wave is ignored and the simple expression is assumed for the ordinary mode, Equation 2-1.

	Arcjet	SPT-100
ν_{ei} (m/s)	$2\text{x}10^5$	$7\text{x}10^5$
ν_{en} (m/s)	$1\text{x}10^4$	$8\text{x}10^3$

Table 2.3. Collision frequencies of arcjet and SPT-100.

2.1.3 Plane Waves in Inhomogeneous and Time Varying Media

The dispersion relation for the ordinary wave in a plasma determines how the wave propagates through the plasma both in time and space. In the case of the electric thrusters, it will be found that the wave number, $k(\bar{r},t)$, varies over space and time. In the most general case, this would be a complicated problem requiring a full-wave solution. By separating the effects of the space and time variations it becomes more tractable.

Further simplification of the spatial variation is possible by assuming the geometric optics or Wentzel-Kramer-Brillouin (WKB) approximation [Ginzburg, Chapter 4, 1970]. This estimation is only valid if 1) the permittivity is not close to zero which is equivalent to the propagation frequency being well above the plasma frequency and 2) the permittivity is relatively constant over an entire wavelength as is stated mathematically in Equation 2.12.

$$\lambda_o < \frac{\varepsilon_r}{|\partial \varepsilon_r / \partial x|} \qquad \bullet 2\text{-}12$$

If these conditions do not hold then the constant phase fronts of the plane wave are deformed and the plane wave no longer maintains a coherent structure through space. Condition 1 is valid since the maximum plasma frequency throughout the plumes is 4 GHz. The validity of condition 2 is demonstrated in Figure 2.1 for a representative cross section where the permittivity divided by the gradient of the permittivity is plotted over a representative cross section of the plume.

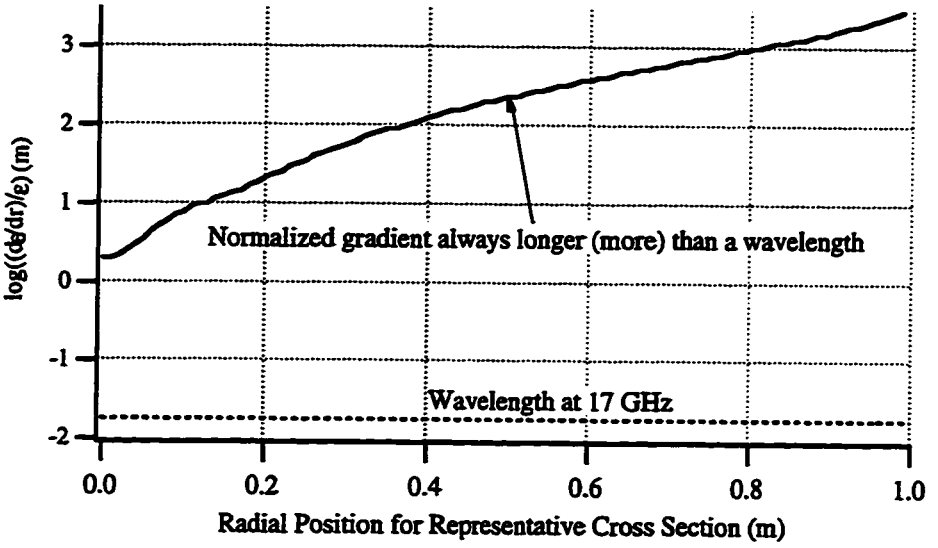

Figure 2.1. Plot of condition for geometric optic for a representative cross section of the SPT-100 plume at 0.09 m from the thruster exit plane.

In the figure, the wavelength limit for 17 GHz is never surpassed, therefore Equation 2.12 holds. Thus, by assuming the geometric optics approximation, the electromagnetic wave can take the traditional form of a plane wave:

$$E = E_o e^{j(kr-\omega t)}. \qquad \bullet 2\text{-}13$$

By taking this form, predicting the spatial variation in the wave front becomes a tractable problem which will be discussed in Section 2.2.

Effects of the wave-number time dependence are simplified by identifying the type of the plasma density variation. One possible method to categorize the time dependence of the plasma density would be as broadband white noise (fast random fluctuations), continuously drifting density (slow random fluctuations), or Fourier components of finite bandwidth (coherent fluctuations). The first situation (white noise) will be found to be inaccurate in Chapter 4 since broadband noise would cause degradation of the signal to noise ratio equally across the spectrum. The second situation (drifting density) will also be found not to be the case since a drifting density variation would indicate an unstable thruster system. Therefore, the variation will be considered as Fourier components of finite bandwidths which will be consistent with the findings here and elsewhere [Dickens, 1995, *et al.* 1995a, *et al.* 1995b]. The Fourier harmonics produce variation in the phase which takes the form of phase modulation, and also cause time-varying wave bending which slightly alters the received power level that takes the form of amplitude modulation.

In summary, the conditions for tractable plane wave propagation of the ordinary mode are 1) the spatial and time variation must be separable; 2) $\omega_{pe} >> \omega_c$ and B_O small; 3) $\omega >> \nu_c$; 4) $\varepsilon_r > 0$ and $\omega > \omega_{pe}$; 5) $\lambda_o < \frac{\varepsilon_r}{\partial \varepsilon_r / \partial r}$; and 6) time can be expressed in a Fourier expansion. Since all of the conditions hold in the two thrusters under consideration, the simple dispersion relation of the ordinary mode is used in Section 2.2 which will review the theory for tracking the components of the wavefront.

2.2 Predictive Model: Ray Tracing

Given the geometric optics approximation established by Section 2.1, spatial variation of plane-wave electric fields can be predicted through the technique of ray tracing. Initially, the electric field is divided into discrete rays, and then spatial transformations of the electric field parameters are used to find the field at any location given the field at an origin. Taking a single ray, a spatial transformation determines the field path. Given a

path, the electric field in Equation 2.14 represents the field at position s_2 given the field at position s_1 multiplied by transformations of phase ($\Delta\phi_{12}$), magnitude (MF_{12}), and polarization ($\hat{e}$).

$$E(s_2) = \hat{e}E(s_1)MF_{12}\exp[-jk_o\Delta\phi_{12}] \qquad \bullet 2\text{-}14$$

The effect on polarization is negligible due to the minimal scattering and small magnetic field, two primary mechanisms of polarization shift. Each of the other transformations are evaluated and applied to this work.

In order to implement ray tracing, a wave is divided into discrete rays each given initial values of direction, phase, amplitude, and polarization. In a plane wave, all of the rays are equal across a semi-infinite span. In the case of interest, a lens corrected horn antenna is transmitting the wave. An antenna has a finite aperture size, and a variable field distribution. It is assumed that all rays in the aperture are aligned along the direction of propagation. The phase is assumed uniform due to the lens correction of the horn antennas. The amplitude is characterized experimentally in Section 2.4 as a Gaussian distribution. Lastly the polarization is assumed to be linearly oriented orthogonal to both the thruster axis and the direction of propagation.

The natural path of these discrete rays, all starting with identical initial value, is determined by the differential Equation 2.15 [Born, *et al.* Chapter 3, 1964] which physically indicates that the ray, *s*, follows the gradients of the electron density that is given by the permittivity. Since this is a continuum statement of Snell's law, the implementation of this equation involves discretizing the media and repeatedly applies Snell's law.

$$\frac{\partial}{\partial s}[n_{IR}(s)\hat{s}] = \nabla n_{IR}(s) \qquad \bullet 2\text{-}15$$

The next field quantity, phase variation, directly uses the ray path established by Equation 2.16 [Born, *et al.* Chapter 3, 1964]. The spatial phase variation is established by the integration of the kx term in the exponent of Equation 2.13. Integration of this term along the ray path gives the phase difference between two points as in Equation 2.16.

$$\Delta\phi_{12} = \phi(s_2) - \phi(s_1) = k_o \int_{s_1}^{s_2} n_{IR}(s)\partial s \qquad \bullet 2\text{-}16$$

A similar method to phase tracking can be applied to the magnitude; however, since it has been assumed there is no attenuation along the path (Section 2.1), the change in amplitude is simply a result of ray bending. This fact leads to a simple method to find amplitude change using the conservation of energy as demonstrated in Figure 2.2. The energy is taken as the field intensity where the intensity per unit area, S, is multiplied by the unit area, dA. A given intensity per unit area, S_1, is assigned to the ray at point 1, which represents the average intensity over a unit area, dA_1. Now take the same ray at point 2 with intensity per unit area, I_2, and occupying unit area, dA_2. Making use of the conservation of energy, Equation 2.17 [Born, *et al.* Chapter 3, 1964] represents the magnitude factor transformation using the ratio of the differential area occupied by the ray at positions one and two.

$$MF^2 = \frac{S(s_2)}{S(s_1)} = \frac{dA(s_1)}{dA(s_2)} \qquad \bullet 2\text{-}17$$

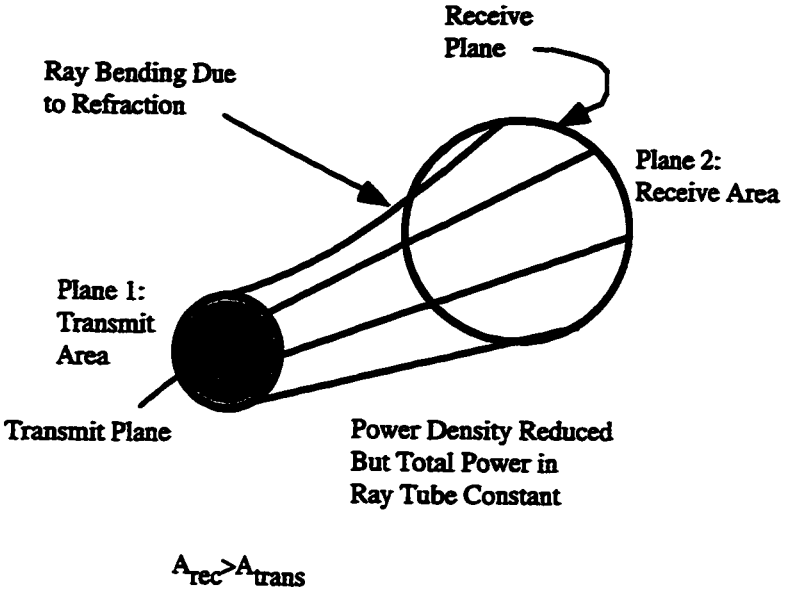

Figure 2.2. Ray tube analysis produces change in power density.

The analytic transformations have been addressed for an electric field starting at a given position and moving to a new position. The ray path can be tracked and the phase and amplitude can be determined at any given point along the ray path given a starting value. The phase tracking is used in microwave interferometry in Section 2.3 to find the index of refraction and hence the density. All of the parameter transformations will be utilized in the analysis of the data in Chapter 4.

2.2.1 Electron Density Diagnostic Technique: Microwave Interferometry

Microwave interferometry uses the phase transformation in Section 2.2 to determine electron number density. The phase transformation relates the phase delay to the line integrated electron density of the plasma along the propagation path. The line integrated density is used to find local electron density through the technique of Abel inversion. Then, the inversion integral is implemented through two methods: (1) assuming an analytical expression for the phase shift or (2) transformation of the Abel integral using the Hankel and Fourier transforms [Smith, 1988].

The phase delay difference of two waves relates to the propagation path difference. By reducing the path difference to only the path difference due to the presence of the plasma, the plasma density is directly related to the phase difference through Equation 2.19 [Heald, *et al.* 1969].

$$\Delta\phi = \phi_{vacuum} - \phi_{plasma} = \frac{\omega}{2cn_c}\int_{s_1}^{s_2} n_e(x,z)\partial s \qquad \bullet 2\text{-}18$$

The derivation of this equation utilized the phase transformation of Section 2.2 for a vacuum and a plasma, and it assumes that the electron density is much less than the critical density at 17 GHz.

A single measurement is of phase difference or integrated electron density; however the local electron density is of greater interest. In order to find local density, a series of spatial measurements as in Figure 2.3 are recorded where the final measurement is of free space.

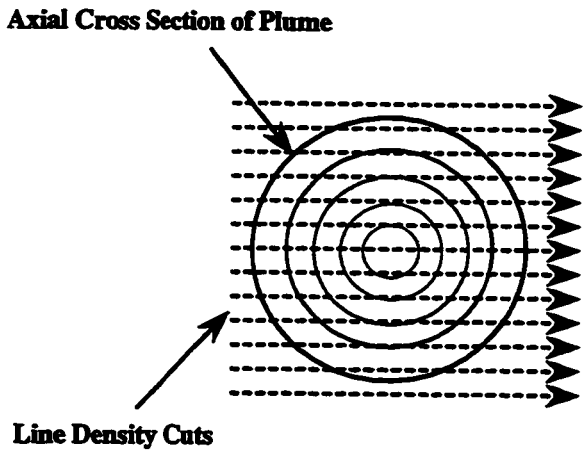

Figure 2.3. Schematic of measurement rays for a cross section.

The spatial map of the line integrated density, Equation 2.19, is mathematically manipulated through Abel analysis into Equation 2.20 [Sips, 1991; Wu, *et al.* 1989; Okada, *et al.* 1989; Smith, 1988, *et al.* 1987] by assuming radial symmetry.

$$n(r) = -\frac{\lambda n_c}{\pi^2} \int_r^R \left(\frac{\partial \phi(x)/\partial x}{\sqrt{x^2 - r^2}} \right) dx \qquad \bullet 2\text{-}19$$

The assumption of radial symmetry is well justified in both cases and will be demonstrated for the SPT-100 in Chapter 4. Physically, the integral starts at the edge of the plasma (r=R) where the permittivity of free space is known. The integral then incrementally adds the effect of the plasma progressing inward to the desired radius using the incremental change in the phase which is proportional to the density increment [Lanquart, 1982].

The implementation of the Abel integral is not straightforward due to the derivative of the phase data and the pole at the integral end point. Two alternatives are implemented with different advantages. The first implementation, which is used for the arcjet measurement, uses an analytical fit to the raw data that closely matches the trends in the measurements. This option provides an analytical solution; therefore, eliminating any issue with the derivative or pole. This also provides greater flexibility in the measurement if the positioning system cannot move sufficiently out of the plasma. The second option which is used for the SPT-100 measurements is to mathematically remove both the derivative and the pole through a Fourier transform and a Hankel transform [Johnson, 1986; Smith, *et al.* 1987; Gopalan, *et al.* 1983; Cavanagh, *et al.* 1979] as stated in Equation 2.21.

$$n_e(r) = 2\lambda n_c \int_0^{+\infty} q J_o(2\pi r q) \int_{-\infty}^{+\infty} \phi(x) \exp(-j2\pi x q) dx dq \qquad \bullet 2\text{-}20$$

This method removes the assumption of a functional form and also provides a convenient step in which to low-pass-filter [Sharma, 1986] the raw data after the Fourier transform; however, this method requires a complete spatial mapping of the phase into a region that is essentially free space. Both methods are utilized in Chapter 4.

2.3 Microwave Measurement System

Sections 2.1 to 2.3 have established a mathematical description of wave propagation in the plasma of the arcjet and SPT-100 thrusters. In order to characterize the wave propagation experimentally, it is necessary to measure the phase difference, magnitude difference, and spectral content of a wave propagating through a plasma compared with free-space propagation. A microwave system to measure these quantities is described and then characterized.

2.3.1 System Description

The measurement system is composed of five primary components: the positioning system, support structure, the antennas, the frequency up-down conversion circuit, and the data acquisition system. All of the components in Figure 2.4 are placed in a vacuum chamber, Figure 2.5, except the data acquisition system which is composed of the network and spectrum analyzers and a computer. Figure 2.6 shows a photograph of the microwave system inside the chamber. In the chamber, the positioning system moves the support structure. The support structure holds the antennas, connecting coaxial cable, and conversion circuit. The conversion circuit is connected to the data acquisition system through a pair of 15 m flexible microwave coaxial cables.

2.3.1.1 Vacuum Facility

The vacuum chamber which is stainless-steel and 9-m-long by 6-m-diameter is located at the Plasmadynamics and Electric Propulsion Laboratory (PEPL) at the University

of Michigan (Figure 2.5 and 2.7). The vacuum facility is supported by six 0.81-m-diameter diffusion pumps each rated at 32,000 L/s (with water-cooled cold traps), backed by two 2,000 cfm blowers, and four 400 cfm mechanical pumps. These pumps give the facility an overall pumping speed of over 300,000 L/sec for H_2. The experimental facilities are described in more detail in Gallimore [*et al.* 1994].

2.3.1.2 Positioning System

A state-of-the-art probe positioning system provides the capability to spatially map plume parameters. The system is driven and monitored with a computer. The positioning system is mounted on a movable platform to allow for measurements to be made throughout the chamber. The positioning system contains two linear stages with 0.9 m of travel in the axial direction and 1.5 m of travel in the radial direction. The axial direction, shown in Figure 2.4, is along the axis of the thruster. The radial axis indicates the direction orthogonal to the plane created by the thruster axis and the microwave transmission direction.

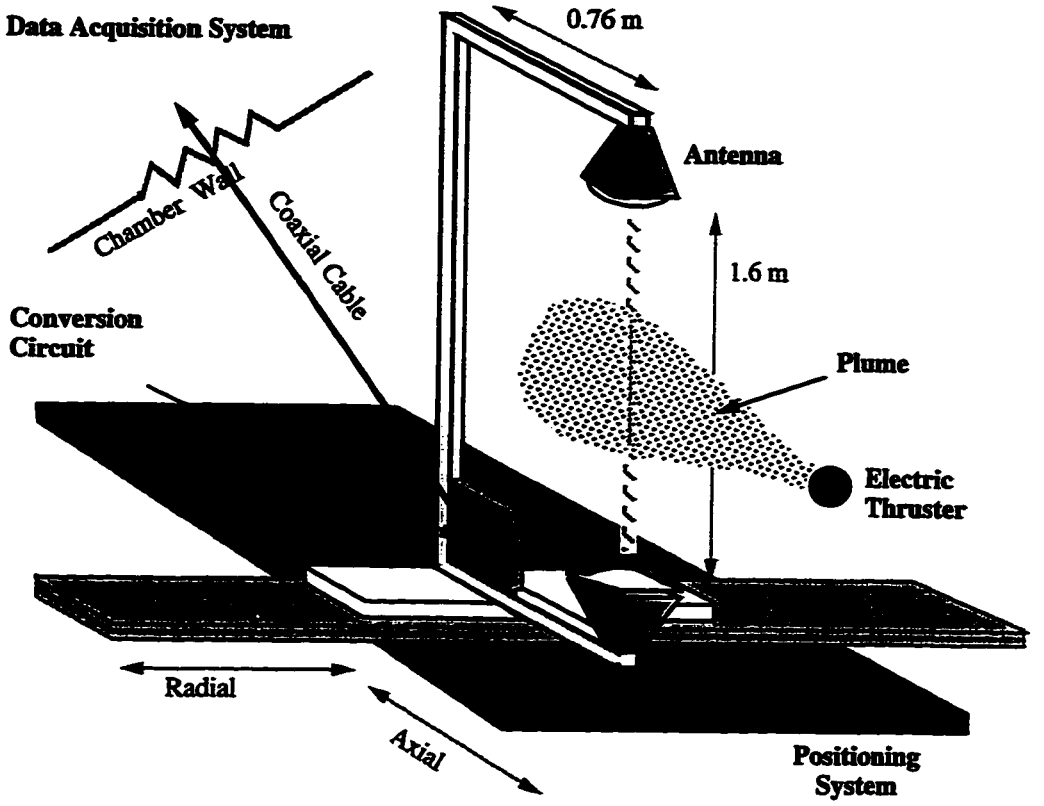

Figure 2.4. Schematic of microwave system.

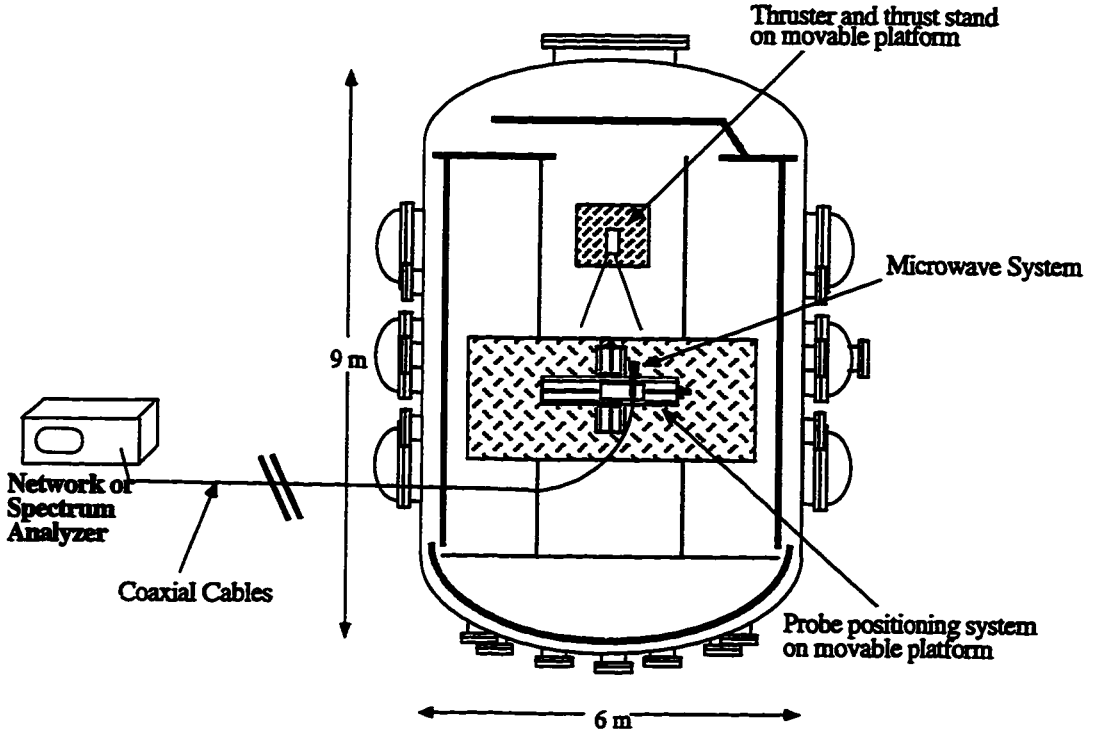

Figure 2.5. Measurement system in vacuum facility.

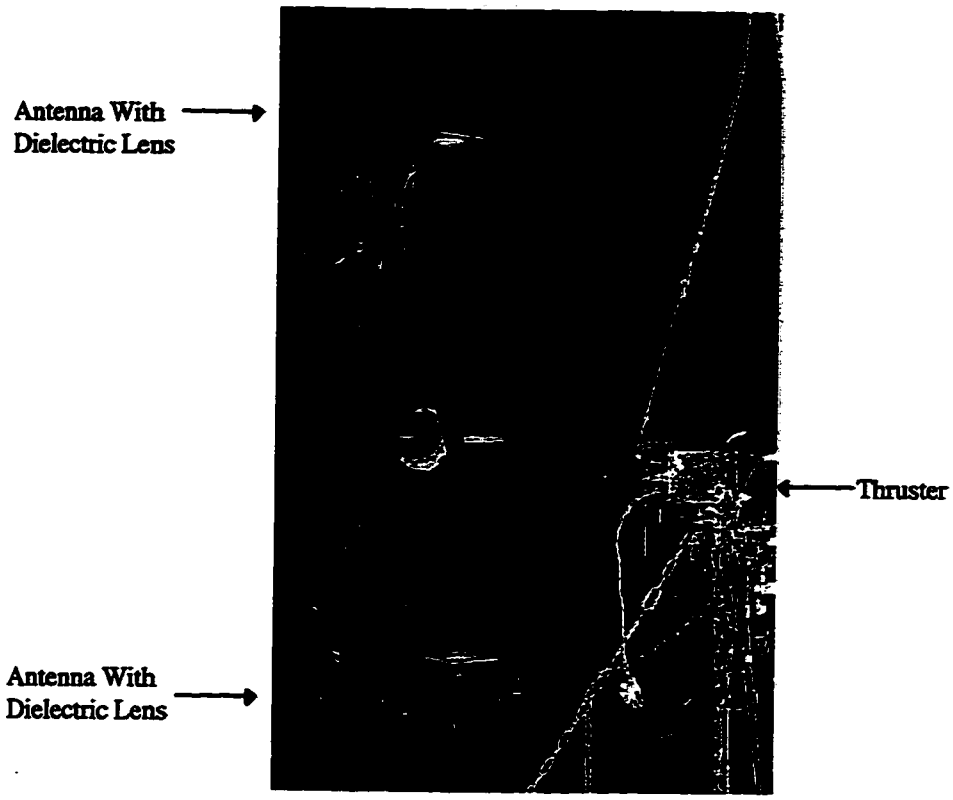

Figure 2.6. Photograph of microwave measurement system in vacuum chamber. Thruster on right is emitting away from photograph.

Figure 2.7. Photograph of vacuum chamber.

2.3.1.3 Support Structure

The steel support structure for the frequency conversion circuit, coaxial cable, and antennas is attached directly to the radial stage of the positioning table. The conversion circuit has been attached to the supports via a copper mounting plate which provides effective heat sinking. Semi-rigid coaxial cable attached to the steel supports connects the circuit to the horn antennas. The antennas are separated by 1.65 m and configured to transmit vertically through the plume. In addition to measurement components, graphfoil is used when necessary, in order to minimize sputtering of the support structure. One characteristic of the support structure is that table movement produces slight vibration in the structure. This vibration contributes to total phase noise which will later be quantified.

2.3.1.4 Antennas

The horn antennas, which are dielectric lens corrected, are designed for a narrow beam that transmits the signal through a narrow section of the plasma. The antennas are designed to minimize overall size while maintaining high gain [Lo, *et al.* 1988; Collin, 1985; Bhartia, *et al.* 1984]. The antenna lens was designed so that its focal point was aligned with the phase center of the horn antenna [Muehldorf, 1970; Lo, *et al.* 1988], and then the lens has been placed experimentally to optimize the power transmitted between the horns. The antennas have full angle half power beam widths between 7° and 8° and approximately 25 dB gain for both the *E*-plane and the *H*-plane. Another antenna characteristic is that they exhibit negligible phase sensitivity to nearby dielectric or metallic scattering sites outside of the line-of-sight between the antenna structures. This fact indicates that the transmitted signal is essentially limited to a collimated beam 0.13 m in diameter (dimension of antenna) between the antennas. The antenna beam distribution will be addressed again in the next section in the discussion on calibration.

2.3.1.5 Up-down conversion circuit

The frequency conversion circuit is utilized due to the long distance between the network analyzer outside of the chamber and the antenna system inside the chamber. The long distance produces unacceptable loss in power and consequently, accuracy, when the Ku band signal is transmitted directly through the 15 m of coaxial cable necessary to connect the network analyzer to the antennas.

The circuit in Figure 2.7 receives a low frequency (1 to 3 GHz) signal from the network analyzer, up converts the signal frequency, filters either the upper or lower sideband, transmits the signal to the antennas, receives the signal from the antennas, down converts back to 1 to 3 GHz, and finally amplifies the signal. The low frequency signal, 1 to 3 GHz, is converted to the Ku band via a mixer using a 15 GHz phase locked oscillator. The oscillator supplies a reference to both the up and down mixing sides of the circuit. The reference signal is guided by the power divider, isolators, and band-pass filter number 2. The isolators and band-pass filter number 2 limit the effects of signal leakage and reflection. The signal from the mixer includes both the upper and lower sidebands either of which is available for use. The desired sideband is chosen by band-pass filter number 1. The upper sideband (16 to 18 GHz) is available with the present configuration. Use of the lower sideband is possible with an alternate band pass filter, making available the range from 12 to 14 GHz. The circuit transmits less than 0.1 mW through the plume, then the received signal is down-converted through the second mixer utilizing the phase locked oscillator. After frequency conversion, the signal is amplified and transmitted back to the network analyzer.

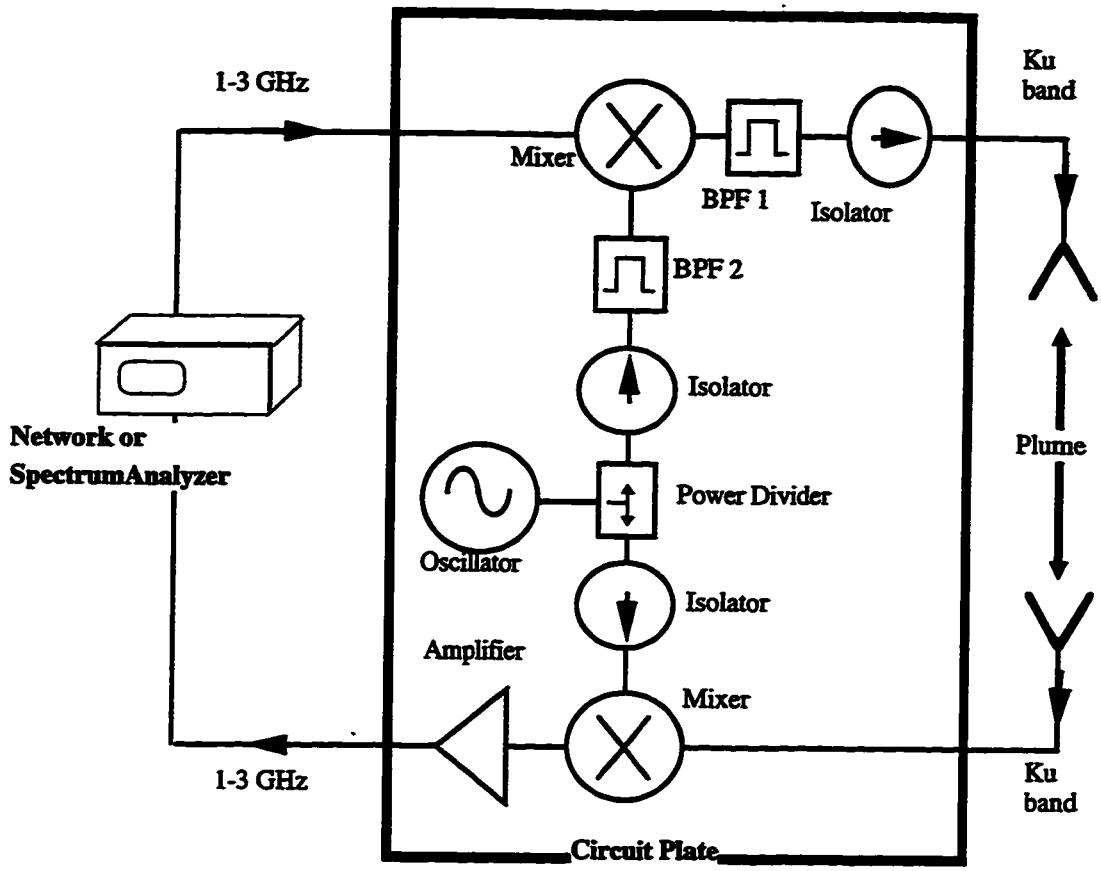

Figure 2.8. Circuit Diagram of Circuit in Figure 2-1.

2.3.1.6 Data acquisition systems

This microwave measurement system utilizes the capabilities of a network analyzer as a stable microwave source and both the network analyzer and a spectrum analyzer as sensitive microwave receivers. The network analyzer quantifies the phase and amplitude of a received microwave signal with reference to the transmitted signal whereas the spectrum analyzer quantifies the absolute spectral content of the received signal which is later referenced to an ambient measurement. Both analyzers are controlled via GPIB by a computer for data storage.

The microwave system has a number of capabilities necessary for accurate measurement of phase and amplitude. The network analyzer and the local oscillator are independently phase locked, providing a stable signal both in phase and amplitude. The

independence of the phased locked oscillators is not a problem since the phase of the conversion circuit is both inserted and removed from the signal during up and then down conversion. Additionally, network analyzers can isolate the test signal through standard time gating techniques when the frequency is swept over a sufficiently wide band width [Ohler, *et al.* 1995b].

2.3.2 System Characterization

General baseline characteristics provide information necessary for proper interpretation of measurements from the microwave system. Two measurable quantities, amplitude and phase noise are characterized in terms of random noise as well as signal drift. For the amplitude and phase measurements, a calibration function was developed to characterize the antenna propagation distribution through the use of a well known dielectric sample. The spectral measurements of the spectrum analyzer are dependent on the phase and amplitude characteristics, but the baseline characteristics can be summarized in ambient spectral measurements.

2.3.2.1 Noise and drift of phase and amplitude

The amplitude and phase noise result primarily from slight variation in the microwave signal from the network analyzer and vibration of the support structure causing variation in transmitter-receiver alignment. The noise level in the network analyzer is specified by the ratio of the return signal to the transmitted power level. The power ratio is -20 to -25 dB indicating theoretical network analyzer noise to be $\pm 0.5°$ and ± 0.2 dB (limitation of the microwave circuitry). The vibrational contribution to noise is found by first finding experimentally the total noise levels to be $\pm 1.5°$ and ± 0.2 dB. This indicates that the vibrational phase noise is $\pm 1.0°$ and the vibrational contribution to amplitude noise is negligible.

The drift in the signal frequency is primarily caused by temperature changes in the components of the system: local oscillator, amplifier, mixer, and coax cable. The temperature of the circuit plate has been monitored in order to establish temperature variation over time. In one experiment, the circuit plate temperature changes from ambient room temperature up to 50°C over the course of a 5 hour period. The variation of the plate temperature indicates significant temperature change of all microwave circuit components. Total drift was experimentally characterized due to the intractable nature of monitoring temperature on all system components and then using that information to calculate a theoretical drift. The total steady state drift was found to be less than 0.08 °K/min and 0.06 dB/min.

2.3.2.2 Calibration function

An antenna calibration function was found by first calculating the theoretical phase shift through a foam cylinder and then comparing the theoretical results to the measured phase shift across the same cylinder [Janson, 1994; Ohler, *et al.* 1995]. The theoretical calculation of phase shift for the cylinder [Ginzburg, 1970] is given by

$$\Delta\phi_{theory} = \frac{180}{\pi}\frac{2\pi}{\lambda}(n_{IR}-1)\left(R^2-x^2\right) \qquad \bullet 2\text{-}21$$

where $\Delta\phi_{theory}$ is the phase difference between a wave transmitted through free space and that transmitted through the cylinder in degrees, R is the radius of the cylinder, and x indicates the displacement of the transmission path from the center of the cylinder. The index of refraction of 1.08 was estimated from the peak of the experimental results. This estimation does not affect the final conclusion concerning the effect on our measurement of electron density.

The calibration function *FN* relates the theoretical, $\Delta\phi_{theory}$, and experimental, $\Delta\phi_{Exp}$, phase mathematically by

$$\Delta\phi_{Exp}(x) = \Delta\phi_{Theory}(x) * FN(x) \qquad \bullet 2\text{-}22$$

$$FN = \frac{1}{\sqrt{2\pi\sigma}} \exp\left[-\frac{1}{2}\left(\frac{x}{\sigma}\right)^2\right]. \qquad \bullet 2\text{-}23$$

The distribution function is spatially convolved with the theoretical phase (Equation 2.22) to arrive at the measured results. The assumed Gaussian distribution function, *FN*, was optimized by varying the standard deviation, σ. An optimal value of σ equal to 0.024 m was found by minimizing the difference between the left and right sides of Equation 2.23. The full width half maximum of the distribution function, which we take as a measure of system resolution indicates the resolution of the system is 2.36σ or 0.057 m. With this transfer function the effect of the finite size of the antenna beam can be removed from the plasma measurements.

2.3.2.3 Spectral baseline

The spectrum analyzer measurements depend on the time varying characteristics of the amplitude and phase, and the important spectral characteristics are summarized by an ambient spectral measurement without a plasma present. Figure 2.9 shows the baseline characteristics for a bandwidth of ±250 kHz and a resolution bandwidth of 10 Hz. The characteristics outside of this range are of less relevance for the thruster characterization. The peak received power level at 17 GHz is -16 dBm where Figure 2.9 shows the noise level relative to the peak power level. The noise level for offsets greater than about 100 kHz are just above -95 dB. The peaks at a number of frequencies such as ±200 kHz are attributed to noise from other vacuum chamber systems.

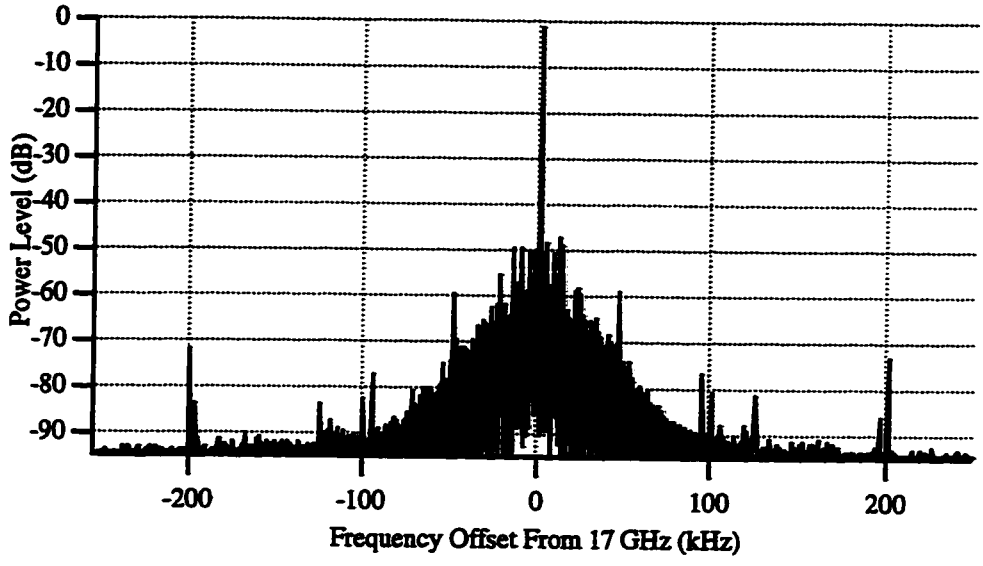

Figure 2.9. Spectral response of a transmitted signal with and without the plasma

CHAPTER 3

MICROWAVE MEASUREMENTS AND ELECTRON DENSITY CALCULATION FOR AN ARCJET AND SPT

3.0 Overview of Chapter

Characterization of both the arcjet and stationary plasma thrusters is important for understanding the physical processes of thrusters and for quantifying the impact to other satellite systems. The electron density of a 1 kW arcjet is spatially characterized through microwave interferometry and Abel inversion. Measurements are also made for comparison by a Langmuir probe. Additionally, a flight qualified stationary plasma thruster is characterized for its effect on microwave transmission. This characterization includes measurements of phase, amplitude, and power spectral density. The phase measurements are used to find electron density also through microwave interferometry and Abel inversion whereas the amplitude (or attenuation) and power spectral density measurements are used in the analysis of Chapter 4. A detailed description is found in Appendix C for the implementation and operation of the microwave system utilized in these measurements.

3.1 Arcjet Characterization

The arcjet is characterized by spatially mapping the electron density over the far-field region of the plume. Initially the experimental configuration is described. Then, phase measurements are presented which, after Abel analysis, yield local electron number density. The results are then compared to Langmuir probe measurements. Finally, the

results are discussed as related to three topics: spatial mapping of density, comparison to previously published results, and analysis of the estimated uncertainty.

3.1.1 Experimental Configuration

The electron density of a 1 kW arcjet (Figure 3.1) is characterized in the far field of the thruster. The arcjet uses hydrogen propellant and operates at 110 V and 10 A with a flow rate of 10 standard liters/minute (15 mg/s). Chamber pressure is maintained below 2.8×10^{-3} Pa (2×10^{-4} Torr) throughout the experiments. The arcjet is given 20 min to reach thermal equilibrium before data is collected.

The positioning system moves across the plume at 0.64 cm/s from -0.45 m to 1.1 m measured radially from the axis of the plume (thruster). The measurements are recorded every 0.5 cm radially in nine planes at constant axial distances from the thruster ranging from 0.3 m to 0.9 m. On an alternate day, with the same thruster stimulus, the Langmuir probe is swept across the arcjet plume to provide comparison data.

The microwave system in these measurements is similar to the general system described in Chapter 2. Two differences are a lower gain amplification and the absence of the bandpass filter #2 connecting the power divider to the mixer (transmit side of the circuit). These two differences produce slightly higher noise levels; however, this is offset by the lower noise characteristics of the thruster when compared to the SPT. The microwave measurements are taken at 17.5 GHz, but a total bandwidth of 2 GHz (16 o 18 GHz) is utilized to time gate the received signal. The total phase noise of the microwave system is ±0.5° peak-to-peak which is primarily due to a 40-dB difference between the transmitted and received signal.

A cylindrical single Langmuir probe is used to measure n_e and kT/e (electron temperature in electron volts) in the plume of the arcjet [Gallimore, *et al.* 1994]. The probe is composed of a rhenium electrode, 0.42 cm in diameter and 5.1 cm long, attached to a triaxial boom that is constructed of titanium with Teflon insulation. The collector electrode

has been formed by vapor-depositing rhenium on a molybdenum mandrill. The boom is approximately 4 mm in diameter and 18 cm long.

The collector electrode of the probe has been biased with respect to the chamber wall with a programmable bi-polar power supply. A function generator has been used to provide a 12.7 Hz triangular source waveform that is amplified to ±10 volts by a bi-polar supply. Given the fact that the electron temperature in the plume has been measured to be approximately 0.1 eV [Carney, *et al.* 1989a], 10 Volts is expected to be more than adequate for ensuring probe saturation. To verify this, probe traces have been observed on a digital oscilloscope and the data acquisition system in real-time to verify that electron and ion saturation are achieved.

Voltage probes and operational amplifiers are used to measure current, via a 10 Ohm shunt, and voltage of the Langmuir probe. Amplifier output signals are collected both by the computerized data acquisition system for storage and later processing, and by the digital oscilloscope for real-time processing. The data acquisition system stores 50 pairs of probe voltage-current values per voltage ramp.

For these measurements the ionization fraction of the plume is estimated to be 0.1% with an electron temperature of approximately 0.1 eV [Carney, *et al.* 1989a]. In the far-field, λ_e and $\lambda_{i,}$, (electron and ion mean free paths, respectively) are expected to be an order of magnitude larger than the radius of the large probe (r_p) and at least two orders of magnitude larger than the Debye length (λ_D) [Carney, *et al.* 1989a]. Furthermore, since r_p/λ_D will be approximately 20 or more throughout the plume, the Bohm thin sheath saturation current model used to analyze probe data is expected to be valid [Gallimore, *et al.* 1994; Tilley, *et al.* 1994]. Thus, the electron temperature and number density were obtained through the following equations [Carney, *et al.* 1989a].

$$\frac{d}{dV}\ln(I_e) = -\frac{e}{KT_e} \qquad \bullet 3\text{-}1$$

$$I_{oe} = A_p e n_e \sqrt{KT_e / 2\pi m_e} \qquad \bullet 3\text{-}2$$

where I_e and I_{oe} are the electron probe current and electron saturation current, respectively, A_p is the probe surface area, e is the characteristic electric charge, K is the Boltzmann constant, m_e is the electron mass, and T_e is the electron temperature in Kelvin.

The probe is rotated to 0, 5, 10, 20, and 30 degrees with respect to the thruster axis at each location. The table position is adjusted automatically at each angle to ensure that the collector electrode of the probe is in the appropriate axial and radial positions. The probe is moved continuously at a radial speed of 1.2 cm/s. Thus, 50 pairs of probe voltage-current data points are collected per millimeter of radial travel (voltage ramp). Only data collected at angles at which the axis of the probe is aligned with the local flow (i.e., minimum ion saturation current) are reported. This is to ensure the validity of the saturation model which assumes a quiescent plasma [Tilley, *et al.* 1994; Patterson, *et al.* 1985].

Figure 3.1. Photograph of an operating arcjet.

3.1.2 Results and Comparison to Langmuir Probe

The phase measured by the network analyzer is referenced to the phase at the perimeter of the plume where the electron density is below the detectability of the microwave system. In addition, the phase is adjusted for a small phase drift of 0.16° per sweep which is due to temperature change and outgassing in the microwave system. The phase noise of the complete system is approximately ±1°, which is the sum of vibrational noise in the positioning system and phase noise inherent in the microwave system.

After the phase shift of the microwave signal is found in a plane of constant axial distance from the thruster, the Abel analysis is applied to the data. Initially, the phase is verified to be approximately symmetric as is required by this implementation of the Abel analysis. The phase data is applied to a least-squares best fit to a reasonable functional form, Gaussian in this case. The functional equivalent to the data is used to analytically deconvolve the antenna pattern out of the phase data and then apply the Abel integral (as described in more detail in Chapter 2).

A representative data set is shown in Figure 3.2 where the phase shift measurements, Gaussian curve fit and derived electron density based on the analysis are shown for a single radial sweep at 0.39 m from the arcjet. Since the Gaussian is fit to the raw phase data, the subsequent electron density is also Gaussian in nature. As seen, the Gaussian curve fit closely follows the phase measurements from the arcjet which is also true at other positions. The standard deviation and variation of phase is typical of all data.

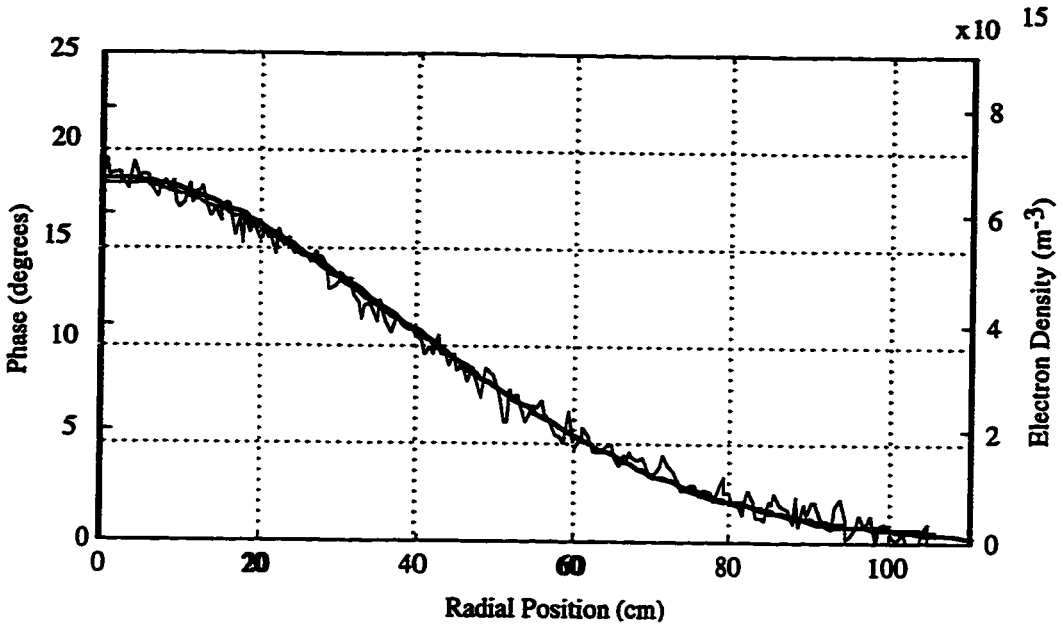

Figure 3.2. Comparison of the measured phase shift with the best fit Gaussian curve and the electron density calculated from the Abel inverted Gaussian curve. The measurement is 0.39 m from the exit plane of a 1 kW hydrogen arcjet.

Multiple sweeps across a path 0.30 m from the thruster indicate the repeatability of the peak density to be ±4%. This variation could, in part, be due to variation in the arcjet plume. Additionally, a peak density of approximately 10^{15} m^{-3} corresponds to a peak phase shift of just under 3° for the arcjet plume. Given that the phase noise is ±1°, density distributions with less than 10^{15} m^{-3} peak density (for distribution similar to the arcjet) are below the limit of detectability for the current system operating at 17.5 GHz.

Langmuir probe density data is found from straight forward analysis of voltage-current traces analyzed using the Bohm thin-sheath ion saturation current model as described earlier. The data as shown in Figure 3.3 and 3.4 is fit to a Gaussian function to highlight the trend in the probe measurements in order to more readily compare them to the microwave interferometry data. As with the interferometry data, the Langmuir probe data follows the Gaussian function well except at the lowest densities where the Langmuir probe data overpredicts the density. The Langmuir probe overprediction is due to the low

measurement sensitivity of this implementation of the Langmuir probe in the lower density regime. Possible sources of error for the Langmuir probe include local perturbation of plasma and uncertainty in the probe area (due to misalignment with the flow). The accuracy of the probe results is estimated to be ±50% [Tilley, *et al.* 1990]. (For further description of the Langmuir probe measurements see Gallimore [*et al.* 1994].)

While the shape of the two data sets matches well, the Langmuir probe predicts a lower density than microwave interferometry, as is the case with past comparisons [Overzet, *et al.* 1993; Neumann, *et al.* 1993]. In this case, Langmuir probe results are as much as a factor of two lower than the microwave interferometry. Aside from the theoretical inaccuracy associated with either diagnostic technique, it is thought that the small perturbations made by the Langmuir probe in the plasma are not modeled completely in the theory of electron density calculation [Overzet, *et al.* 1993]. These perturbations may in fact affect the manner in which charged particles are collected.

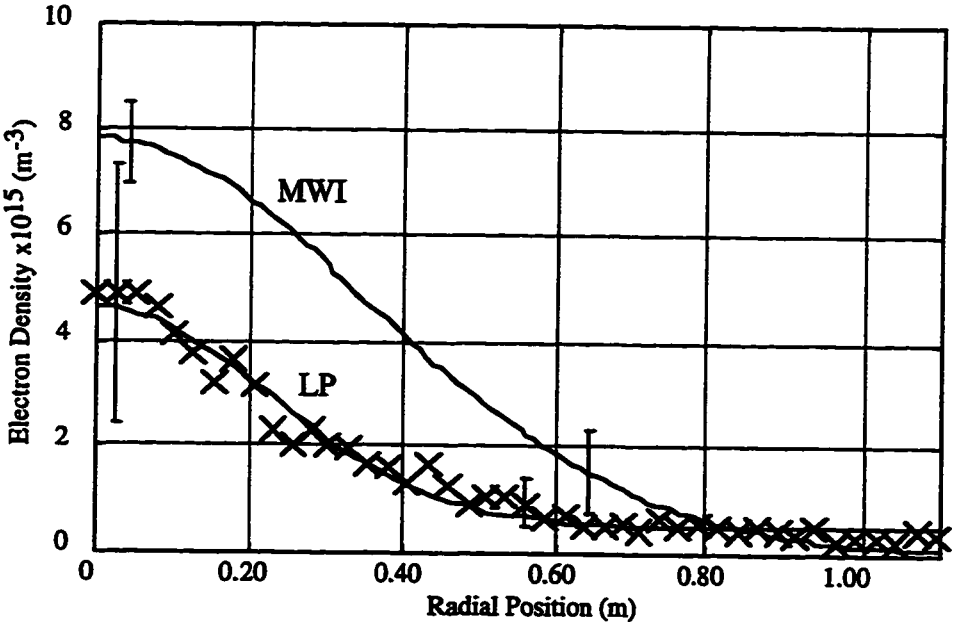

Figure 3.3. Comparison of electron density measured by a microwave interferometer with that of a Langmuir probe at 0.30 m from the exit plane of the arcjet.

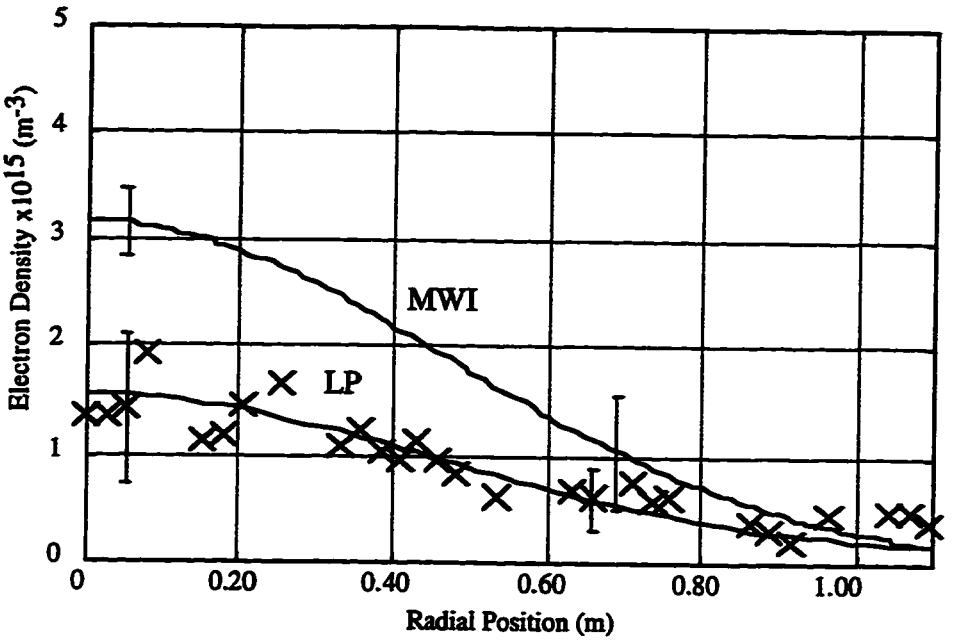

Figure 3.4. Comparison of electron density measured by a microwave interferometer with that of a Langmuir probe at 0.30 m from the exit plane of the arcjet.

3.1.3 Discussion

A mapping of the electron density was developed by sweeping across the plume at many axial positions. The position of the interferometer was limited by other diagnostic instruments to not closer than 0.3 m from the thruster. The nonuniform spacing results from measurements during diagnostics with spatial requirements different from the interferometer. Figure 3.5 shows the resulting electron density contours. This figure highlights the Gaussian nature across the radial direction and a nearly linear decrease of density along the axis. Figure 3.6 shows a plot of the peak electron density and the full-width half-maximum as they vary along the axial direction. A linear fit has been applied to both curves

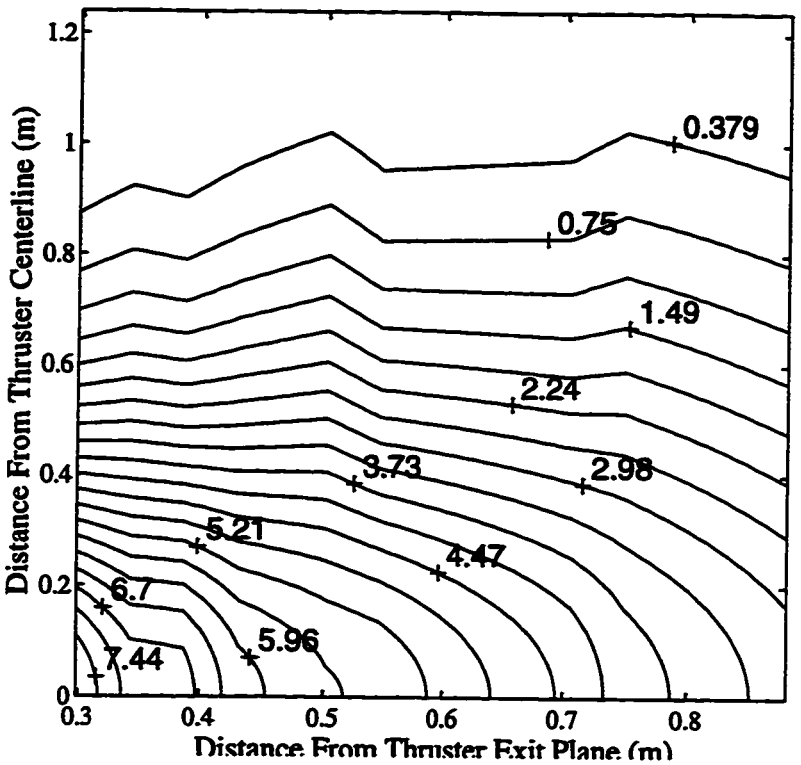

Figure 3.5. Electron density contour mapping developed from a 1 kW hydrogen arcjet. Measurements are taken at various axial distances from the exit plane of the arcjet. Phase measurements are taken every 0.5 cm radially.

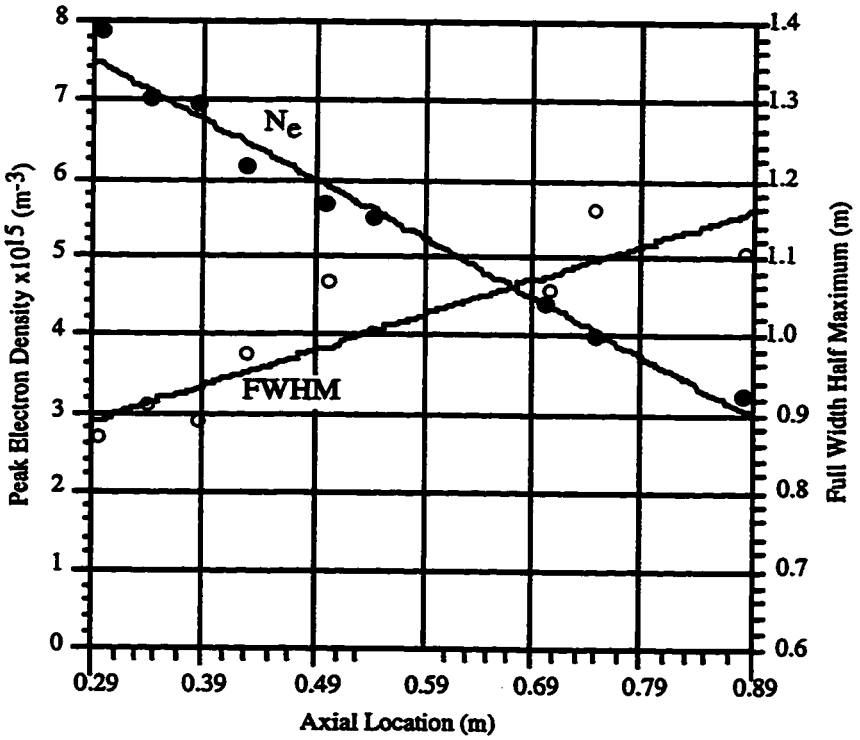

Figure 3.6. Peak electron density and full width half maximum both along the thruster axis.

Although no references were found reporting on a 1 kW arcjet using hydrogen, Carney [1988] reported on a similar device with simulated hydrazine (N_2H_4), which should have a lower electron density than pure hydrogen. Carney's measurement of the peak density at 0.30 m from the exit plane concurs with our own measurements. The peak density for hydrazine of $2x10^{15}$ m^{-3} at 0.30 m from the exit plane is at the limit of detectability with our present system. Additional comparison is found in Birkner [*et al.* 1990] who also reports on arcjet data where the distribution is reported to fit to

$$n_e = n_0 \exp(-c\theta)/\rho^2 \qquad \bullet 3\text{-}3$$

where θ is the angle off centerline and ρ is the distance from the thruster. The data presented here can be fit with this functional form. Birkner's data could be fit with a Gaussian in the radial direction; however, the linear axial variation is not appropriate. Additional data closer to the thruster is necessary to establish this functional form for our data set.

The accuracy of the microwave interferometer was estimated by a total error analysis and compared to the repeatability of the experimental system. The percent accuracy varies from most accurate near the peak density to less accurate at the edge of the density profile where the results are near the noise limit of the system. The significant sources of error evaluated at the center of the density profile were phase drift and noise (1%), positional uncertainty (0.5%), and finite horn separation (2.3%). The effect of error sources on the final results were found by experimentally determining the uncertainty for each of the sources and then simulating the effect on a representative data set. The last two error is a downward biases inherent in the experimental system whereas the first two are random noise terms. The finite horn separation refers to the inaccuracy due to the horns passing through the fringe region of the plume. An additional 1% of uncertainty is necessary to account for all other errors. A measured repeatability of 4% on any given day

correlates well with the predicted random error suggesting a slight variability on the order of 2.5% in the plasma plume due to arcjet operation. The accuracy of the system decreases towards the edge of the density profile with the sum of the error terms increasing by a factor of five. Thus, the interferometer evaluated in this analysis is highly accurate with better than 10% accuracy near the center of the density profile while maintaining a good degree of precision even in the fringe measurements.

3.2 Fakel Thruster Characterization

The Fakel thruster is characterized by spatially mapping phase, amplitude, and power spectral density. Initially the experimental parameters are described. Then, phase measurements are presented which, after Abel analysis, yields local electron number density over the transition region between near and far field. The results are compared to previous Langmuir probes measurements. Lastly, the results are presented for attenuation and power spectral density over a subset of the spatial region characterized in the phase measurements.

3.2.1 Experimental Parameters

The Fakel SPT, which is shown in Figures 3.7, is characterized in the transition region between the near and far field of the thruster. The Fakel thruster is operated at 300 V and 4.5 A for a discharge using xenon propellant at a flow rate of 5.5 mg/s through the anode and 0.29 mg/s through the hollow cathode. The flow is varied slightly in order to maintain the discharge current. The tank pressure is maintained below $6x10^{-3}$ Pa ($5x10^{-5}$ Torr) throughout the experiments. (For a more detailed description of the thruster see Appendix B).

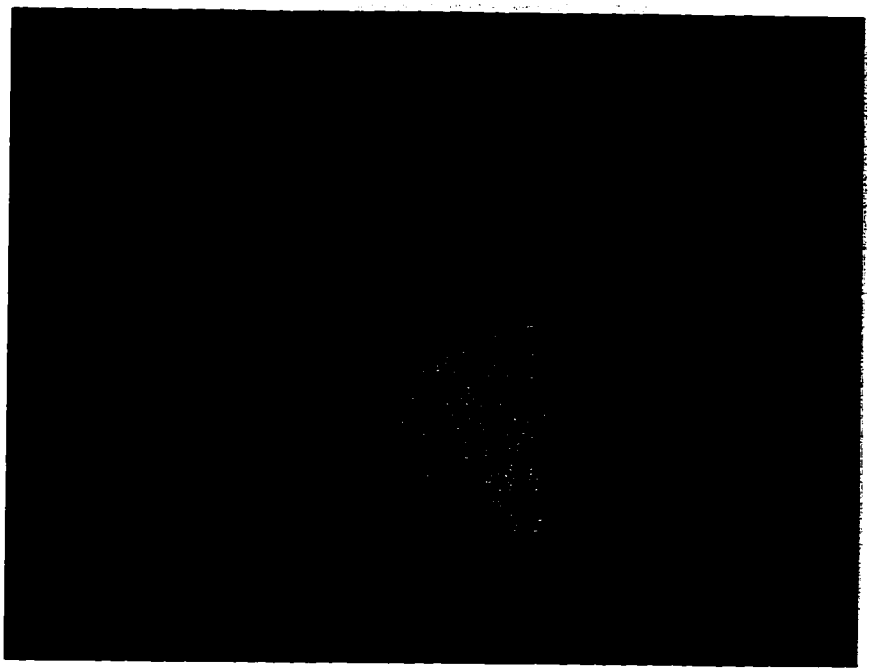

Figure 3.7. Picture of Fakel thruster plume.

Measurements of differential phase, differential amplitude, and power spectral density are presented. The phase measurements provide a direct indication of the electron density while the amplitude and spectral measurements indicate additional effects of the thruster plume on a microwave signal.

The positioning system provides the capability to spatially map all three parameters. Differential phase measurements have been taken in planes orthogonal to the thruster axis. The positioning system moves the microwave system throughout the plume at a rate of 0.01 m/s for the phase characterization. Measurements were recorded along the plane approximately every 0.005 m for averaging purposes. The planes are located between 0.09 m and 0.90 m axially from the thruster. Along the axial direction, measurements were taken in 0.03 m increments from 0.09 m to 0.39 m and every 0.06 m farther out from the thruster. The attenuation and power spectral density measurements are recorded for a subset of the positions of the phase. The attenuation measurements are taken in five axial planes from 0.09 m to 0.33 m from the thruster. The power spectral density

measurements are taken at three locations: 0.15 m axial, 0 m radial; 0.75 m axial, 0 m radial; and 0.15 m axial, 0.25 m radial.

The microwave system for these measurements is described in detail in Chapter 5. A transmission frequency of 17 GHz is used in all three measurements where no time gating is necessary (verified experimentally). The phase noise of the microwave system alone is ±0.2° peak-to-peak which is due primarily the inherent limitations of the network analyzer for a 20 dB power difference between the transmitted and received power. Additional phase noise is produced by system vibration during positioning that results in total system phase noise of ±2.0°. The random noise in the amplitude measurements is ±0.2 dB where the positioning vibration did not increase the noise level higher than the noise inherent in the microwave circuit.

3.2.2 Phase Measurements and Electron Density Results

The phase measurements are recorded in a number of planes at constant axial distance from the thruster. The phase measurements are an indication of the line-integrated density. Abel analysis is implemented to find the local density. In order to implement Abel analysis, the planes are assumed to be radially symmetric. (This assumption is addressed in more detail in Chapter 4.) A detailed description of the analysis is found in Appendix C.

To determine the local electron number density, the antenna pattern first is removed from the measurements via deconvolution using the calibration distribution function as described in Chapter 2. A low pass filter then removes the high frequency noise from the measurement and deconvolution process. The Abel inversion through the transform method then finds the local electron number density in the plume. Finally, for data analysis purposes, the data are transformed from a Cartesian coordinate system into a spherical coordinate system through linear interpolation. Figure 3.8 shows one set of phase data 0.09 m from the thruster exit plane overlaid with the resulting electron density distribution. From a set of planar characterizations a spatial mapping is developed as in Figure 3.9

where the contours qualitatively show the beam-like nature of the electron density. Only half of the plane is needed since the density is assumed to be radially symmetric. The axial density profile (Figure 3.10) provides a scale for the contour plot.

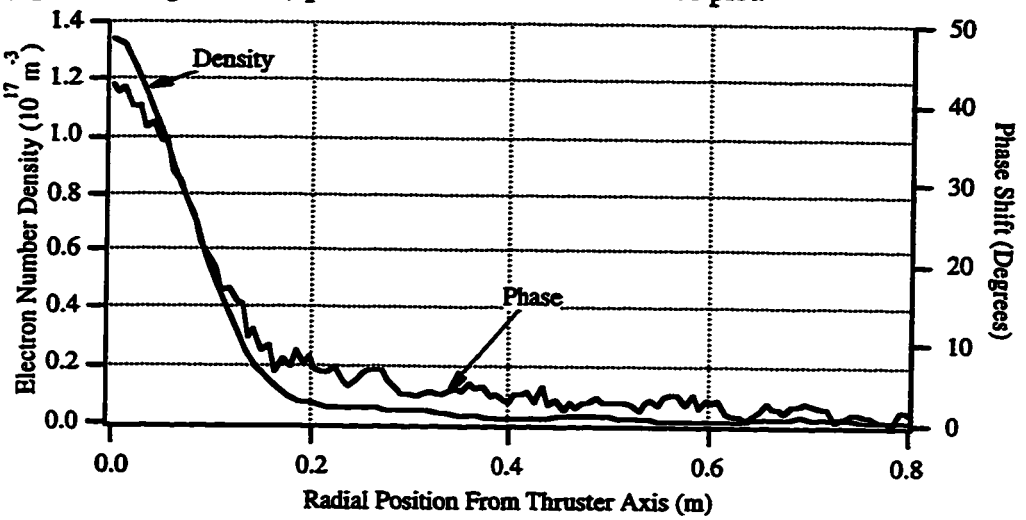

Figure 3.8. Overlay of phase measurements and calculated electron density for the Fakel thruster at 0.009 m from the thruster exit plane.

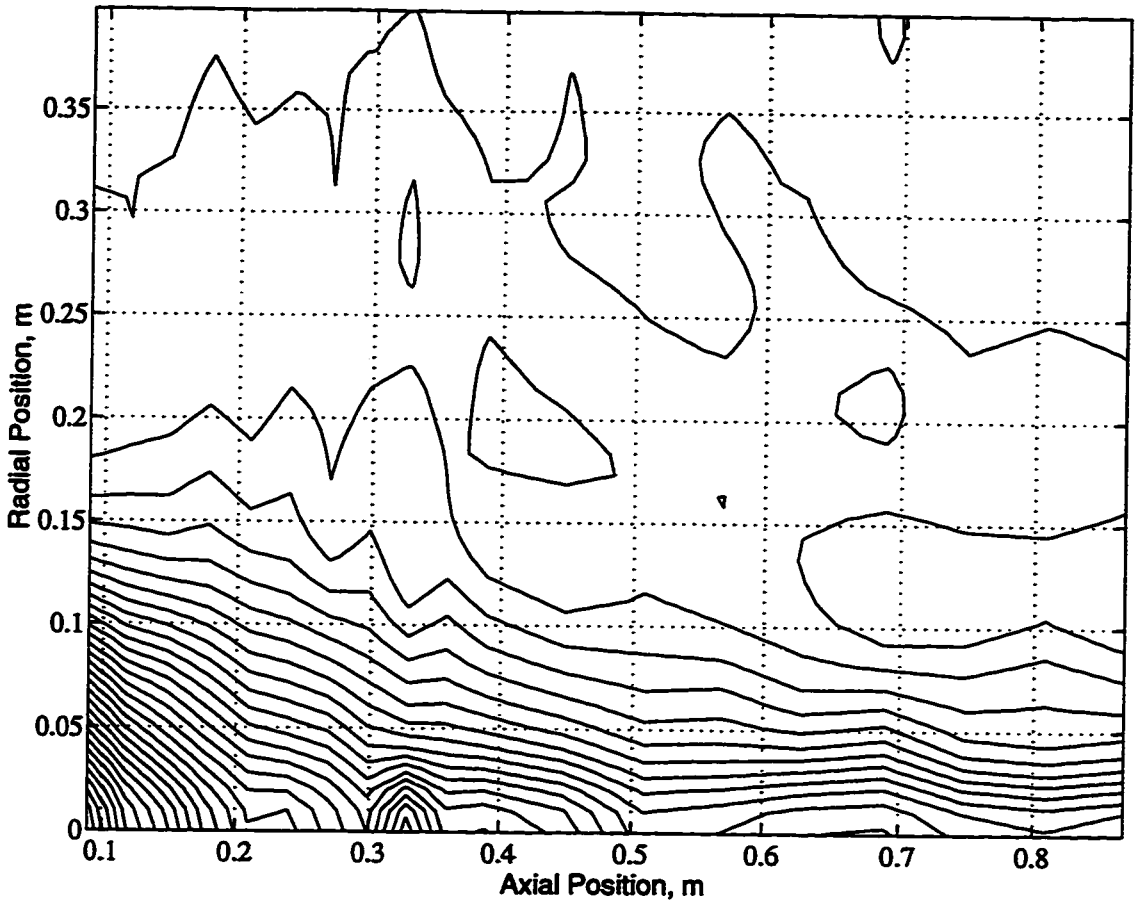

Figure 3.9. Electron density contours found from Abel inversion of the phase measurement spatial map.

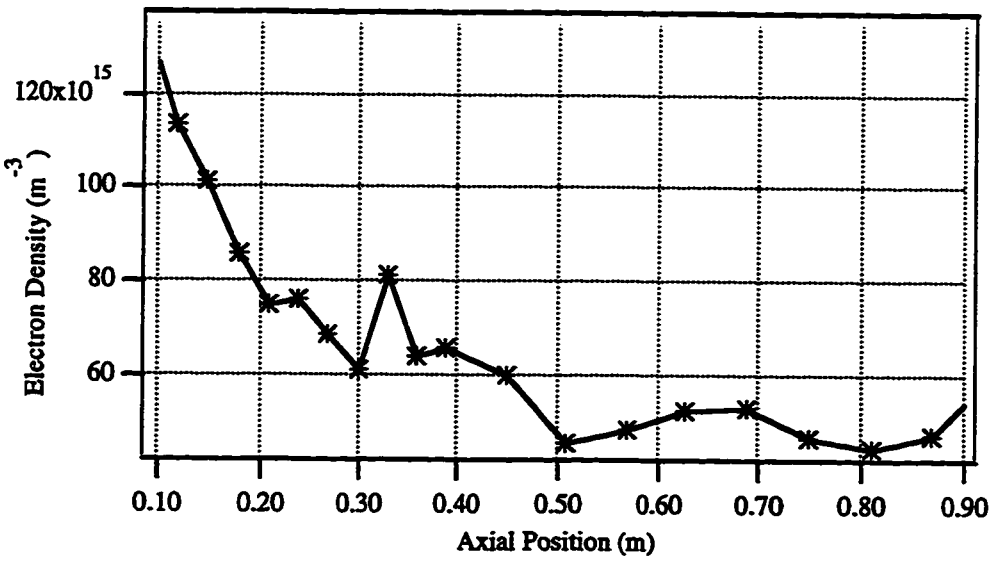

Figure 3.10. Axial variation of electron density corresponding to the spatial mapping of electron density.

The results presented here are comparable to the previously reported data [Myers, *et al.* 1993] within the uncertainty of the measurements. Figure 3.11 shows density measurements at 0.30 m for both the microwave measurements and previously reported Langmuir probe data [Myers, *et al.* 1993]. The measurements reported here show a peak density of 6.2×10^{16} m^{-3} and reduction by a factor of three along a similar contour at 21° off center line. The Langmuir probe measurements found a peak density of 5.7×10^{16} m^{-3} decreasing by factor of three at 22° off center line for the SPT-100 at 0.30 m. The difference in measurements is well within the uncertainty expected of the separate measurements.

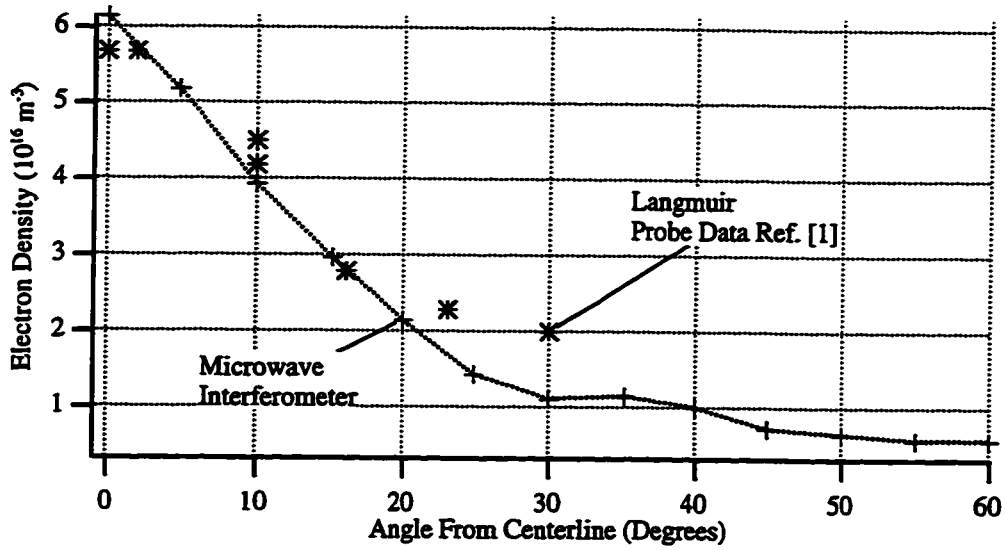

Figure 3.11. Comparison of microwave measurements and Langmuir probe results [Myers, *et al.* 1989] both at 0.3 m from the thruster exit plane.

The total system measurement error for electron density is estimated by examining the individual sources of uncertainty within the measurement and the analysis phases. A basic model of the density based on the phase measurements is used in simulations to assess uncertainty. Each of the factors is varied individually to determine the effect on the final results. The percent difference in the peak electron density for a sweep is used as a figure of merit for the system. Uncertainty in position, phase reference, and filter cutoff in

the Abel inversion analysis have all been evaluated. The positioning uncertainty results in a peak density variation of ±3%. Varying the phase reference produces ±1% variations. Lastly the filter cutoff variation produces ±10% variation in peak density. The 2% error allocated to the effect from asymmetry is also included. An additional 1% is included to account for other uncertainties in the diagnostic system such as a slight nonideal behavior affecting the plasma model. The total uncertainty is estimated to be ±17%. The system has shown a repeatability in the peak density to within 10%, well within the estimated uncertainty.

3.2.3 Attenuation Measurements

Signal power reduction has been explored due to the high peak density and density gradients which could cause refraction of an electromagnetic signal. The Fakel thruster plume produces a small degradation in the transmitted signal which is slightly over 2 dB of loss at the closest measurement point of 0.09 m. Beyond 0.24 m axially from the thruster and 0.05 m from the thruster axis, the loss is less than 1 dB. Figure 3.12 presents attenuation measurements for the thruster. The small reduction in power does not impact the phase measurements (greater than 10 dB loss would be required to affect the microwave system resolution).

3.2.4 Power Spectral Density Measurements

The phase noise produced by the microwave system and the positioning system is ±2°. It was expected that oscillations in the discharge current and the plasma found previously by Dickens[1995] for the SPT-100 thruster might produce significant additional phase noise. Figure 3.13 shows the power spectral density for transmission through the plume center 0.15 m from the exit plane of the SPT-100 compared with the power spectral density without the plasma plume. Measurement of the broadband noise floor did show the

noise power raised above the -110 dBm instrument threshold by 5 to 25 dB for offsets between 10 kHz and 1 MHz from the 17 GHz signal. In addition, coherent peaks in the frequency spectrum occur at 26 kHz harmonic sidebands with largest peaks at approximately -30 dB below the carrier. Additional characterization is shown for transmission through the plume center and 0.5 m from the thruster (Figure 3.14) and 0.25 m from the plume center and 0.15 m from the thruster (Figure 3.15). In the first case, 0.5 m downstream, the first harmonic at 26 kHz is significantly lower power (-45 dBc), but the broadband noise is still high even at 150 kHz from the transmission frequency. In the case of the plume axis, almost no additional noise is present. The absence of noise due to the plume is primarily due to the much lower integrated density for that transmission path and verifies we are observing plasma induced noise.

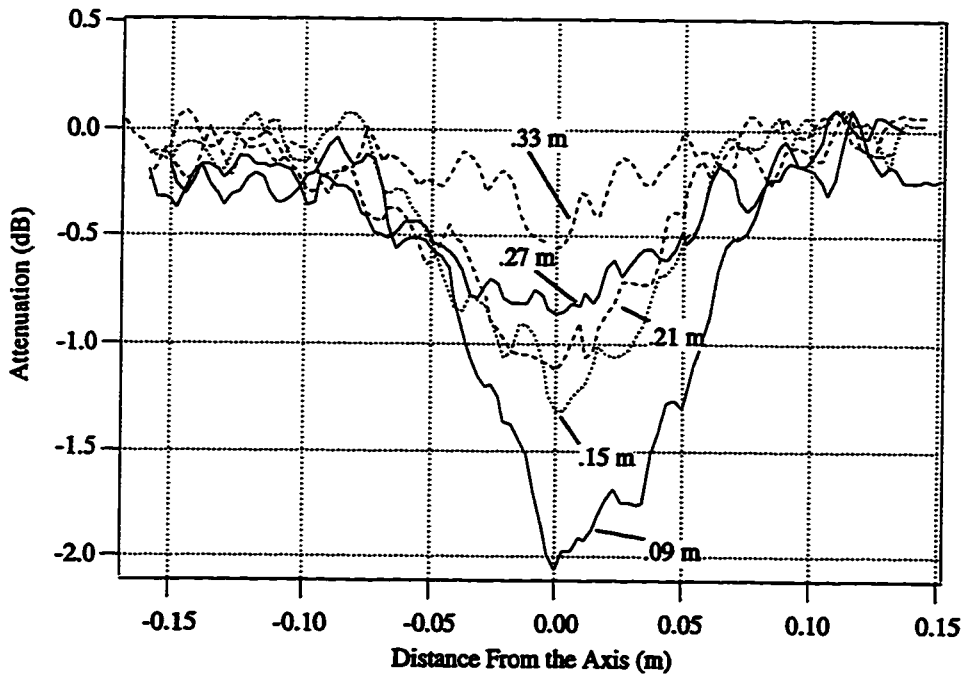

Figure 3.12. Attenuation data in five planes of constant axial postion (Fakel thruster).

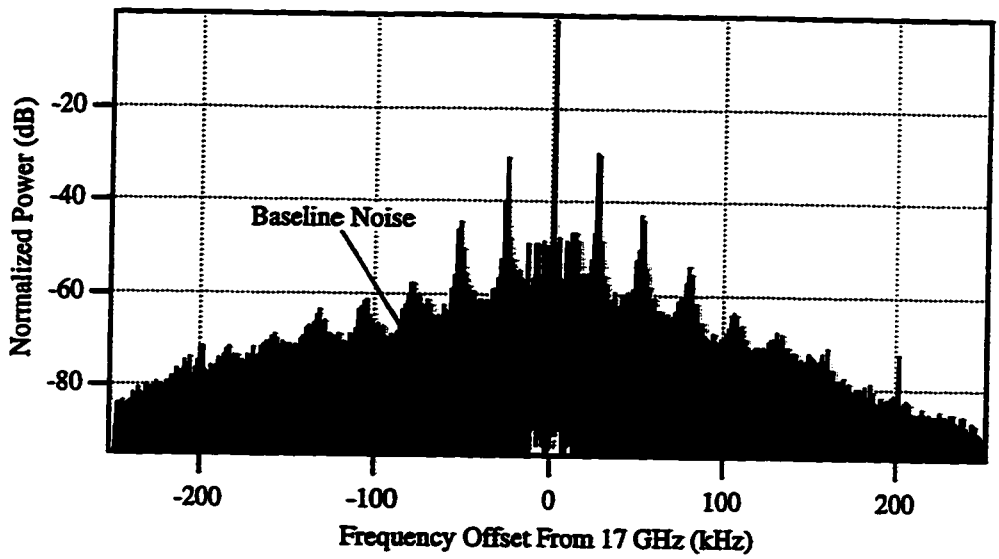

Figure 3.13. Power spectral density for a 17 GHz signal transmitted through the center of the Fakel thruster plume 0.15 m downstream.

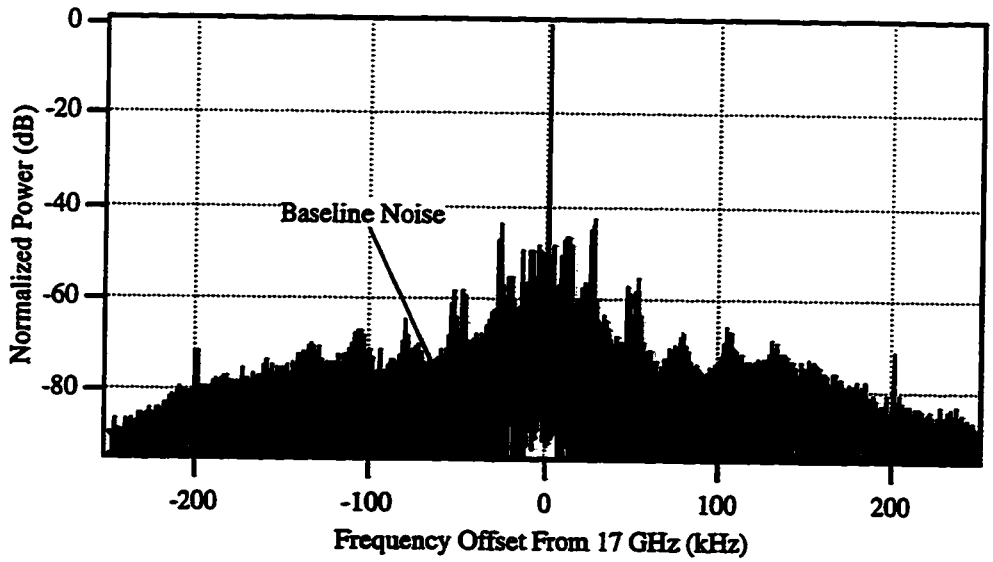

Figure 3.14. Power spectral density for a 17 GHz signal transmitted through the center of the Fakel thruster plume 0.5 m downstream.

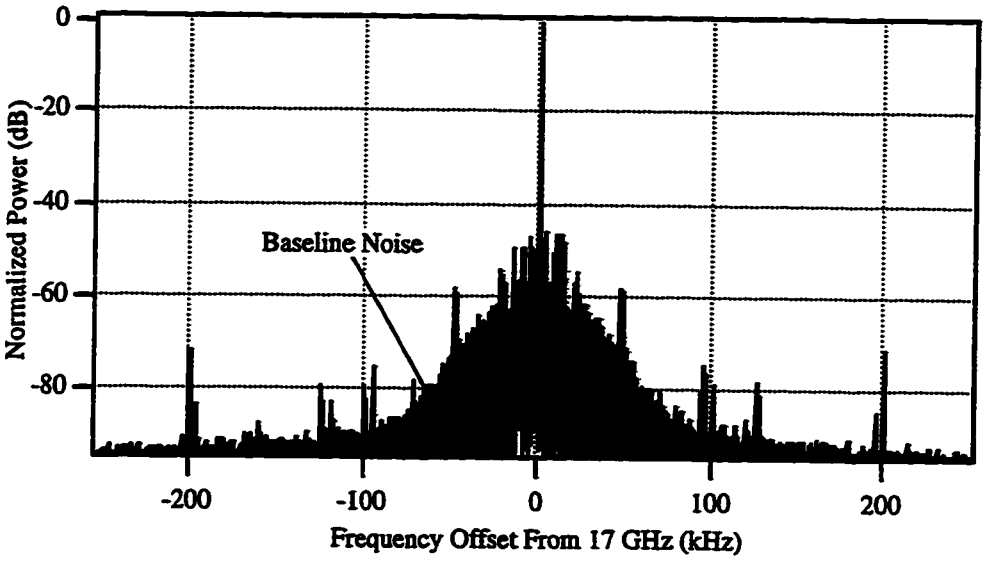

Figure 3.15. Power spectral density for a 17 GHz signal transmitted through the Fakel thruster plume 0.25 off center and 0.15 m downstream.

CHAPTER 4

ANALYSIS OF MICROWAVE MEASUREMENTS AND MICROWAVE PROPAGATION FOR THE SPT PLUME

4.0 Overview of Chapter

Characterizing microwave propagation in a plasma plume is useful in determining general plume characteristics as well as providing information about the impact to electromagnetic systems on a satellite. First, the measurements of electron density are used to find a functional model which not only provides insight into the physical processes of the plume, but also provides convenient access to the electron density throughout the plume. Then, the raw integrated phase measurements are used to estimate the asymmetry in the plume by evaluating the integrated density in planes emanating radially outward from the thruster. Lastly, the method of ray tracing is used to simulate wave propagation through the plasma plume. Initially, ray tracing simulations are validated through comparison with measurements, then the simulations are extended to a range of frequencies. The effect of microwave propagation is quantified through calculation of modulation factors for both amplitude and phase.

4.1 Functional Electron Density Model

In order to more effectively utilize the electron density measurements, the plume density contours are modeled by a combination of two functions that attempt to bridge the near- and far-field distributions. The near-field term treats the distribution as an ideal Gaussian beam while the far-field term models the point source expansion of a plume

[Birkner, *et al.* 1990; Ling, *et al.* 1991]. The following expression mathematically summarizes the plume model:

$$n(\rho,\theta) = C_1 \cdot \exp\left(-\left(\frac{\rho\sin\theta}{C_2}\right)^2\right) + \frac{C_3}{\rho^2}\exp\left(-\frac{\theta}{C_4}\right) \qquad \text{•4-1}$$

The $\rho\sin\theta$ term in the Gaussian exponential argument is to account for variation in the plane orthogonal to the thruster axis. The coefficients for the expression are obtained through a least squares minimization of the difference between the data and the model from 0.12 m radially out to 0.70 m and for angles 0 to 50° with respect to the thruster center line. Table 4.1 contains the coefficients for this expression used for the SPT-100.

C_1	$4.7\ 10^{16}\ m^{-3}$
C_2	0.073 m
C_3	$1.3\ 10^{15}\ m^{-1}$
C_4	1.1 rad

Table 4.1. Coefficients of the functional model of electron density

Figure 4.1 shows the model overlaid with the density measurements comparing closely within the region where the coefficients were optimized. The slight variation in the measurements are representative of typical thruster variation over time. The measurements shown in Figure 4.1 are taken over 30 minutes. In a test where the microwave system has been held at a constant position, the phase varied by 3° over a ten-minute span. This indicates a possible change in average density of 7%.

Figure 4.2 shows the model density contour. As would be expected, farther away from the thruster axis, the free expansion term matches the observed distribution. The model is valid within the region from 0.12 to 0.90 m radially and out to at least 70°. It is expected that additional factors will need to be considered outside this region. For example, the first term is a constant as a function of ρ for $\theta = 0$. However, this term must

decay at some distance depending on some level of free expansion and plasma neutralization effects.

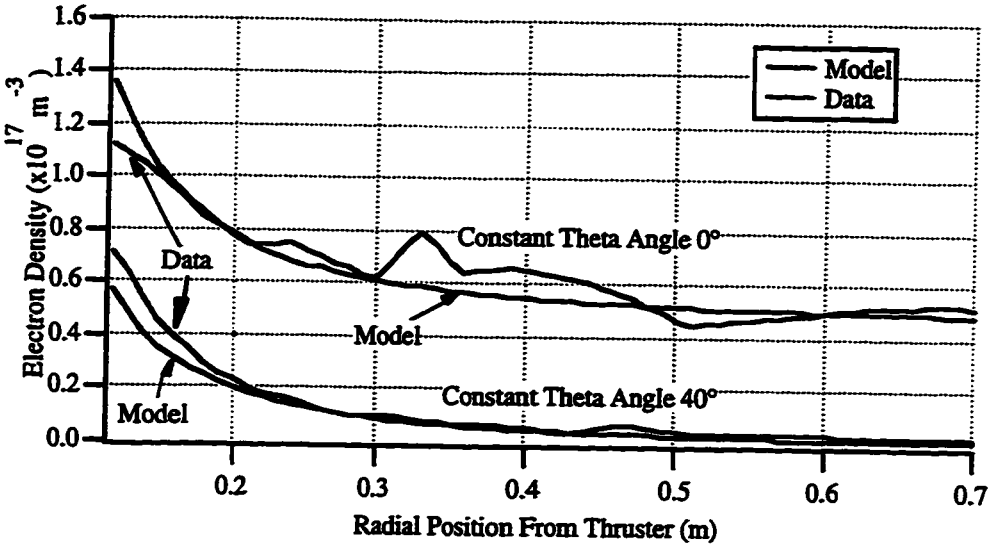

Figure 4.1. Electron density of the function model overlaid on the measured data for constant angles with respect to the thruster centerline

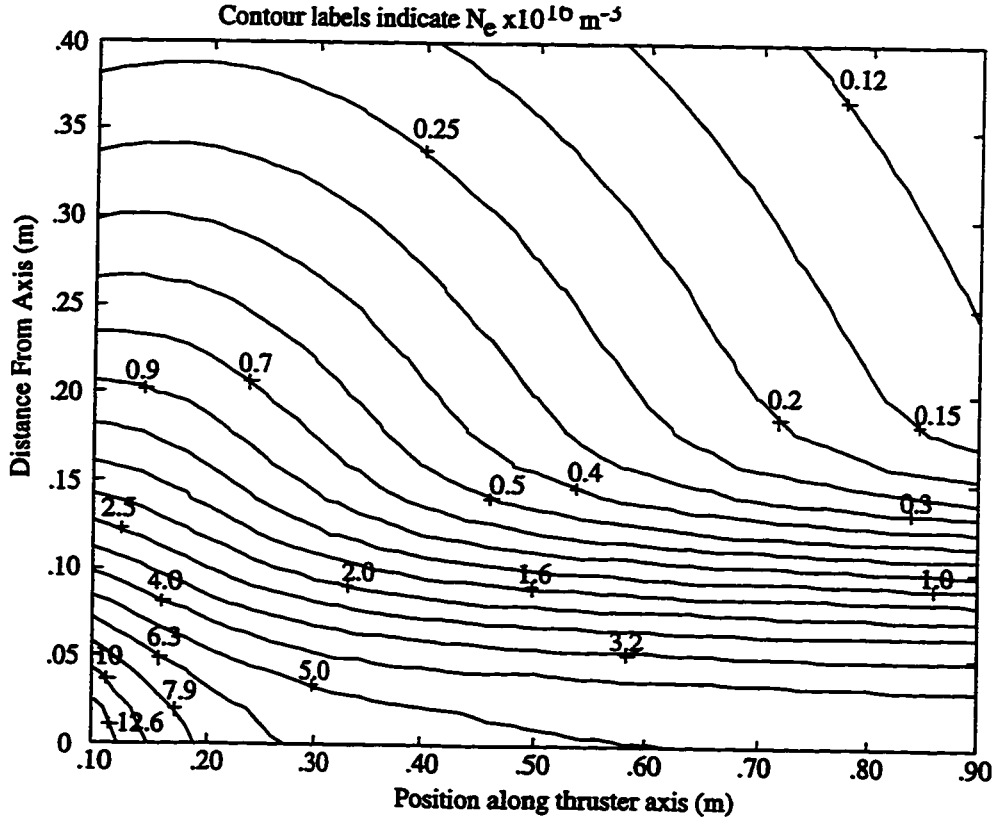

Figure 4.2. Electron density function model contour plot.

4.2 Estimation of Plume Asymmetry

The Abel integral depends on an assumption of radial symmetry; however, the SPT is thought to exhibit a small asymmetry [Manzella, 1994]. If the primary asymmetry in the SPT thruster configuration is assumed to be caused by the cathode placement, an estimation of the asymmetry due to the cathode can be determined through comparison of the phase data from measurements on either side of the thruster axis when the cathode is placed entirely on one side.

The estimation of asymmetry is found by using the phase shift which measures the line integrated plasma density along the transmission path. Summing the phase shift measurements along lines radially outward from the thruster gives an indication of the number of particles in a particular direction. By summing the phase data in the two half planes with and without the cathode, an asymmetry estimate can be made. The first step is to integrate the number of particles along distinct angular directions. Figure 4.3 shows the particle flow diagram for the thruster where the magnitude is a measure of the average number of particles per m per radian along a certain angular direction. By summing the particle number values on either side of the cathode, the off-axis particle vector for the thruster is estimated to be 1.3% of the total or 0.8° degrees away from the axis. Manzella [1994] reports the off axis thrust vector is 2% of the total thrust. The thrust vector is a slightly different quantity, which also accounts for the velocity, but the indication of asymmetry is similar. If all other asymmetry mechanisms produce less variation, then it is expected that the local density error for individual measurement sweeps will be less than 2% of the peak density along the thruster center line.

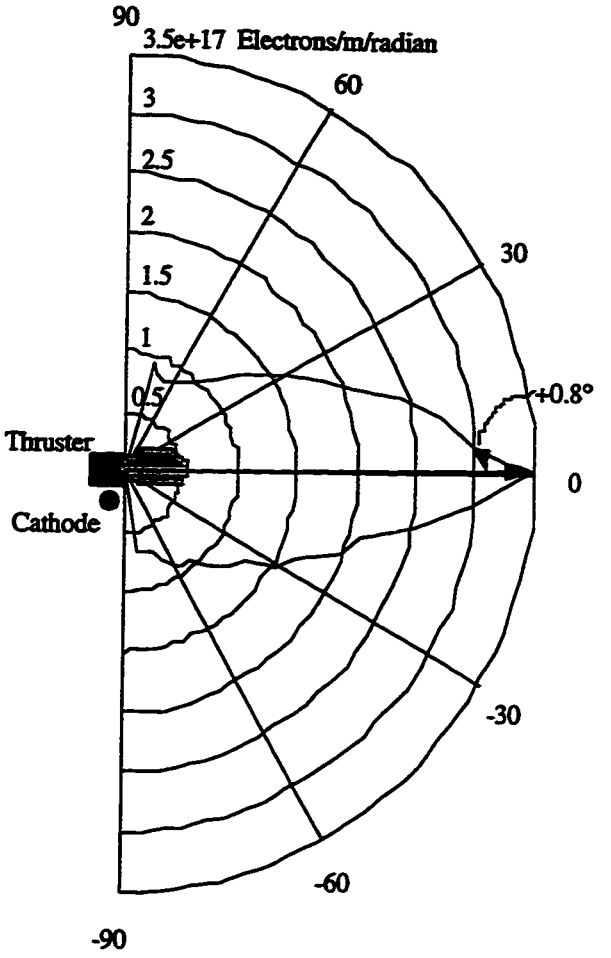

Figure 4.3. Particle density at angles from thruster axis and the total particle vector.

4.3 Ray Tracing Simulations

Electromagnetic signals are known to interact with a plasma [Heald, *et al.* 1969; Sheffield, 1975; Stix, 1992] by altering the phase, amplitude, direction, and power spectral density of a transmitted signal such as described in Equation 4-2:

$$E = E_o\left[1 + m_{amp}(t)\right]\cos\left[\left(k(r)r - (\omega - m_{freq}(t))t - m_{phase}(t)\right)\right]. \qquad \bullet 4\text{-}2$$

Equation 4.2 is most general form of modulation where m_{amp}, m_{freq}, and m_{phase} correspond to the modulation coefficients for amplitude, frequency, and phase. The plume-signal

interaction is determined by the electromagnetic dispersion relation, which is primarily dependent on electron number density and the gradients of electron number density (both are time varying in the SPT plume). The plume can impact an electromagnetic signal in three different ways: amplitude, frequency, and phase. Amplitude and phase noise are produced by electron density oscillations in the SPT plume; however, the plume effect on the frequency component is negligible. Modification of these basic parameters needs to be generally characterized both experimentally and through computer modeling in order to determine the effect on particular systems of interest where signal to noise degradation can significantly affect data rates or signal resolution. The experimental characterization is presented in Chapter 3, and the ray trace modeling is presented in this section. The computer model will first be validated with the experimental results, and then extended to a range of frequencies.

Ray tracing is an extremely useful tool for predicting high frequency electromagnetic transmission characteristics[Ling, *et al.* 1991; Kim, *et al.* 1991; Born, *et al.* 1964]. Using the basic equations introduced in Chapter 2, the spatial density model introduced in this chapter, and a temporal model suggested by Dickens[*et al.* 1995a], the phase change, ray path, and power density reduction (attenuation) are predicted for a wave traversing the plume of an SPT. Initially, a physical simulation scenario is suggested that is similar to the experimental configuration of Chapter 3. Next, the ray path divergence is simulated to find the attenuation of a wave traversing the plume, and then the results are compared to the measurements of signal attenuation. Amplitude modulation due to variable attenuation is modeled by applying a temporal plume model to the attenuation simulations. The phase shift produced by the plume is also modeled using a method similar to Dickens [*et al.* 1995a]. Amplitude and phase modulation simulations provide information necessary for comparison with the power spectral density measurements. Finally, the ray tracing simulations are used to find the amplitude and phase modulation effects over a range of

frequencies. A listing of the computer code used for the ray tracing simulation is included in Appendix D.

4.3.1 Physical Simulation Scenario

The ray tracing analysis is applied to transmission paths in a plane orthogonal to the flow of plasma, 0.15 m from the exit plane of the thruster, where the center of the antenna intersects the axis of the thruster (see Figure 4.4). This axial distance is chosen to provide comparison with previous measurements with Ku-band horn antennas operating at 17 GHz. The computer model simulates the coupling (or transmission) between the two antennas through a standard Gaussian distribution pattern,

$$FN = \frac{1}{\sqrt{2\pi\sigma}} \exp\left[-\frac{1}{2}\left(\frac{x}{\sigma}\right)^2\right] \qquad \text{• 4-3}$$

with standard deviation of 0.024 m. The square root of *FN* is taken to separate the effects of the transmit and receive antennas by assuming the two antennas have identical patterns.

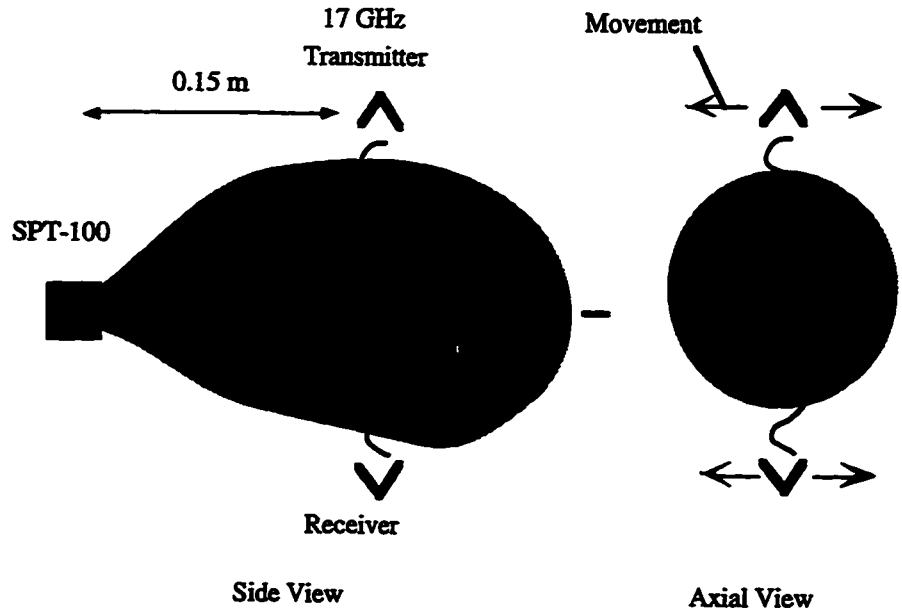

Figure 4.4. Physical system for ray trace modeling.

The electron density is taken from measurements of the Fakel SPT-100 thruster operating at nominal conditions of 300 V, 4.5 A, and 5.8 mg/s of xenon. The combined density model is the product of a static model and a temporal model. The static density is given by Equation 4-1 where r and θ are shown in Figure 4.4 and the temporal model is given by Equation 4-4 [Dickens, 1995]:

$$n_{temp}(\bar{r},t) = 1 - m_{noise}\cos(\omega_{noise}t - k_{noise}\bar{r}) \qquad \bullet 4\text{-}4$$

$$m_{noise} = 0.12,\ \omega_{noise} = 2\pi x 26 x 10^3 \text{ rad/sec},\ k_{noise} = 10.9.$$

The density oscillation frequency is ideally represented as the entire frequency spectrum of the thruster; however, for simplicity in demonstration of the amplitude modulation the dominant oscillation frequency (26 kHz) is used to represent the density oscillations. This assumption provides worst case results for noise produced by the plume.

4.3.2 Static Modeling

This ray tracing method utilizes a combined static and temporal model of the SPT plume. Initially, the static model is implemented and compared to experimental measurements. In the simulations, the rays bend (Figure 4.5) slightly producing small attenuation; however at lower frequencies the attenuation is more severe as shown later. The attenuation due to the plasma is calculated for each ray tube by finding the change in area of the ray tube (see Chapter 2). The initial or transmitted area is determined by the simulation parameters. The final or receiver ray tube area is determined by two dimensions: 1) the length between the rays in the simulation plane which is determined by the simulation and 2) the length in the direction orthogonal to the simulation plane which is assumed constant since the density gradient is much less in that direction, thereby producing minimal refraction.

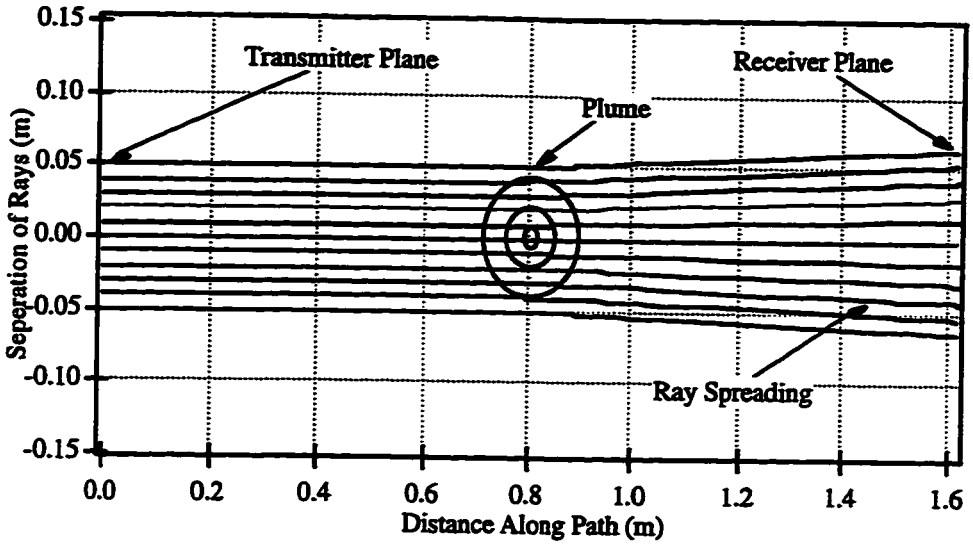

Figure 4.5. Ray paths of the simulated antenna for a single time step (0.15 m, 17 GHz).

A series of rays are used to simulate an antenna aperture through the superposition of the electric fields across the aperture. The amplitude and phase of each ray are used to find the field quantities which are then weighted by the antenna distribution function. The amplitude and phase of the individual rays are plotted in Figures 4.6 and 4.7. The amplitude of the rays actually has a small power gain on the edge of the plume where the rays density is higher than in free space. The weighted fields are distributed across each ray tube so that the power density is constant across a ray tube. The sum of the weighted fields is used to find the total power at the receiver. The calculations are summarized in expressions for attenuation and phase (Equations 4-5 and 4-6) for an antenna with a distribution function, *FN*.

$$P_{ant} = \frac{\left| \sum_{N=1}^{N_{ant}} \sqrt{wl_{Npl}} \left[FN(x_{Npl}) \right]^{1/2} \left[FN(x_{Nnopl}) \right]^{1/2} \left(\frac{l_{Nnopl}}{l_{Npl}} \right)^{1/2} e^{j\Delta\phi_{ant}} e^{j\phi_{Nnopl}} \right|^2}{\left| \sum_{N=1}^{N_{ant}} \sqrt{wl_{Nnopl}} \left[FN(x_{Nnopl}) \right] e^{j\phi_{Nnopl}} \right|^2} \quad \text{• 4-5}$$

$$\phi_{ant} = angle\left\{\sum_{N=1}^{N_{max}} \sqrt{wl_{Npl}}\left[FN(x_{Npl})\right]^{1/4}\left(\frac{l_{Nnopl}}{l_{Npl}}\right)^{1/2} e^{j\Delta\phi_{Npl}} e^{j\phi_{Nnopl}}\right\} - angle\left\{\sum_{N=1}^{N_{max}} \sqrt{wl_{Nnopl}}\left[FN(x_{Nnopl})\right] e^{j\phi_{Nnopl}}\right\}$$

• 4-6

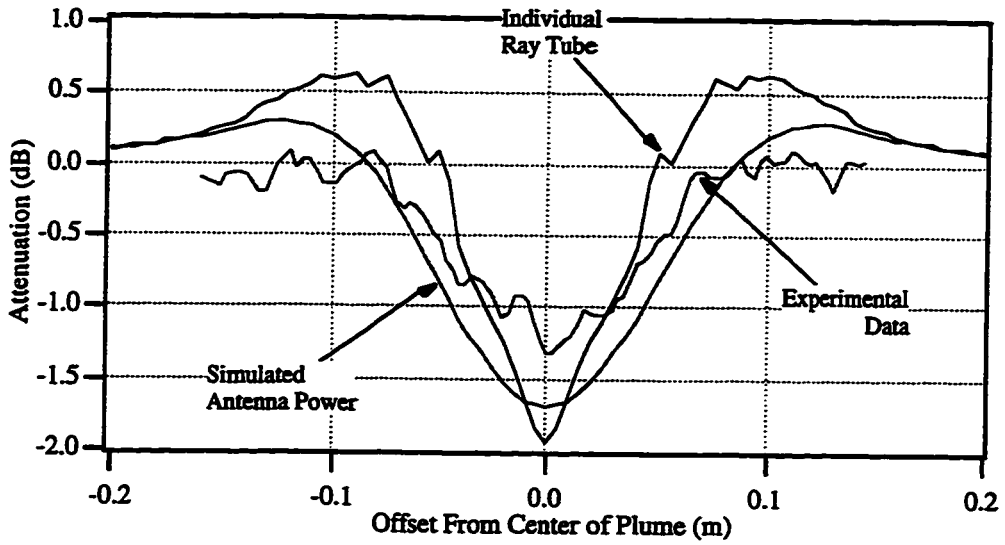

Figure 4.6. Power change due to plasma for individual ray tubes, simulated antenna, and experimental results; 0.15 m downstream, 17 GHz.

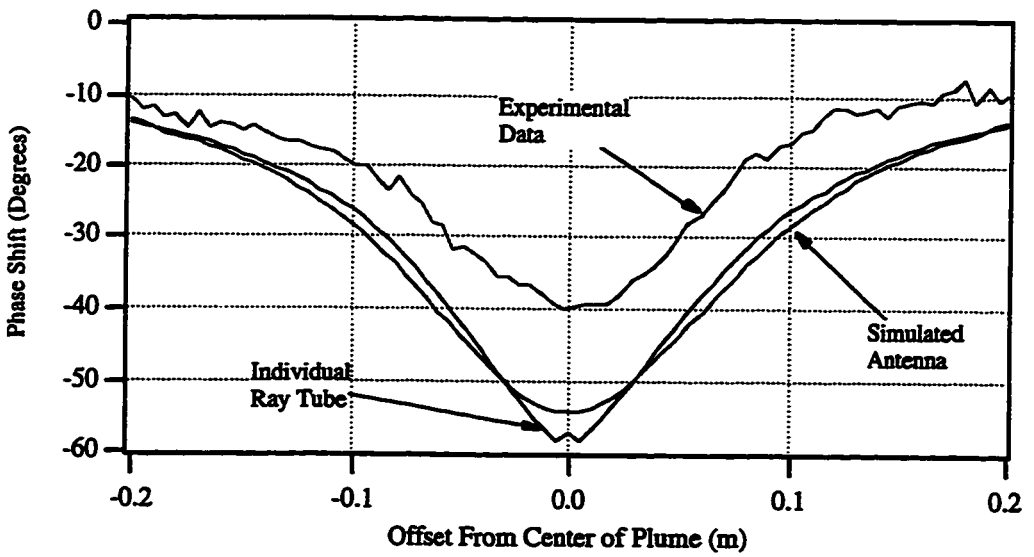

Figure 4.7. Phase shift due to plasma for ray tubes, simulated antenna, and experimental results; 0.15 m downstream , 17 GHz.

The attenuation and phase for a simulated antenna are calculated from Equations 4-5 and 4-6, and the results are shown in Figures 4.6 and 4.7. The individual ray tube results exhibit slight noise which is attributed to the numerical aspects of ray sampling and step size. In both the attenuation and phase, the plots show the expected relationship between the individual rays and the antenna; the antenna results are the convolution of the individual rays and the antenna function.

In addition, experimental data are also plotted in Figures 4.6 and 4.7 for comparable conditions. For both amplitude and phase, the simulation tends to over predict the effect of the plume on the transmitted signal when compared to the experimental data (5% for attenuation and 30% for phase). These differences can be attributed to the inherent limitations of the ray tracing technique. Two simulation limitations are the finite ray sampling and step size, both having greater importance at smaller wavelengths where the error tends to affect the phase more than the amplitude. Two other limitations are the electron density model which is known to be accurate only to ±20% and the limited accuracy of the antenna distribution function. Given these factors, the difference between the ray tracing simulations and the experimental measurements are expected.

4.3.3 Time Varying Modeling

The time variation of a transmitted signal can be determined by using a temporal density model as well as the static density model. When the attenuation level varies over time due to oscillations in density, then amplitude noise or modulation is produced on the transmitted signal (Figure 4.8). The most attenuation is -1.92 dB and least is -1.46 dB. The variation of ±0.23 dB corresponds to the experimental noise in Figure 4.6. The simulations have been implemented with a 26-kHz plasma oscillation which is the dominant frequency component; however, amplitude variations of smaller magnitude exist at other frequencies.

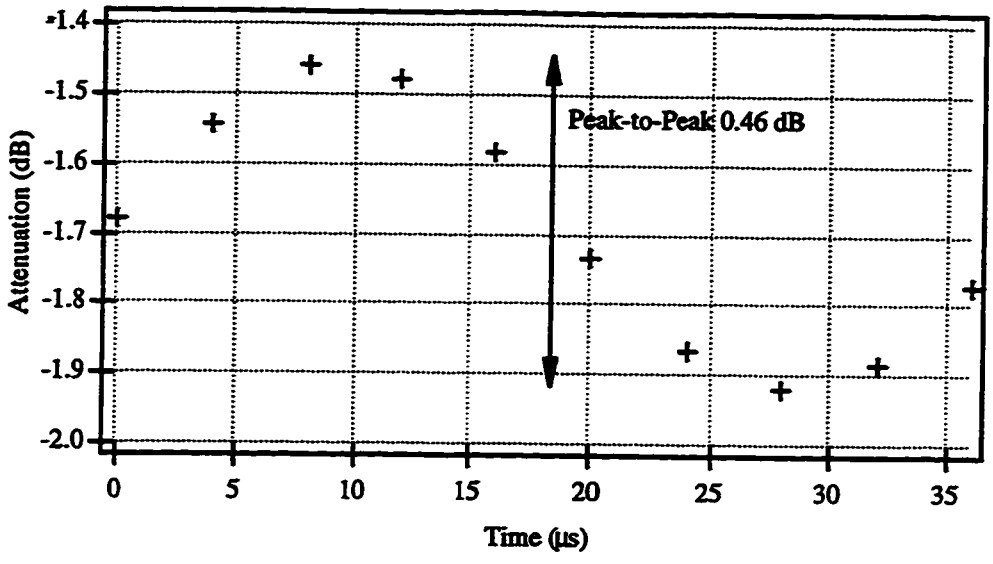

Figure 4.8. Simulated amplitude variation over time for a 17 GHz signal transmitted through the plume 0.15 m from the exit plane (relative to power with no plume present).

The ray tracing simulation indicates amplitude modulation at 26 kHz which is described mathematically by Equation 4-1. In that equation the modulation factor, m_{amp}, is represented by $|m_{amp}|\cos(\omega_{oscill}t)$ where ω_{oscill} is the radial frequency of the density oscillation and $|m_{amp}|$ is the peak-to-peak signal amplitude normalized by the mean amplitude value. $|m_{amp}|$ is found to be 0.053 (note: this is a unitless number, not dB) and the mean attenuation is -1.68 dB (0.68 V/m). The corresponding phase variation (Figure 4.9) is found through similar methods where m_{phase} is $|m_{phase}|\cos(\omega_{oscill}t)$. $|m_{phase}|$ is the phase variation in degrees relative to the mean phase value ($|m_{phase}| = 0.094$rad(5.4°)), The phase shift relative to transmission through a vacuum is -0.96 rad (-55°).

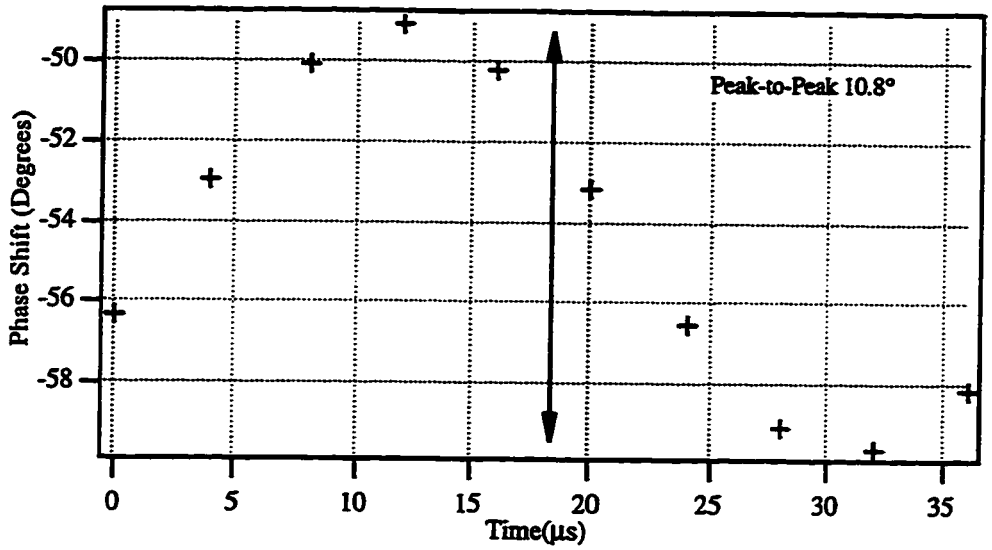

Figure 4.9. Simulated phase variation over time for a 17 GHz signal transmitted through the plume 0.15 m from the exit plane (relative to power with no plume present).

The power spectral density is a useful description for determining the quality of an electromagnetic signal. Ideally, the carrier power would be contained in a narrow bandwidth relative to the modulation and the noise power would be near the thermal noise floor (<<-90 dB) for a wide range of frequency offsets. The power spectral density is calculated for a 17 GHz signal transmitted through the plume 0.15 m from the exit plane using modulation parameters from the ray tracing simulation (Figure 4.10).

The plasma oscillations produce 26 kHz harmonics where the first harmonic is produced through a combination of the amplitude and phase modulation. In this particular case, the amplitude modulation produces 3 dB more power in the first harmonic than with the phase modulation alone. The first harmonic compares well (within 2 dB) with the measured results in Figure 4.11; however, the simulation under predicts the measured second harmonic. In addition, the broadband noise exhibited in the measurements is not predicted by the single frequency oscillation model. These similarities and differences are common throughout other comparisons of the simulations and experiment. The differences

between simulations and experiments would decrease with a more accurate model of the frequency spectrum of plume oscillations.

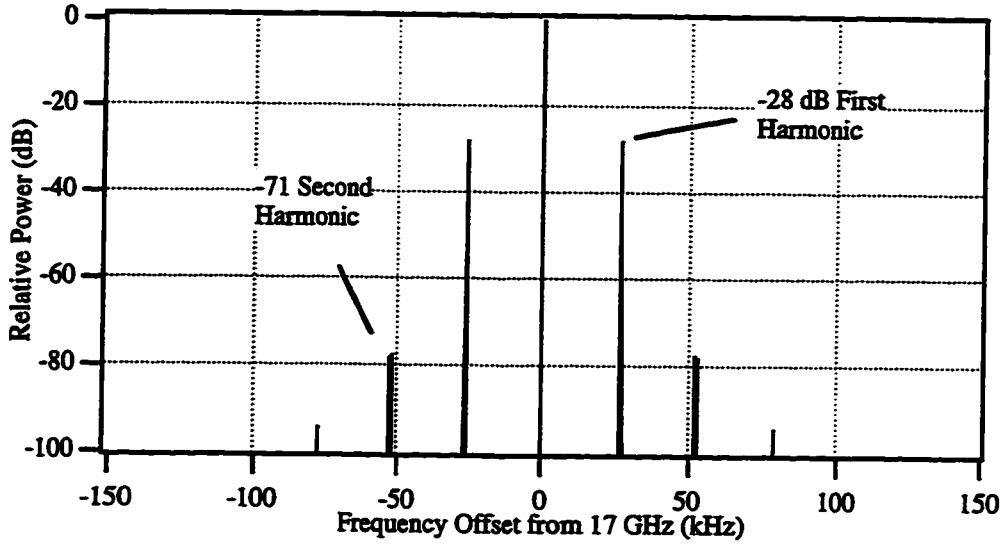

Figure 4.10. Simulated effect of density oscillations for a 17 GHz signal transmitted across the plume 0.15 m from the exit plane.

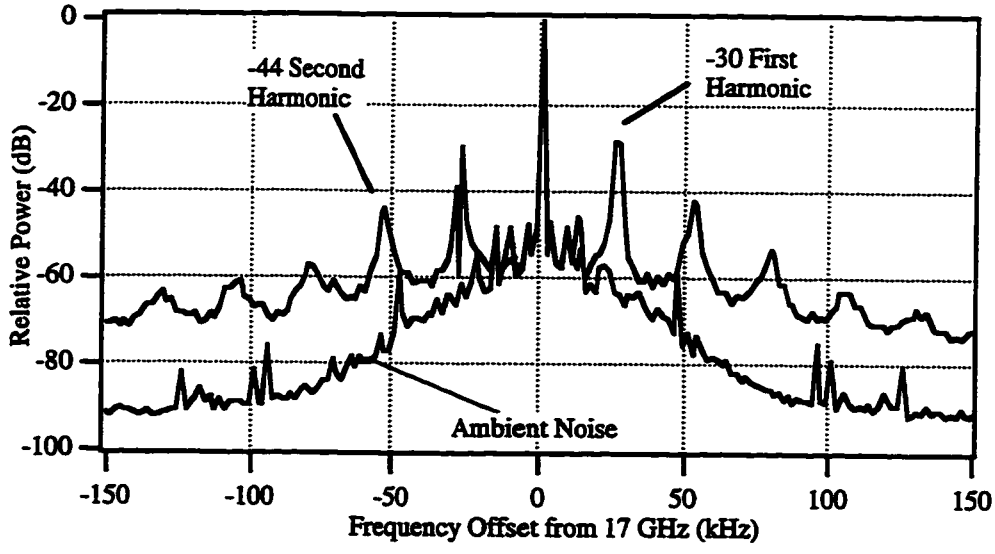

Figure 4.11. Measured power spectral density of a 17 GHz signal transmitted across the plume 0.15 m from the exit plane.

Density oscillations in the plume produce both amplitude and phase modulation. This evaluation demonstrated the mechanism of amplitude modulation by the plume through ray tracing simulations. Additionally, the simulations compared well to phase, amplitude, and power spectral density measurements for a similar experimental situation.

4.3.4 Extension of Model to Frequencies Beyond 17 GHz

The SPT plume affects the phase, amplitude, and power spectral density of a transmitted electromagnetic signal. The signal impact is evaluated over a wide range of frequencies and transmission paths using the ray tracing algorithm. Then, attenuation results are compared to the theoretical limit of the ray tracing method across a range of frequencies. Additional measurements at 1.575 GHz [Ohler, *et al.* 1996] compare well with the simulation trends in this section even though 1.575 GHz is below the simulation capabilities of ray tracing.

The ray tracing technique is used to establish trends in the impact of both amplitude and phase to a transmitted signal. These simulations are completed for 0.25, 0.5, 1, and 1.5 m from the thruster exit plane and for transmitted signals of 3, 4, 5, 6, 7, 9, 12, 15, and 17 GHz. The static density model uses a weighted average of the density model in Section 4.1 and Equation 4.7 [Dickens, *et al.* 1995a] because the first equation is more accurate in the closer simulation region and the second equation is more accurate in the farther simulation region.

$$n_{static}(\rho,\theta)=\frac{n_o \exp\left\{-\left[p(1-\cos\theta)\right]^m\right\}}{\rho^2\cos^2\theta}, \qquad \bullet 4\text{-}7$$

$$n_o=10^{16}\ m^{-1},\ p=50,\ \text{and}\ m=0.6.$$

All of the summary simulations are calculated for the plume effect on a single ray in order to make the results more general. This implementation produces worst case results for

transmission across the plume since the center ray experiences the greatest impact from the plume.

The attenuation simulations (Figures 4.12 and 4.13) indicate a sharp increase in power loss at the lower frequencies, but also a quick reduction in plume impact with increasing distance. The results show less than 3 dB attenuation for frequencies greater than 10 GHz except for the very closest positions. The modulation coefficient follows similar trends indicating up to 25% modulation at the closest measurement point at 3 GHz and also indicating less than 5% modulation for all distances at 17 GHz; however, as was demonstrated earlier with the 17 GHz simulation, even small modulation coefficients produce significant increases in the noise power.

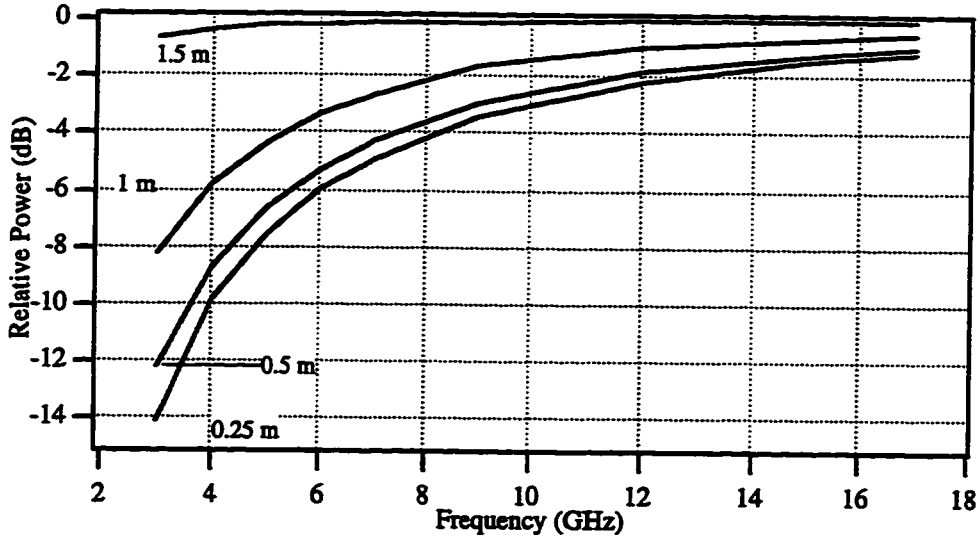

Figure 4.12. Simulated attenuation of an electromagnetic signal transmitted through an SPT plume.

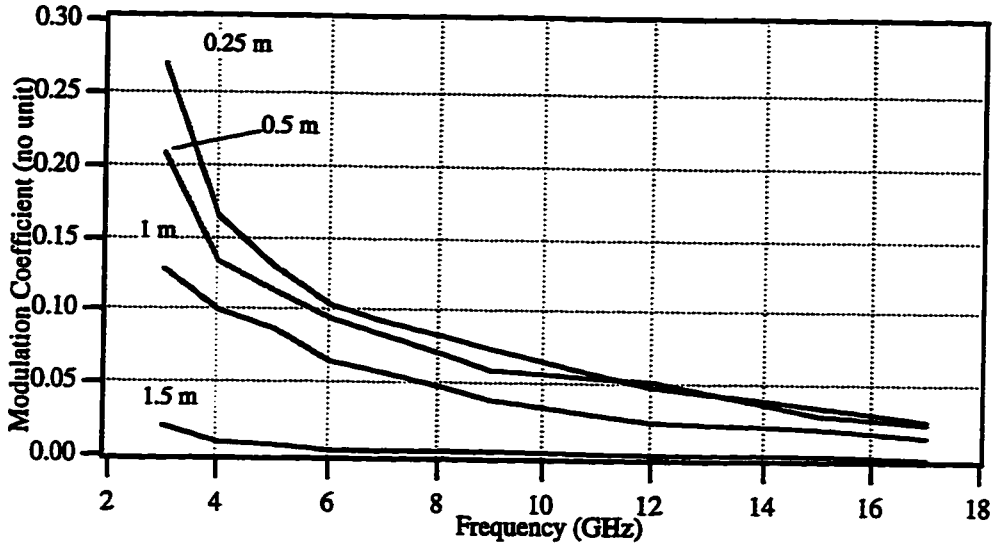

Figure 4.13. Simulated amplitude modulation coefficient of an electromagnetic signal transmitted through an SPT plume

The phase simulations are completed over the same spatial and frequency simulations set as the attenuation (Figures 4.14 and 4.15). The phase is more sensitive to simulation error than the amplitude as the frequency approaches the theoretical limit of geometric optics; hence, the lower frequency values at the closest simulation point did not produce reliable results. Overall, the general trends are similar to the attenuation simulations; however, the rate of decline in the signal impact is slower as the frequency or position increases. Again, even a small modulation factor can produce significant increase in the noise power.

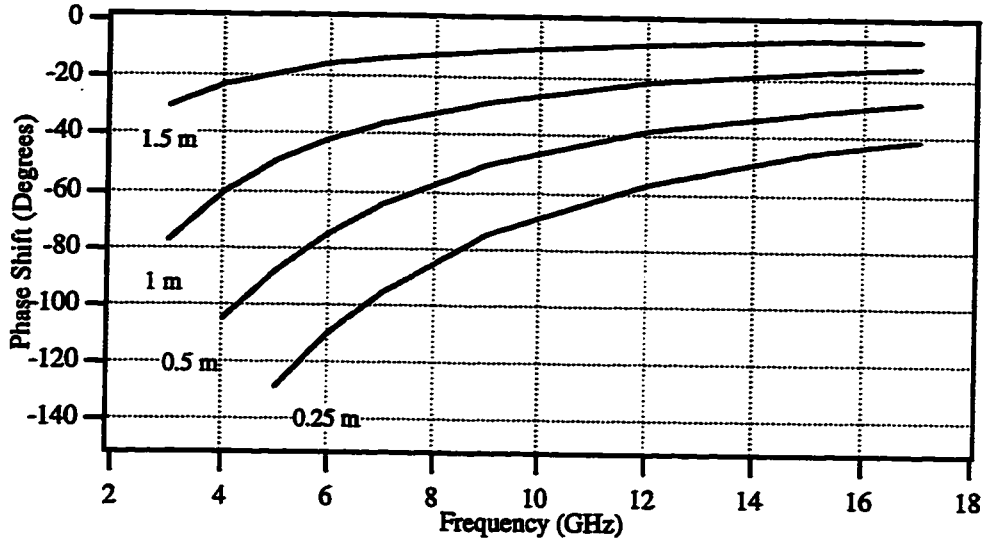

Figure 4.14. Simulated phase shift of an electromagnetic signal transmitted through an SPT plume (referenced to the phase shift with no plasma).

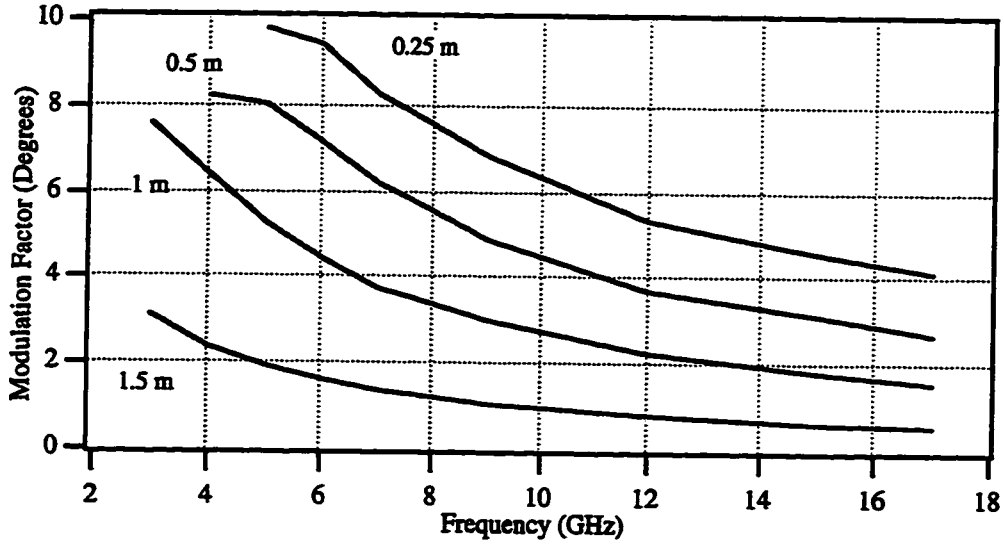

Figure 4.15. Simulated phase modulation factor of an electromagnetic signal transmitted through an SPT plume.

The theoretical limit of the simulations or the limit of geometric optics, Equation 4-8 [Born, *et al.* 1964], states the wavelength must be much smaller than scale length of changes in the wave number or in this case the permittivity (which directly relates to the density).

$$\lambda_o << \frac{\varepsilon_r}{\frac{\partial}{\partial path}\varepsilon_r} \qquad \bullet 4\text{-}8$$

This condition implies that if the density changes quickly, the ray will bend faster than ray tracing can reliably predict. In some instances, the plasma appears to be a perfect conductor under the circumstances where this condition fails. The condition for validity of the ray tracing analysis is evaluated for a geometry similar to Figure 4.4 for a range of axial positions. For any given position the failure point for the highest frequency is along the thruster axis.

The contour defining the limiting frequency is plotted in Figure 4.16. Additionally, attenuation simulations are also summarized in Figure 4.16 where the attenuation is evaluated for a range of axial positions and frequencies. The contours are shown for 3 dB and 10 dB levels of attenuation.

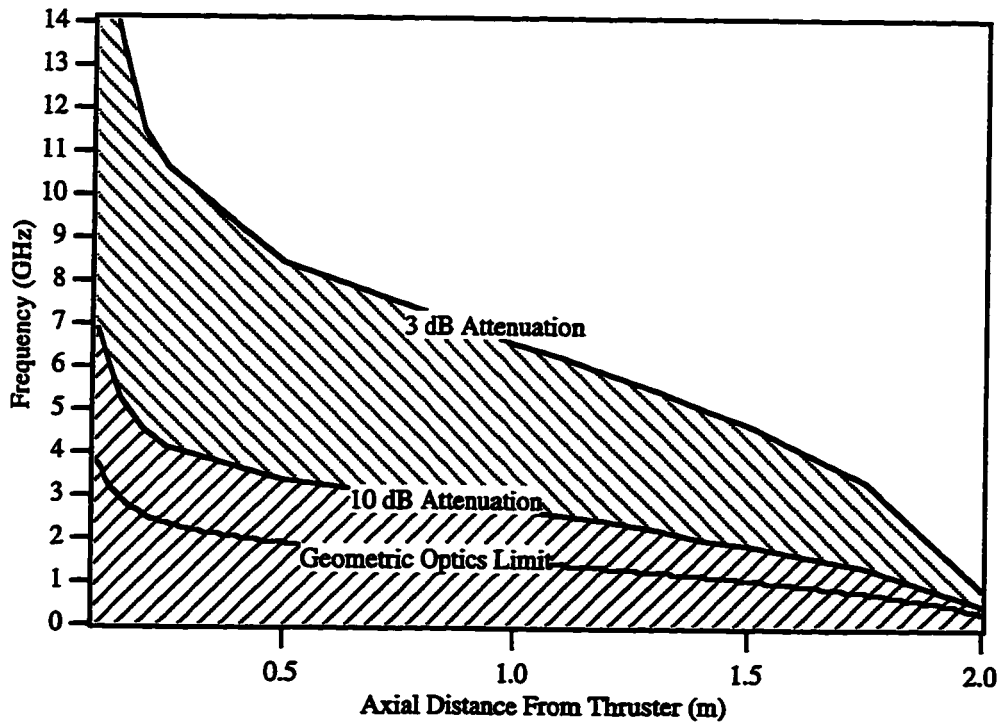

Figure 4.16. Theoretical frequency limit of geometric optics with respect to transmitting across the plume at a given axial distance from the thruster exit plane.

CHAPTER 5

METHODOLOGY AND BACKGROUND OF ION ACOUSTIC WAVE MEASUREMENTS

5.0 Overview of Chapter

Exciting ion acoustic waves in a flowing plasma can provide information concerning the flow velocity, electron temperature, and ion temperature. Knowledge of these quantities is desirable in many plasmas to provide a better understanding of the physical processes taking place in the plasma. In particular, the physical processes in the plasma plume of a stationary plasma thruster are currently of interest due to the near-term implementation of the thruster on commercial satellites. Ion acoustic waves are potentially useful for characterizing plasma parameters due to their simple dispersion relation and generally straightforward propagation characteristics.

Ion acoustic wave excitation and propagation is reviewed in this chapter in order to provide the basis for a diagnostic technique utilizing ion acoustic wave propagation information. Initially, general wave propagation is explored through a set of dispersion relations which predict wave propagation characteristics for possible electrostatic waves. The dispersion relations are evaluated to verify the dominance of the ion acoustic wave for the relevant experimental situation. The dispersion relation for ion acoustic waves is re-derived for a simple ideal plasma using the fluid equation in order to assess the validity of the assumptions in the derivation. The dispersion relation is also evaluated to assess the effects of collisional and Landau damping. Next, non-ideal characteristics are returned to the analysis to assess the effects on propagation of a flowing nonhomogeneous time

varying plasma. Using the dispersion relation in a flowing plasma, the propagation characteristics are explored for a cylindrical wire probe to develop a relation between the propagation characteristics and plasma parameters. Lastly, in order to provide a characterization of propagation, a measurement system is described.

5.1 General Plane Wave Propagation in a Homogeneous Non-flowing Plasma

A plasma can support both electrostatic and electromagnetic propagation modes. Electromagnetic waves are not useful for finding flow velocity and temperature (especially for a small magnetic field, see Table 5.2) since they are not affected by the plasma flow and are generally independent of the temperature. The electrostatic modes that generally propagate are as follows: electron plasma oscillations, upper hybrid oscillations, ion electrostatic waves, electrostatic ion cyclotron waves, lower hybrid oscillations, and ion acoustic waves.

Propagation of each electrostatic mode is governed by a dispersion relation where Table 5.1 [Chen, 1984] lists the traditional expressions for undamped propagation. Each of the dispersion relations are evaluated to determine possible propagation in these experiments. They are evaluated based on the experimental system described in Section 5.5 and estimates of characteristic parameters for the SPT-100 thruster [Ohler, *et al.* 1995, 1996; Myers, *et al.* 1993; Absalamov, *et al.* 1992; Manzella, 1993, 1994, *et al.* 1995; Patterson, *et al.* 1985; Pencil, 1993] presented in Section 2.1 and summarized again in Tables 5.2. Each of the modes are evaluated to determine possible propagation in these experiments.

Electrostatic waves	Condition	Dispersion Relation
Electron plasma oscillations	B_o=0 or $k \| B_o$	$\omega^2 = \omega_{pe}^2 + \frac{3}{2}k^2 v_{the}^2$ • 5-1
Upper hybrid oscillations	$k \perp B_o$	$\omega^2 = \omega_{pe}^2 + \omega_{ce}^2 = \omega_h^2$ • 5-2
Electrostatic ion cyclotron waves	$k \perp B_o$	$\omega^2 = \omega_{ci}^2 + k^2 V_{iaw}^2$ • 5-3
Lower hybrid oscillations	$k \perp B_o$	$\omega^2 = \omega_{ce}\omega_{ci} = \omega_l^2$ • 5-4
Ion acoustic waves	B_o=0 or $k \| B_o$	$\omega^2 = k^2 \frac{KT_e + 3KT_i}{m_i} = k^2 V_{iaw}^2$ • 5-5

Table 5.1. Dispersion relations for electrostatic waves in plasmas.

n_o (m^{-3})	10^{17}
T_e (eV)	3
T_i (eV)	0.1
m_i (kg)	2.2×10^{-25} (Xe)
B (T)	$<10^{-3}$
P (Pa)	7×10^{-4}
υ_{ei} (s^{-1})	7×10^5
υ_{en} (s^{-1})	8×10^3
v_{flow} (km/s)	14-18 10^3

Table 5.2. Typical plume plasma parameters for the SPT-100.

Based on the typical physical characteristics, electrostatic mode dispersion relations are evaluated for the SPT-100 where the ion acoustic wave is determined to be the dominant mode through a process of elimination. The electrostatic modes are all dependent on the plasma flow; however, only the ion acoustic wave is dependent on both the ion and electron temperature. Aside from this basic limitation, other physical factors limit practical use to the ion acoustic wave. Both the electron plasma oscillations and the upper hybrid oscillations travel at speeds much faster than the flow velocity; therefore, the flow effect on propagation will be minimal. The ion cyclotron wave propagation is determined by the magnetic field, which determines the ion cyclotron frequency. In this case the maximum ion cyclotron frequency is less than 100 Hz. If the wave is at a low frequency it will be

damped through collisional damping. If the wave is excited at a higher frequency the electrostatic ion cyclotron wave is essentially an ion acoustic wave. The lower hybrid oscillations depend strongly on the particle interaction with the magnetic field; however, the oscillations only occur at a distinct frequency and in a direction orthogonal to the magnetic field. Given the nonhomogeneous magnetic field, the SPT plume would not easily support a lower hybrid oscillation. The ion acoustic wave is the only mode possible given the approximate plasma parameters.

5.2 Dispersion Relation for Ion Acoustic Wave Propagation in a Homogeneous Stationary Plasma

To fully understand ion acoustic wave propagation the dispersion relation is rederived from fundamental equations (for a detailed derivation see one of the following: Stix, 1992; Chen, 1984; Season, *et al.* 1989; or Jones, *et al.* 1985). The derivations highlight the assumptions in order to assess the accuracy and validity of the ion acoustic wave propagation dispersion relation applied to the non-ideal nature of the SPT plume. First, the traditional ion acoustic wave dispersion relation is derived for a stationary collisionless homogeneous plasma using the fluid equations. Next collisions are added to the fluid equations in order to assess the effects of collisional damping. Finally, the dispersion relation is rederived again in a stationary collisionless plasma; however the more complete kinetic theory is used in order to quantify Landau damping and estimate the possible error in the fluid equations. These results are necessary in order to determine the accuracy of the measurement method.

5.2.1 Fluid Theory Dispersion Relation

To determine the dispersion relation for an ion acoustic wave through fluid theory, certain restrictions are placed on the plasma where these restrictions are imposed to simplify the derivation for this case and are not necessarily limitations to ion acoustic wave

propagation. The primary restriction of fluid theory is that the plasma is in thermodynamic equilibrium which implies the plasma constituents are described by discrete temperature values. Furthermore, the plasma is composed of primarily singly ionized particles where the magnetic field is negligible (see ion cyclotron wave explanation in this chapter). The plasma parameters that support the electrostatic wave are described by linear theory (small perturbation):

$$n_e = n_{eo} + n_{ep}, \quad \bullet 5\text{-}6$$

$$n_i = n_{io} + n_{ip}, \quad \bullet 5\text{-}7$$

$$v_e = v_{eo} + v_{ep}, \quad \bullet 5\text{-}8$$

$$v_i = v_{io} + v_{ip}, \quad \bullet 5\text{-}9$$

$$E = E_o + E_p \quad \bullet 5\text{-}10$$

where the subscript o indicates the steady state value, p indicates the perturbation, and subscripts e and i indicate electron and ion, respectively (note: ω_{pe} and ω_{pi} and are the electron and ion plasma frequency not a perturbation frequency). The initial derivation is for a stationary collisionless homogeneous plasma where the ion acoustic wave propagation is undamped. Given these assumptions, the following quantities are zero for both electron and ions: $\nabla n_o, v_o, E_o, \partial n_o / \partial t, \partial v_o / \partial t, \partial E_o / \partial t$. Lastly, each of the perturbation variables can be described by their space and time Fourier components:

$$B_p = |B_p| \exp(j\omega t - j\mathbf{k} \cdot \mathbf{r}) \quad \bullet 5\text{-}11$$

where B_p is one of the perturbation values in Equations 5-6 to 5-10.

The propagation of the wave is governed by five equations: Poisson's equation (5-12), the continuity equation for both electrons (5-13) and ions (5-14), and the equation of motion for both electrons (5-15) and ions (5-16).

$$\nabla \bullet E = \rho / \varepsilon_o = \frac{1}{\varepsilon_o}(n_i q_i + n_e q_e) \quad \bullet 5\text{-}12$$

$$\frac{\partial n_e}{\partial t}+\nabla\bullet\left(n_e v_e\right)=0 \qquad \bullet 5\text{-}13$$

$$\frac{\partial n_i}{\partial t}+\nabla\bullet\left(n_i v_i\right)=0 \qquad \bullet 5\text{-}14$$

$$m_e n_e\left[\frac{\partial v_e}{\partial t}+\left(v_e\bullet\nabla\right)v_e\right]=n_e q_e E-\nabla P_e \qquad \bullet 5\text{-}15$$

$$m_i n_i\left[\frac{\partial v_i}{\partial t}+\left(v_i\bullet\nabla\right)v_i\right]=n_i q_i E-\nabla P_i \qquad \bullet 5\text{-}16$$

These equations can be simplified with the assumptions already stated and the relation describing the pressure exerted by the particles:

$$\nabla P_e=\gamma_e K T_e\nabla n_e \text{ and} \qquad \bullet 5\text{-}17$$

$$\nabla P_i=\gamma_i K T_i\nabla n_i. \qquad \bullet 5\text{-}18$$

The simplified equations follow:

$$-jkE_p=\rho/\varepsilon_o=\frac{1}{\varepsilon_o}\left(n_{ip}q_i+n_{ep}q_e\right), \qquad \bullet 5\text{-}19$$

$$\omega n_{ep}-kn_{eo}v_{ep}=0, \qquad \bullet 5\text{-}20$$

$$\omega n_{ip}-kn_{io}v_{ip}=0, \qquad \bullet 5\text{-}21$$

$$v_{ep}m_e n_{eo}\omega=-jn_{oe}q_e E_p+\gamma_e K T_e k n_{ep}, \text{ and} \qquad \bullet 5\text{-}22$$

$$v_{ip}m_i n_{io}\omega=-jn_{oi}q_i E_p+\gamma_i K T_i k n_{ip}. \qquad \bullet 5\text{-}23$$

To determine the dispersion function for the ion acoustic wave we solve Equations 5-21 and 5-22 for v_{ep} and v_{ip} which is applied in Equations 5-23 and 5-24 to solve these equations for n_{ep} and n_{ip}, which is applied to Equation 5-19. This equation can be manipulated into the form after taking q_e and q_i to be unit charges, e:

$$D(\omega,k)E=0 \qquad \bullet 5\text{-}24$$

$$D(\omega,k)=1+\frac{\omega_{pe}^2}{\omega^2-k^2v_{te}^2}-\frac{\omega_{pi}^2}{\omega^2-k^2v_{ti}^2}=0 \qquad \bullet 5\text{-}25$$

$$v_{te}^2=\frac{\gamma_e K T_e}{m_e} \qquad \bullet 5\text{-}26$$

$$v_{ti}^2=\frac{\gamma_i K T_i}{m_i} \qquad \bullet 5\text{-}27$$

where D is the dispersion function and v_{te} and v_{ti} are the electron and ion thermal velocities. Now additional assumptions are necessary: $\omega \ll \omega_{pi} \ll \omega_{pe}$ and

$v_{ti} << \omega / k << v_{te}$ which indicate that the propagation frequency must be much less than the ion and electron plasma frequency and that the phase velocity of the wave is much faster than the ion thermal speed. These assumptions are all valid for the experimental system described in Section 5.5 which allow simplification of Equation 5-25:

$$\frac{\omega^2}{k^2} = v_{ti}^2 + \frac{\omega_{pi}^2}{\omega_{pe}^2} v_{te}^2 \quad \text{• 5-28}$$

Equation 5-28 can be manipulated further by making the approximation in the bulk plasma density that $n_{oe}=n_{oi}$ and by assuming adiabatic compression for the ions ($\gamma_i=3$) and isotropic compression for the electrons ($\gamma_e=1$) as shown in Equation 5-29. These are all good assumptions given the expected density and temperature (Table 5.2).

$$V_{iaw}^2 = \frac{\omega^2}{k^2} = \frac{KT_e + 3KT_i}{m_i} \quad \text{• 5-29}$$

This equation is the traditional ion acoustic wave dispersion relation (Equation 5-5).

As will be shown later, all of the assumptions made throughout the derivation of the dispersion relation are very good for the system of interest. The initial assumptions of a stationary collisionless homogeneous plasma with a discrete temperature will be removed individually in the following sections.

5.2.2 Extension of Dispersion Relation to Include Collisional Damping Using the Fluid Equations

Collisional effects can be included in fluid theory by adding an effective pressure term to account for collisions in the equations of motion:

$$m_e n_e \left[\frac{\partial v_e}{\partial t} + (v_e \bullet \nabla) v_e \right] = n_e q_e E - \nabla P_e - n_e m_e \upsilon_{cen} v_e, \quad \text{• 5-30}$$

$$m_i n_i \left[\frac{\partial v_i}{\partial t} + (v_i \bullet \nabla) v_i \right] = n_i q_i E - \nabla P_i - n_i m_i \upsilon_{cin} v_i. \quad \text{• 5-31}$$

Both electron-neutral (υ_{cen}) and ion-neutral (υ_{cin}) collisions are included since they are momentum absorbing whereas coulomb collisions such as electron-electron or ion-ion do not absorb momentum from the wave. After linearization and transformation into the Fourier transform domain for both space and time, the equations of motion simplify to:

$$m_e n_{eo}[\omega - k v_{eo}] = -j n_{oe} q_e E_{p1} + \gamma_e K T_e k n_{ep} - n_{eo} m_e \upsilon_{cen} v_{ep} \qquad \bullet 5\text{-}32$$

$$m_i n_{io}[\omega - k v_{io}] = -j n_{oi} q_i E_p + \gamma_i K T_i k n_{ip} - n_{io} m_i \upsilon_{cin} v_{ip}. \qquad \bullet 5\text{-}33$$

Using the same derivation procedure as in the previous section for a collisionless plasma, the resulting dispersion function is:

$$D(\omega,k) = 1 + \frac{\omega_{pe}^2}{\omega(\omega + j\upsilon_{cen}) - k^2 V_{ep}^2} - \frac{\omega_{pi}^2}{\omega(\omega + j\upsilon_{cin}) - k^2 V_{ip}^2} = 0 \qquad \bullet 5\text{-}34$$

With one additional assumption, υ_{cen}, $\upsilon_{cin} \ll \omega_{pi}$, the dispersion relation is manipulated into the familiar form of Equation 5-29:

$$\frac{\omega(\omega + j\upsilon_c)}{k^2} = \frac{K T_e + 3 K T_i}{m_i} \qquad \bullet 5\text{-}35$$

$$\upsilon_c = \frac{m_e \upsilon_{cen} + m_i \upsilon_{cin}}{m_e + m_i}. \qquad \bullet 5\text{-}36$$

The electron-neutral collision frequency is found in Table 5.2 (8×10^3 s^{-1}) and the ion-neutral collision frequency [Ginzburg, 1970] is calculated:

$$\nu_{cin} = \frac{8\pi^{1/2}}{3} \frac{m_n}{m_i + m_n} n_n \sigma^2 \left(\frac{2KT_i}{m_i} + \frac{2KT_n}{m_n} \right)^{1/2}. \qquad \bullet 5\text{-}37$$

In order to estimate the ion collision frequency the necessary parameters are included Table 5.3. The neutral density was calculated through Equation 2-11. The ion-neutral collision frequency is less than 150 s^{-1}. Given Equation 5-36 the effective collision frequency is equivalent to the ion-neutral collision frequency (υ_c=150 s^{-1}) which is consistent with the knowledge that the momentum of an ion acoustic wave is transmitted by the ions and not

the electrons; therefore any attenuation is through the momentum loss in the ions and not the electrons.

Neutral Density, n_n (m^{-3})	1.75×10^{17}
Estimated Interaction Radius, (m)	4×10^{-10}
Estimated neutral mass, m_n (kg)	1.67×10^{-26}
Ion mass, m_i, Xe (kg)	2×10^{-25}
Ion temperature, T_i (eV)	0.1
Neutral temperature, T_n (eV)	0.025

Table 5.3. Parameters necessary to find ion-neutral collision frequency.

The dispersion relation (Equation 5-35) can now be evaluated by assuming a complex wavenumber (Equation 5-38) since the experiment is a steady state or boundary value problem (as opposed to transient which would require a complex frequency).

$$k = k_r + jk_i \qquad \bullet 5\text{-}38$$

By separating Equation 5-35 into real and imaginary components, the real and imaginary components of the wavenumber are found:

$$k_r^2 = \frac{\omega^2}{V_{iaw}^2}\left[\left(1+\frac{\upsilon_c^2}{\omega^2}\right)^{1/2}+1\right], \qquad \bullet 5\text{-}39$$

$$k_i^2 = \frac{\omega^2}{V_{iaw}^2}\left[\left(1+\frac{\upsilon_c^2}{\omega^2}\right)^{1/2}-1\right] \qquad \bullet 5\text{-}40$$

where V_{iaw} is specified as in Equation 5.29. In these calculations, a frequency is chosen that satisfies all of the derivation assumptions. Given that υ_c=150 s^{-1} and ω=$2\pi 50 \times 10^3$ rad/s, the real wavenumber is very close to the collisionless wavenumber and the imaginary wavenumber is zero to an accuracy better than 0.1% (ratio of imaginary to real wavenumber is less than 0.001); therefore, for this work, a collisionless model is sufficient.

5.2.3 *Kinetic Theory Prediction of Landau Damping and Estimation of Error in Fluid Analysis*

Kinetic theory predicts the dispersion relation of an ion acoustic wave without assuming isothermal components (electrons and ions) which is the main assumption in the fluid analysis that is not justified through comparison of experimental parameters such as frequencies or masses. By allowing a temperature distribution of the constituents, kinetic theory will not only provide an estimation of the accuracy of the fluid analysis result, but kinetic theory will also predict the degree of Landau damping. Just as with fluid theory, the following analysis will consider a homogeneous, collisionless, stationary two-component plasma where the magnetic field is negligible and linear theory is applicable.

A kinetic analysis begins with linearized distribution functions, f_e and f_i, for electrons and ions that are applied to Vlasov's equations (5-41 and 5-42) and Gauss's law (5-43) where the particle density is the first velocity moment of the distribution function (5-44 and 5-45).

$$\frac{\partial f_e}{\partial t}+(v\cdot\nabla)f_e+\frac{q_e}{m_e}E\cdot\frac{\partial f_e}{\partial v}=0 \qquad \bullet 5\text{-}41$$

$$\frac{\partial f_i}{\partial t}+(v\cdot\nabla)f_i+\frac{q_i}{m_i}E\cdot\frac{\partial f_i}{\partial v}=0 \qquad \bullet 5\text{-}42$$

$$\varepsilon_o\nabla\cdot E=q_e n_e+q_i n_i \qquad \bullet 5\text{-}43$$

$$n_e=\int_{-\infty}^{+\infty}f_e(r,v,t)dv_e \qquad \bullet 5\text{-}44$$

$$n_i=\int_{-\infty}^{+\infty}f_i(r,v,t)dv_i \qquad \bullet 5\text{-}45$$

Equations 5-41 and 5-42 are immediately linearized and either Fourier or Laplace transformed into the following equations:

$$j(\omega-kv)f_e(k,v,\omega)=\frac{-q_e}{m_e}\frac{\partial f_{oe}}{\partial v}E \qquad \bullet 5\text{-}46$$

$$j(\omega-kv)f_i(k,v,\omega)=\frac{-q_i}{m_i}\frac{\partial f_{oi}}{\partial v}E \qquad \bullet 5\text{-}47$$

$$-jkE=\frac{1}{\varepsilon_o}\left(q_e\int_{-\infty}^{+\infty}f_e(k,v,\omega)dv+q_i\int_{-\infty}^{+\infty}f_i(k,v,\omega)dv\right) \qquad \bullet 5\text{-}48$$

These equations are manipulated in a similar manner as the fluid equations to arrive at the dispersion function of an ion acoustic wave.

$$D=1+\int_{-\infty}^{+\infty}\frac{q_e^2}{k\varepsilon_o m_e}\frac{1}{\omega-kv}\frac{\partial f_e}{\partial v}dv+\int_{-\infty}^{+\infty}\frac{q_i^2}{k\varepsilon_o m_i}\frac{1}{\omega-kv}\frac{\partial f_i}{\partial v}dv=0 \qquad \bullet 5\text{-}49$$

The two integrals can be evaluated by assuming a reasonable form for the distribution function such as a Maxwellian distribution with an average thermal velocity for each of the constituents:

$$f_{e,i}=\frac{n_{oe,i}}{v_{the,i}\pi^{1/2}}e^{-v_{e,i}^2/v_{the,i}^2} \qquad \bullet 5\text{-}50$$

$$v_{the,i}=\left(\frac{2KT_{e,i}}{m_{e,i}}\right)^{1/2} \qquad \bullet 5\text{-}51$$

With the Maxwellian distribution and a few additional substitutions, the ion acoustic wave dispersion function can be manipulated into a simple form that includes the general plasma dispersion function.

$$s_e=\frac{v}{v_{the}},\ s_i=\frac{v}{v_{thi}},\ \zeta_e=\frac{\omega}{kv_{the}},\ \zeta_i=\frac{\omega}{kv_{thi}} \qquad \bullet 5\text{-}52$$

$$D=1-\frac{\omega_{pe}^2}{k^2v_{the}^2\pi^{1/2}}\int_{-\infty}^{+\infty}\frac{e^{-s}}{s-\zeta_e}\partial s-\frac{\omega_{pi}^2}{k^2v_{thi}^2\pi^{1/2}}\int_{-\infty}^{+\infty}\frac{e^{-s}}{s-\zeta_i}\partial s=0 \qquad \bullet 5\text{-}53$$

The integrals take the form of the derivative of the well known plasma dispersion function [Chen, 1984]:

$$Z'(\zeta)=\frac{1}{\pi^{1/2}}\int_{-\infty}^{+\infty}\frac{e^{-s}}{s-\zeta}ds. \qquad \bullet 5\text{-}54$$

The ion acoustic wave dispersion function can further be simplified by inserting the plasma dispersion function, manipulating the equation, and finally, substituting in for the plasma frequency and the thermal velocities:

$$2\lambda_d^2 k^2 \frac{T_i}{T_e} = Z'(\zeta_e)\frac{T_i}{T_e} + Z'(\zeta_i) \qquad \bullet 5\text{-}55$$

Given this general form of the ion acoustic wave, dispersion function simplifications can be made for the SPT-100 plasma parameters outlined earlier in this section and in Section 2.1. First, the plasma dispersion function is approximated for large and small values of ζ.

$$\zeta_i >> 1 \quad Z'(\zeta_i) = -2j\pi^{1/2}\zeta e^{-\zeta^2} + \zeta^{-2} + \frac{3}{2}\zeta^{-4} + .. \qquad \bullet 5\text{-}56$$

$$\zeta_e << 1 \quad Z'(\zeta_e) = -2j\pi^{1/2}\zeta e^{-\zeta^2} - 2 - \frac{8}{3}\zeta + .. \qquad \bullet 5\text{-}57$$

With these approximations $Z'(\zeta_e)$ is found to be much larger than $Z'(\zeta_i)$. The resulting equation (5-58) can be evaluated given the expected plasma parameters ($T_e = 3$ eV, $T_i = 0.1$ eV).

$$\left[2j\pi^{1/2}\zeta_e e^{-\zeta_e^2} + 2 + \frac{8}{3}\zeta_e\right]\frac{T_i}{T_e} = -2j\zeta_i e^{-\zeta_i^2} + \zeta^{-2} + \frac{3}{2}\zeta_i^{-4} \qquad \bullet 5\text{-}58$$

The solution of the equation defines the values for the wavenumber and frequency of a wave. A solution can be found by defining a steady state or boundary value problem which implies a complex wavenumber (as opposed to a complex frequency). Given a complex wavenumber the ion acoustic wave dispersion relation (Equation 5-58) can be solved iteratively to find the relative attenuation due to Landau damping (ratio of the imaginary part to the real part k_I/k_R). For the expected constituent temperatures the relative attenuation (k_I/k_R) is less than 0.02 which indicates minimal loss for a small number of

wavelengths. With this in mind, the loss is ignored and the wavenumber is taken to be purely real.

The results of Equation 5-58 can also be compared against the results of the ion acoustic dispersion relation derived from the fluid equation. Assuming a real wavenumber and the same constituent temperatures the fluid equation result is within 1% of the result of the kinetic derivation. This conclusion can be justified when examining the approximations necessary to transform Equation 5-58 (kinetic theory dispersion relation) into Equation 5-30 (fluid theory dispersion relation).

To transform Equation 5-58 into the traditional ion acoustic dispersion relation we first take only the real part of Equation 5-58, then approximate $Z'(\zeta_e) \approx -2$:

$$2\frac{T_i}{T_e} = \zeta_i^{-2} + \frac{3}{2}\zeta_i^{-4} \qquad \bullet 5\text{-}59$$

Now, we substitute the equivalent values for ζ_e and ζ_i in terms of T_i, T_e, and ω/k, and manipulate to the form:

$$\frac{\omega^2}{k^2} = \frac{kT_e + 3kT_i\left(\frac{kT_e/m_i}{\omega^2/k^2}\right)}{m_i} \qquad \bullet 5\text{-}60$$

From this expression, the term in parenthesis is close to one if T_e is greater than T_i which it is in Hall thruster plumes [Manzella, *et al.* 1995]; therefore, the fluid equation derivation is accurate to better than 1% as long as T_e is much greater than T_i. When this condition does not hold then the kinetic solution is necessary not only to find the phase velocity, but also to determine the effect of Landau damping.

5.3 Implications for a Nonideal plasma: Flowing, Inhomogeneous, Time Varying

The ion acoustic wave dispersion relation in the previous section was found by assuming a stationary plasma that is homogeneous over space and time. These assumptions are not correct in the plasma plume of an SPT. In order to evaluate the validity of the approximations, three quantities which have the greatest variation are quantified: the directed velocity of electron and ions, the spatial variation of density, and the time variation of density. The findings have implications for any experimental implementation.

5.3.1 Propagation Given a Finite Flow Velocity

An ion acoustic wave can propagate even in a moving plasma. All of the assumptions are the same as in Section 5.2.1 except a finite flow velocity, v_o, is returned to Equations 5-20 to 5-23 to determine the implications of plasma flow on the propagation of an ion acoustic wave where 5-61 to 5-64 are the resultant equations:

$$\omega n_{ep} - k n_{eo} v_{ep} - k n_{ep} v_{eo} = 0 \qquad \text{• 5-61}$$

$$\omega n_{ip} - k n_{io} v_{ip} - k n_{ip} v_{io} = 0 \qquad \text{• 5-62}$$

$$m_e n_{eo}[\omega - k v_{eo}] = -j n_{oe} q_e E_p + \gamma_e K T_e k n_{ep} \qquad \text{• 5-63}$$

$$m_i n_{io}[\omega - k v_{io}] = -j n_{oi} q_i E_p + \gamma_i K T_i k n_{ip} \qquad \text{• 5-64}$$

These equations, Equation 5-20, and the same assumptions as in Section 5.1 provide the basis for the dispersion function (Equation 5-65) as in the fluid derivation in Section 5.1.

$$D(\omega,k) = 1 + \frac{\omega_{pe}^2}{(\omega - k \bullet v_{eo})^2 - k^2 v_{te}^2} - \frac{\omega_{pi}^2}{(\omega - k \bullet v_{io})^2 - k^2 v_{ti}^2} = 0 \qquad \text{• 5-65}$$

In a similar manner to Section 5.1, Equation 5-65 is reduced to the simplified form of the dispersion relation for an ion acoustic wave in a flowing plasma.

$$\left(\frac{\omega}{k}-\hat{k}\bullet v_{eo}\right)^2=\frac{KT_e+3KT_i}{m_i}=V_{iaw}^2 \qquad \bullet 5\text{-}66$$

In this expression the frequency and wavenumber define the propagation of an ion acoustic wave that is superimposed onto a flowing plasma. Equation 5-66 can be expressed in an alternate form (Equation 5-67) that more clearly shows that the ion acoustic wave propagation is determined by the vector sum of the wave velocity and the flow velocity.

$$\frac{\omega}{k}=V_{iaw}+\hat{k}\bullet v_{eo} \qquad \bullet 5\text{-}67$$

This expression is used in the analysis of the ion acoustic wave propagation.

5.3.2 Propagation in an Inhomogeneous Plasma

Interpreting propagation can be a complex problem if the dispersion relation is spatially varying. Normally the problem is simplified by assuming the geometric optics or Wentzel-Kramer-Brillouin (WKB) approximation; however, this estimation is not strictly valid in the region of interest given the strong density gradients in the plume (see Chapter 4, Equation 4-1 for electron density model). Even though the geometric optics condition does not hold, the density gradient is still small compared to the scale lengths of interest such as the measurement system and the wavelength. To determine the effect of the density variation on the wave, a one dimensional analysis of the fluid equations [Jones, *et al.* 1985] is used to quantify the phase variation over the measurement region.

The one-dimensional analysis begins at the fluid Equations 5-20 to 5-24 where the density variation ($\nabla\cdot(n_o v_p)$) is returned to the continuity equations for the electron and ions. The derivation [Jones, *et al.* 1985] follows similar approximations as the fluid

analysis derivation for the ion acoustic wave dispersion relation; however, this derivation results in a second order differential equation:

$$\frac{d^2 n_{norm}}{dx^2} + \frac{1}{n_o(x)} \frac{dn_o(x)}{dx} \frac{dn_{norm}}{dx} + k_{iaw}^2 n_{norm} = 0, \qquad \bullet 5\text{-}68$$

$$n_{norm} = {}^{n_p}\!/_{n_o}. \qquad \bullet 5\text{-}69$$

The solution of this differential equation (Equations 5-70 to 5-71) is found through assuming a modified wavenumber, k_m..

$$k_m^2 = k_{iaw}^2 - \left[\frac{1}{n_o(x)}\right]^{1/2} \frac{d^2[n_o(x)]^{1/2}}{dx^2} \qquad \bullet 5\text{-}70$$

$$n_p(x) = B n_o(x)[n_{o(x)}]^{3/2} \exp[j k_m(x) x] \qquad \bullet 5\text{-}71$$

To determine the modified wavenumber, the ion acoustic wavenumber is estimated to be 21 m^{-1} (the wavelength is 0.3 m) by applying Equation 5-67 to the values in Table 5.2, using a frequency of 50 kHz, and assuming the wave vector is along the flow direction. The wavelength should be slightly longer than the experiment region. In order to completely define the modified wavenumber, the functional model of the plasma density distribution is utilized from Chapter 4, Equation 4-1.

The modified wavenumber, k_m is used to quantify the possible effect of the density gradients on the propagation of the ion acoustic waves. Since the density gradient is positionally dependent, the modified wavenumber is evaluated along a number of representative propagation paths. The paths are chosen to be rays emanating from the thruster (approximately aligned with the flow) since the propagation is limited to a narrow cone originating from a wave excitation source and directly aligned with the flow (see Section 5.4 for a more detailed discussion). The modified wavenumber is evaluated along these rays in order to track the phase variation. In Figure 5.1, theta is the angle formed by the thruster centerline and the ray path where the origin is the thruster.

The phase is calculated for both a wave governed by the modified wavenumber and a wave governed by the normal ion acoustic wave number, k_{iaw}. The phase is normalized to zero at the starting point (0.4 m axial distance from the thruster) of the calculation for both wavenumbers. The difference between the two phase calculations (Figure 5.1) gives an indication of the effect of the density gradient. Three possible propagation paths are represented by the graph. The first is given by theta = 0° where the entire path is in the core of the plume where the density gradient is very small. The second is given by theta = 10° where the path starts in the core of the plume and progresses into the periphery where the density gradient starts small, increases, and finally decreases in the edge region of the plume. The third case is given by both theta = 20° and theta = 30° where the path is entirely in the edge region of the plume where the density gradient is continuously decreasing. Two factors indicate the significance of the phase variation. First, the total phase variation (Figure 5.1 inset) is much larger than the phase variation caused by the density gradient. Second, the phase difference is very small over the scale length of measurement, which is also shown in Figure 5.1.

The conclusion drawn from the phase calculation is that even though the geometric optics approximation does not strictly hold, a pseudo-geometric optics approximation can be made over the measurement region. This implies that the phase variation over the wavefront changes very little over the region of interest. This conclusion also allows the analysis to assume the traditional form of an oscillating electric field and density:

$$E = E_o e^{j(kr-\omega t)} \qquad \bullet 5\text{-}72$$

$$n = n_o e^{j(kr-\omega t)} \qquad \bullet 5\text{-}73$$

The Fourier electric field component is necessary for the previous fluid analysis to find the dispersion relation to be used in the measurement analysis.

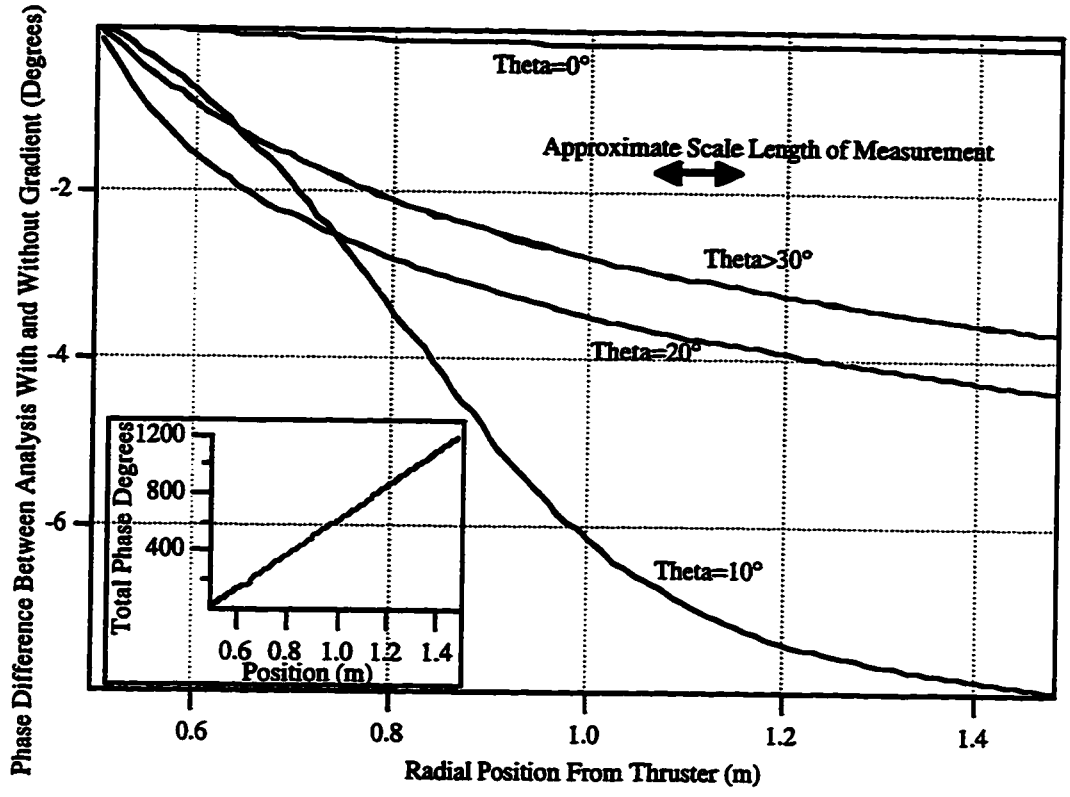

Figure 5.1. Effect of plasma parameter gradients on phase.

5.3.3 Propagation in a Time Varying Plasma

The plume of the SPT is known to exhibit noise that produces temporal density variation. The noise is described by a continuous Fourier spectrum summarized by ω_{noise}. The plasma noise contains strong harmonics in the 20 to 30 kHz range, but it also contributes significantly to the broadband noise characteristics over the entire frequency range of interest (DC up to 1 MHz). The noise characteristics are measured experimentally through the microwave characterization in Chapter 3 and the passive high impedance probe characterization of Chapter 6. The noise amplitude modulates the density in the form given by Equation 5-74 (Dickens, 1995; Dickens, *et al.* 1995a)

$$n_o = n_{const}\left[1 + m\exp(j\omega_{noise}t)\right] \qquad \bullet 5\text{-}74$$

where n_{const} is the density given by the static model in Chapter 4 and m is the modulation factor with typical value 0.1 which has been found experimentally for the SPT (Dickens, 1995; Dickens, *et al.* 1995a).

The time varying density is returned to the fluid equations and in particular to the continuity equations:

$$\omega a n_{econst} + \omega n_{e1} - k n_{eo} v_{e1} = 0 \qquad \bullet 5\text{-}75$$

$$\omega a n_{iconst} + \omega n_{i1} - k n_{io} v_{i1} = 0 \qquad \bullet 5\text{-}76$$

The fluid derivation is repeated with the density time variation to find the ion acoustic dispersion relation. The dispersion relation indicates the noise affects phase velocity through a modulation of the electrons:

$$\frac{\omega^2}{k^2} = \frac{3KT_i}{m_i} + \frac{KT_e}{m_i}\left[1 + m\omega_{noise}\exp(-j\omega_{noise}t)\right]. \qquad \bullet 5\text{-}77$$

The modulation factor, $m\omega_{noise}$, is a number less than one that is dependent on particle mass, wave velocity, perturbation electric field, and noise frequencies. The time variation of the density directly produces phase noise on the ion acoustic wave; therefore, the measurement frequency is chosen to avoid the dominant noise frequency components of the thruster.

5.4 Ion Acoustic Wave Excitation and Propagation Characteristics

The dispersion relation (Equation 5-66) for a flowing plasma provides the theoretical basis for a diagnostic technique that uses ion acoustic wave propagation characteristics to find plasma parameters. Propagation is explored through modeling excitation with an infinitesimally thin cylindrical probe. The general propagation

characteristics are investigated and explained. Finally, possible propagation characterization is related to three plasma parameters: flow velocity, electron temperature, and ion temperature.

5.4.1 Exciter Characteristics

Ion acoustic waves can be excited by a metallic probe inserted in a plasma that is driven with an oscillating potential. The waves can be excited by a number of geometries: grids, spheres, bipolar probes, or cylindrical probes [Chen, 1977; Gould, 1964; Schott, 1992; Nakamura, *et al.* 1993]. In this research, a small cylindrical wire probe (on the order of a Debye length in diameter) is used in order to minimize both electrostatic and fluid dynamic disturbance. The probe length (normal to flow) is chosen smaller than a wavelength so that it appears as a small monopole source which produces an electric field radially outward. The probe is driven by an applied oscillating potential which is less than the floating potential. The applied potential is maintained less than the floating potential (ion saturation region) in order to produce an ion sheath which minimizes the disturbance to the plasma. However, the amplitude is greater in magnitude than the electron temperature in order to produce a sheath oscillation which effectively launches an ion acoustic wave [Widner, 1970; Hong, *et al.* 1993].

Most of the exciter probe potential is dropped across the sheath; however, the presheath, which contains electrons, actually excites the ion acoustic wave [Chen, 1977]. One implication of the presheath launching the wave is that the excitation area is much larger than that physical area of the probe (this is relevant to the analysis in Chapter 7). Additionally, since the majority of the probe potential is lost in the sheath, the probe excitation efficiency is small (less than 1%) where the efficiency is the ratio of the potential disturbance of the wave to the applied probe potential.

5.4.2 Propagation Pattern

The radiation pattern for a wire probe is developed through a basic physical interpretation to qualitatively explain the measurement. The propagation pattern of the probe is evaluated in the plane orthogonal to its length (see Figure 5.2) which is also the measurement plane. Propagation from a wire probe is produced by applying a time varying potential to the probe. When a potential is applied, a sheath forms a cylinder around the probe which is a few Debye lengths in thickness. Around the sheath, a presheath which can be many Debye lengths thick, launches the ion acoustic waves. The presheath electric field radiates radially outward from (or inward to) the probe producing a longitudinal ion acoustic wave radiating isotropically in the X-Z plane in a non-flowing plasma as in Figure 5.2.

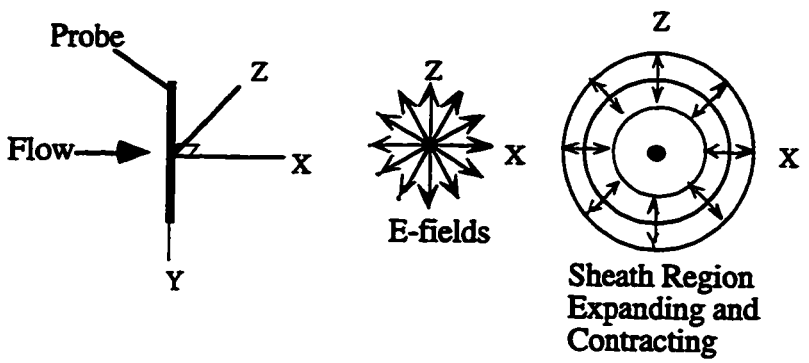

Figure 5.2. Coordinate system for discussion of propagation.

On the other hand, in a flowing plasma, the pattern is skewed in the direction of the flow (see Figure 5.3). In a plasma moving slower than the wave velocity the wave is expanded (or Doppler shifted) in the direction of the flow and compressed in the direction opposite the flow. When the flow velocity is faster than the wave velocity, the wave cannot propagate opposite to the flow and is limited to a propagation zone which is defined by the wave velocity and flow velocity. The last case is of interest in this research.

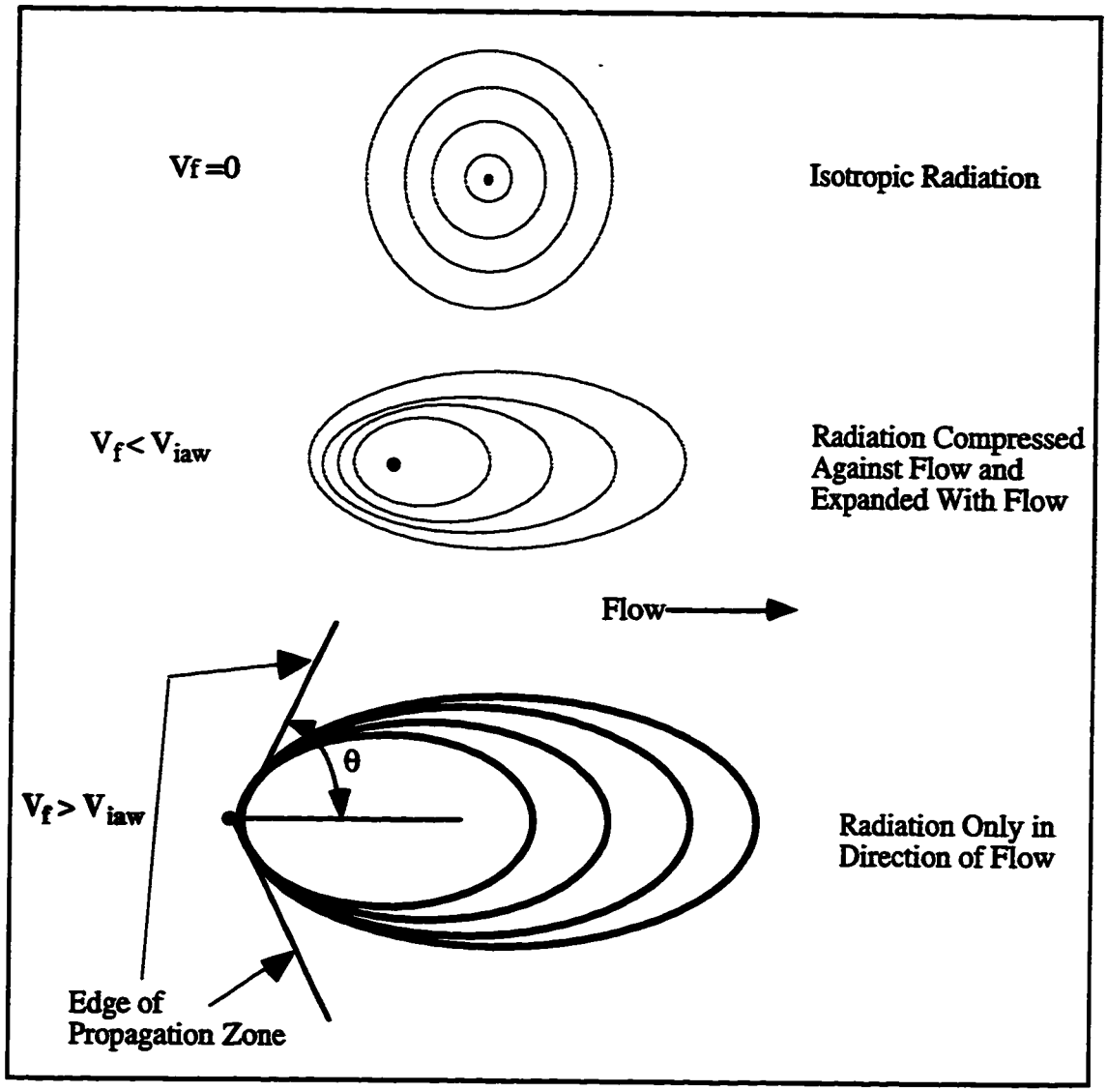

Figure 5.3. Qualitative comparison electrostatic propagation in a flowing plasma for three levels of plasma flow velocity relative to the propagation velocity.

The skewed propagation of the ion acoustic wave is first described here by a simple model and then is later expanded to explain the experimental results. Initially, the wave is excited (or radiates) isotropically from the source. After initial excitation, the wave propagates with the wave number which is determined by the vector sum of the ion acoustic wave velocity and the flow velocity (Equation 5-67). With this model no propagation occurs opposite the flow. Propagation initiated orthogonal to the flow follows

a path determined by the vector sum of the velocities where the angle of this vector defines the theoretical propagation zone of the wave (Figure 5.4). Lastly, propagation parallel to the flow direction moves with a velocity equal to the sum of the ion acoustic wave velocity and the flow velocity (Figure 5.5).

5.4.3 Determining Flow Velocity, Electron Temperature, and Ion Temperature

The velocity of both the ion acoustic wave and the plasma flow are found by quantifying the propagation along the two limiting direction: orthogonal and parallel to the flow. The wave initiated orthogonal to the flow follows a path that is the boundary of the propagation zone; experimentally determining the propagation zone (θ) defines the ratio of the two velocities through Equation 5-78. The wave propagating parallel to the flow is defined by the wavenumber and frequency which are directly related to the sum of the velocities through Equation 5-79. The wave is excited with a known frequency and the wavenumber is determined through a measurement of the wavelength. The two measurements (Equations 5-78 and 5-79) uniquely determine the wave velocity and flow velocity.

$$\theta = \tan^{-1}\left(V_{iaw} / V_{flow}\right) \qquad \bullet 5\text{-}78$$

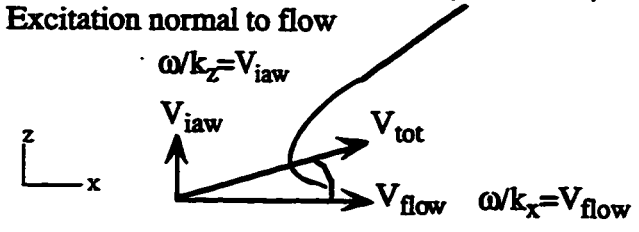

Figure 5.4. Velocity vector for excitation orthogonal to flow.

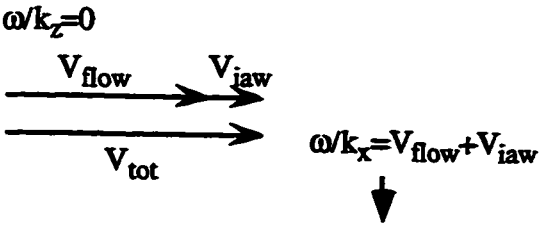

$$\lambda = 2\pi\left(V_{flow} + V_{iaw}\right) / \omega \qquad \bullet 5\text{-}79$$

Figure 5.5. Velocity vector for excitation parallel to flow.

Determining the wave velocity and flow velocity did not require the knowledge that the electrostatic wave is an ion acoustic wave. The only assumption is that a coherent electrostatic wave propagates in the plasma, and it is superimposed onto the flowing plasma. By experimentally verifying that the electrostatic wave is an ion acoustic wave, additional information is obtained through the ion acoustic wave dispersion relation. The ion acoustic wave velocity is proportional to the sum of the electron and the ion temperatures. In our experimental situation the ion temperature is less than the electron temperature and the ion temperature could be approximated as zero in order to estimate the electron temperature from the phase velocity. The ion temperature can also be estimated if an the electron temperature is found independently such as with a Langmuir probe; however, the ion temperature determination is very sensitive to the accuracy of electron temperature and phase velocity. A description of the measurement is found in Section 5.5 and the estimation of accuracy is found in Chapter 7.

5.5 Ion Acoustic Wave Measurement System

Sections 5.1-5.4 have established a mathematical description of ion acoustic wave propagation in the plasma of a SPT-100 thruster. In order to characterize the wave propagation experimentally, it is necessary to measure the spatial variation in phase and

magnitude of the wave. A system to measure these quantities is described in general terms and detailed later in the experimental results of Chapters 6 and 7.

5.5.1 System Description

The ion acoustic wave probe system is composed of three primary components: the positioning system, the exciter and detector probes, and the data acquisition system. The first two components are placed in a vacuum chamber (Figure 5.6). Probe characteristic are transmitted in and out of the chamber via coaxial cable to the data acquisition system which comprises a lock-in-amplifier and computer.

5.5.2 Vacuum Facility

The stainless steel vacuum chamber used for these experiments is 9 m long by 6 m in diameter and located in the Plasmadynamics and Electric Propulsion Laboratory (PEPL) at the University of Michigan. The vacuum facility is supported by six 0.81-m-diameter diffusion pumps each rated at 32,000 L/s (with water-cooled cold traps), backed by two 2,000 cfm blowers, and four 400 cfm mechanical pumps. The experimental facilities are described in more detail in Gallimore [*et al.* 1994].

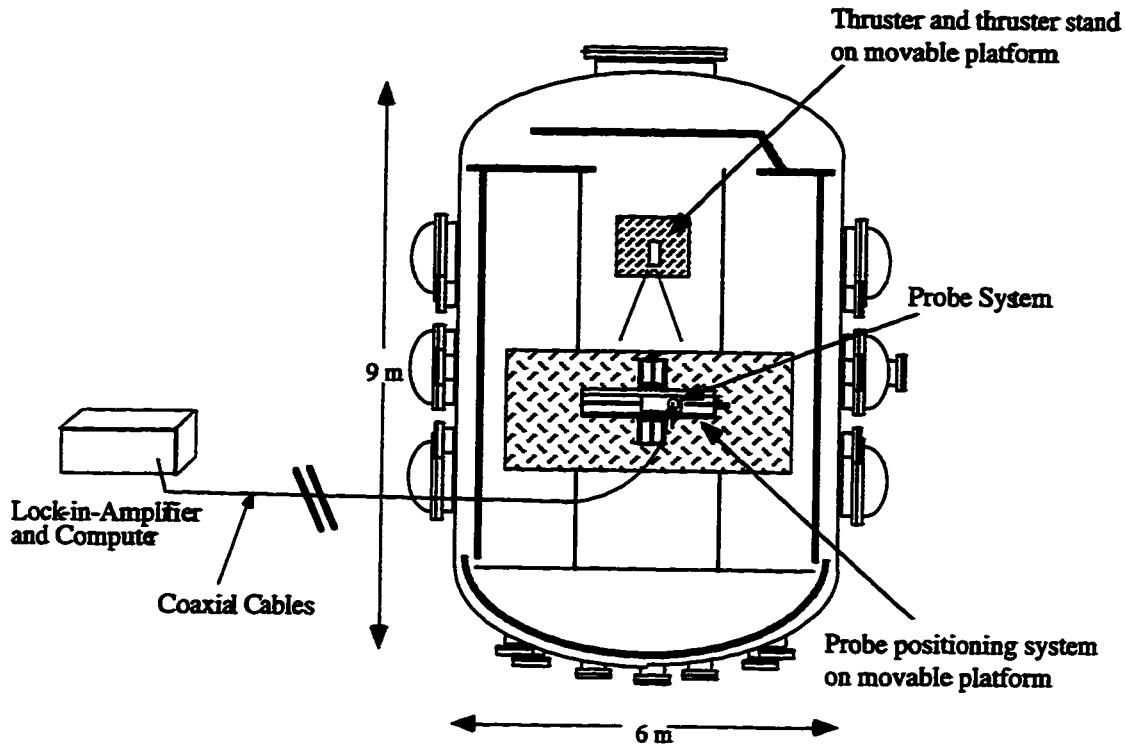

Figure 5.6. Measurement system in vacuum chamber.

5.5.3 Positioning System

A state-of-the-art probe positioning system provides the capability to spatially map plume parameters. The system is driven and monitored with a computer. The positioning system is mounted on a movable platform to allow for measurements to be made throughout the chamber. The positioning system contains two linear stages with 0.9 m of travel in the axial direction and 1.5 m of travel in the radial direction. Additionally, two rotary platforms are mounted to the radial stage that provide precise probe rotation around a given axis. The axial direction, shown in Figure 5.7 or 5.8, is along the axis of the thruster. The radial axis indicates the direction orthogonal to the plane created by the thruster axis and the probe axis.

5.5.4 Probe Configurations

The ion acoustic wave measurements utilize two probing configurations where the cylindrical wire probes are always mounted vertically. The first uses one stationary (with respect to the thruster) probe and one probe mounted to the linear tables (Figure 5.7). This configuration allows complete mapping of the ion acoustic wave propagation characteristics for a single exciter position. The second configuration (Figure 5.8) uses 3 probes: the first mounted on the axis of the rotary table, the second mounted 5-10 cm from the rotary axis on a bar attached to the rotary axis, the third probe is mounted 1-5 cm farther from the rotary axis. This configuration allows all probes to be concurrently moved with respect to the thruster; hence it provides the capability for plasma parameter mapping throughout the plume. This configuration also provides the two desired propagation characteristics: wavelength which is derived from accurate differential phase measurements between the detectors for a known separation, and maximum propagation angle which is found through amplitude measurements over a range of emitter-detector angles for a constant radial distance from the emitter.

5.5.5 Data acquisition systems

The data acquisition system controlled the excitation characteristics of the exciter probe such as the voltage and frequency and also received and processed the voltage measured from the detector probe. The voltage signal is controlled and monitored through a lock-in amplifier (Stanford Research Systems SR850) which serves as a highly sensitive transmitter and receiver. The lock-in amplifier uses digital processing to both produce an extremely noise-free signal and process the return signal. In some cases an amplifier is used to obtain larger amplitude or bias levels than provided by the lock-in amplifier. The lock-in amplifier is controlled via GPIB by a computer which stores voltage and phase measurements.

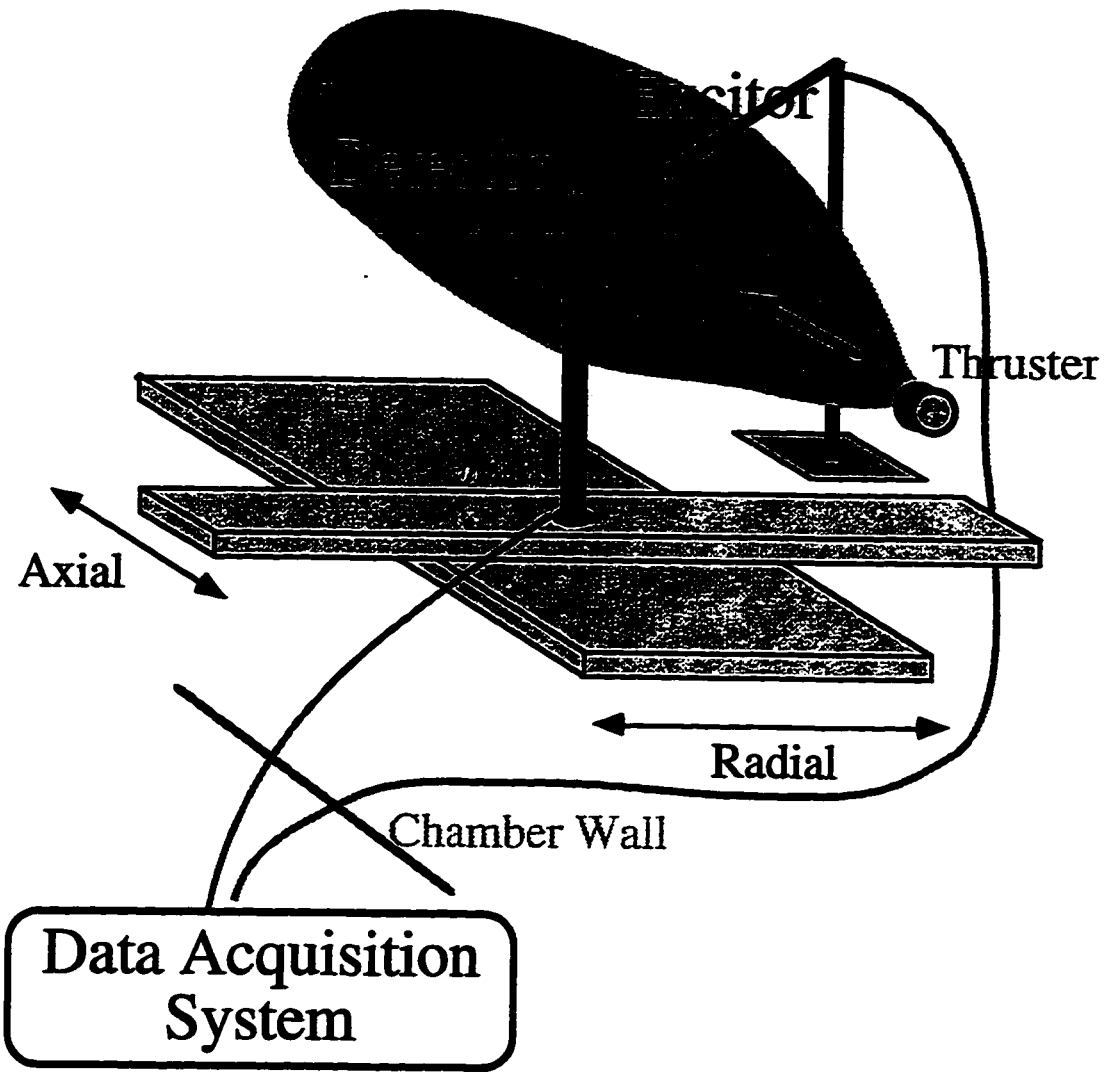

Figure 5.7. Schematic of probe system for detailed characterization of propagation characteristics.

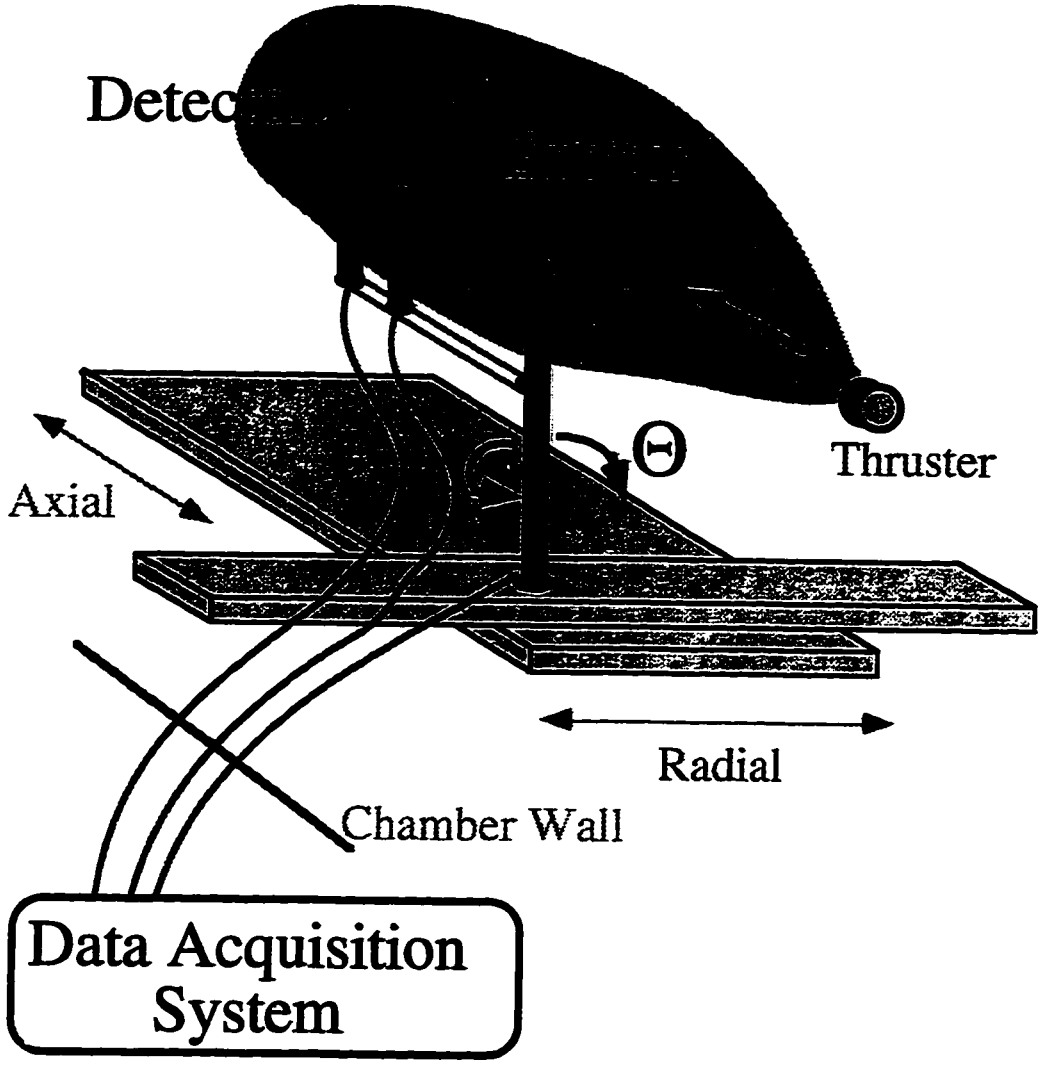

Figure 5.8. Schematic of probe system for ion acoustic wave diagnostic which characterizes propagation zone and phase shift over a known distance.

CHAPTER 6

GENERAL ION ACOUSTIC WAVE CHARACTERIZATION

6.0 Overview of Chapter

In order to utilize the propagation characteristics of ion acoustic waves (Chapter 5) to measure flow velocity, electron temperature, or ion temperature in the plume of a stationary plasma thruster, it is necessary to understand ion acoustic wave propagation in a non-ideal plasma. This Chapter presents an evaluation of the problem by exploring the experimental issues of ion acoustic wave excitation, propagation, and detection.

Three primary questions are resolved through this experimental evaluation: what is a reasonable probe geometry and excitation signal, does an ion acoustic wave coherently propagate, and over what parameter set is ion acoustic wave propagation consistent? The answers to these questions provide the basis for a simple diagnostic to find flow velocity, electron temperature, and ion temperature to be presented in Chapter 7. Initially, the experimental setup is outlined (Section 6.1), then experimental results are given for a variety of experimental conditions (Section 6.2), and finally an analysis and summary provide answers to the questions just posed (Section 6.3).

6.1 Experimental Setup

Experiments to characterize ion acoustic wave propagation have been completed in the research for a range of conditions and experimental configurations. The results of these experiments are presented for two thrusters, a number of probe sizes, and a number of circuit acquisition system configurations that excite and detect the signals.

6.1.1 Thrusters

For the development of the ion acoustic wave diagnostic, two stationary plasma thrusters have been studied (Figure 6.1), the Fakel SPT-100 and Moscow Aviation Institute (MAI) SPT, both built in Russia. The primary thruster is a commercial grade flight model SPT-100 built by the Russian Fakel Enterprises which is on loan from Space System/Loral and previously tested by NASA Lewis [Myers, *et al.* 1993; Manzella, 1993, 1994, 1995; Absalamov, *et al.* 1992] as well as others presented in Appendix B. This thruster is operated with xenon gas propellant and nominal operating conditions of 300 V anode-cathode potential, 4.5 A discharge current, 5.0 mg/s (xenon) through the anode, and 0.56 mg/s xenon through the hollow cathode.

The second thruster is a lab model SPT on loan from the Moscow Aviation Institute (MAI). The thruster is similar to the Fakel thruster but it has not been refined for flight qualification status in terms of the materials and operating conditions. This thruster is operated with either argon, krypton, or xenon propellant with flow rates 2 to 5 mg/s through the anode, 0.3 to 0.8 mg/s through the cathode. The electrical inputs include voltage applied to the anode, cathode, and ignitor and the current applied to the heater, inner magnet coil, and outer magnet coil. A range of operating conditions existed for the electrical parameters. The cathode-anode discharge potential is between 120 and 310 V with a discharge current of 3 to 5 A. The ignitor is floating during operation with a potential between 15-1000 V necessary to ignite the discharge. The heater current is 8 A, and the inner and outer magnets are set between 2 and 4 A.

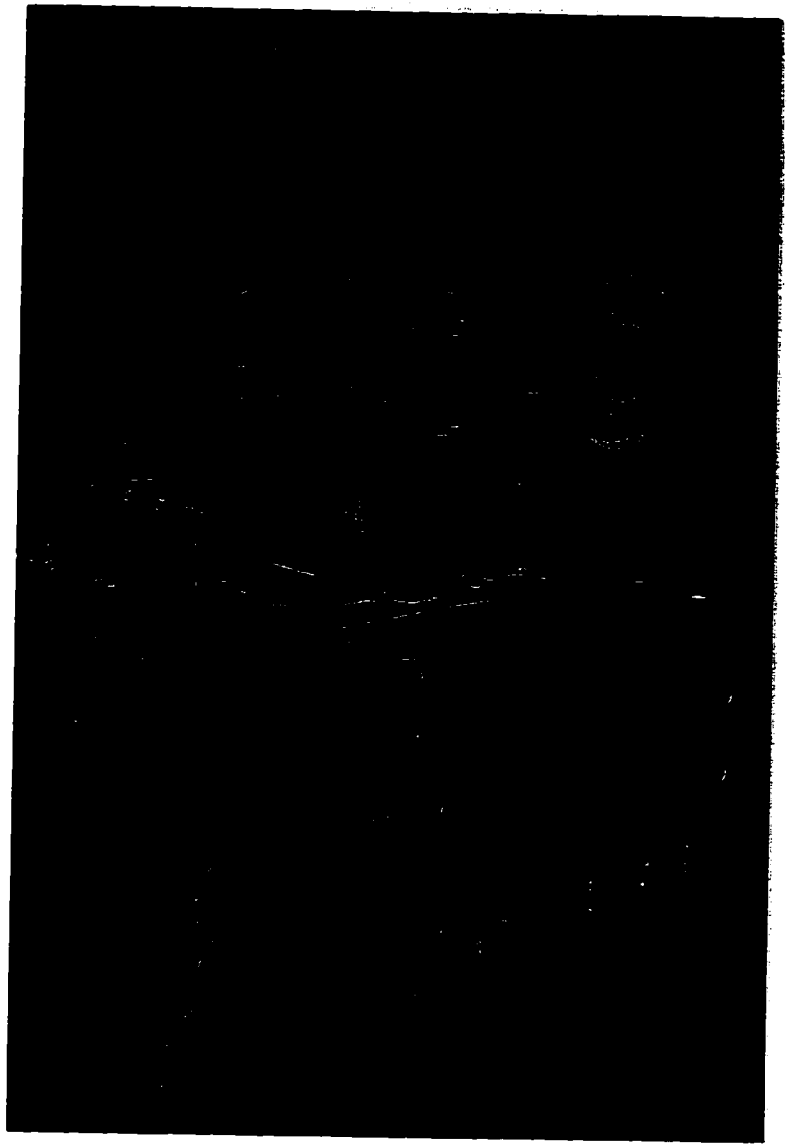

Figure 6.1. Photograph of a stationary plasma thruster (SPT-100) on a thruster stand.

6.1.2 Probes

The probes used for excitation and detection of voltage signals are oriented orthogonal to the direction of flow. In all cases a tungsten wire is fed through a ceramic or Teflon insulator and connected to RG-58 coaxial cable which is protected and supported in a metal shield (see Figure 6.2). The tungsten wires vary in thickness from 0.12 to 2.64 mm outer diameter and from 0.2 to 2.1 cm in length. The outer diameter of the insulator is 2-4

times the outer diameter of the wire and the metal shield is stainless steel tube. The stainless steel tube is connected to ground via the support structure which is either connected to the positioning table for the movable probes or the chamber floor for stationary probes.

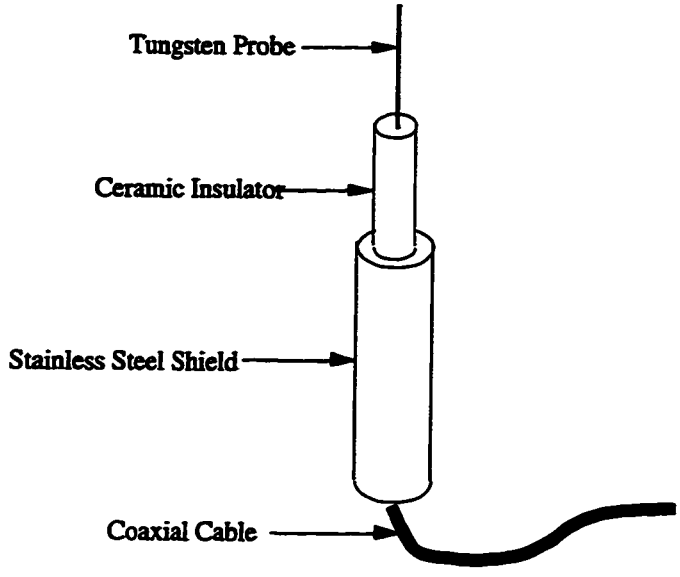

Figure 6.2. Schematic of probe assembly.

6.1.3 Data Acquisition System

The primary measurement system consists of a lock-in-amplifier connected to a computer via a GPIB cable and is controlled through LabView software (Figure 6.3). The lock-in-amplifier acted as a sensitive transmitter and receiver through digital control of the transmitted signal and digital filtering of the received signal. The processing capabilities included filtering with better than 0.1 Hz bandwidth and 18 dB/octave attenuation. This allowed detection of an extremely small signal in the noisy and relatively large ambient voltage signal. The excitation signal from the lock-in-amplifier had a maximum peak-to-peak voltage of ±5 V and testing is reported in the frequency range of 1 to 100 kHz (maximum frequency of this lock-in-amplifier model).

Additional measurements are presented for larger excitation voltage signals which utilize the Tektronix AM501 op amp with a voltage range of ±40 V, BK Precision 1651 DC power supply, and a Kepco bipolar amplifier. A dc-bias is applied to the lock-in-amplifier signal using the op-amp and power supply as shown in Figure 6.4 and a larger peak-to-peak voltage signal is produced through use of the bipolar power supply as in Figure 6.5.

Characterization of plasma noise characteristics are obtained through the direct connection of a Tektronix TDS 540 oscilloscope to a probe. The floating potential is obtained from voltage-current sweeps implemented in a circuit utilizing the op amp, a BK Precision 3026 function generator, and the oscilloscope as shown in Figure 6.6.

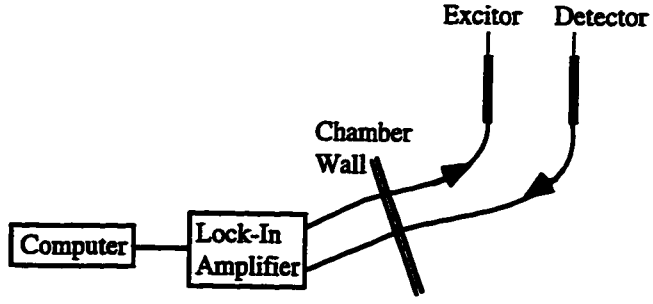

Figure 6.3. Schematic of primary circuit for characterization of ion acoustic waves.

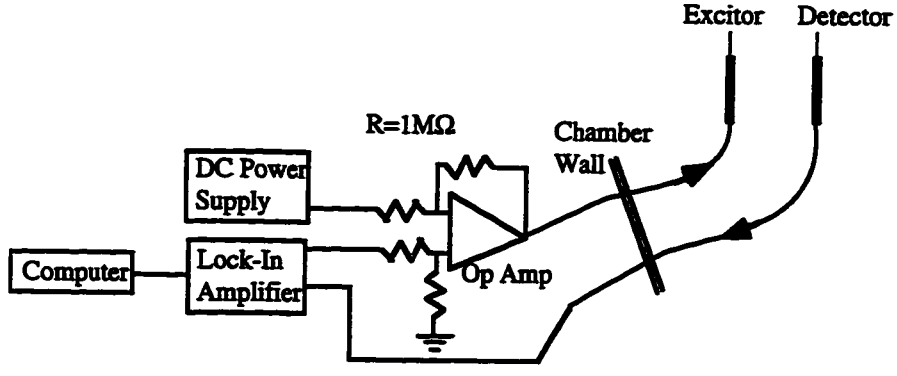

Figure 6.4. Schematic of circuit to evaluate probe bias potential.

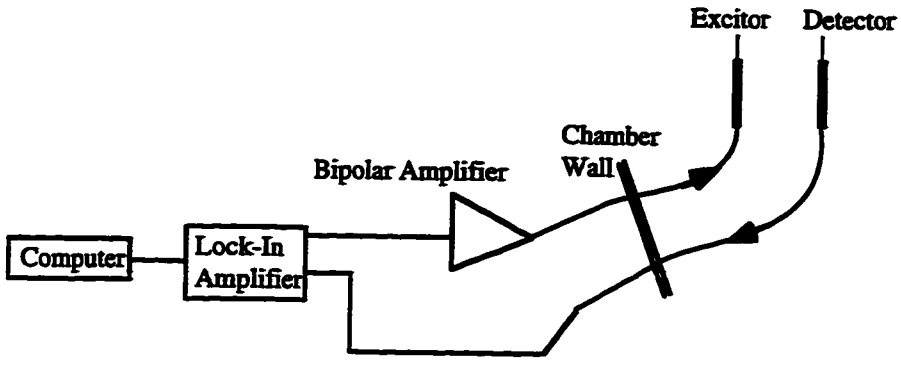

Figure 6.5. Schematic of circuit to evaluate large amplitude excitation potentials.

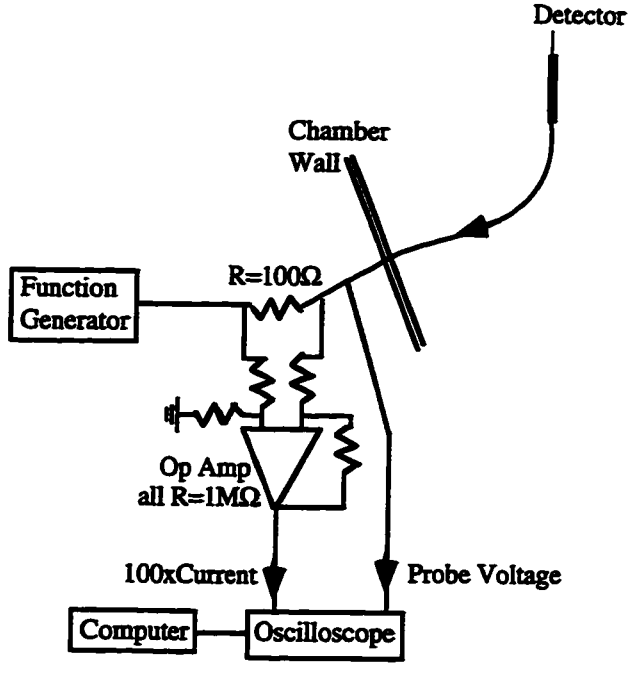

Figure 6.6. Schematic of circuit to characterize plasma floating potential.

6.2 Results of General Ion Acoustic Wave Characterization

Ion acoustic wave excitation, propagation, and detection are characterized in this work through comparison and evaluation of different experimental situations. Initially, the plasma is characterized in terms of the floating potential and plasma noise. This supplements the general plasma parameters already discussed in Chapter 5: electron density, electron temperature, ion temperature, and collision frequencies. Next the general

propagation patterns are discussed to provide an overview of probe-plasma coupling characteristics. The probe-plasma coupling is evaluated through separate comparison of detection characteristics for different excitation potentials, probe sizes, and excitation frequencies. Lastly, detection characteristics are presented for a number of thruster propellants. A summary of the tests to characterize ion acoustic wave excitation and propagation is given in Table 6.1.

Section	Parameter	Parameter Set	Axial Spatial Mapping (cm)	Radial Spatial Mapping (cm)
6.2.1	Floating Potential	NA	+55 to +144	-100 to +40
6.2.1	Power Spectral Density of Probe Noise (kHz)	DC to 15	NA	NA
6.2.2	General Propagation	NA	-3 to +3	0 to +25
6.2.3	Excitation Amplitude (V)	±5 to ±40	0 to +25	-3 to +3
6.2.3	Excitation Bias (V)	0 to -30	0 to +25	NA
6.2.4	Detector Probe Size (diameter, cm)	0.022 to 0.083	0 to 33	NA
6.2.4	Exciter Probe Size (diameter, cm)	0.046 to 0.26	0 to 25	-7 to +7
6.2.5	Excitation Frequency (kHz)	3.2 to 100	0 to +51	NA
6.2.6	Plasma Gas	Ar, Kr, Xe	0 to +40	-5 to 3

Table 6.1. Summary of Experiments to Characterize Ion Acoustic Wave Excitation and Propagation in a Flowing Plasma.

6.2.1 Plasma Characterization of Floating Potential and Plasma Noise

A factor in probe-plasma coupling is the voltage-current characteristics of the probe over the excitation voltage range. Previous work has demonstrated the effective excitation of ion acoustic waves with probe excitation levels in the ion saturation region. This is due to the strong control of electrons in that region of the voltage-current characteristics [Chen, 1977]. Other benefits of operating in the ion saturation region include an approximately constant coupling response over the excitation range and the minimal probe current which minimizes probe intrusiveness.

In order to verify operation in the ion saturation region, the floating potential has been monitored in each test. Measurement with a voltmeter indicates the floating potential, for both the Fakel and MAI thrusters, varies between +4 and +8 V which is dependent upon the operating conditions and propellant. Additional spatial characterization using the experimental setup in Figure 6.6 determined the floating potential using the zero current point in the voltage current characteristics (Figure 6.7). The spatially resolved measurements indicate only slight variation over a wide spatial range from -100 to +50 cm radially and from +55 to +144 cm axially (Figure 6.8). The results in Figures 6.7 and 6.8 are from measurements during operation of the Fakel thruster at nominal operating conditions of 300 V and 4.5 A.

In addition to the floating potential, the plasma noise characteristics are also measured in terms of the voltage noise characteristics on the floating probe. The noise characteristics of the probe are important since the ion acoustic wave is detected through the voltage variation on the probe due to the plasma. Natural plasma oscillations can degrade the signal that the lock-in-amplifier receives. In addition to signal degradation, the natural oscillations of the plasma could potentially dampen the excited ion acoustic wave and make characterization of the propagation characteristics difficult.

The natural oscillations of the plasma are measured by connecting the probe via coaxial cable to an oscilloscope with high input impedance. Representative measurements were taken with the MAI thruster operating at 300 V and 4.5 A using krypton propellant and with the Fakel thruster operating at 300 V and 3.2 A using xenon propellant. The amplitude variation with time (Figure 6.9 and 6.10) indicates that the Fakel thruster produces a stronger and more coherent oscillation than the MAI thruster (as expected since the Fakel thruster is tuned for a higher standard of operation). The frequency components of the plasma oscillations (Figures 6.11 and 6.12) show the dominant frequency of both thrusters to be between 20 to 30 kHz as expected from the microwave measurements of the Fakel thruster presented in Chapter 3. The resolution of the frequency domain is low

(especially for the Fakel thruster) due to sampling characteristics used for the particular data sets; however, important information still exists for the ion acoustic wave measurements. Propagation near 21.5 kHz for the MAI thruster and 29 kHz (26 kHz according to the more accurate results of Chapter 3) for the Fakel thruster should not be used for excitation, propagation, and detection of ion acoustic waves. First and second harmonics of these frequencies should also be avoided if possible.

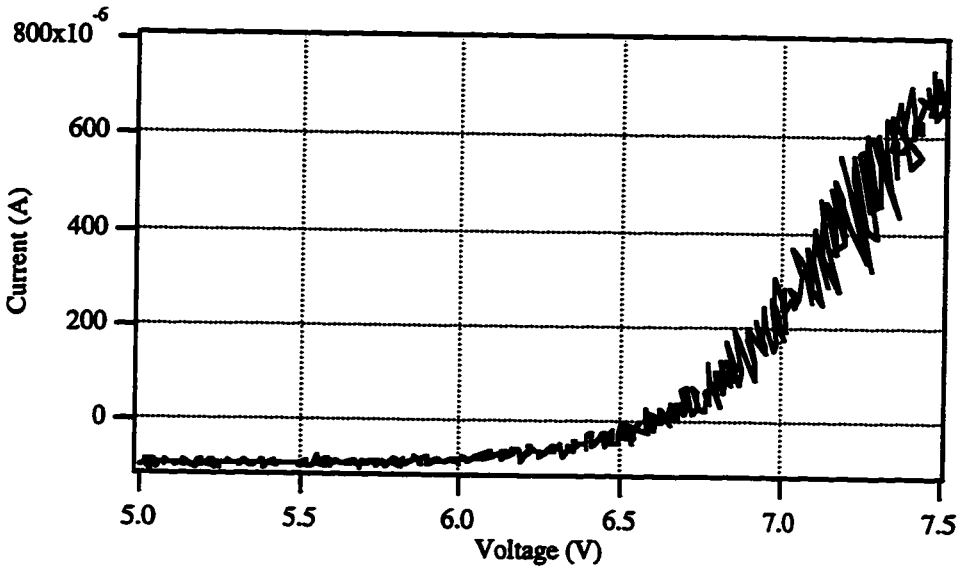

Figure 6.7. Representative current voltage characteristics of a cylindrical wire probe orthogonal to the flow in the plume of the SPT-100 approximately 1 m from the thruster.

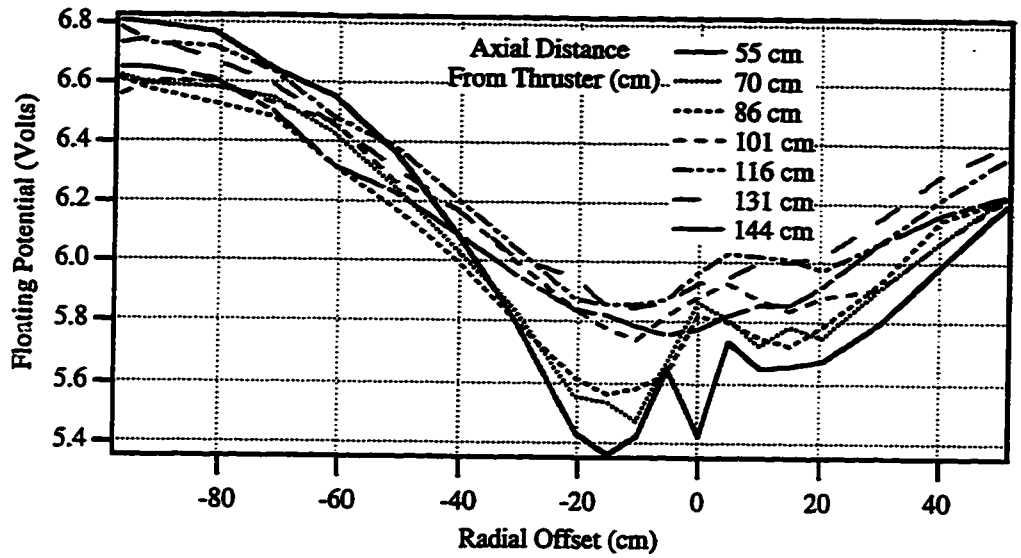

Figure 6.8. Spatial mapping of the floating potential in the plume of the SPT-100.

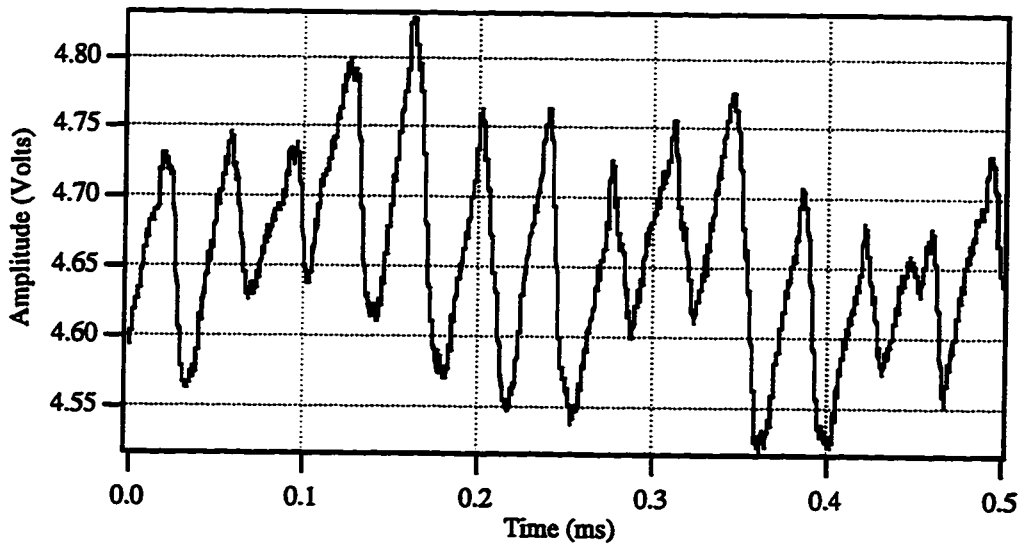

Figure 6.9. Time variation of the voltage on a wire probe in the SPT-100 plume.

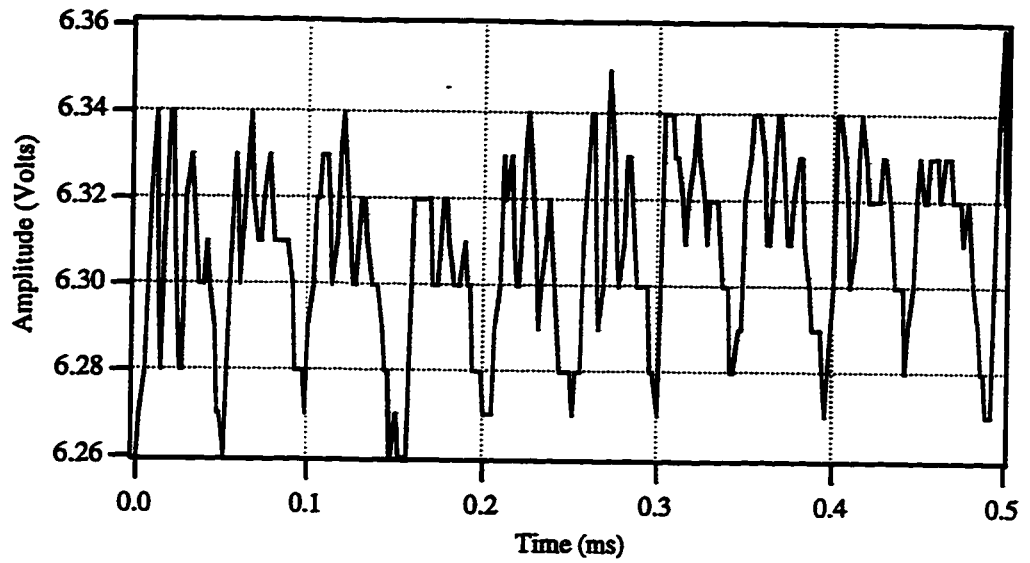

Figure 6.10. Time variation of the voltage on a wire probe in the MAI thruster plume.

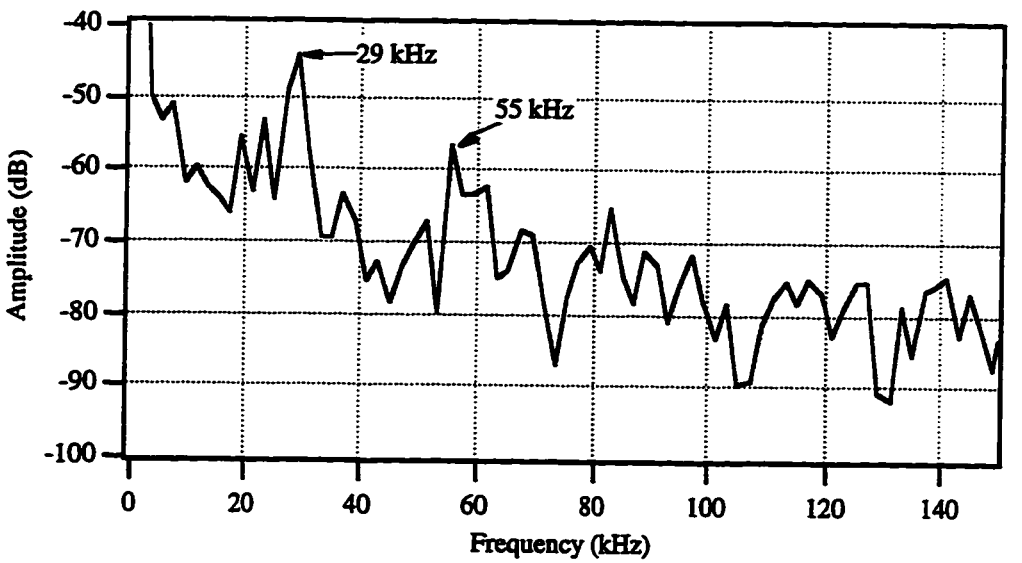

Figure 6.11. Frequency spectrum of the time domain voltage signal for the SPT-100 thruster.

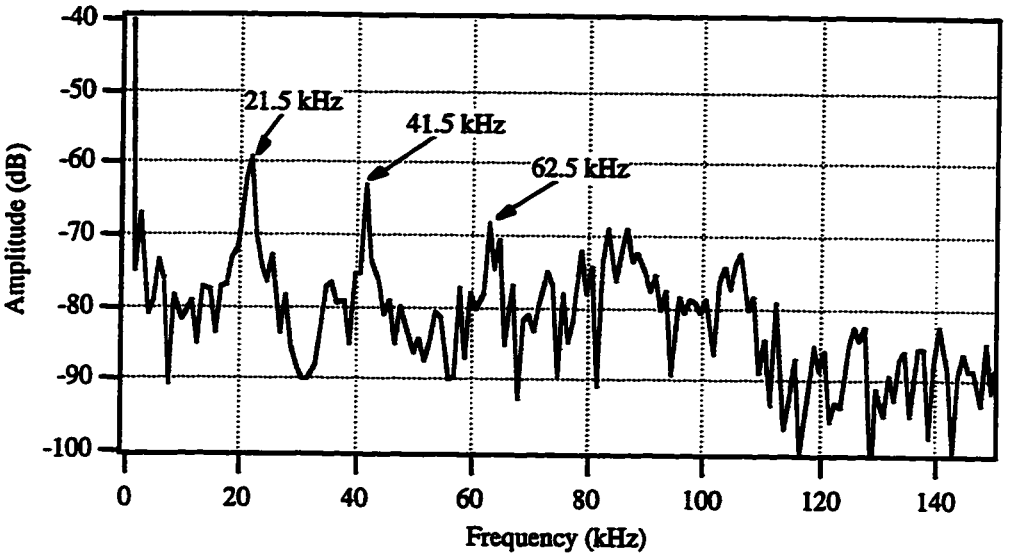

Figure 6.12. Frequency spectrum of the time domain voltage signal for the MAI thruster.

6.2.2 General Propagation Characteristics

A general idea of the propagation characteristics is necessary in order to understand the comparisons of various experimental information in the following sections. Measurements are presented that have been taken using the MAI thruster (krypton, 120 V, 3.3 A) in the configuration of Figure 5.7 and with the circuit of Figure 6.3. The lock-in-amplifier has been operated at ±5V and 25 kHz (not an optimal frequency). The stationary probe (Figure 5.7) is on the thruster centerline 1m from the exit plane. The movable probe is swept spatially over a range of axial and radial positions with respect to the stationary probe in order to characterize the amplitude and phase spatial variation. Both probes are 0.22 mm diameter.

An ion acoustic wave coupled into a mesosonic plasma would ideally only propagate downstream. Experiments verified that, indeed, propagation only occurred downstream; however, slight disturbances are detected for a short distance upstream which is thought to be near-zone presheath coupling. The measured characteristics upstream are essentially noise as indicated by low voltage amplitude and erratic voltage and phase.

Downstream of the excitation signal the wave generally propagates with decreasing amplitude in a cone radiating from the exciter which has previously been referred to as the propagation zone (Figure 6.13). The edge of the cone in the far-zone (>5 cm) is determined by the ion acoustic wave velocity and the plasma flow velocity . In general, the amplitude of the ion acoustic wave is primarily proportional to the electron number density since the electron-electron electrostatic coupling produces the ion acoustic wave. Another prominent feature is the interference pattern (or amplitude nulls) in the radial direction which also propagates outward from the exciter. Nulls also occur in the axial direction very close to the excitation source where, in addition to the nulls, two large peaks in amplitude occur (Figure 6.14). The peak in the propagation pattern generally occurs in the direction of the flow. In Figure 6.15, the peak is slightly off axis (~0.5°), but is within the alignment accuracy of the measurements.

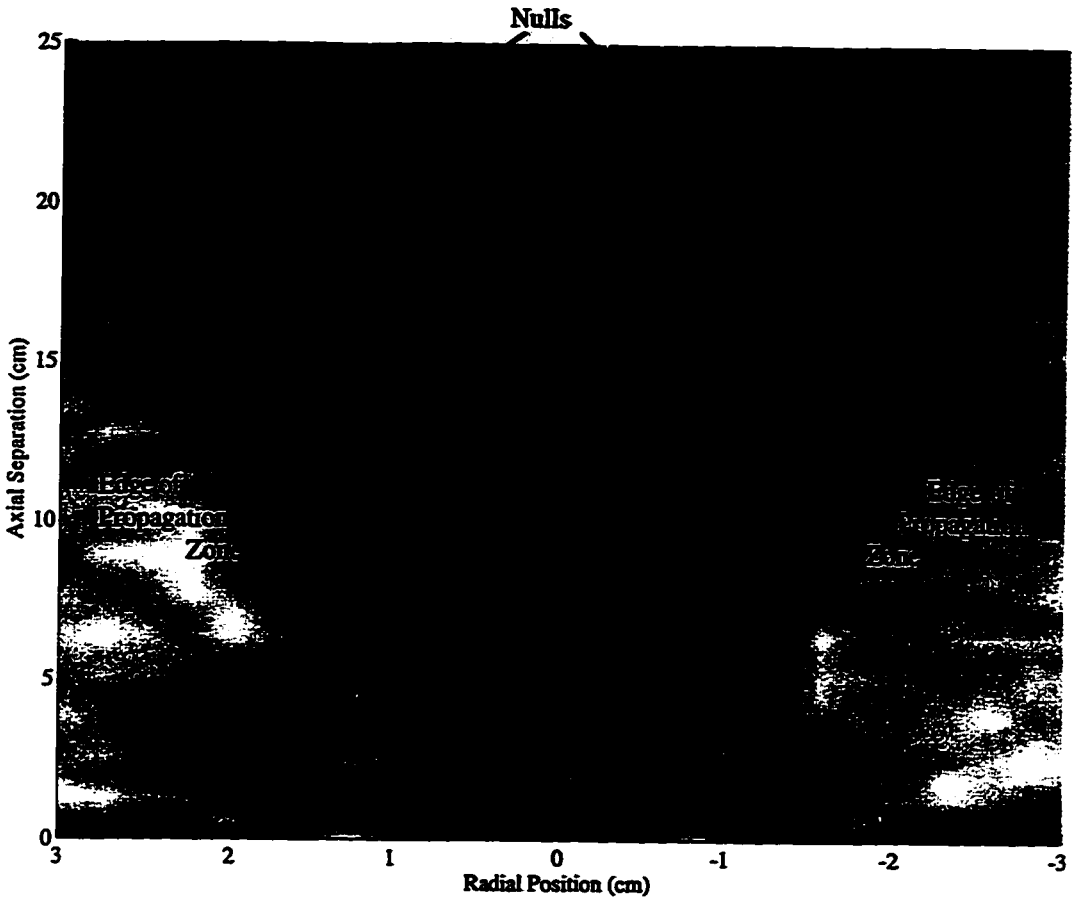

Figure 6.13. Amplitude variation of an ion acoustic wave (top view).

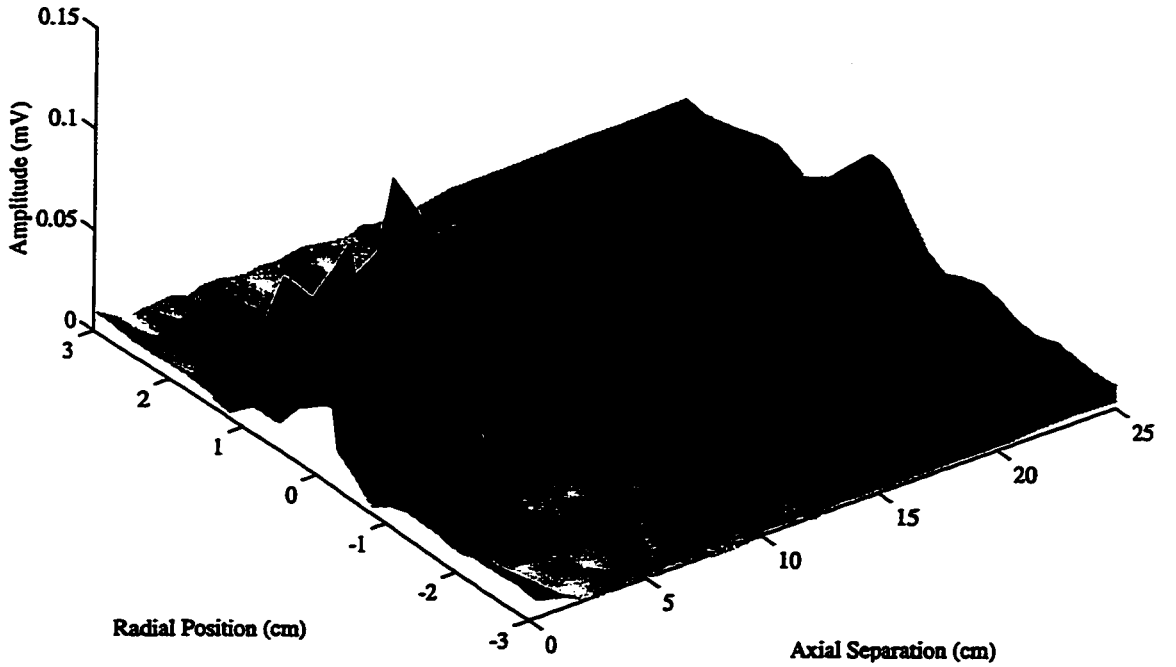

Figure 6.14. Amplitude variation of an ion acoustic wave (off angle view).

The spatial change in the phase tracks closely to the variation in amplitude (Figure 6.15 and 6.16). Radially from the center, the phase changes gradually except near the amplitude nulls where 180° changes in phase occur. The phase decrease along centerline in the far-zone (for increasing separation) corresponds to the expected phase shift of a propagating wave moving at a velocity which is the sum of the ion acoustic wave and the flow velocity. Near the edges of the propagation zone the phase is erratic, indicative of no propagation in that region. The interference pattern exhibited in the ion acoustic wave measurements is attributed to the wake of the excitation probe and is discussed in the following section after further results are presented.

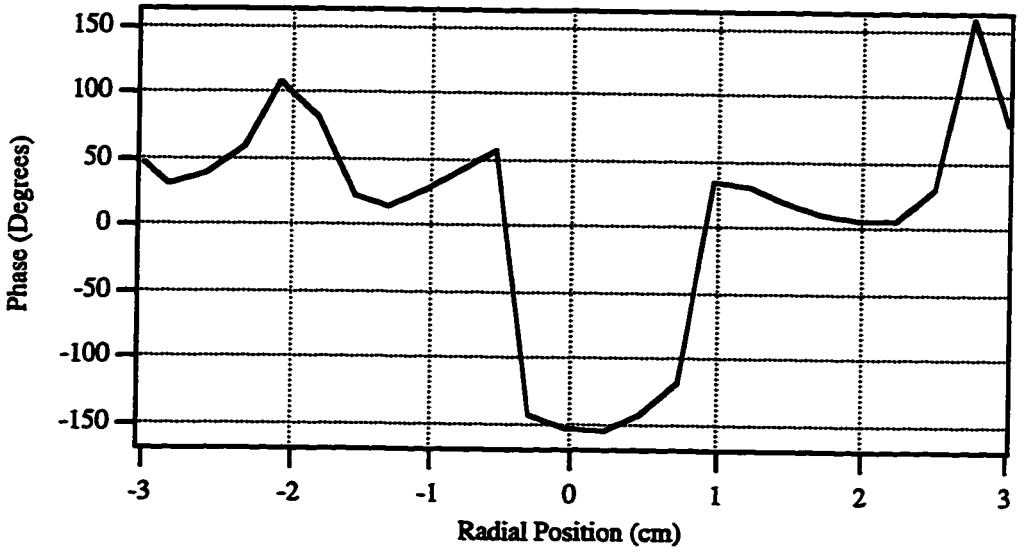

Figure 6.15. Radial phase variation of an ion acoustic wave in the MAI thruster plume (0.5 m downstream, 10 cm probe separation).

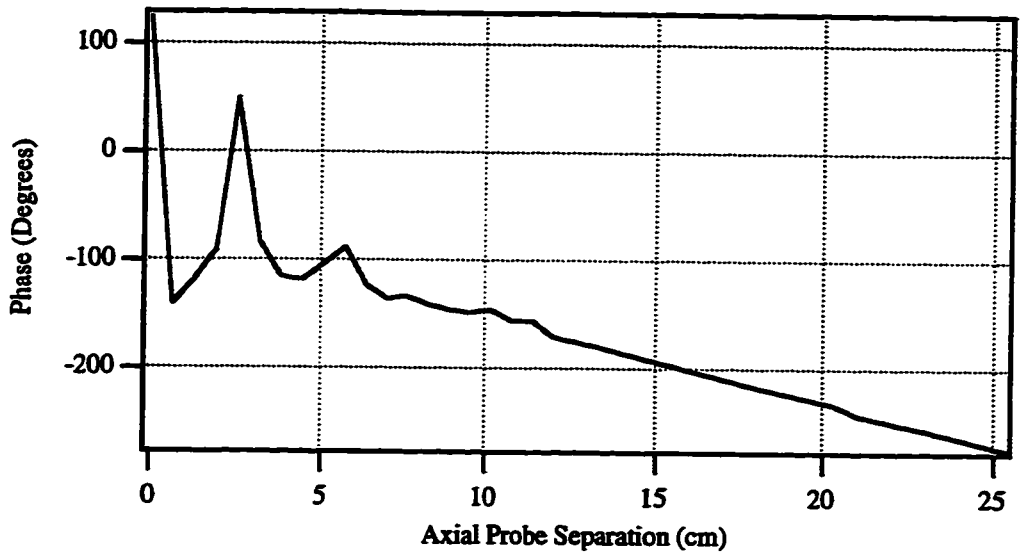

Figure 6.16. Axial phase variation of an ion acoustic wave in the MAI thruster plume.

6.2.3 Excitation Potential

In order to qualitatively determine acceptable excitation voltages, a range of signal magnitude and bias levels have been tested. The tests indicate coupling effectiveness and dependence on excitation through comparison for different excitations of amplitude and phase of the detected signal. The measurements have demonstrated strong dependence of the received voltage amplitude on excitation amplitude in the near-zone but much less dependence on excitation amplitude in the far-zone. The phase exhibited little change for various excitation levels in both regions. Lower voltage levels have been tested with similar trends as are exhibited by the higher voltage levels.

The amplitude variation testing is completed through use of the circuit in Figure 6.5 where the propagation pattern is reported for a number of excitation levels: ±5, ±10, ±20, and ±40 V with no bias (higher excitation levels were not tested due to the intrusive nature of amplitudes approaching the accelerating potential of the thruster). The tests have been completed using the MAI thruster on krypton and operating at 245 V and 4.2 A. As expected, the higher amplitude excitations generally produce higher detected signals (Figure

6.17 and 6.18). The exception to this is that the ±5 V excitation level generally produces a higher amplitude signal than the ±10 V level in the plot of variation with separation distance and both the ±10 V and ±20 V levels in the plot of variation in the radial direction. One explanation that could account for this result is the ±5 V excitation is not as noisy as the somewhat higher voltage signals since the ±5V signal comes directly from the lock-in amplifier whereas higher voltage signals are amplified by a high voltage bipolar amplifier with significantly worse noise characteristics than the lock-in amplifier output. The amplitude of the waves for all excitation levels tend to converge at larger distances from the exciter.

The phase measurement both axially and radially indicated only slight dependence on the applied excitation voltage (Figures 6.19 and 6.20). Differences primarily occur in the near-zone where wake effects and probe excitation levels have the greatest influence. The phase noise is slightly better for the higher excitation amplitudes.

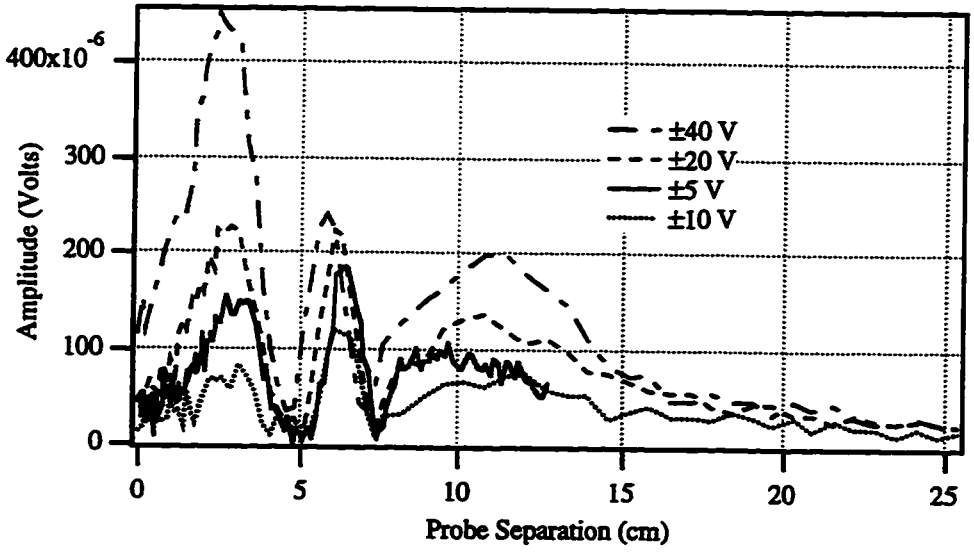

Figure 6.17. Axial variation in received signal amplitude for various excitation amplitudes.

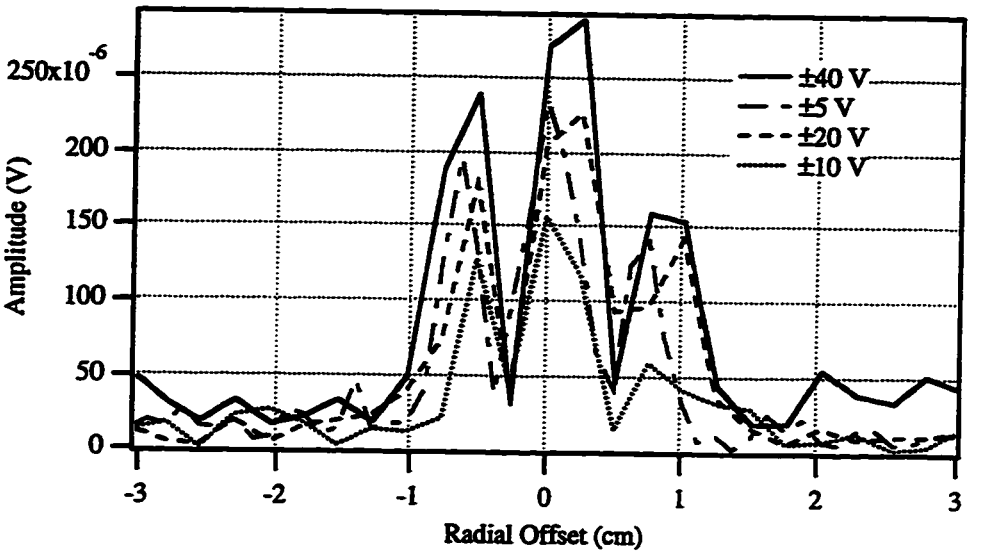

Figure 6.18. Radial variation in received signal amplitude for various excitation amplitudes for an axial probe separation of 6.35 cm.

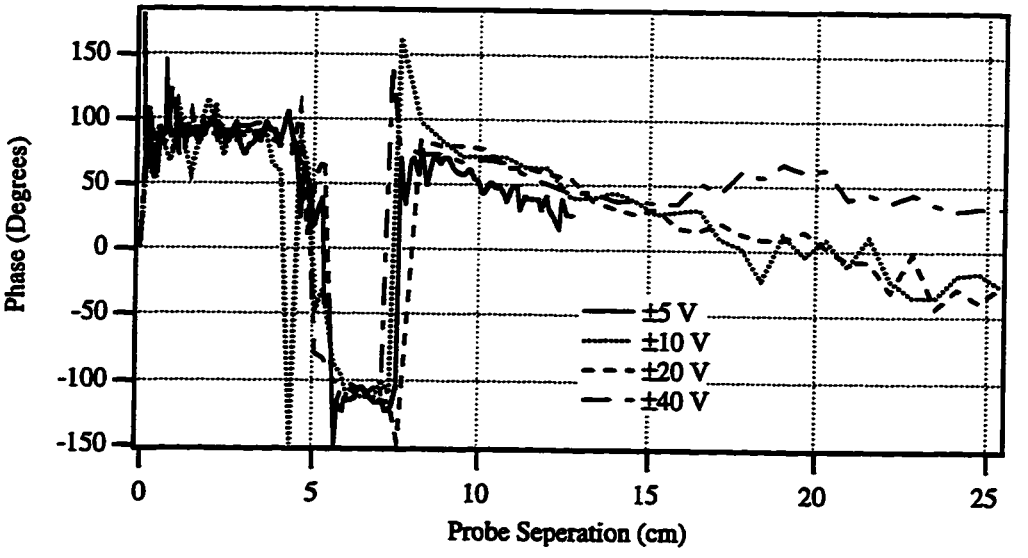

Figure 6.19. Axial variation in phase of received signal phase for various excitation amplitudes.

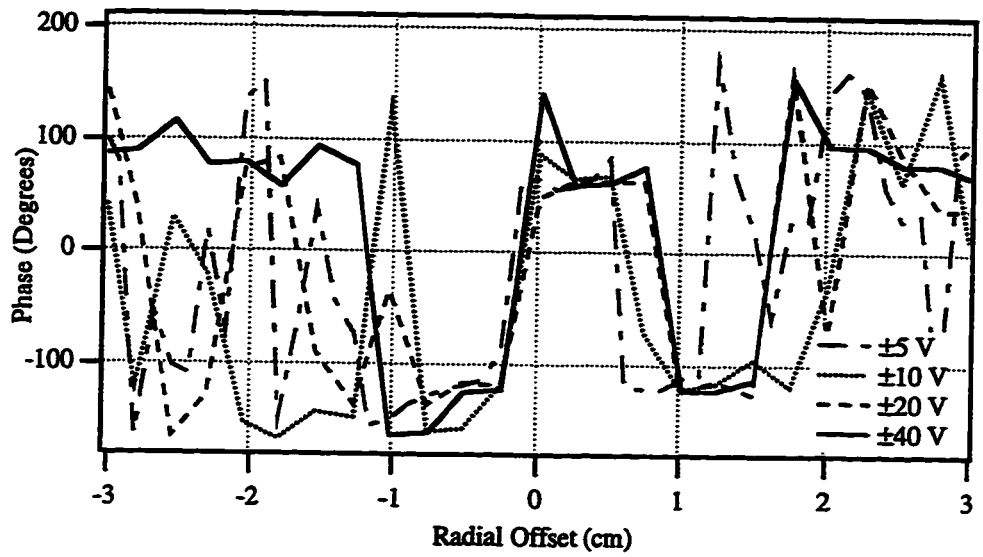

Figure 6.20. Radial variation in phase of received signal phase for various excitation amplitudes for an axial probe separation of 6.35 cm.

The bias voltage variation testing is completed through use of the circuit in Figure 6.4 where the variation with axial separation is reported for ±5 V amplitude and 3 bias levels: 0 V, -10 V, and -30 V. No positive bias levels were tested due to the desire to remain biased in the ion saturation region. (Biasing in the ion saturation region minimizes plasma perturbation and wake effect.) The tests have been completed using the Fakel thruster with xenon propellant and operating at 300 V and 4.5 A. The received signal is affected less by excitation bias voltage than for excitation amplitude. For the purposes of this study, the trends in all three cases are similar for both amplitude and phase (Figures 6.23 and 6.24) with the most significant variation in the near-zone region. The phase jump for the no bias case is an anomaly not seen in most other similar data sets. Differences in the phase characteristics of Figure 6.19 and 6.22 are attributed to different thruster operating conditions.

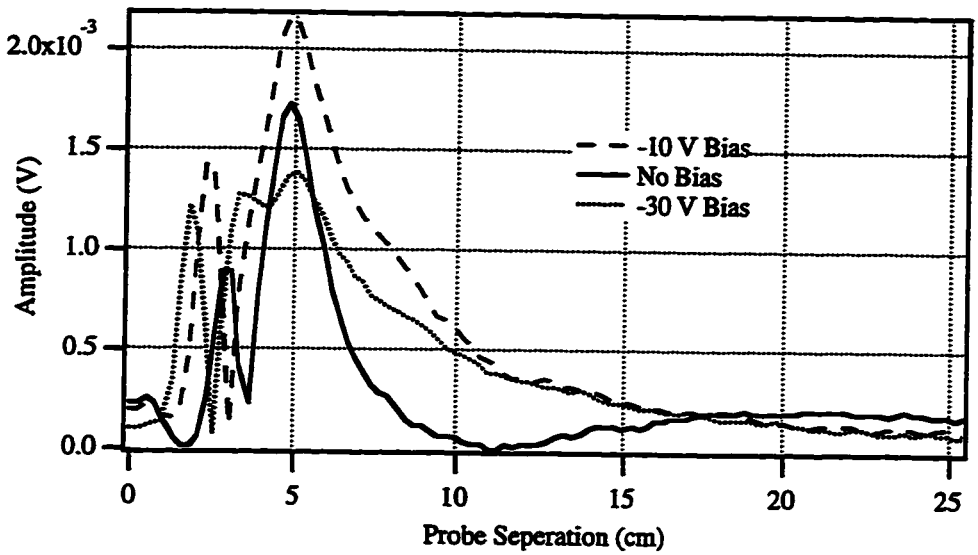

Figure 6.21. Axial variation in amplitude of received signal for three excitation voltage biases.

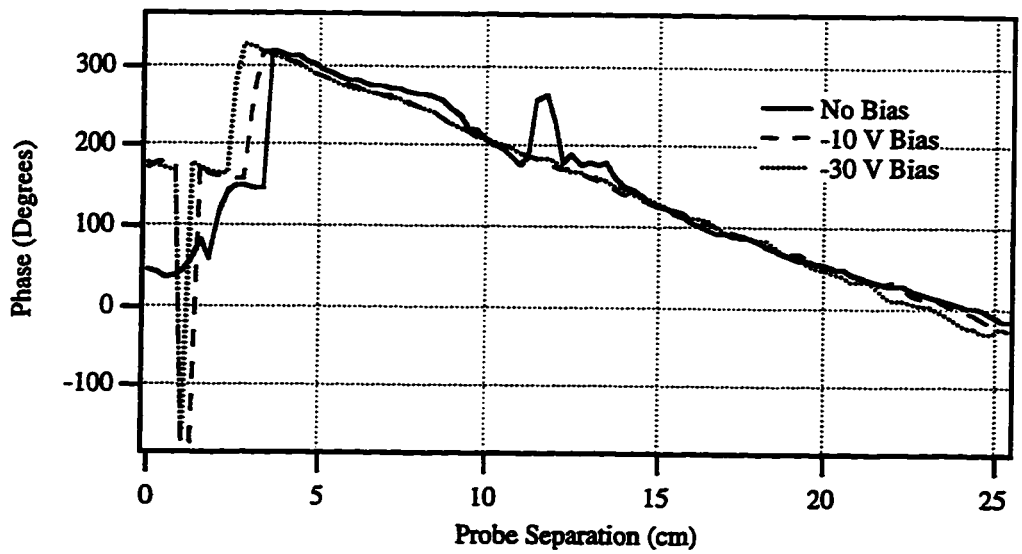

Figure 6.22. Axial variation in phase of received signal for ±5V excitation amplitude and three excitation voltage bias levels.

6.2.4 Probe Size

Various probe sizes have also been tested to qualitatively determine how probe size affects the excitation and detection of the ion acoustic wave. Two experiments are presented which compare the effect of different excitation and detection probes. In the first experiment, four different size detector probes are tested where the measurement results provide comparison of amplitude and phase for a range of separation distances along the flow axis in order to determine coupling effectiveness and possible phase differences between probes. In the second experiment which compares two excitation probe sizes, not only is the axial characterization presented, but measurements are also presented for radial amplitude variation in a number of axial planes in order to demonstrate the wake effects from a larger probe.

In the first experiment, four tungsten wire probes are tested; the size of each probe is listed in Table 6.2. The MAI thruster is operated with krypton at 120 V and 3.4 A. As expected, the larger probes are more effective at detecting the voltage variation of the ion acoustic wave (Figure 6.23); however, the relationship is not directly related to the area of the probe. For instance, an increase in area by a factor, M, produces less than a factor M increase in detected amplitude. The phase, on the other hand, does not exhibit significant difference between probes except for probe 4 which is much shorter than the other three (Figure 6.24). In general, given amplitude and phase considerations, a range of probe sizes is acceptable for the detector probe.

	Outer Diameter (cm)	Length (cm)
Probe 1	0.083	1.0
Probe 2	0.022	1.0
Probe 3	0.012	1.0
Probe 4	0.022	0.02

Table 6.2. Detector probe dimensions for first probe experiment.

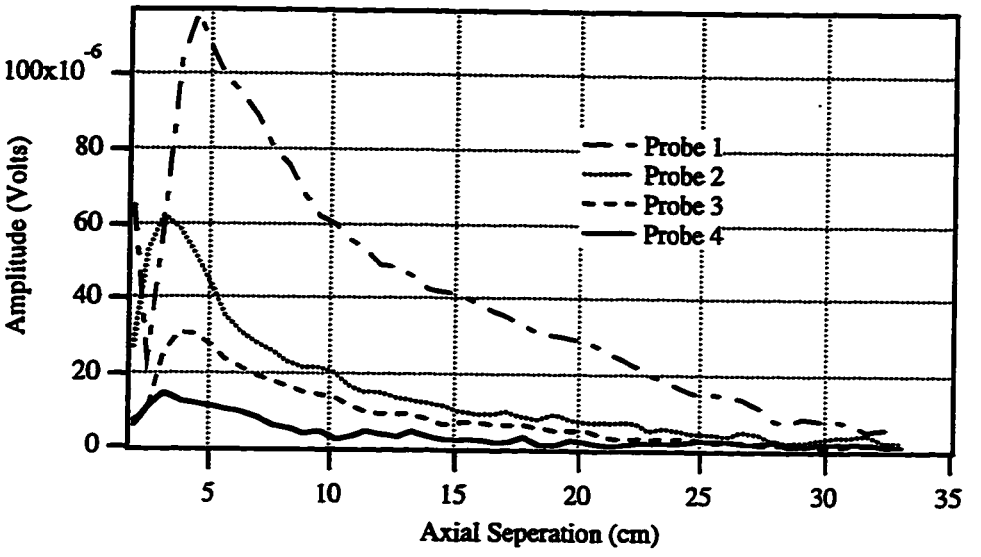

Figure 6.23. Amplitude variation for different size detector probes.

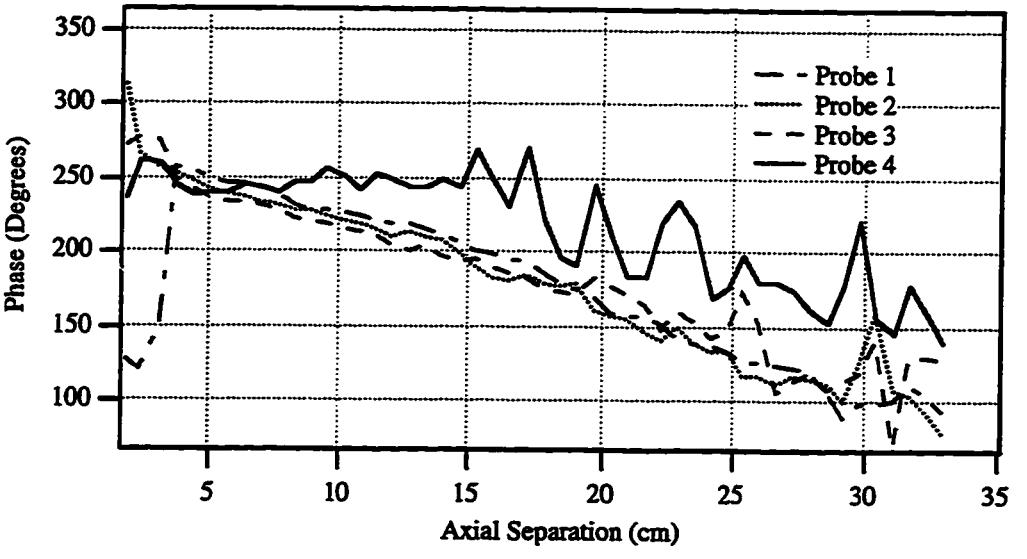

Figure 6.24. Phase variation for different size detector probes.

In the second experiment, two tungsten probes are compared as exciters where the sizes are listed in Table 6.3. In this test the Fakel thruster is operated with xenon at 300 V and 4.5 A. For both probes the amplitude and phase follow the same trends as the previous experiment. However, the probe area ratio is much larger in this experiment; therefore, as expected, the amplitude and phase difference is larger (Figures 6.25 and

6.26). The amplitude differs by a factor of 4 to 5; however, the amplitude ratio is still not as large as the area ratio. The phase in this experiment, for both the small and large probes, exhibit the same differential spatial change; however, the difference in probe size produces a phase shift in the detected signal. The phase jump for the small probe axial sweep is an anomaly not seen in most other similar data sets.

	Outer Diameter (cm)	Length (cm)
Probe 5	0.26	2.1
Probe 6	0.046	0.83

Table 6.3. Detector probe dimensions for first probe experiment.

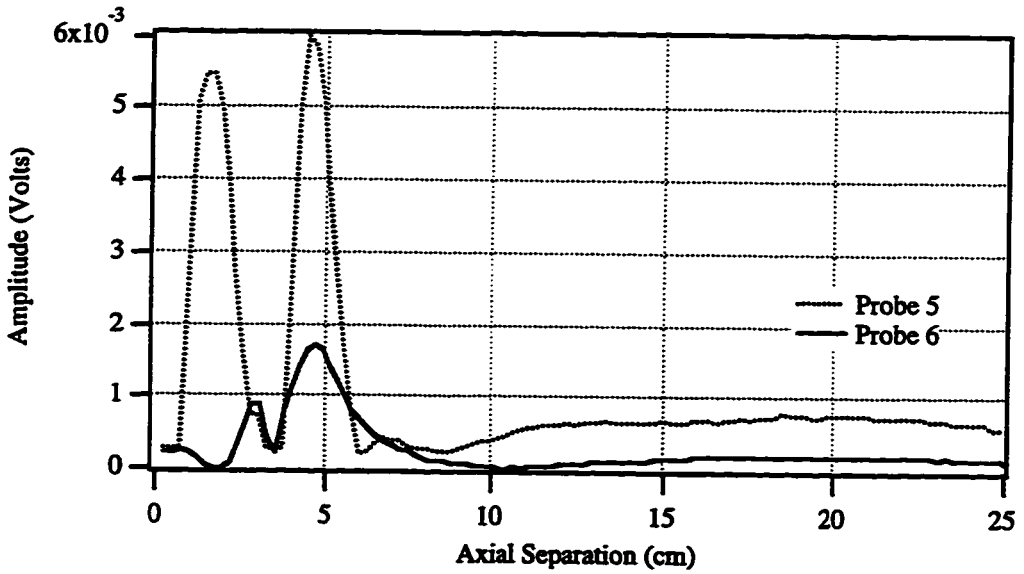

Figure 6.25. Amplitude variation for different size exciter probes.

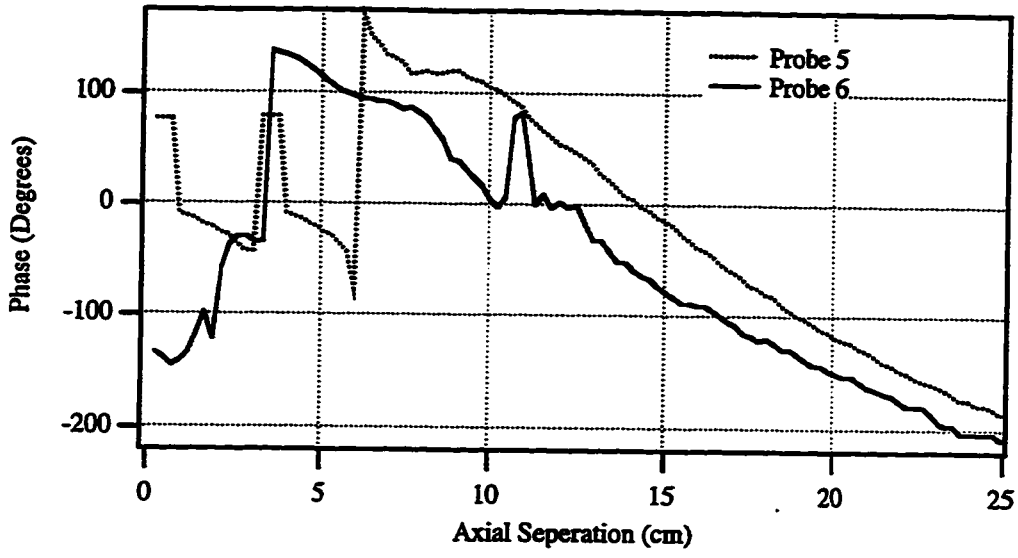

Figure 6.26. Phase variation for different size exciter probes.

Additional measurements of the amplitude variation in the radial direction highlight the wake effect that is measurable with the larger probe. Radial sweeps have been recorded at ten axial positions for the large probe and four axial positions for the small probe (Figures 6.27 and 6.28). More detailed spatial mapping has been completed for a small probe under different thruster conditions. These measurements have been recorded for the Fakel thruster operating with xenon at 300 V and 4.5 A.

The near-zone character demonstrated in the measurements with the large probe (Figure 6.27) resolve the null in the signal directly behind the probe where no particles are present (direct wake region). This null transforms (changes) into the main lobe observed in the downstream measurements, also indicated in Figure 6.27, which is typical of wakes behind cylindrical probes [Fournier, *et al.* 1975; Stone, *et al.* 1973, *et al.* 1972; Stone, 1981; Morgan, *et al.* 1989; Chan, *et al.* 1986]. In the mid- to far- zone region the amplitude signal does not decay as would be expected for a wake response, rather it propagates with the characteristics of an ion acoustic wave that is superimposed on a flowing plasma as seen for both the large and small probes (Figures 6.27 and 6.28). The

far-zone wave pattern is that of an ion acoustic wave in a flowing plasma with the amplitude modified by the near-zone wake amplitude pattern.

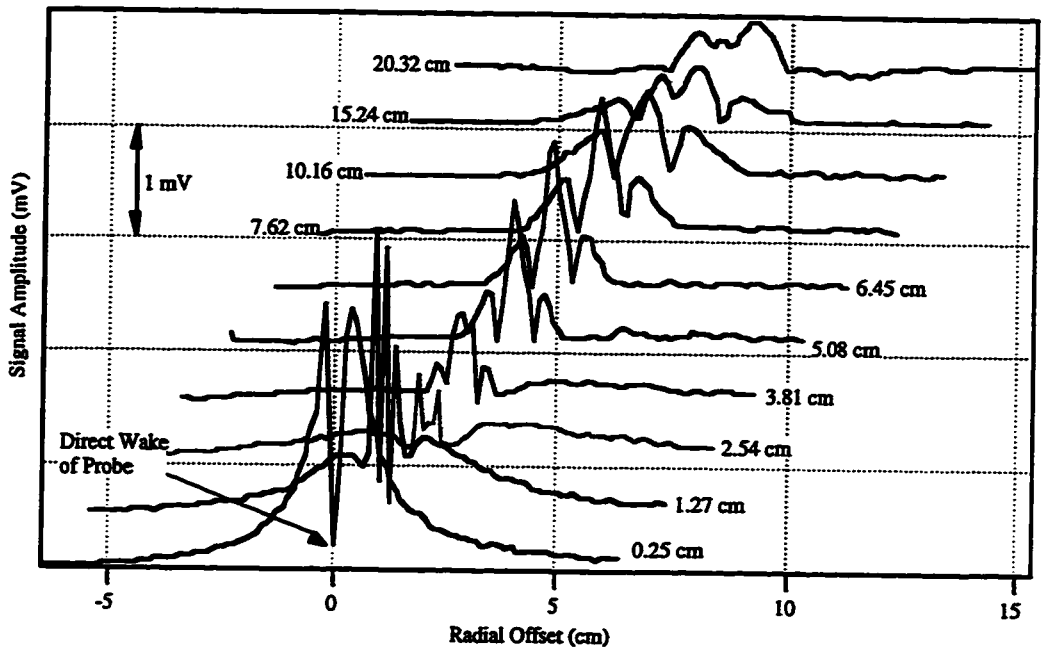

Figure 6.27. Radial profiles in axial planes for probe 5(large) in experiment 2.

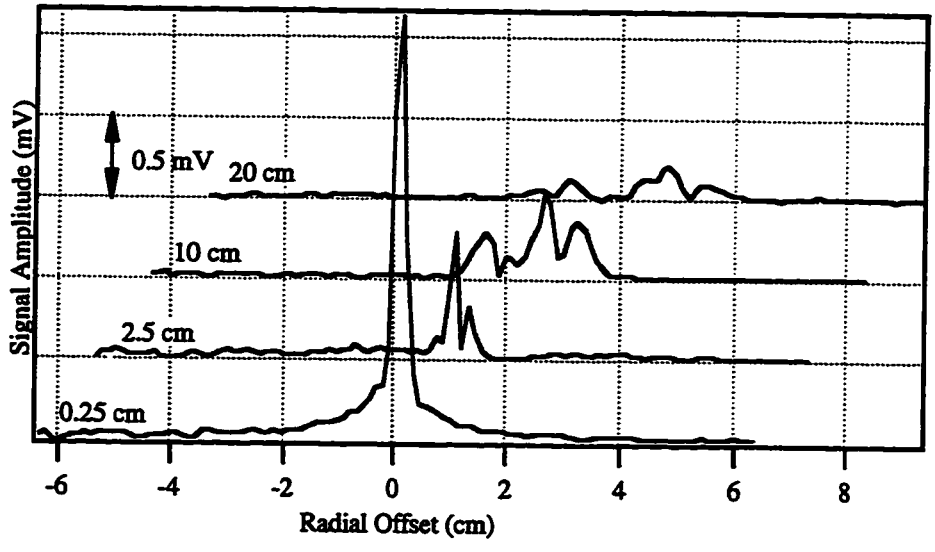

Figure 6.28. Radial profiles in axial planes for probe 6(small) in experiment 2.

6.2.5 Excitation Frequency

A number of different probe excitation frequencies were tested in order to determine the effect of excitation frequency on the results and also to characterize the dispersion relation for an ion acoustic wave. In this test, the MAI thruster was operated with xenon at 278 V and 4.9 A and tungsten wire probes are used with 0.22 mm outer diameter and 1 cm long. The probes were approximately on the centerline of the thruster, hence they were aligned along the flow axis. Measurements are presented for five frequencies from 3.2 kHz to 100 kHz.

All frequencies follow similar trends in amplitude with a strong peak and null followed by a region where the amplitude slowly decreases out to the farthest measurement point (Figure 6.29). The detected amplitude varies linearly with frequency where the highest frequency produces the lowest amplitude; however, even the highest test frequency excites a wave well within the resolving capability of the lock-in amplifier. The higher frequencies are desirable due to the noise characteristics of the stationary plasma thrusters as described in Section 6.2.1.

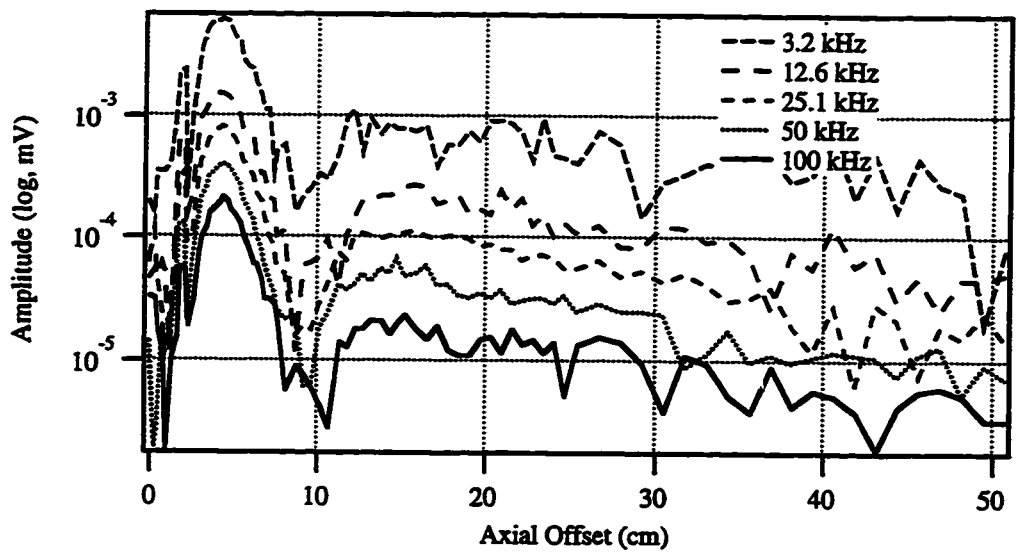

Figure 6.29. Amplitude variation with increasing axial separation for different excitation frequencies.

The phase also exhibits similar characteristics across the frequency range with more noisy phase measurements in the near-zone where the probe still has an effect and in the farthest measurement points where the amplitude is lowest (Figure 6.30). Phase jumps occur at the same separation distance as the nulls in the amplitude for all of the frequencies. Aside from the phase jump at 8 cm, the phase progresses at a constant rate for each of the tests for distances greater than 2.5 cm (near-zone). The phase shift is higher over the same distance for higher frequencies as would be expected. At the lowest frequencies, characterizing the phase change per distance is difficult due to the small phase shift even over the large measurement range.

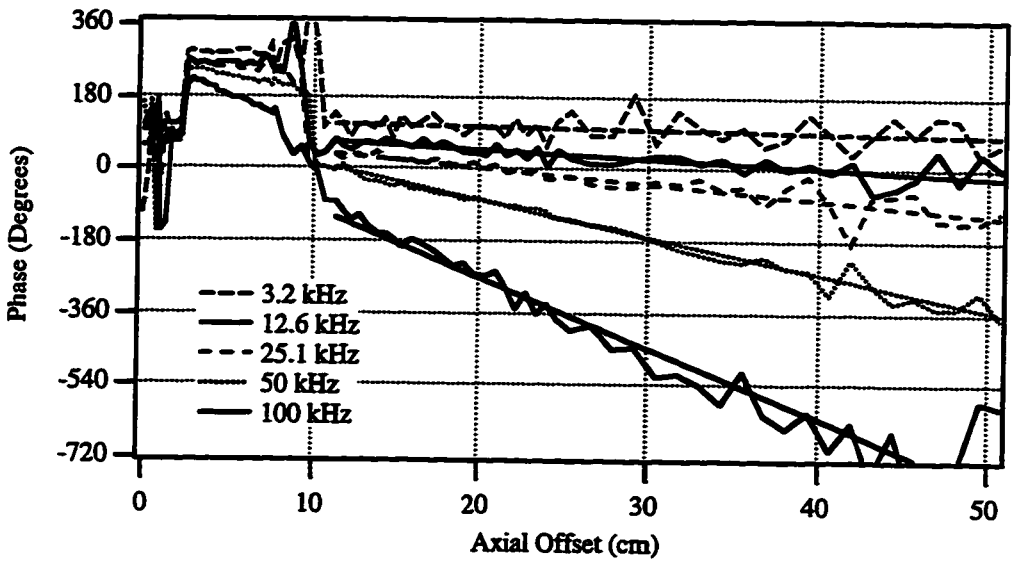

Figure 6.30. Experimental phase variation and the linear fit plotted with increasing axial separation for different excitation frequencies.

6.2.6 Thruster Propellants

The amplitude variation both radially and axially has been found in the MAI thruster plume using three difference propellants. Similar operating conditions have been used for

each of the three gases: argon, 310 V, 3.8 A; krypton, 298 V, 4.5 A; and xenon, 278 V, 4.9 A. This test also used tungsten wire probes 0.22 mm thick and 1 cm long.

The phase variation with probe separation (Figure 6.31) is measured at 50 kHz and up to 50 cm probe separation. For measurements past the near-zone (~5 cm), the phase velocity (slope of the line) is constant except for the phase jump at 7 to 10 cm. The measurements indicate a progressively noisier signal for lighter gases. This would be expected since the stationary plasma thruster operates more effectively with the heavier particles (such as xenon). The comparison demonstrates the expected trend of a slower velocity for the heavier propellants as would be expected with comparable discharge potentials.

The amplitude contours for the three gases (Figures 6.32 to 6.34) are developed from eight to ten radial spatial sweeps at axial distances on centerline ranging from 0.25 cm to 40 cm (depending on which trial). The radial sampling ranged from 0.25 cm at the center to 1.25 cm at the edges of the sweep. Reference lines highlight the important features of the contours including peak, nulls, and signal edges.

Each of the reference lines is extracted directly from the raw data. The peak is the maximum amplitude for each radial sweep. The nulls are the first minimum to either side of the peak. The signal edge is the approximate point where the amplitude decreases to the noise level in each plot.

A number of factors contribute to uncertainty or variation in the measurements. Due to the limited spatial sampling in the measurements, identification of the three quantities (peaks, nulls, signal edges) is generally accurate to only ± 0.5 cm within each data set. Additional uncertainty exists in the absolute position relative to other data sets. The positional uncertainty accounts for the deviation in individual points and also the shift in all three quantities for a number of data sets. Lastly, in the farthest measurement points, plasma non-homogeneity could cause slight aberration in the measurements.

The general trends are consistent in all three data sets. First, the peak propagation is slightly off center indicating a slight angle with respect to the flow. The null point tends to expand away from the peak, but not as quickly as the signal edge. Finally, the signal edge angles out sharply in the near-zone, but quickly assumes a smaller expansion rate in the far-zone. Comparison of all three data sets leads to the observation that in the far-zone the propagation expands at approximately equal angles which is independent of the propellant.

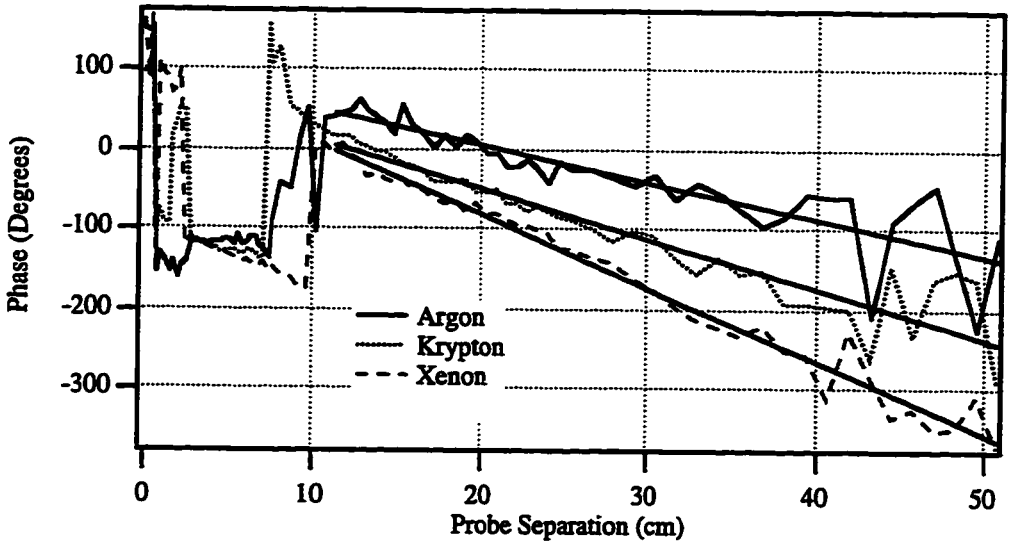

Figure 6.31. Ion acoustic wave phase progression at 50 kHz (argon, krypton, and xenon).

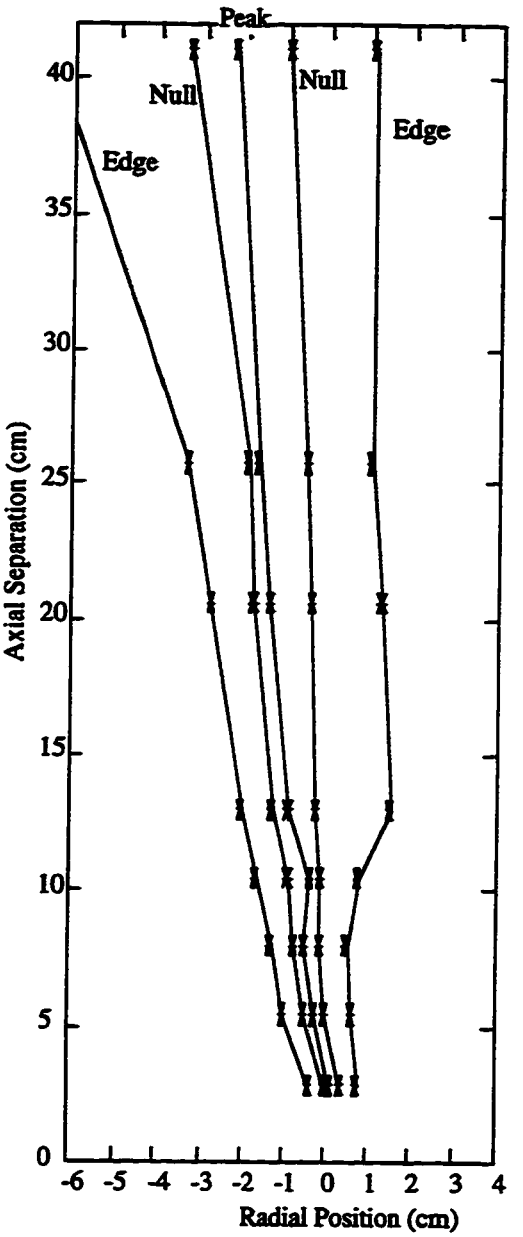

Figure 6.32. Contour of ion acoustic wave amplitude (argon).

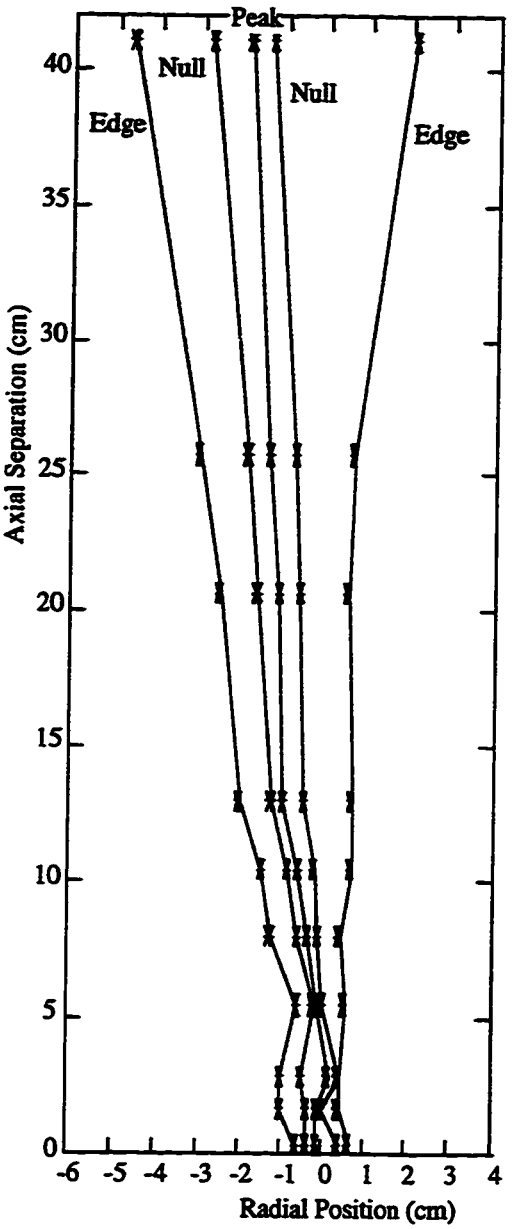

Figure 6.33. Contour of ion acoustic wave amplitude (krypton).

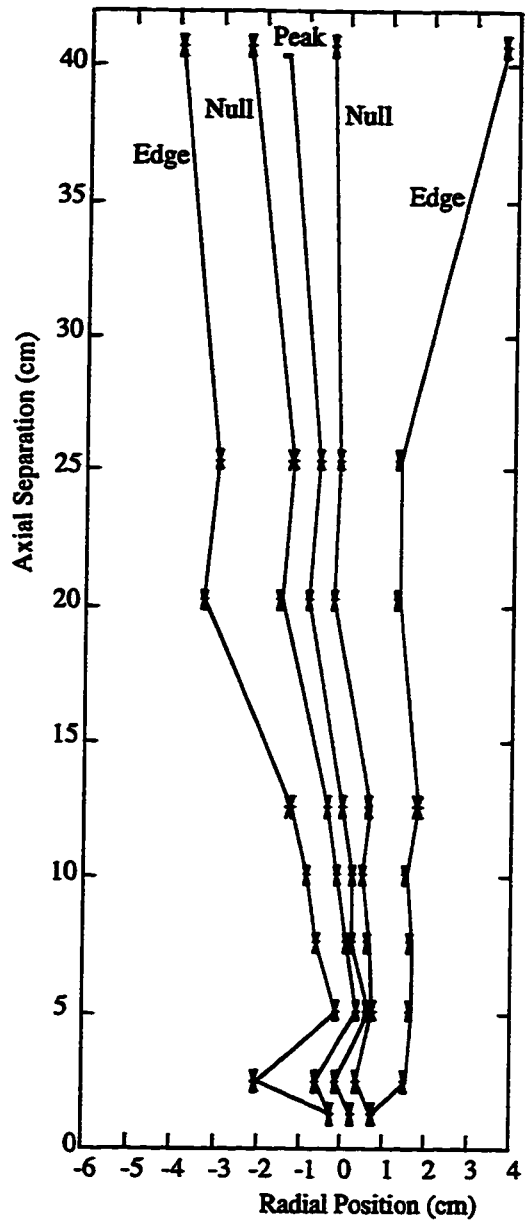

Figure 6.34. Contour of ion acoustic wave amplitude (xenon).

6.3 Analysis and Summary

The results just presented characterize ion acoustic wave propagation in a stationary plasma thruster plume and provide information helpful in developing a simple method to utilize the propagation characteristics to ascertain flow velocity, electron temperature, and estimate ion temperature. First, the wake-wave pattern is discussed in more detail in order to determine what information can be derived from the propagation pattern (Section 6.3.1). Then, the spatial mapping of amplitude and phase is utilized in order to estimate plasma flow velocity, ion acoustic wave velocity, and the sum of the plasma thermal temperatures (6.3.2). Finally, the results are utilized to affirm the presence of an ion acoustic wave in this plasma (as opposed to assuming this fact *a priori*), establish acceptable excitation levels and probe size, and establish the region over which ion acoustic wave propagation is consistent.

6.3.1 Discussion of Wake-Wave Pattern

The wake-wave interference pattern exhibited in the propagation characteristics close to the excitation probe (<5 cm) are very similar to the results reported in studies of the wakes behind small cylindrical probes in a flowing plasma. Previous work has studied wake structure through both theoretical modeling [Senbetu, *et al.* 1989; Taylor, 1967; Coggiola, *et al.* 1991; Konemann, *et al.* 1978; Biasca, *et al.* 1994] and experimental investigation [Fournier, *et al.* 1975; Stone, *et al.* 1973, *et al.* 1972; Stone, 1981; Morgan, *et al.* 1989; Chan, *et al.* 1986]. Additional work related to the observed wave pattern has studied near-field interference patterns of antennas exciting ion acoustic waves [Christensen, *et al.* 1977; Nakamura, *et al.* 1979]. The studies have been reported in plasmas with similar temperature ratios ($T_e / T_i \approx 10$) and velocity ratios ($V_{flow} / V_{iaw} \approx 10$) when compared to the expected plasma parameters in this study. The previous wake studies demonstrated that the density perturbation is measurable behind even a small probe

in a region up to 100 times the probe diameter [Stone, 1981; Fournier, *et al.* 1975]. The mechanism of disturbance for the wake studies are primarily a fluid effect and not a result of a varying electrostatic signal on the probe. Also, in the wake studies, the ratio of the ion acoustic velocity to the plasma flow velocity determined the shape of the wake cone; however, for cylindrical probes the edge of the cone is not necessarily directly related to the velocity ratio where the wake angle is larger than predicted by the ratio of the velocities [Stone, 1981].

The ion acoustic wave pattern is similar to the wake studies in a number of ways in the near-zone. These similarities are most evident in the results for characterization of the largest probe. In particular, the null directly behind the probe is measured just as in wake studies where the axial position of the null is related to the probe size, flow velocity, and ion acoustic wave velocity. The trends are also similar in formation of the initial main lobe which evolve into side lobes as the wave moves downstream. In addition to the studies with the large probe, the experiments in Section 6.2.6, which spatially characterizes the propagation pattern, indicate that close to the probe the expansion angle is significantly larger than in the far-zone where in this study, the expansion angle is thought to be dominated by the ion acoustic wave propagation expansion angle.

As just stated, the interference pattern close to the excitation probe is similar to the pattern of the wake behind a cylindrical probe; however, the differences are significant farther than 50 probe diameters from the probe. In the near-zone for both the wake experiments and this study, a null in the center directly behind the probe is found to progress into the main lobe with two side peaks just as the wake structure would predict. However, in the wake studies for distance greater than 50 probe diameters the lobe structure decays significantly, while in this study, the propagation pattern persists to the limit of the measurements as in Figure 6.13 and 6.14 (up to 1000 diameters). This result indicates that the near-zone of the probe wake significantly affects the wave amplitude; however, in the far-zone the expansion of the propagation is determined by the ion acoustic

wave propagation. The nulls in the propagation pattern are therefore a consequence of the near-zone interference pattern produced by the wake of the probe. Additionally, the edge of the propagation zone in the far-zone is determined solely by the ion acoustic wave, since the wake region as seen in the near-zone is actually expected to expand at a greater angle than the ion acoustic wave.

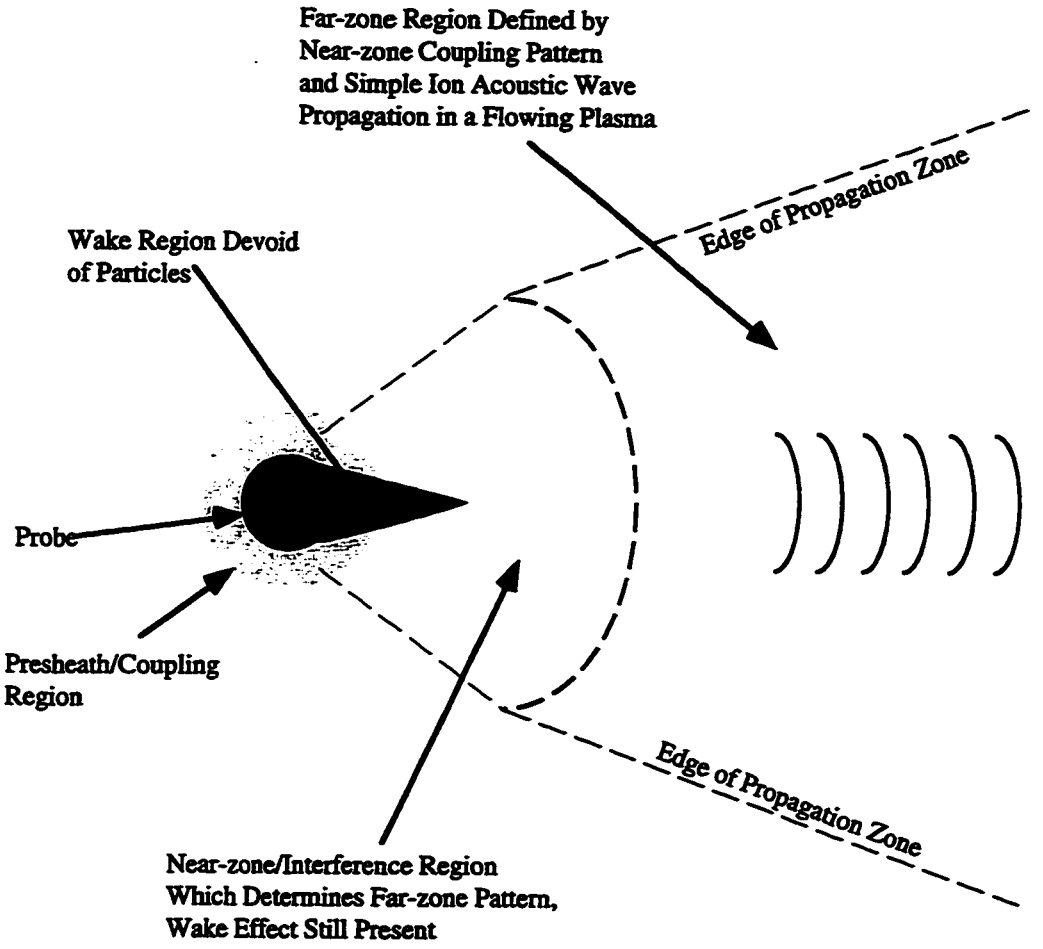

Figure 6.35. Schematic of excitation and propagation regions.

To summarize the results of the ion acoustic wave characterization, the excitation and propagation of a wave can be divided into four regions as shown in Figure 6.35: the presheath region, wake region, near-zone region, and far-zone region. A sinusoidally varying probe potential produces an oscillating sheath and presheath. The presheath region

launches the ion acoustic wave into the plasma. The region directly downstream of the probe is shielded; hence, no particles exist in this region. After the wave is launched by the presheath, the wake of the probe produces an interference pattern dependent on the probe size, plasma density, thermal temperatures, and flow velocity. The wake-interference pattern is a density disturbance that attenuates quickly in comparison to the ion acoustic wave propagation; however, the coupling effect of the wake-interference pattern partially determine the ion acoustic wave propagation pattern in the far-zone (since the ion acoustic wave amplitude is proportional to particle density). In the far-zone the wave propagates as a normal ion acoustic wave in a flowing plasma where the amplitude distribution is determined by the near-zone interference pattern.

6.3.2 Calculation of Plasma Parameters Using Spatial Characterization of Propagation

Phase data can be used as described in Chapter 5 to find the wavelength and total velocity of the ion acoustic wave that is superimposed on the flowing plasma. Using the data from Figure 6.30 these quantities are found from a linear fit to the phase over the region from 11 to 50 cm separation (see Table 6.4). The slope of the linear fit is related to the wavelength through Equation 6-1 since the slope is just the unit change in phase over distance.

$$\lambda = \frac{360^\circ}{\Delta\phi} d = \frac{360^\circ}{slope} \qquad \bullet 6\text{-}1$$

The plasma drift velocity of the plasma is assumed to be constant with respect to excitation frequency; therefore, any difference in total wave velocity as a function of the frequency would be due to velocity difference in the excited wave. However, the measurements summarized in Figure 6.32 show a constant velocity at all frequencies within the expected

accuracy of the measurement; therefore, the results are consistent with the constant phase velocity expected from an ion acoustic wave (Equation 5-5). Overall, the individual measurements are within ±15% of the average velocity value for xenon propellant. Additional measurements using argon and krypton propellants are also consistent with these findings where each gas has an average velocity constant as a function of excitation frequency. In addition to measurement noise, one possible source of error in these measurements is misalignment with the flow axis which would produce a smaller slope in the phase data, thus inflating the velocity calculation by up to 15%.

Frequency (kHz)	Intercept (degrees)	Slope (degrees/cm)	Wavelength (cm)	Total Velocity (km/s)
3.2	119	0.65	554	17.7
12.6	90	2.1	171	21.6
25.1	83	4.0	90	22.6
50	102	9.2	39	19.7
100	117	19.7	18	18.3

Table 6.4. Curve fit coefficients, wavelength, and velocity found from the phase change over space for different excitation frequencies.

As discussed in Section 5.4.3, in order to find the flow velocity and the ion acoustic wave phase velocity, two measurements are necessary: phase variation along flow axis, and amplitude variation in the radial direction. As just demonstrated, the spatial phase variation provides information concerning the sum of the two velocities. Furthermore, the radial amplitude variation provides the information necessary to determine the edge of the propagation zone.

The propagation zone edge is found from the data in Figures 6.32 through 6.34. The edge in these Figures is approximated for each radial sweep by defining the peak noise level and then determining when the amplitude falls to the noise level. The accuracy of the interpretation is limited due to the lack of spatial sampling in these measurements. An

expansion angle is determined for each radial sweep by taking half the angle formed by two far-zone edge points and the exciter position. This angle is not precisely the expansion angle since the near-zone expansion creates a small offset; however, the difference in the two angles is within the accuracy of the propagation zone edge determination (±1.5°). The average angle in the far-zone is given in Table 6.5 for each of the three propellants tested. All of the individual angles are within ±1.5° of the averages. The expansion angle is related to the ratio of the velocities:

$$\tan\theta = \frac{V_{iaw}}{V_{flow}}. \qquad \bullet 6\text{-}2$$

The slope of the phase versus distance is calculated using the data from Figure 6.33 for the three gases, and it is also listed in Table 6.5. These measurements provide the information to find the plasma flow velocity and ion acoustic wave velocity. Additionally, the ion acoustic phase velocity and dispersion relation yield the sum of the electron and ion temperatures.

	Argon	Krypton	Xenon
Slope (degrees/cm)	4.6	6.2	9.2
θ (degrees)	6.0	4.9	6.0
V_{tot} (km/s)	38.8	29.0	19.6
V_{flow} (km/s)	35	27	18
V_{iaw} (km/s)	3.7	2.3	1.9
T_e+3T_i (eV)	5.7	4.6	4.9

Table 6.5. Parameters found from spatial characterization of wave propagation.

The trends in the results are not surprising. The flow velocity and ion acoustic wave velocity decrease with increases in propellant mass. The plasma flow velocity for all three gases is slightly higher than expected but within the accuracy of this analysis. The

plasma flow velocity for xenon is similar to other published measurements for stationary plasma thrusters running on xenon which report velocities between 13 and 18 km/s [Manzella, 1994]. Also, the sum of electron temperature and ion temperatures in Table 6.5 is also similar to previous results which report electron temperatures between 1 to 6 eV and ion temperature of 0.1 eV [Manzella, *et al.* 1995; Myers, *et al.* 1993, Patterson, *et al.* 1985; Szabo, *et al.* 1995]. Additionally the wave expansion angle is approximately the same for all three propellants. This would be expected since in the far-zone the propagation expands at an angle proportional to the ratio of the ion acoustic velocity to the directed flow velocity. Both velocities are proportional to the inverse square root of the mass; therefore, the expansion angle should be independent of propellant mass given similar electron temperature and accelerating voltage.

6.3.3 Summary of Wave Propagation Studies

The experiments and calculations in this chapter describe ion acoustic wave propagation in flowing plasma, in particular, in the plume of a stationary plasma thruster. In order to develop an effective diagnostic technique, the results are summarized as applied to three questions: (1) does a coherent ion acoustic propagate in the plume, (2) what probe geometry and signal will effectively excite and detect ion acoustic waves, and (3) for what exciter-detector separation distances are the propagation parameter meaningful and resolvable (far-zone region)? The answers provide a basis for the experimental configuration of Chapter 7.

The coherent propagation of an ion acoustic wave was established through multiple corroborating experiments. Initially, experiments confirmed the type of excited wave as an electrostatic wave moving slower than the flow velocity since no signal is detected upstream of the exciter (Section 6.2.2). Additionally, the velocity was found to be constant across the frequency spectrum (Section 6.2.5) which is in agreement with the dispersion relation of an ion acoustic wave (Section 5.3). Moreover, the propagation pattern in the

far-zone cannot be solely explained from the wake of the probe but was explained by ion acoustic wave propagation (6.3.1). Lastly, the flow velocity and electron temperature found from the phase shift and propagation zone measurements (Section 6.3.2) was consistent with previous results for the stationary plasma thruster. Therefore, the experiments have established the propagation of an ion acoustic wave.

The effect on the excitation and detection of the ion acoustic wave has been explored for a number of excitation amplitude and bias voltages. Differences in propagation characteristics between excitation levels were greatest in the near-zone of the probes; however, in the far-zone differences between excitation levels were small (Section 6.2.3). The excitation voltage was chosen to maintain simplicity and minimize noise from other components; therefore, the majority of testing used the lock-in amplifier directly as the excitation source where the maximum peak-to-peak voltage is ±5V.

The experiments with various size exciter and detector probes indicated that a wide range of probe sizes work effectively in terms of acceptable amplitude and phase measurements (Section 6.2.4). A larger probe was attractive due to its increased signal amplitude; however, a smaller probe produces a smaller wake region which was important in order to utilize the propagation information. For typical stationary plasma thruster plume density, probes greater than 0.2 mm and less than 1 mm will excite and detect ion acoustic waves with sufficient amplitude to obtain good resolution with the lock-in amplifier and still limit the wake region to less than 5 cm. In general, no phase bias was exhibited by probes of similar size.

The excitation frequencies were tested up to 100 kHz (maximum frequency of the available lock-in amplifier). The lower frequency signals produce a larger amplitude signal, but the higher frequencies produce a larger phase shift (Section 6.2.5). Additionally, for the SPT plume, the noise power spectral density peaks between 20 to 30 kHz and decreases for increasing frequency (Section 6.2.1). Since the ion acoustic wave oscillations are physically similar to the natural oscillations, the excitation frequencies

should be chosen with low noise and interference. In the range available , the frequencies above 50 kHz provide sufficient phase shift and amplitude to produce good measurement resolution. In these experiments the maximum frequency was determined by the capabilities of the lock-in-amplifier.

In order to optimize spatial resolution of the plume diagnostic, the acceptable detector distance from the exciter should be minimized. In this case, the spatial mapping in Section 6.2 provides the information necessary to qualitatively determine a minimum acceptable distance. The spatial mapping in Section 6.2 was implemented by linear radial sweeps in axial planes. This provided general information about the ion acoustic wave; however, for characterization of the propagation zone, the characterization should be implemented for a constant distance from the excitation probe in order to more closely follow an equiphase contour of the spherical wave emanating from the probe (see Chapter 7). Additionally, the sampling resolution should be much finer than used in Section 6.2 in order to accurately determine the propagation zone edge. Given the good consistency in the propagation pattern, the characterization can be implemented at a single distance from the excitation probe. The phase shift can also be sampled at two distances to get an estimate of the phase shift.

The spatial characterization of the MAI thruster and Fakel thrusters has established an area of consistent propagation where more limited spatial characterization is sufficient to obtain necessary information. For the MAI thruster, measurements 10 cm or farther down stream will yield consistent results. For the Fakel thruster measurements 5 cm downstream will yield consistent results. The longer distance for the MAI thruster is primarily due to a null in the amplitude pattern at approximately 7 cm. For a given plasma source and probe configuration, a limited axially characterization provides sufficient information necessary to determine a minimum acceptable detector distance.

CHAPTER 7

IMPLEMENTATION OF ION ACOUSTIC WAVE PROBE TO SPATIALLY MAP PLASMA PARAMETERS

7.0 Overview of Chapter

Ion acoustic wave propagation in plasmas is intrinsically related to the properties of the plasma. In a flowing plasma, propagation is not only dependent on the electron and ion temperatures, but also the flow velocity as described in Chapter 5. The plasma parameters can be quantified by characterizing the propagation of the ion acoustic wave as demonstrated in Chapter 6. The experimental implementation of Chapter 6 addressed the general measurement issues related to propagation characterization and also effectively characterized the propagation pattern through measurements of phase and propagation zone edge. The same information needs to be obtained with a less rigorous characterization in order to characterize the plasma at multiple points.

Two measurements are necessary: phase shift over distance and maximum propagation angle. These quantities can be found with two probes at two separate and constant distances from an exciter which are spatially swept through the propagation zone. Such a system is implemented in the plume of a stationary plasma thruster. Measurements are completed at three distances from the thruster between 77 cm and 144 cm. The measurement results are used to find directed velocity and electron temperature, and three possible analyses are discussed where the last presents a method to find ion temperature using the ion acoustic wave information and Langmuir probe information.

7.1 Experimental Description

The plasma parameter characterization using ion acoustic wave has been implemented for the Fakel SPT-100 thruster using the second experimental configuration outlined in Chapter 5 (Figure 5.8). The Fakel thruster, which is discussed in detail in Appendix B, is operated on xenon at the nominal operating level of 300 V and 4.5 A with 5.0 mg/s xenon to the anode and 0.56 mg/s xenon to the cathode. The critical components to the measurement are the positioning system, exciter and detector probes, and lock-in amplifier.

Measurements have been recorded in three planes which are 0.77, 1.0, and 1.4 m from the thruster exit plane. Within each plane, twenty measurements have been recorded at distances from the thruster axis over the range from -1.0 m to 0.5 m where the positive radial positions correspond to the cathode side of the thruster. At each location, approximately 200 amplitude/phase measurements are recorded for each detector probe which are swept through an angle ±20° around the geometric line from the thruster (see Figure 7.1).

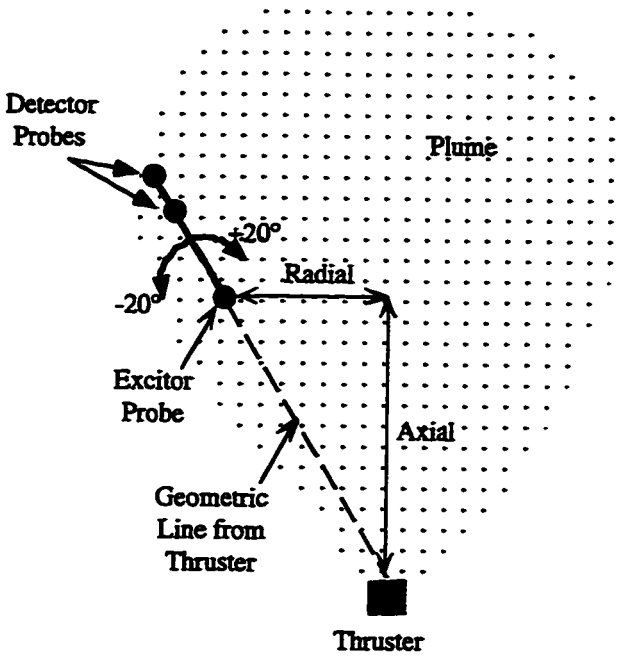

Figure 7.1. Guide for measurement positioning.

The probes used for excitation and detection of voltage signals are oriented orthogonal to the direction of flow. The exciter and both detectors, as shown in Figure 7.2, are tungsten wire probes where the exciter is 0.55 mm outer diameter and the detectors are both 0.43 mm outer diameter. The probes are approximately the same lengths ranging from 10.5 mm to 11.6 mm. The insulator protrudes from the metal shield from 9 to 20 mm and the top of the shield is 15 cm from the support which is mounted to the positioning table. The first detector probe is 9.26 cm from the exciter and the two detector probes are separated by 4.46 cm

The data acquisition is implemented through a lock-in amplifier controlled via GPIB by a computer running LabView. The lock-in-amplifier (Stanford Research Systems SR850), which is directly connected to the probes acted as a sensitive transmitter and receiver obtaining high performance data through digital control of the transmitted signal and digital processing of the received signal. The signal processing settings are generally 1 s time constant, 18 dB/oct filter, and maximum reserve (maximum resolution which is used

to extract signals from noise). All of the measurements, except the frequency sweeps, are implemented at 100 kHz and ±5 V, both are maximum settings of the available lock-in amplifier, a Stanford Research Systems model SR850.

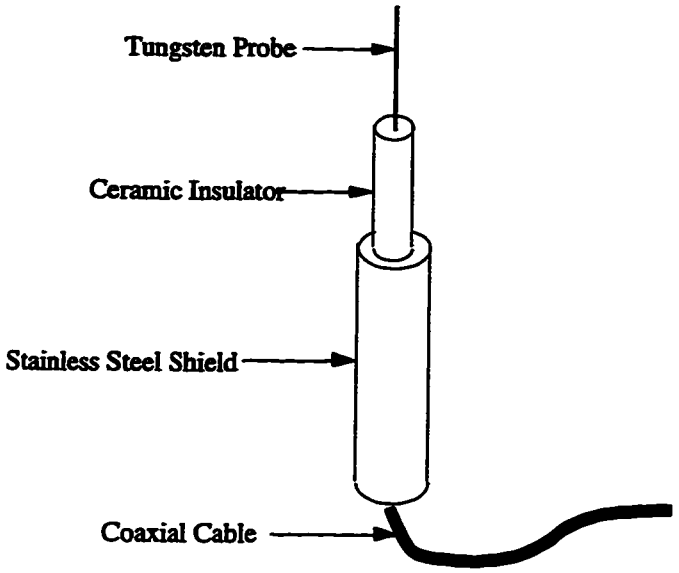

Figure 7.2. Schematic of exciter and detector probes.

7.2 Results of Propagation Characterization at Different Positions

The spatial variation of an ion acoustic wave amplitude and phase are measured in order to provide information concerning the flow velocity, ion acoustic phase velocity, and electron and ion temperatures. Initially, baseline measurements are completed in order to determine stability and repeatability. Example data is then presented and general characteristics are summarized. Finally, general data interpretation is discussed and then applied to produce a spatial mapping of the two measured quantities: phase shift and propagation zone edge angle.

7.2.1 Baseline Measurements

In order to assess the stability and repeatability of the measurements, multiple data points have been recorded at the same position over time. In the first test, the transmitter was located on center line 1 m from the thruster exit plane. The amplitude and phase were

recorded every 2 seconds for 7 minutes. For the probe closest to the exciter, the mean amplitude was 1.4 mV, the standard deviation is 0.015 mV (1%), and the range is from 1.35 (-3.6%) to 1.43 mV (+2.1%). For the same probe the average phase is 125.1° with a standard deviation of 0.55° (0.4%) and a range from 123.5° (-1.2%)to 127.4° (+1.8%). For the second probe, farthest from the exciter, the mean amplitude is 0.43 mV with a standard deviation of 0.01 mV (2.3%) and a range from 0.41 (-4.7%) to 0.46 mV (+6.5%). The mean phase of the second probe was 25.4° with standard deviation of 1.1° (4.4%) and a range of 22.5 (-11%) to 28.5° (+12%).

In the second test, additional measurements were recorded for multiple rotary sweeps. Six consecutive sweeps, each taking approximately 3 minutes, have been taken where the amplitude and phase are extremely stable between the measurements (Figures 7.3 and 7.4). In the amplitude data, the average deviation at each position was 0.02 mV and the maximum deviation was 0.058 mV. The deviation in the phase data was generally below 2° except at rotary angles of 4.5° and 0.75° positions where the 180° phase jump occurs. In both experiments the amplitude and phase is extremely stable given the noise inherently present in the SPT plume.

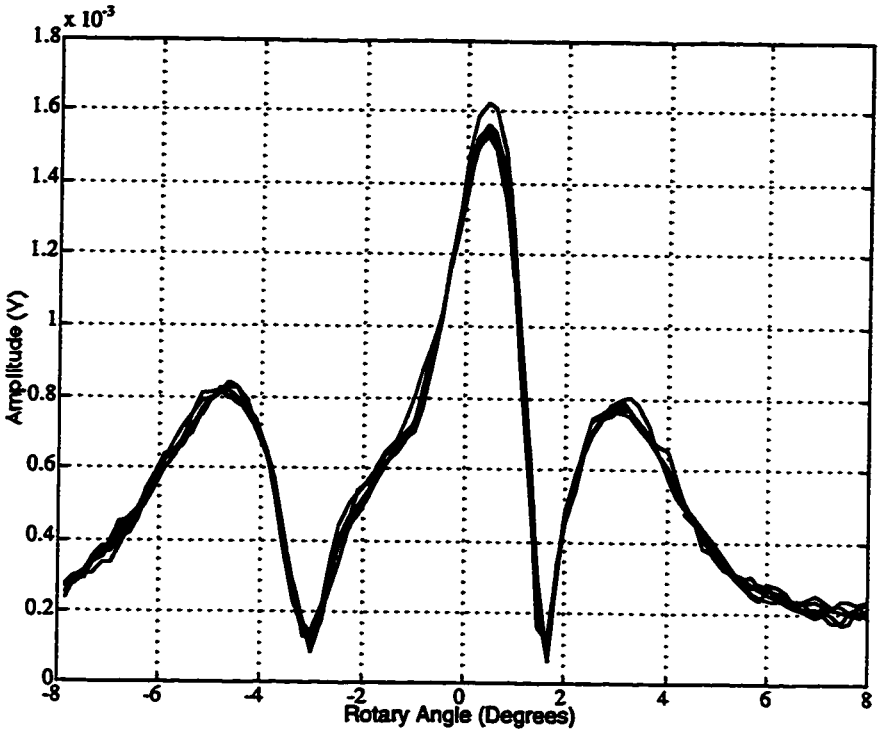

Figure 7.3. Amplitude varying over multiple rotary sweeps (1m from thruster on axis).

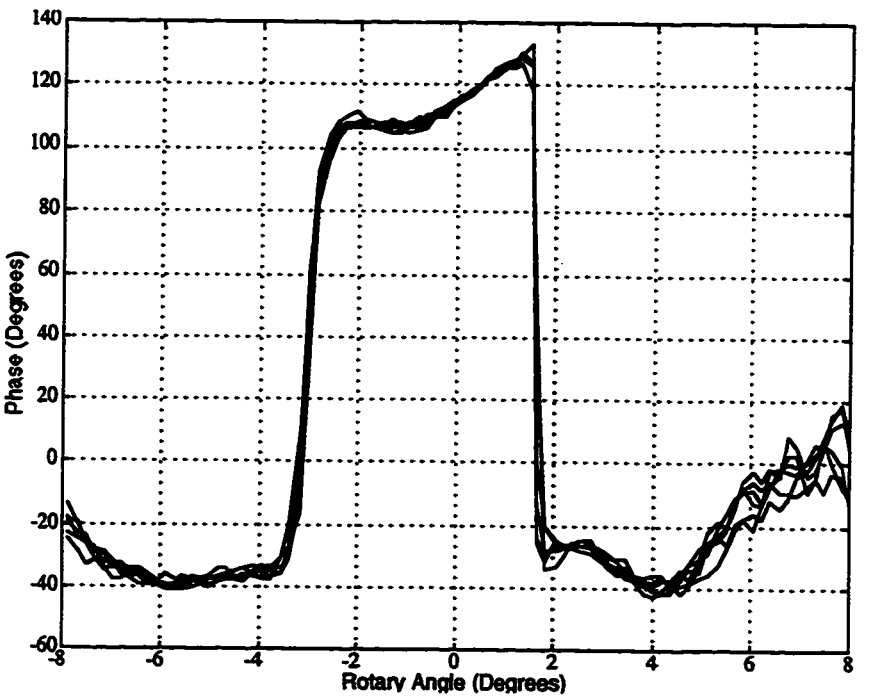

Figure 7.4. Phase varying over multiple rotary sweeps.

7.2.2 Amplitude and Phase Data and General Characteristics

The amplitude pattern of ion acoustic waves can vary significantly with position in the plasma plume. Generally, the pattern resembles an interference pattern caused by a wake from the exciter probe which produces an anisotropic probe-plasma coupling (see Chapter 6). Since the interference pattern is dependent on position, this indicates a direct dependence on several plasma parameters that vary throughout the plume such as density, flow velocity, temperature, and gradient in any of these quantities. This dependence is justified since a wake structure is determined by particle density and particle velocity (both directed and thermal). The center of the propagation zone is approximately aligned with the geometric line to the thruster. Additionally, the propagation zone for exciter positions away from the thruster axis deviate (rotate) slightly (0-4°) towards the thruster axis (see Figure 7.6). The edge of the propagation zone is clearly evident for data sets near the center of the plume and sometimes difficult to determine at measurement points farthest from the plume centerline.

Two examples of amplitude patterns, Figures 7.5 and 7.6, demonstrate the sensitivity to the plasma parameters. Both cases exhibit the low coupling efficiency expected of a cylindrical probe [Stone, 1986] where the coupled signal is less than 1 mV peak for an excitation level of 5 V. The first data set is taken near the thruster centerline. The pattern is generally symmetric with a strong lobe in the center and a single lobe on either side of the middle where the amplitude is strong and distinct in the propagation zone. The second example is taken off the thruster axis in a region of significantly lower density (one to two orders of magnitude). In this data set, negative values of rotary position are towards the thruster centerline. The amplitude is lower on the second data set but not directly in proportion with the density. In this pattern five lobes exist, and the center lobe is not the strongest amplitude. The general trend is for the higher amplitude lobes to be towards the centerline of the thruster where there is expected to be higher density. Generally in the higher density regions a stronger coupling exists producing higher signals;

however, measurements completed at 0.5 m indicate strong coupling into the natural fluctuations of the plasma which make results noisy and interpretation difficult. In order to minimize this problem, the ion acoustic wave should be excited in a frequency region with lower levels of noise such as higher than 50 kHz for the SPT. Improvements are also possible for specific situations by optimization of other parameters such as the excitation voltage levels.

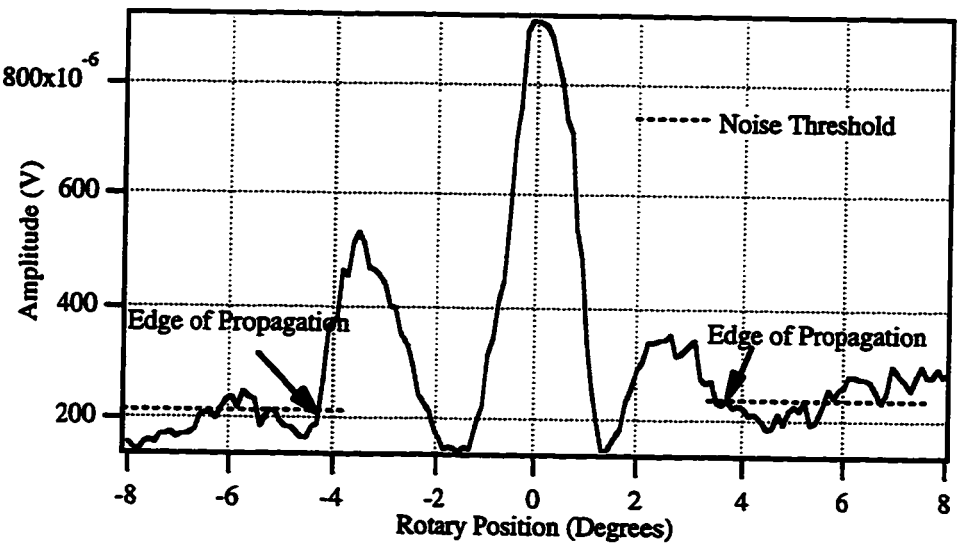

Figure 7.5. Example of amplitude pattern near plume axis (the reference angle is with respect to the geometric line from the thruster).

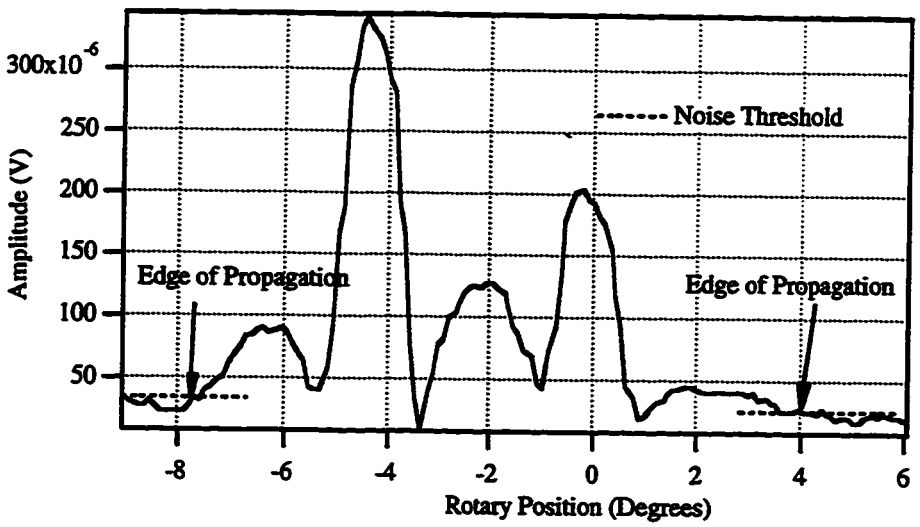

Figure 7.6. Example of amplitude variation away from the plume axis (the reference angle is with respect to the geometric line from the thruster).

Phase variation (Figures 7.7 and 7.8) at the two positions also demonstrates the sensitivity to plasma parameters. In order to clarify the phase data, 360° is added or subtracted as appropriate. The phase change corresponds closely to the amplitude variation where nulls in amplitude pattern correspond to phase shifts in the phase pattern. Just as with the amplitude nulls, more phase shift occurs for measurements farther from the thruster axis where the density and velocity are lower. The phase shift is recorded at the center of the propagation zone. Generally the phase shift is less noisy near locations of peak amplitude which aids in accurate interpretation of the phase shift. Just as with the amplitude, interpretation of data in the fringes of the plume is difficult due to low signal levels and also near the thruster due to strong noise coupling.

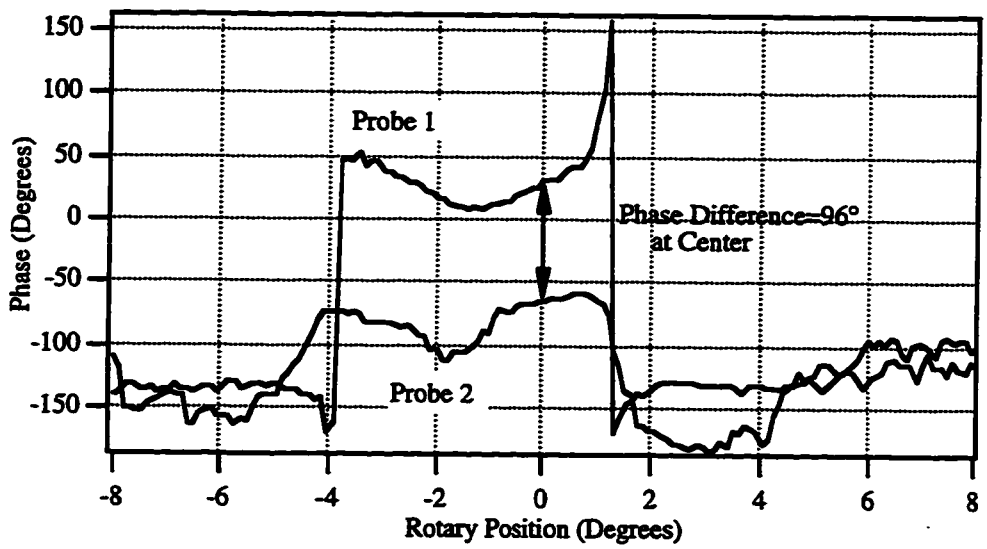

Figure 7.7. Example of phase variation near the plume axis for both detector probes (the reference angle is with respect to the geometric line from the thruster).

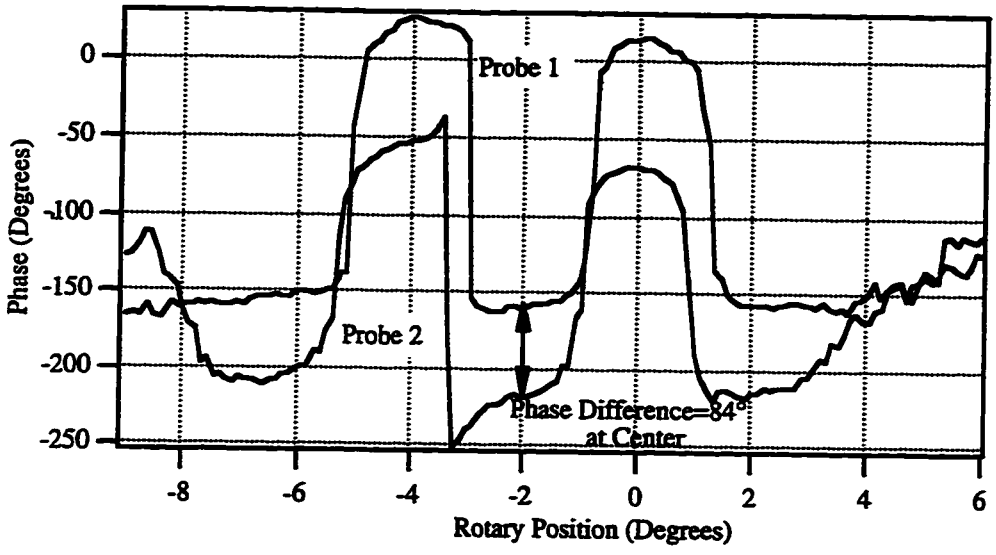

Figure 7.8. Example of phase variation away from the plume axis for both detector probes (the reference angle is with respect to the geometric line from the thruster).

7.2.3 General Data Interpretation and Spatial Mapping

Amplitude and phase measurements provide two quantities to characterize a plasma: the maximum propagation angle and the phase shift over distance both for an ion acoustic wave superimposed on a flowing plasma. The propagation angle is proportional to the ratio of the phase velocity of an ion acoustic wave and flow velocity of the plasma. The phase shift is proportional to the inverse of the phase velocity of the ion acoustic wave superimposed on the flowing plasma. The quantities are characterized for a number of positions in the Fakel thruster plume.

The propagation zone angle is found by determining the maximum angle where propagation is detected (noise threshold). There exists a number of uncertainties in determining this angle accurately. First, the noise might overwhelm the signal in regions where low signal to noise ratios exist close to the thruster or in the periphery of the plume (low density). Generally, in these measurements, it is difficult to accurately determine the measurement value when the peak signal level is less than 50 μV. Second, nulls in the

pattern might cause the signal strength to drop prematurely into the noise. Lastly, the signal level sometimes decreases very gradually, making accurate determination of the edge difficult. Each of these issues has less impact in homogeneous higher density plasma with low noise levels. Through careful interpretation using the phase information as a guide the propagation edge can be evaluated to well within ±1° in most cases; however, this determination is difficult if the amplitude at the center is small or if a phase reversal occurs near the center.

The phase shift is obtained through finding the difference in the phase detected by the two probes at the center of the propagation zone. At the center, the phase shift of the wave detected by the probes is related to the sum of the ion acoustic phase velocity and the flow velocity. Two primary uncertainties also exist in determination of this quantity. First, the phase noise inherent in the measurement produces phase variation up to ±3°. Second, the center of the propagation zone is not always well defined. This produces an error since the phase velocity is the vector sum of the components of the two velocity vectors in the direction of interest. If the measurement is not along the flow direction then the total phase velocity is not exactly the arithmetic sum of the two velocities. This error is usually small if the flow velocity is much larger than the ion acoustic phase velocity since the phase velocity around the center varies as the cosine of the rotary angle. In many instances the phase shift is constant (±1° phase angle) around the center (±1° rotary angle) demonstrating minimal change in velocity. Precise determination of the propagation center is more important for instances where the flow velocity is only slightly faster (a factor of 4 or less) than the ion acoustic phase velocity.

Variation in the propagation pattern exists due to the inhomogeneities that exist in the plume of an SPT. Strong density gradients exist in certain regions that cause anisotropic coupling evident in the non-symmetric nature of some propagation patterns. The flow velocity and thermal properties change less rapidly than density, but also contribute to uncertainty in the propagation pattern especially in the plume periphery where

the magnitude of the velocity, the temperature, as well as the density tends to decrease. Although, variation in plume properties tends to distort the propagation pattern, the results of the ion acoustic wave characterization nonetheless quantify the average properties over the measurement region.

The amplitude and phase shift has been found for 3 axial distances and 20 positions radially out from the axis (Figures 1.9 and 1.10). The error bars in both cases indicate the uncertainty due to noise and edge interpretation. Both quantities vary only slightly across the measurement region except for the measurements at very large angles from the thruster centerline. This result is expected given the small variation in flow velocity and temperatures throughout this region of the plume.

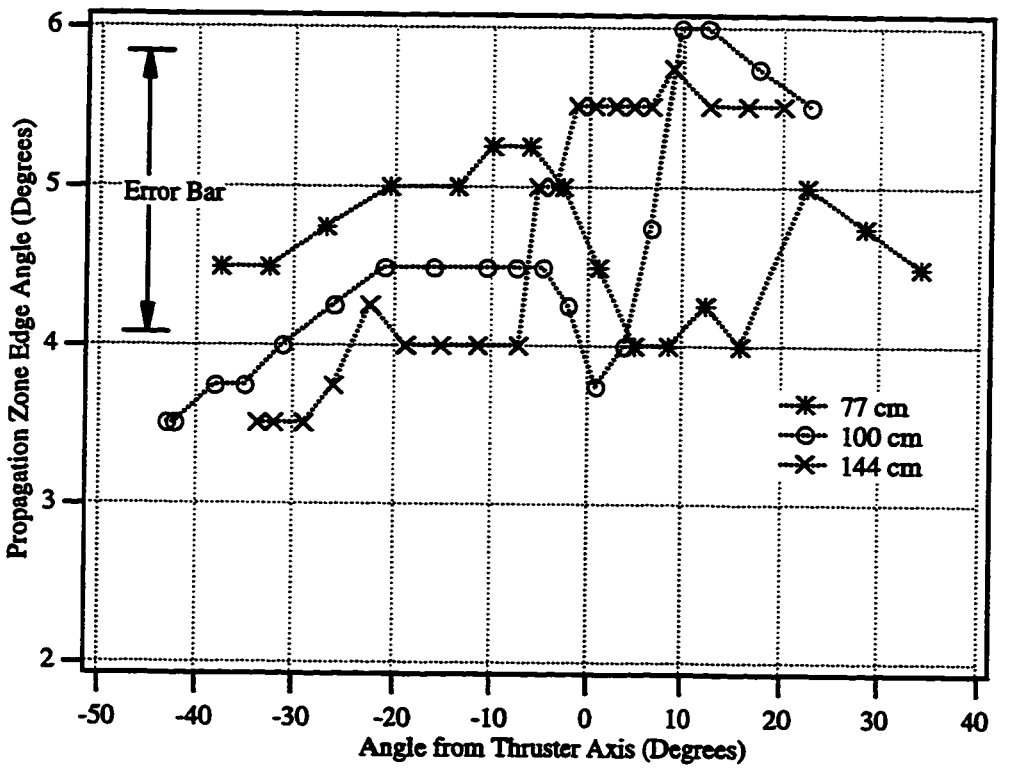

Figure 7.9. Spatial variation of propagation zone edge between detectors.

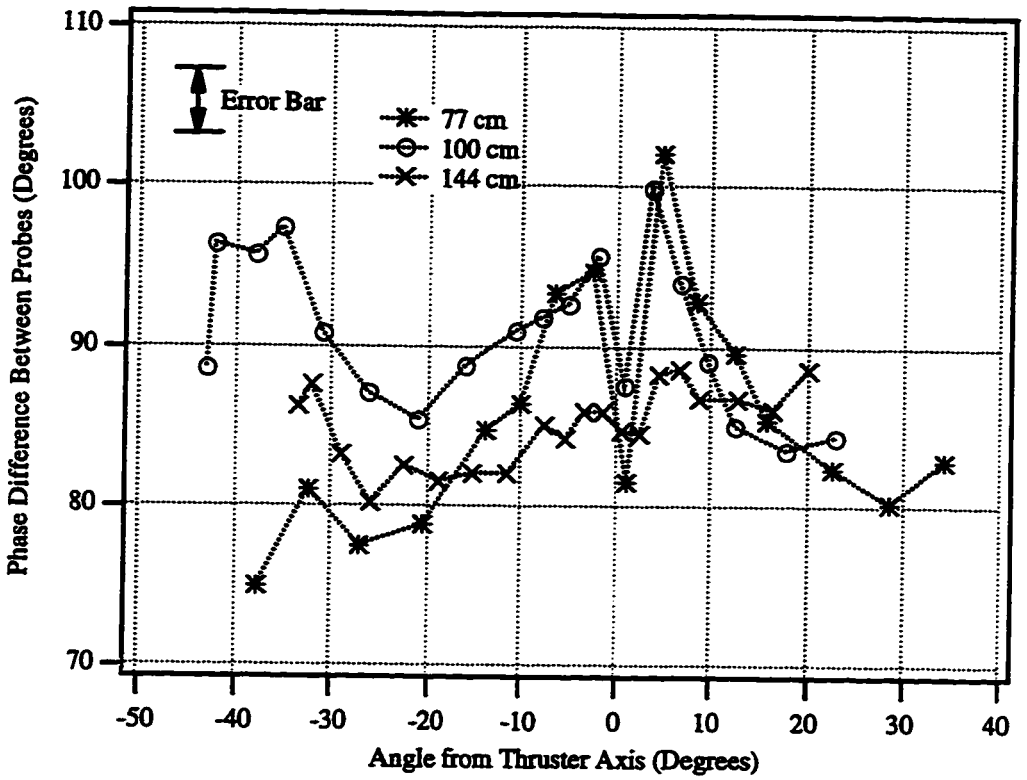

Figure 7.10. Spatial variation of phase difference between detectors.

7.3 Analysis of Ion Acoustic Wave Diagnostic Methods

Knowledge of the phase shift and propagation zone edge provide information directly about the flow velocity and ion acoustic wave velocity. Additionally the ion acoustic wave velocity relates to the electron and ion temperatures. The ion acoustic wave information can be used as a diagnostic tool to quantify the plasma parameters. The accuracy of the method depends on the relative values of flow velocity, electron temperature, and ion temperature. Three analyses are presented utilizing the wave propagation information and in the third method, Langmuir probe data is also used. The second analysis method is applied to the data presented earlier in order to find flow velocity, ion acoustic wave velocity, and electron temperature.

7.3.1 Review of Relation Between Measurements and Plasma Parameters

The spatial variation of amplitude and phase is related to the plasma flow velocity and ion acoustic wave velocity (see Chapter 5 for a more detailed discussion). Propagation is ideally limited to a cone downstream of the excitation source. The half-angle of the cone is a direct measurement of the ratio of the ion acoustic velocity and flow velocity:

$$\tan(\theta) = \frac{V_{iaw}}{V_{flow}}. \qquad \bullet 7\text{-}1$$

The phase variation over space is determined by the phase velocity of the ion acoustic wave that is superimposed on the flowing plasma. In the frame of reference of the probe this velocity along the flow direction is the sum of the ion acoustic phase velocity and the plasma flow velocity:

$$V_{tot} = f\lambda = fd\frac{360^\circ}{\Delta\phi} = V_{iaw} + V_{flow} \qquad \bullet 7\text{-}2$$

In this relation the wavelength is determined directly from the measurement of phase shift over a known distance (the detector probe separation, d). Using this information the flow and ion acoustic velocity are easily found:

$$V_{flow} = fd\frac{360^\circ}{\Delta\phi}\left(\frac{1}{1+\tan(\theta)}\right) \qquad \bullet 7\text{-}3$$

$$V_{iaw} = fd\frac{360^\circ}{\Delta\phi}\left(\frac{\tan(\theta)}{1+\tan(\theta)}\right) \qquad \bullet 7\text{-}4$$

The ion acoustic velocity is related to plasma parameters through the dispersion function:

$$V_{iaw} = \sqrt{\frac{kT_e + 3kT_i}{m_i}} \qquad \bullet 7\text{-}5$$

The velocity provides information concerning the sum of the electron and ion temperatures. The analysis to utilize this relationship varies depending on the plasma and other available information as is discussed in the following three methods.

7.3.2 Calculation of Plasma Parameters

Four possible analysis approaches are described which utilize varying information and assumptions. In addition to the basic description, an estimation of total error is given based on estimations of measurement uncertainty and parameter values. In all cases the uncertainty in the probe separation distance and frequency is ignored since it is much smaller than the other source of error uncertainty.

7.3.2.1 Method 1

As a first estimation, the flow velocity can be found directly from the phase velocity of the wave if the ion acoustic phase velocity is thought to be much less than the flow velocity [Boyle, 1974]:

$$V_{flow} \approx f d \frac{360°}{\Delta\phi}. \qquad \bullet 7\text{-}6$$

The error in this estimation is a function of the relative amplitude of the ion acoustic phase velocity and the uncertainty in the phase measurement.

For the general parameters in this study the error is approximated through the following relations:

$$V_{flow} = \frac{360°}{\Delta\phi} df\left(1 + Err_{tot}\right) \qquad \bullet 7\text{-}7$$

$$Err_{tot} = \pm Err_{\phi} - \frac{V_{iaw}}{\frac{360°}{\Delta\phi} df} \qquad \bullet 7\text{-}8$$

The error expression assumes that the phase error is smaller than 10% which is well within the measurements presented here. For general parameters of this study, such as a flow velocity of 18 km/s, ion acoustic velocity of 1.7 km/s, and a phase uncertainty of 3%, the uncertainty for the flow velocity would be ±12%. The uncertainty is dominated by the ion acoustic velocity. In order for the error contribution from the ion acoustic velocity to be less than the experimental error of phase uncertainty, the flow velocity would need to be 57 km/s. Therefore, in general, in order to obtain flow velocity measurement with accuracy better than 12%, an estimation of the ion acoustic velocity is needed. This can be obtained either through method 2 (as presented below) or through independent measurement of electron and ion temperatures.

7.3.2.2 Method 2

A second method to utilize the ion acoustic wave information uses both the phase shift and propagation zone edge measurements. This method provides the flow velocity, ion acoustic wave velocity, and electron temperature, hence ignoring the ion temperature ($T_e >> T_i$). By utilizing Equation 7-3 and 7-4 the two velocities are found with the primary error due to measurement uncertainty. The electron temperature is estimated from Equation 7-5 where the ion temperature is ignored; thus, the electron temperature error is the combination of measurement uncertainty and the bias due to assuming the ion temperature is zero.

The uncertainty estimation for the three parameters is given by the following set of expressions:

$$V_{flow}\left(1 \pm Err_{flow}\right) = \frac{360°}{\Delta\phi} df \left(1 \pm Err_{\phi}\right) \frac{1}{\left(1 + \tan(\theta)\left(1 \pm Err_{\theta}\right)\right)}, \qquad \bullet 7\text{-}9$$

$$V_{iaw}\left(1 \pm Err_{iaw}\right) = \frac{360°}{\Delta\phi}\left(1 \pm Err_{\phi}\right) df \frac{\tan(\theta)\left(1 \pm Err_{\theta}\right)}{1 + \tan(\theta)\left(1 \pm Err_{\theta}\right)}, \text{ and} \qquad \bullet 7\text{-}10$$

$$Te\left(1 \pm Err_{T_e}\right) = \left[\frac{360°}{\Delta\phi} df \frac{\tan(\theta)}{1 + \tan(\theta)}\right]^2 \left(1 \pm Err_{iaw}\right)^2 \frac{m_i}{e} - Err_{Ti}. \qquad \bullet 7\text{-}11$$

The error due to the ion temperature is just $3T_i$ as would be found from the dispersion relation. The electron temperature uncertainty is approximately twice the uncertainty of the ion acoustic wave velocity with a small bias from assuming a negligible ion temperature. In order to estimate the error given by these expressions, representative parameters are listed in Table 7.1.

V_{flow} (km/s)	18
V_{iaw} (km/s)	1.77
T_e (eV)	3
T_i (eV)	0.1
θ	5.6
Err_ϕ	±3%
Err_θ	±20%

Table 7.1. Representative parameters for total error calculation in method 2.

By applying the parameters to the error expressions given above the flow velocity uncertainty is found to be ±5%, the ion acoustic wave velocity uncertainty to be ±21%, and the electron temperature uncertainty to be ±67%. This method gives a reasonable estimate of the flow velocity and the ion acoustic velocity, but the electron temperature uncertainty is high in comparison to other diagnostic techniques that measure electron temperature. In order to improve the electron temperature accuracy, the estimation of the propagation zone edge needs to be improved significantly which would be the case in more ideal plasmas than the SPT plume.

7.3.2.3 Method 3

An additional technique which also estimates the ion temperature utilizes measurements from a Langmuir probe to find electron temperature. The same probe can be used as the ion acoustic wave exciter or an additional probe can be implemented. In this case, the flow velocity and ion acoustic velocity are found just as in method 2. The ion temperature is found from the dispersion function utilizing the ion acoustic velocity and

electron temperature measurements. The error estimation is found through the following expression:

$$T_i\left(1\pm Err_{T_i}\right)=\left[fd\frac{360^\circ}{\Delta\phi}\frac{\tan(\theta)}{1+\tan(\theta)}\right]^2\frac{m_i}{3e}\left(1\pm Err_{iaw}\right)^2-\frac{T_e}{3}\left(1\pm\frac{Err_{LP}}{3}\right).\bullet \qquad 7\text{-}12$$

The uncertainty in the electron temperature measurement is estimated to be ±10 % which is well within the capability of most Langmuir probe implementations [Tilley, *et al.* 1990].

The uncertainty in the ion acoustic velocity contributes a much larger amount of error than the uncertainty in electron temperature resulting in a worst case result of 0.78 eV when the assumed value is 0.1 eV. This degree of uncertainty primarily limits the usefulness of this technique to determining an upper bound for the ion temperature. The technique could potentially be helpful where other diagnostics to measure ion temperature are not easily implemented as is the case in an SPT plume. In order to more accurately determine ion temperature using this method, the edge of the propagation zone needs to be characterized more accurately through three possible methods: data averaging, more precise characterization of the propagation region, and a better understanding of the propagation pattern produced by the probe wake affecting the ion acoustic wave coupling.

7.3.2.4 Method 4

One last technique to utilize the ion acoustic wave propagation characteristics utilizes the phase shift along the flow direction and results from a Langmuir probe to find flow velocity and electron temperature. This technique simplifies the demands of the positioner by not requiring rotational movement (if aligned with the flow axis) and eliminates the uncertainty present in interpretation of the ion acoustic wave propagation zone. Additionally, the same probe used as the ion acoustic wave exciter can be used as the Langmuir probe to accurately find electron temperature.

The electron temperature is found through a standard Langmuir probe analysis [Chung, *et al.* 1975; DeBoer, 1994]. The phase shift of the wave along the flow axis is

found through the method described earlier. Using these two measurements, the flow velocity and flow velocity uncertainty are found through the following equation:

$$V_{flow}(1 \pm Err_{flow}) = f d \frac{360°}{\Delta\phi} - \sqrt{\frac{kT_e}{m_i}} \pm Err_\phi \pm Err_{LP}. \qquad \bullet 7\text{-}13$$

Given a phase uncertainty of 3%, an electron temperature uncertainty of 10% [Chung, 1975], and the experimental parameters presented in the Table 7.1, the total uncertainty for the flow velocity is 4%.

This method is attractive due to the simpler implementation and interpretation when the propagation zone information is not necessary. Furthermore, the same probe can be used as an exciter and Langmuir probe.

7.4 Plasma Parameters Found Using Method 2

The measurements of phase shift and propagation zone edge angle presented earlier provide the information necessary to implement method 2 to find flow velocity, ion acoustic wave velocity , and electron temperature (Figures 7.11 through 7.13). The data is shown for three different axial distances from the exit plane of the thruster and for varying angles with respect to the thruster centerline (note, this does not indicate constant distance from the thruster). The absolute error must be calculated for each point; however, error bars representative of the data set are placed on each figure where the higher data values have larger error bars and the smaller data values have smaller error bars.

In all cases, the range of measured values is small in comparison to the error bars indicating only slight variation of velocities and temperature across the plume as is expected for the SPT. Data points at the closest axial distance (0.77 m) and at angles greater than 40° indicate a sharp drop in flow velocity to less than 5 km/s (not shown in the figure) and a drop in electron temperature to less than 0.1 eV. This significant decrease is expected in the periphery of the plume, but this could also be partially due to the low density at the edge of the plume producing slightly greater uncertainty in those measurements. In all data sets

the values tend to decrease for positions away from the center of the plume. In the flow velocity measurements, a high velocity core is surrounded by a slight depression in the velocity. In general these results agree with past findings for the stationary plasma thruster [Manzella, 1994; Myers, *et al.* 1993; Patterson, *et al.* 1985; Szabo, *et al.* 1995].

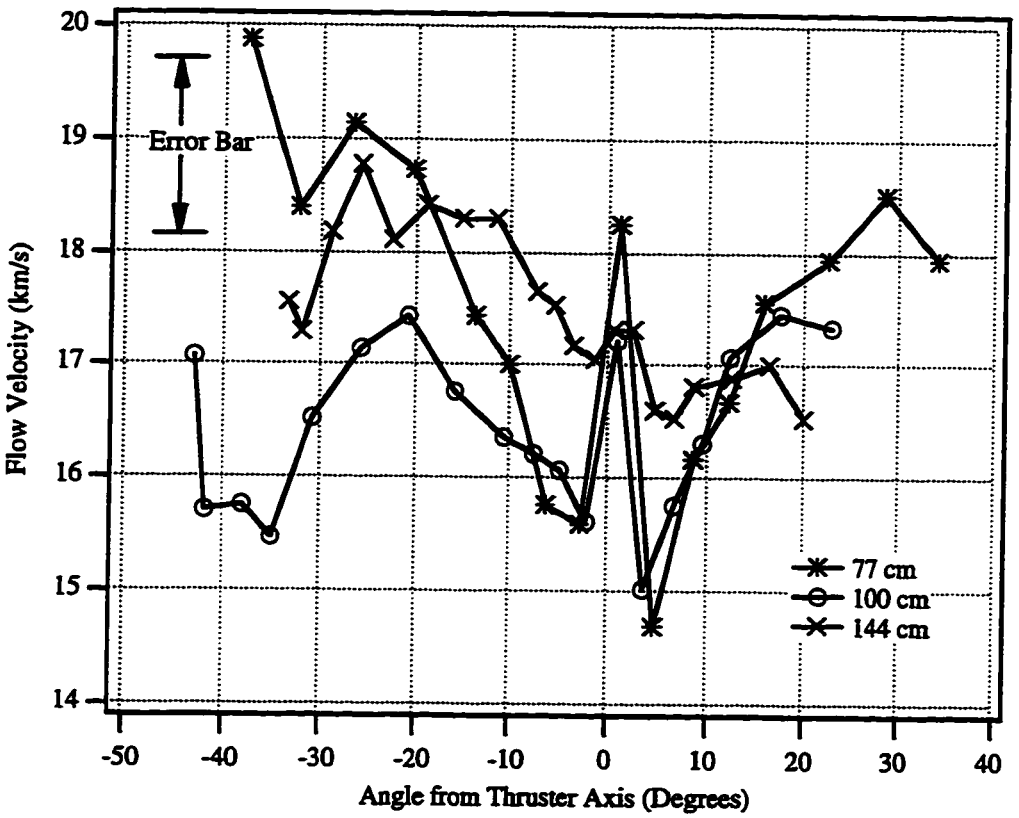

Figure 7.11. Flow velocity found from ion acoustic wave characterization.

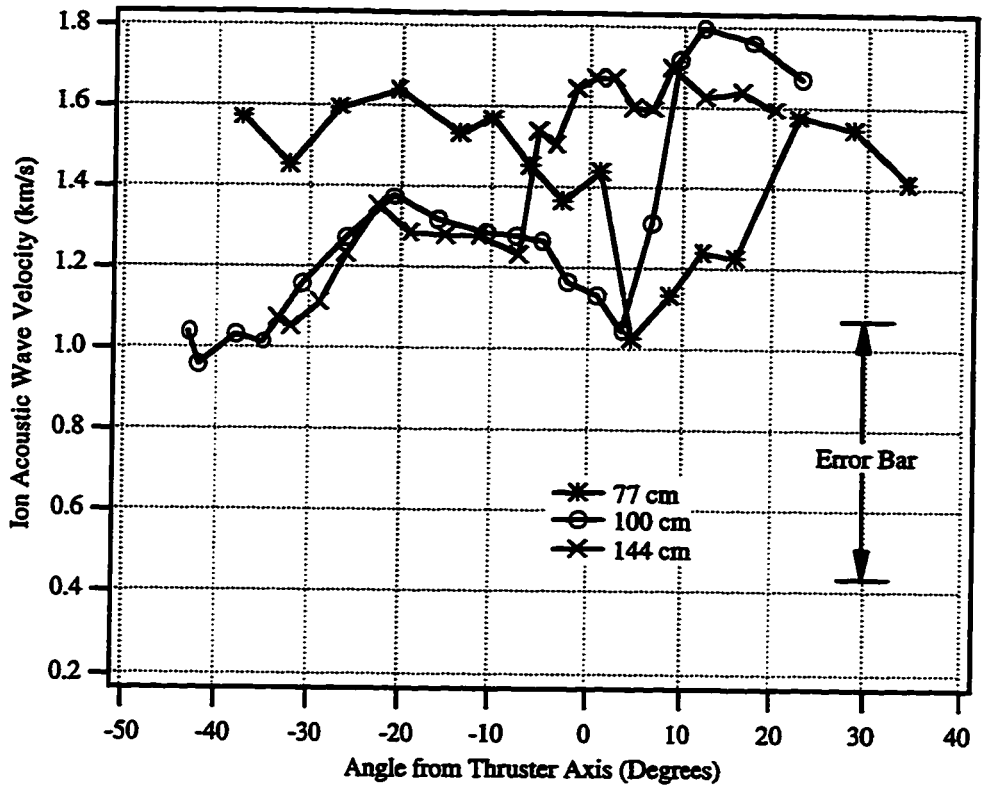

Figure 7.12. Ion acoustic phase velocity found from ion acoustic wave characterization.

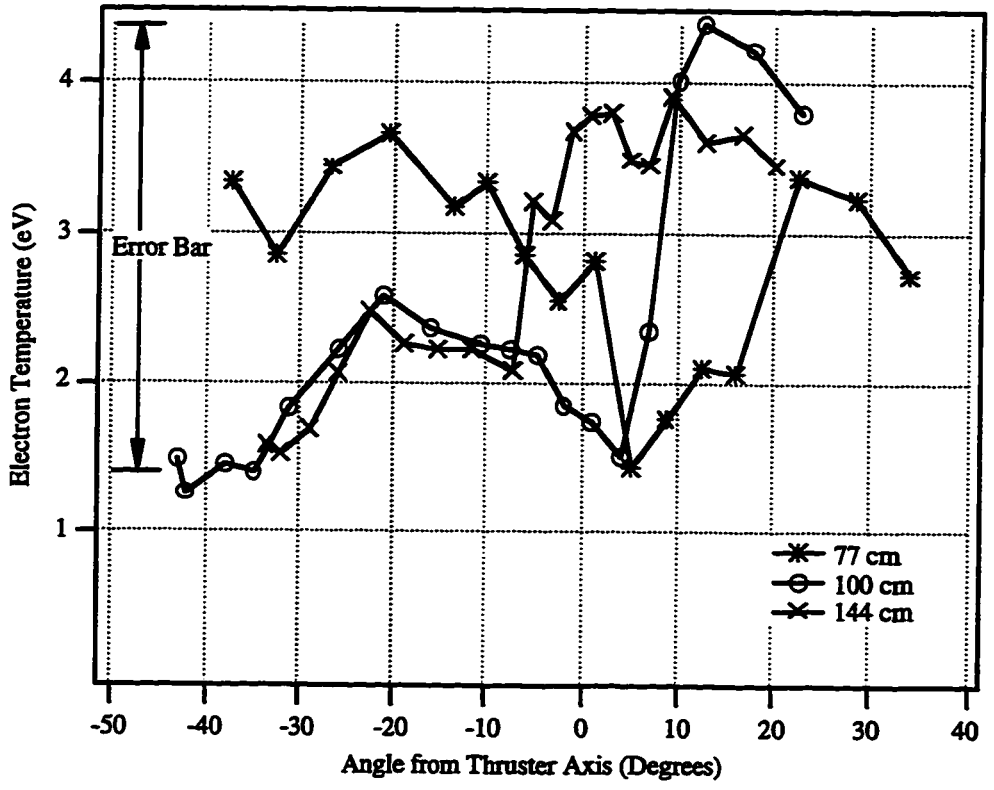

Figure 7.13. Electron temperature found from ion acoustic wave characterization.

CHAPTER 8

CONCLUSION

8.0 Overview of Chapter

The use of satellite technology is essential in modern society for communications, navigation, remote sensing, and space exploration as well as other applications. Control of the attitude and position of satellites is critical in nearly all applications; hence, propulsion technology is a key component of satellites. Electric propulsion has emerged as the next step in satellite propulsion technology due to its often ideal thrust characteristics leading to increased lifetime and higher economic benefits than traditional chemical propulsion systems. Utilization of electric propulsion technology requires an understanding of thruster operation and impact on other satellite systems.

This research has explored electric propulsion systems through innovative development and implementation of thruster plume diagnostics. Initially, the plume was characterized by transmitting a microwave signal through the plume. A novel microwave system was developed to operate in the large vacuum chamber which is ideal for plume studies due to the minimization of plume interaction with the chamber wall. The microwave system provides a direct measurement of line average electron density through interferometric analysis and also provides local electron number density through inversion of spatially resolved phase measurements in cross sections of the plume. In addition to the basic measurement of electron density, new information concerning the impact to electromagnetic systems has been obtained through direct experimental characterization of amplitude, phase, and the power spectral density. The electromagnetic impact has also

been explored through innovative computer modeling utilizing a ray tracing code verified through newly acquired experimental results which is extended to a range of experimental configurations.

In addition to characterization of microwave propagation, ion acoustic wave propagation has been more fully characterized and related to flow velocity, electron temperature, and ion temperature. Initially general wave propagation was characterized to extend previous research in order to determine the feasibility of an innovative ion acoustic wave diagnostic technique. The excitation and detection characteristics were then explored to identify appropriate experimental configurations. Finally, a novel diagnostic approach produced one possible configuration which was implemented. Four possible analytical methods were demonstrated, and the accuracy has been assessed for each analysis.

8.1 Characterization of Microwave Propagation in an Electric Thruster Plume

In this work, an innovative microwave system has been developed to quantify both the electron density and the electromagnetic signal impact of an electric thruster plasma plume. The novel measurement system provides spatial mapping along two linear axes. It uses a microwave network analyzer and spectrum analyzer to quantify phase, magnitude, and power spectral density. The system is implemented with three innovative features: (1) provides a much wider bandwidth than previous systems for communications studies by covering the Ku communication band, (2) minimizes chamber wall effects to the microwave system and the plasma thruster system due to the large vacuum chamber, and (3) controls phase and attenuation errors due the long line lengths (as a result of the large vacuum chamber) through frequency conversion.

Initially, the microwave system characterizes the phase of a wave transmitted across the plasma plume for both the arcjet and stationary plasma thrusters. The method of microwave interferometry is used to find the integrated electron density, and then Abel

inversion is used to find the local electron density. Both characterizations compare well with Langmuir probe measurements in the plumes where new information about the thrusters is obtained in both cases. The electron density is found to be accurate to within ±20% (Chapter 3).

The phase measurements and electron density for the SPT were further analyzed to estimate any plume asymmetry and to find a functional model of the electron density distribution. The asymmetry in the plume is evaluated to understand and confirm physical processes present in the plume and to justify the use of Abel inversion (since the inversion process assumes radial symmetry). The integrated phase measurements (which do not assume any symmetry) are evaluated along paths radiating radially from the thruster. The total particle velocity vector is found to be only 0.8° off axis which is within the accuracy of the measurements. This confirms previous findings of the thrust vector and also justifies the use of Abel inversion.

The electron density is also studied to determine a convenient functional model in the near- to far- zone region of the plasma plume. The electron density in this region was not measured previously and a model had not been developed. An innovative two component model closely approximated the measured density and is physically justified. The novel first component is a Gaussian beam term which relates to the near-zone plume shape, and the second component is a free expansion term ($1/r^2$) that approximates the far-zone distribution. The model is applicable from approximately 0.1 m to 1 m from the thruster exit plane where the model at both ends of the region over predict the measured density by up to 50%.

New measurements are also implemented to characterize the effect of the SPT plume on the amplitude and power spectral density in order to directly determine the impact to electromagnetic systems (such as on a satellite). The amplitude measurements indicate a power loss up to 2 dB at the closest measurement distance. The attenuation is significantly reduced for transmission 0.1 m off the plume axis. The power spectral density indicates

significantly increased noise levels at 26 kHz harmonics off of the main signal. Broadband noise is increased up to 20 dB from the -90 dBc noise floor. The measurements of phase, amplitude, and power spectral density are used to validate computer simulations which model the experimental configuration as well as additional scenarios.

Electromagnetic transmission through the plume is simulated through an innovative application of a ray tracing algorithm. The ray tracing simulations use the electron density functional model as well as a temporal model [Dickens, *et al.* 1995a] of the electron density. The modeling simulates the attenuation measured by the microwave system by quantifying the beam spreading experienced by a wave transmitted through the plume. The phase shift is simulated by comparing the integrated phase with and without the plasma present. Simulations are also implemented which model the temporal nature of the plume. Not only is phase modulation modeled, but amplitude modulation is newly demonstrated through ray tracing modeling. The amplitude and phase modulation simulations compare well with the power spectral density measurements. The simulations are extended down to the frequency limit of the simulation validity in order to provide an indication of the signal impact trends. The amplitude and phase modulation can be significant at 17 GHz, but the effects are greater for the lower frequencies. For transmission at frequencies lower than 3 GHz, greater than 10 dB of loss can occur if transmitting through the core of the plume. Additionally, the phase modulation at the lower frequencies can exceed 90°. The simulations provide a first ever summary of the amplitude and phase effects of transmitting through the center of the plume at a range of frequencies from 100 Mhz to 17 GHz.

8.2 Ion Acoustic Wave Diagnostic Technique for Mesosonic Directed Plasmas

In previous research, ion acoustic wave propagation has been studied extensively in static plasmas and to a limited extent in flowing plasmas. Excitation and propagation have been explored to a new level in this study for high speed moving plasma. The results from

the general characterization are utilized to establish an innovative simple sensor using ion acoustic waves which can measure directed flow velocity, electron temperature, and ion temperature.

In order to explore ion acoustic wave propagation in the plume of a stationary plasma thruster, the amplitude and phase characteristics have been spatially mapped in a region surrounding an excitation source. The wave characteristics have been compared for a number of excitation frequencies and three different plasma species. The results verify the excitation of an ion acoustic wave and are consistent with previous work. In particular, the wake structure in amplitude measurements directly behind the excitation probe is consistent with the results of experiments with cylindrical probes without an excitation signal. However, the expected progression and attenuation of the wake structure does not occur due to the excitation of the ion acoustic wave. In effect, the wake spatially modulates the ion acoustic wave producing a signal interference pattern in the probe-plasma coupling region. This is seen in the ion acoustic wave propagation as far as measurements have been recorded, which is well beyond the physical dimensions of the wake region. This phenomena has not been previously reported.

After exploring general ion acoustic wave propagation characteristics, the probe geometry and excitation levels were investigated in order to determine the sensitivity of the measurements to the exciter and detector probes and also to identify a reasonable experimental configuration. The results indicated a wide range of acceptable conditions. The limitation on frequency is primarily due to two conditions: avoidance of a high noise level in the plasma plume and the necessary spatial resolution to accurately determine the wavelength of the wave through phase measurements. Within the capabilities of the available instrumentation (up to 100 kHz), the higher frequencies are optimal both in terms of the thruster noise characteristics and the higher phase accuracy due to a larger phase shift over the same distance. In addition to the excitation frequency, the voltage excitation levels have been explored. In past work, excitation in the ion saturation region was suggested.

Within this region varying amplitudes and bias levels have been compared. Amplitudes greater than or equal to the thermal temperatures (~4 eV) are required; however, extremely large amplitude signals do not produce unlimited improvement. An optimal excitation amplitude would likely be between ±10 and ±40V; however, due to the limitations of the lock-in amplifier and the desire to maintain simplicity in the system an excitation level of ±5 V was used here. Bias levels have also been explored. This did not affect the coupling efficiency as strongly as the amplitude, but biasing the signal significantly below the floating potential tends to decrease the coupling level. In the work here, to maintain simplicity the signal was not biased since the floating potential has been measured to be above +5V (and up to 15 V). Lastly, experiments also investigated the size of acceptable exciter and detector probes. In general the probes are slightly larger than a Debye length. Probe sizes in the range from 0.2 to 1 mm are found to excite or detect a sufficiently large signal while at the same time minimizing the wake or near-zone region of the plume.

After establishing general probe geometry and propagation characteristics, an innovative technique was implemented to relate the propagation characteristics of an ion acoustic wave to plasma properties that does not require extensive characterization of wave propagation. In particular, the amplitude is mapped for a single constant distance from an exciter to find the extent of the propagation zone. The phase is then recorded at two distances along the flow direction in order to find the total phase velocity of the ion acoustic wave that is superimposed on the flowing plasma. The two measurements provide the sum and the ratio of the ion acoustic wave phase velocity and the directed flow velocity of the plasma. The measurements are implemented using a two-axis linear position table to obtain a spatial mapping of the plasma parameters. Four novel methods are introduced to utilize the information to find flow velocity, ion acoustic wave velocity, electron temperature, and ion temperature. The first method only utilizes the phase measurement to estimate the flow velocity to within 12%. This method assumes a negligible ion acoustic velocity which is the primary source of error in the measurement. The second method, which is later applied

to the data, utilizes both the phase and the propagation zone measurements to find the flow velocity (±5%), ion acoustic wave velocity (±21%), and the electron temperature (±67%) where the ion temperature is ignored in this case. This method provides a good estimate of flow velocity and a reasonable estimate of the ion acoustic velocity; however, the uncertainty in the electron temperature is greater than comparable diagnostics such as the Langmuir probe. A third method evaluates the possibility of finding the ion temperature by utilizing Langmuir probe measurements in addition to the phase and propagation zone measurements. This produces similar results to method 2 for the two velocities, but by using the electron temperature from the Langmuir probe (±10%) the ion temperature is estimated from the ion acoustic wave dispersion relation. The results indicate poor accuracy, only providing an upper bound to the ion temperature, but given the difficulty in finding ion temperature this could potentially provide useful information. The spatial mapping of flow velocity and electron temperature successfully indicates general agreement with past measurements showing only slight variation (within the measurement accuracy) over the measurement region. An additional result of the spatial mapping utilizing the reduced wave characterization format indicates strong wave propagation sensitivity to the plasma parameters in the details of the propagation pattern. However, the limiting characteristics of the pattern (the phase along axis and the propagation zone edge) seemed to be relatively independent of this phenomena.

In the future a number of modifications could be implemented to improve the measurement accuracy and opportunities exist for further exploration of ion acoustic wave propagation. Initially, added dimensional control (degree of freedom) to the probe positioner would enhance both the measurement accuracy and ion acoustic wave study. The added desired positioning flexibility would be the positioning capability to move the detector axially in the same experiment as rotary capability is available. This added capability would allow detailed propagation characterization over a wide range of plasma conditions such as variation in density and density gradients. This detailed characterization

would provide general information about the propagation of the ion acoustic wave as well as increase the analytical accuracy of the diagnostic technique. The detailed wave characterization could provide the basis for a theoretical as well as experimental investigation into the precise details of the wake-wave coupling that would potentially provide information necessary for more accurate interpretation of the propagation zone for plasma characterization.

Additional improvements in signal strength and hence noise level could be attained through more careful optimization of the excitation parameters of frequency, amplitude, and bias level. Implementations could include systems with an alternative lock-in amplifier or use of an integrated precision voltage amplification and bias circuit. An alternative circuit could do real time interferometric phase comparison instead of post processing. All of the suggestions would improve the accuracy of the measurements especially the accuracy of the ion temperature.

This novel ion acoustic wave diagnostic technique has a number of advantages over other techniques. First, the ion acoustic wave diagnostic is relatively independent of the exact nature of the probe-plasma coupling. Second, the analysis is straight forward although precise interpretation of the propagation angle is sometimes difficult. Lastly, the probe experimental setup is compatible with other diagnostic techniques such as a Langmuir probe and resonance probe which accurately measure electron temperature and electron density respectively. Two issues requiring improvement are more accurate determination of propagation zone edge and increased spatial resolution (each measurement point takes the average plasma characteristics for the measurement region).

APPENDICES

APPENDIX A

RESEARCH FLOW DIAGRAM

The flow diagram traces the progression and motivation leading to the research in this dissertation. The diagram starts at the basic question of what propulsion system is optimal for spacecraft and progresses towards the specific issues dealt with in this work where the research opportunities that this work has addressed are designated by a '?'.

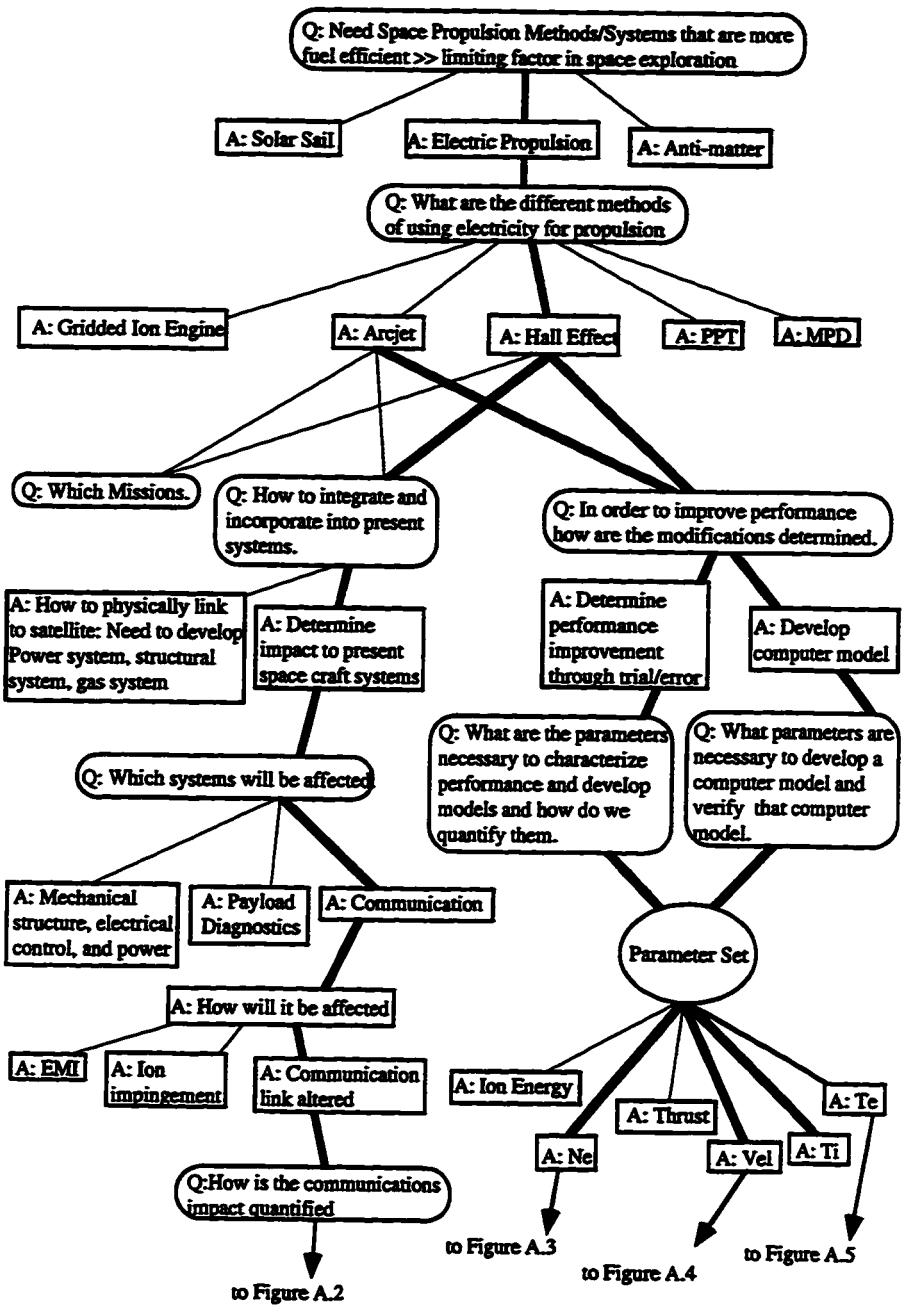

Figure A.1. Main node diagram for research flow.

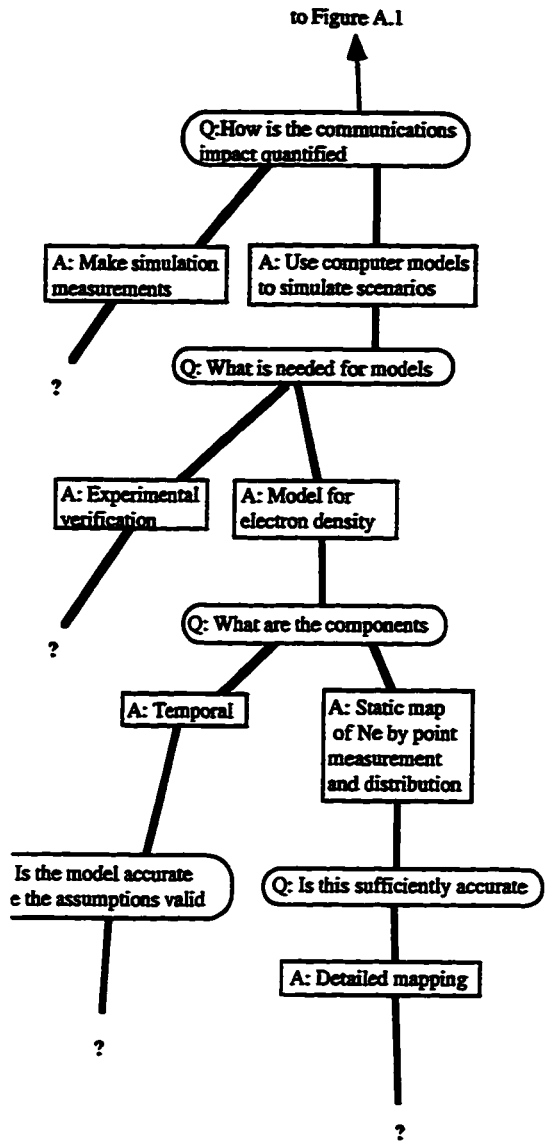

Figure A.2. Flow diagram 2.

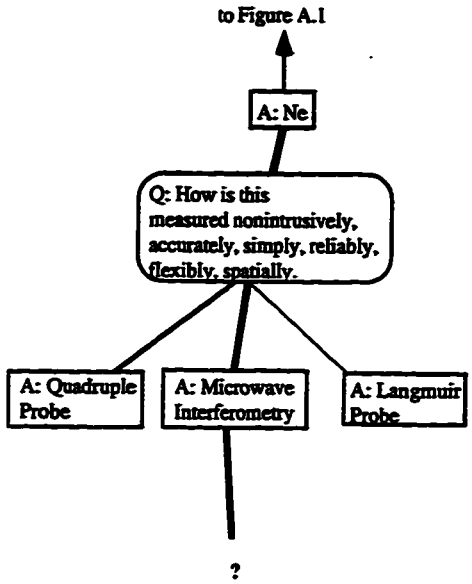

Figure A.3. Flow diagram 3.

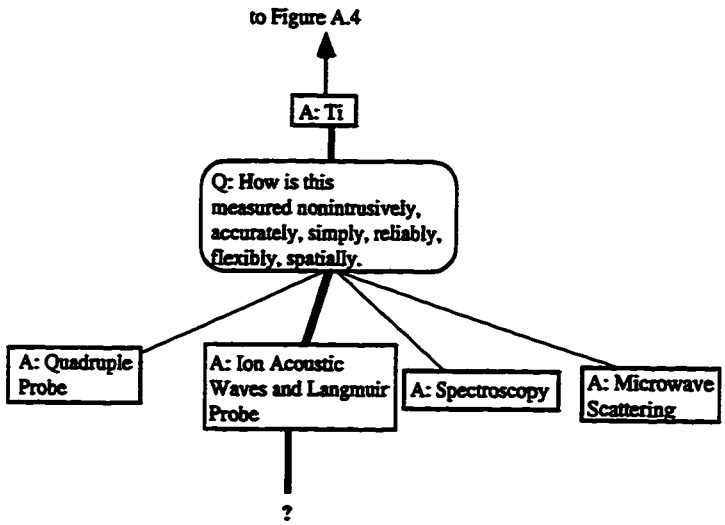

Figure A.4. Flow diagram 4.

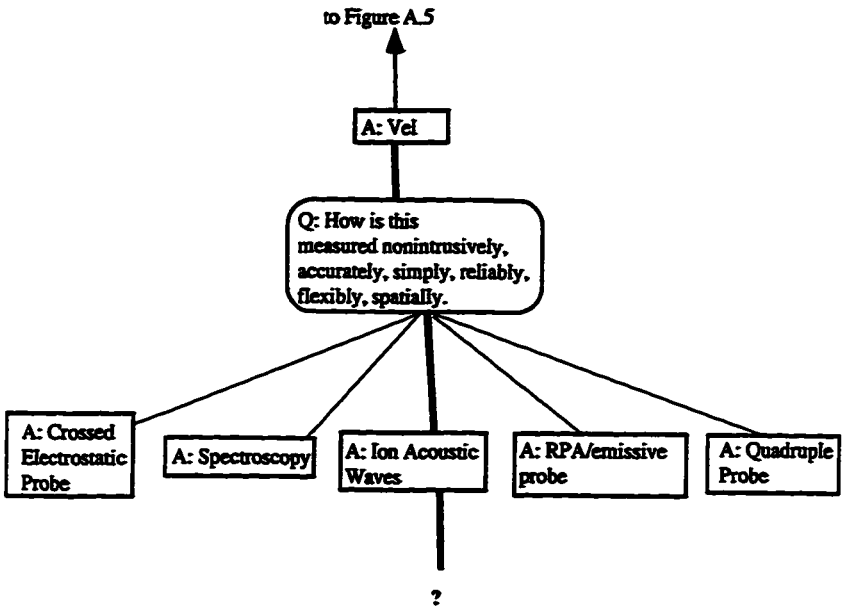

Figure A.5. Flow diagram 5.

APPENDIX B

THRUSTER DESCRIPTION

Three thrusters are tested in this research. The first half of the research relates to microwave propagation arcjet and a stationary plasma thruster (SPT) made by Fakel Enterprises. The second half of the research relating to ion acoustic wave propagation investigates two SPT's, one made by Fakel and the other made by the Moscow Aviation Institute.

An arcjet operates by exciting a plasma discharge by applying a high voltage across the small gap between the anode and cathode. After ionization, the gas expands through the acceleration nozzle similar to traditional chemical propulsion systems. A cross sectional view of the 1 kW-class arcjet shows the critical components (Figure B.1). The engine features a 2%-thoriated tungsten cathode and a nozzle of the same material that serves as the anode. The arcjet has a 0.51-mm-diameter by 0.25-mm-long constrictor, a 30 degree half-angle converging nozzle section upstream of the constrictor, and a 20 degree half-angle diverging section. The exit diameter of the nozzle is 9.52 mm, giving the expansion section an area ratio of 350. The electrode gap spacing is 0.51 mm and the outer housing of the device is constructed of titaniated zirconiated molybdenum (TZM).

The arcjet is operated by using primarily a hydrogen propellant with a flow rate of 10 standard liters/minute (15 mg/s). The plasma discharge operates at 110 V and 10 A. During the tests, chamber pressure is maintained below 2×10^{-4} Torr. A photograph of the thruster plume is shown in Figure B.2.

The arcjet has been studied extensively as evidenced by numerous articles concerning arcjets [Gallimore, *et al.* 1994; Zana, 1987; Sankovic, *et al.* 1991; Riehle, 1995; Polk, 1991; Pencil, 1993; Toulouzan, 1986; Hoskins, *et al.* 1992; Goodfellow,

1995; Butler, *et al.* 1995; Bufton, *et al.* 1995; Coutrot, *et al.* 1995; Carney, *et al.* 1989a, *et al.* 1989b; Cassady, 1991, 1995; Curran, *et al.* 1992].

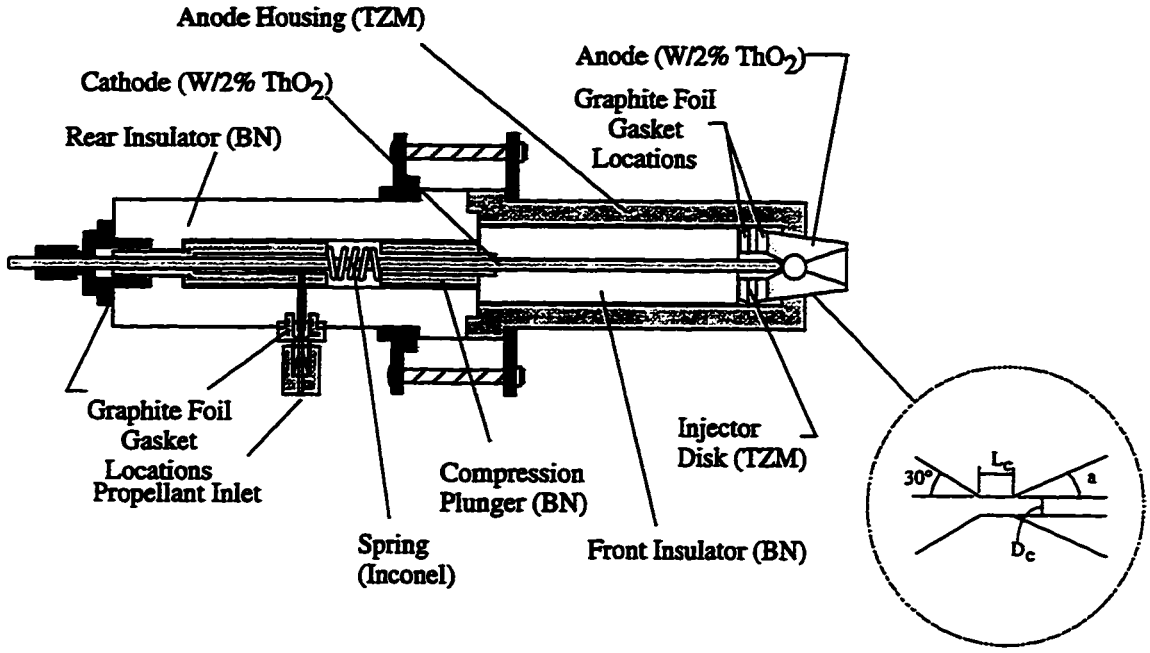

Figure B.1. Arcjet schematic.

Figure B.2. Plume of an arcjet.

An SPT, in general, operates through utilization of a radial magnetic field and an axial electric field (Figure B.3). The radial magnetic field is formed by inner and out magnetic poles. The magnetic field serves to contain and control the cloud of electrons emitted by the cathode. The cloud of electrons at the exit plane and in the discharge region of the thruster ionizes the propellant emitted around the anode. After ionization, the electric field between the anode and cathode that is along the axis of the thruster accelerates the ions to produce the propelling force [Sankovic, *et al.* 1993, Garner, 1993; Kaufmann, 1983]. A picture of an SPT on a thrust stand is shown in Figure B.4 and the plume is shown in Figure B.5.

The primary thruster, a Fakel stationary plasma, is a commercial grade SPT-100 built by the Russian Fakel Enterprises presently on loan from Space System/Loral and previously tested by a number of individuals and organizations [Myers 1993; Manzella, 1994, 1993, *et al.* 1995; Absalamov, *et al.* 1992; Garner, *et al.* 1993, *et al.* 1985; Brophy, 1992; Gallimore, *et al.* 1996; Ohler, *et al.* 1995, *et al.* 1996; Dickens, 1995, *et al.* 1995a, *et al.* 1995b; Day, *et al.* 1995; Kim, *et al.* 1996; Pencil, *et al.* 1993; Sankovic, *et al.* 1993]. The inner diameter of the outer ceramic ring is 0.1 m and the cathodes are flight model LaB_6 thermionic emitters. This thruster is a flight model and is controlled by an engineering model of the PPU. The SPT thruster is operated with Xenon gas propellant with minimal user control of the operating parameters in the present configuration (the only user defined parameter is the flow rate through an MKS flow meter). The thruster nominal conditions are 300 V anode-cathode potential, 4.5 A discharge current, 5.0 mg/s Xe to the anode, and 0.56 mg/s Xe to the cathode.

The second thruster, is also an SPT-100 type thruster, but is a lab model SPT on loan from the Moscow Aviation Institute (MAI). This thruster is similar to the Fakel thruster but does not have refined conditions for flight qualification status in terms of the materials and operating. Again the inner diameter of the outer ceramic ring is 0.1 m, and the cathode is a laboratory model LaB_6 thermionic cathode. The anode and cathode flow

rates are independently controlled through MKS flow meters. This thruster is operated with either argon, krypton, or xenon propellant with flow rates 2 to 5 mg/s for the anode, 0.3 to 0.8 mg/s for the cathode. The thruster electrical inputs are manually controlled with laboratory power supplies. The electrical inputs include the potential applied to the anode, cathode, and ignitor and the current applied to the heater and inner and outer magnet coils. A range of operating conditions existed for the electrical parameters. The cathode-anode discharge potential is between 120 and 310 V with a discharge current of 3 to 5 A. The ignitor is floating during operation with a potential between 15-1000 V necessary to ignite the discharge. The heater current is 8 A, and the inner and outer magnets are set to between 2 to 4 A.

Many studies exist on stationary plasma thrusters aside from those already mentioned some of which include Kim, 1995, Kim 1995, Marresse, *et al.* 1995; Chourerri, 1994, Bougrova, Ashkenzy, 1995; Peterson, 1985, Szabo, 1995, Yamaguvia, 1991.

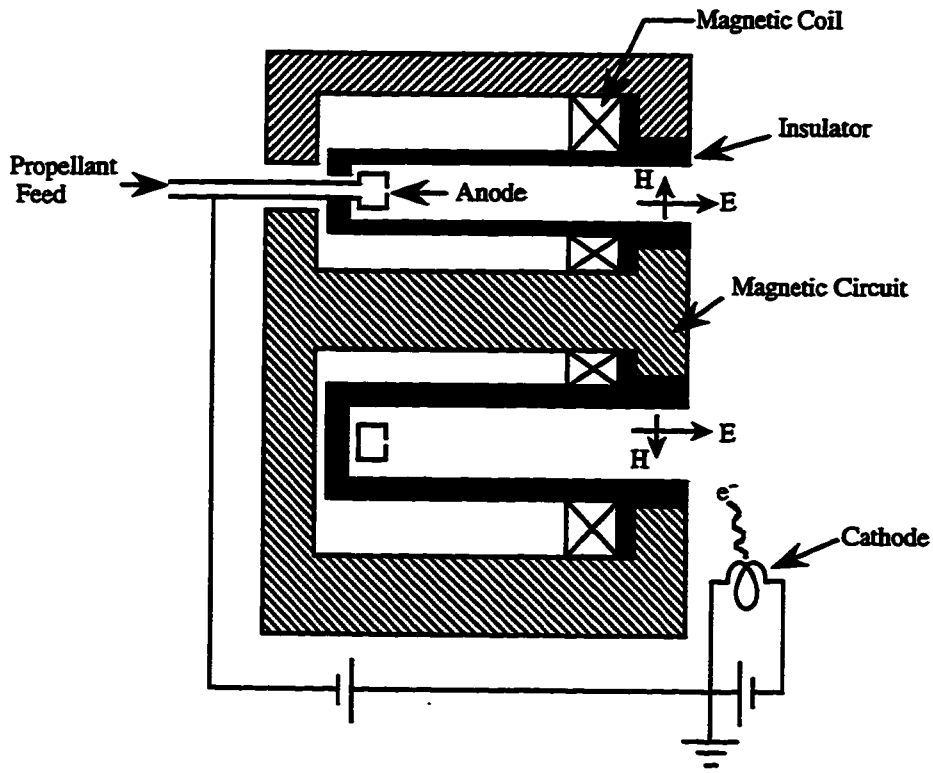

Figure B.3. Stationary plasma thruster schematic.

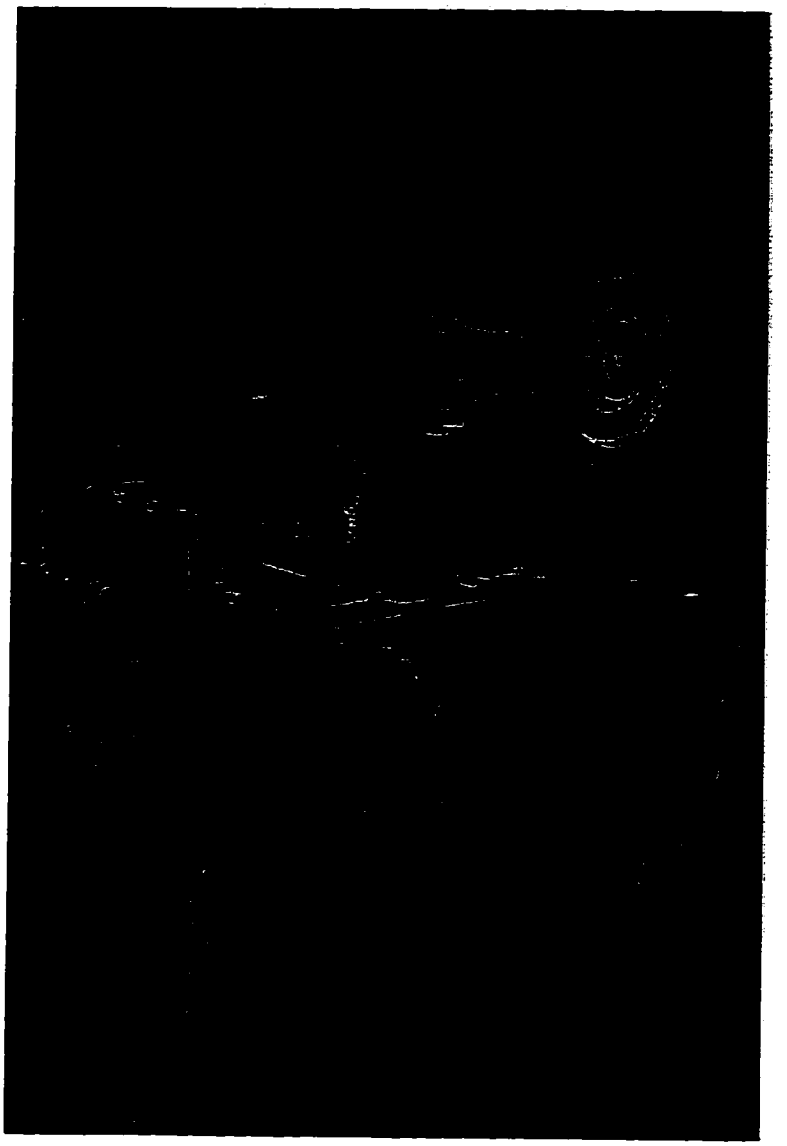

Figure B.4. Photograph of a stationary plasma thruster.

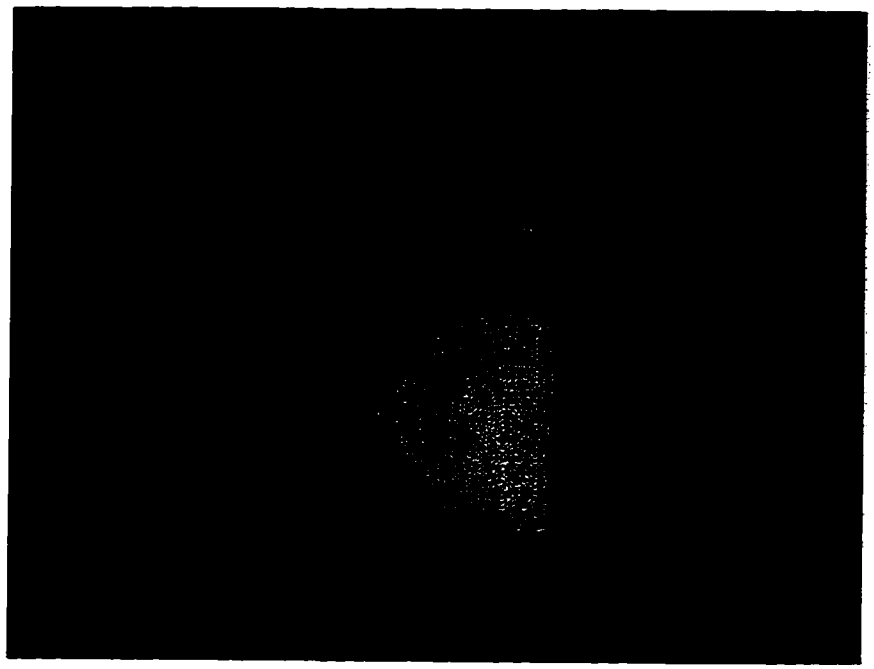

Figure B.5. Plume of an SPT.

APPENDIX C

MANUAL FOR IMPLEMENTATION OF MICROWAVE INTERFEROMETER

Overview

The following discussion focuses on the implementation of a microwave interferometer; however, measurements of amplitude with the network analyzer and power spectral density with the spectrum analyzer are a straight forward extension of the process. For amplitude, do baseline measurements for amplitude and record amplitude instead of phase during plume characterization. For power spectral density, connect the spectrum analyzer to the return signal and record traces from the spectrum analyzer.

The manual is divided into two parts: an experimental guide and an analysis guide. The experimental guide covers testing of the microwave system, installation of the system, and implementation of a phase shift (density) characterization. The analysis guide reviews the theory behind microwave interferometry, discusses Abel inversion and two methods of implementation, and includes computer code to implement an analysis to find electron density from phase measurements.

Part 1: Experiment Guide

The first section describes the general system configuration, functional role of the components, and baseline noise characteristics. This information is also found in Chapter 2 of the thesis and in Ohler [to be published in *Review of Scientific Instruments*]. The second section discusses testing of the microwave system outside of the vacuum chamber and assembly of the system inside the vacuum chamber.

General Component and System Description

The Ku-band (12-18 GHz) microwave measurement system is composed of five primary components: the positioning system, support structure, the antennas, the frequency up-down conversion circuit, and the network analyzer. The network analyzer is essentially a highly sensitive heterodyne quadrature receiver. All of the components in Figure C.1 and C.2 are placed in a vacuum chamber except the network analyzer. In the chamber, the positioning system moves the support structure. The support structure holds the antennas, connecting coaxial cable, and conversion circuit. The conversion circuit is connected to the network analyzer through 15 m of flexible coaxial cable.

A state-of-the-art positioning system provides the capability to spatially map plume parameters. The system is driven and monitored with a computer. The positioning system is mounted on a movable platform to allow for measurements to be made throughout the chamber. The positioning system contains two linear stages with 0.9 m of travel in the axial direction and 1.5 m of travel in the radial direction. The axial direction, shown in Figure C.1, is along the axis of the thruster. The radial axis indicates the direction orthogonal to the plane created by the thruster axis and the microwave transmission direction.

The steel support structure for the frequency conversion circuit, coaxial cable, and antennas is attached directly to the radial stage of the positioning table. The conversion circuit has been attached to the supports via a copper mounting plate which provides effective heat sinking. Semi-rigid coaxial cable attached to the steel supports connects the circuit to the horn antennas. The antennas are separated by 1.65 m and configured to transmit vertically through the plume. In addition to measurement components, graphfoil is used when necessary in order to minimize sputtering of the support structure.

The horn antennas, which use dielectric lens correction, generate a narrow beam that transmits the signal through a narrow section of the plasma. The antennas are designed to minimize overall size while maintaining high gain. The antenna lens was designed so

that its focal point was aligned with the phase center of the horn antenna, and then experimentally optimized to maximize power transmitted between the horns. The antennas have full angle half power beam widths between 7° and 8° and approximately 25 dB gain for both the *E*-plane and the *H*-plane. Another antenna characteristic is that they exhibit negligible phase sensitivity to nearby dielectric or metallic scattering sites outside of the line-of-sight between the antenna structures. This fact indicates that the transmitted signal is essentially limited to a collimated beam 0.13 m in diameter (dimension of antenna). The antenna beam distribution will be addressed again in the next section in the discussion on calibration.

The frequency conversion circuit is utilized due to the long distance between the network analyzer outside of the chamber and the antenna system inside the chamber. The long distance produces unacceptable power loss and phase accuracy degradation when the Ku band signal is transmitted directly through the 15 m of coaxial cable necessary to connect the network analyzer to the antennas.

The circuit in Figure C.3 receives a low frequency (1 to 3 GHz) signal from the network analyzer, chooses the upper or lower side band, transmits the signal to the antennas, receives the signal from the antennas, down converts to 1 to 3 GHz, and finally amplifies the power. The low frequency signal, 1 to 3 GHz, is converted to the Ku band via a mixer using a 15 GHz phase locked dielectric resonator oscillator. The oscillator supplies a reference signal to both the up and down mixing sides of the circuit thereby minimizing oscillator frequency drift and phase noise effects. The signal is guided by the power divider, isolators, and band pass filter 2. The isolators and band pass filter 2 limit the effects of low-frequency signal leakage and reflection. The signal from the mixer includes both upper and lower side bands either of which is available for use. The desired side band is chosen by band pass filter 1. The upper side band (16 to 18 GHz) is available with the present configuration. The circuit transmits less than 0.1 mW through the plume

to the receive antenna. The received signal is then down-converted, amplified, and transmitted via coaxial cable back to the network analyzer.

This measurement system utilizes the capabilities of a network analyzer as a stable microwave source and highly sensitive heterodyne quadrature receiver in order to obtain post-processing interferometric phase information. The network analyzer and the local oscillator are independently phase locked providing a stable signal both in phase and amplitude. The independence of the phased locked oscillators is not a problem since the phase of the conversion circuit is both inserted and removed from the signal during up and down conversion. This up-down frequency conversion scheme also allows the use of a much less expensive lower frequency network analyzer. Additionally, network analyzers can isolate the test signal through the use of standard time gating techniques when the frequency is swept over a sufficiently wide band width (see network analyzer's user manual).

General baseline characteristics provide information necessary for proper interpretation of measurements from the microwave system. Two measurable quantities, amplitude and phase, are characterized in terms of random noise and signal drift. A calibration function was developed to characterize the antenna propagation distribution through the use of a well known dielectric sample. The microwave noise and system noise should be characterized for each experiment to verify system operation since the noise levels will depend slightly on the exact implementation. (Particularly the system noise which is dependent on the vibrations of the table that vary from day to day.)

The amplitude and phase noise result primarily from slight variation in the microwave signal from the network analyzer and vibration of the support structure causing variation in transmitter-receiver alignment. The noise level in the network analyzer is specified by the ratio of the return signal to the transmitted power level. The power ratio is -20 to -25 dB indicating network analyzer noise to be $\pm 0.5°$ and ± 0.2 dB. The received test signal at the analyzer is 20 to 25 dB below the transmitted signal from the analyzer

resulting in an amplitude and phase of ±0.2 dB and ±0.5°, respectively. Mechanical vibration was found to introduce an additional ±1.0° resulting in final system level noise performance of ±0.2 dB and ±1.5°.

The drift in the signal is primarily caused by temperature changes in the components of the system: local oscillator, amplifier, mixer, and coax cable. The temperature of the circuit plate has been monitored in order to establish temperature induced drifts over time. In general, the circuit plate temperature increases 30 °C from ambient room temperature over the course of an initial 5 hour period resulting in signal drift. The total steady state drift was found to be less than 0.08 °/min and 0.06 dB/min which is corrected in post processing.

An antenna calibration function was found to remove effects of finite antenna size. This is done by first calculating the theoretical phase shift through a foam cylinder and then comparing the theoretical results to the measured phase shift across the same cylinder. The theoretical calculation of phase shift for the cylinder is given by:

$$\Delta\phi_{theory} = \frac{180}{\pi}\frac{2\pi}{\lambda}(n-1)\left(R^2 - x^2\right). \qquad \text{•C-1}$$

In the equation, $\Delta\phi_{theory}$ is the phase difference between a wave transmitted through free space and transmitted through the cylinder (degrees), λ is the wavelength (meters), n is the index of refraction, R is the radius of the cylinder, and x indicates the displacement of the transmission path from the center of the cylinder (meters). The index of refraction of 1.08 was estimated from the peak of the experimental results. This estimation does not affect the final conclusion concerning the effect on the measurement of local electron density.

The calibration function FN relates the theoretical, $\Delta\phi_{theory}$, and experimental, $\Delta\phi_{Exp}$, phase mathematically by:

$$\Delta\phi_{Exp}(x) = \Delta\phi_{Theory}(x) * FN(x) \qquad \text{•C-2}$$

$$FN = \frac{1}{\sqrt{2\pi}\sigma}\exp\left[-\frac{1}{2}\left(\frac{x}{\sigma}\right)^2\right]. \qquad \text{•C-3}$$

The distribution function is spatially convolved with the theoretical phase (Equation. C-1) to arrive at the measured results. The assumed Gaussian distribution function, FN, was optimized by varying the standard deviation, σ. An optimal value of σ equal to 0.024 m was found by minimizing the difference between the left and right sides of Equation C-2. The full width half maximum of the distribution function, which we take as a measure of system resolution, indicates the resolution of the system is 2.36σ or 0.057 m. With this transfer function the effects of the finite size of the antenna beam are removed from the plasma measurements.

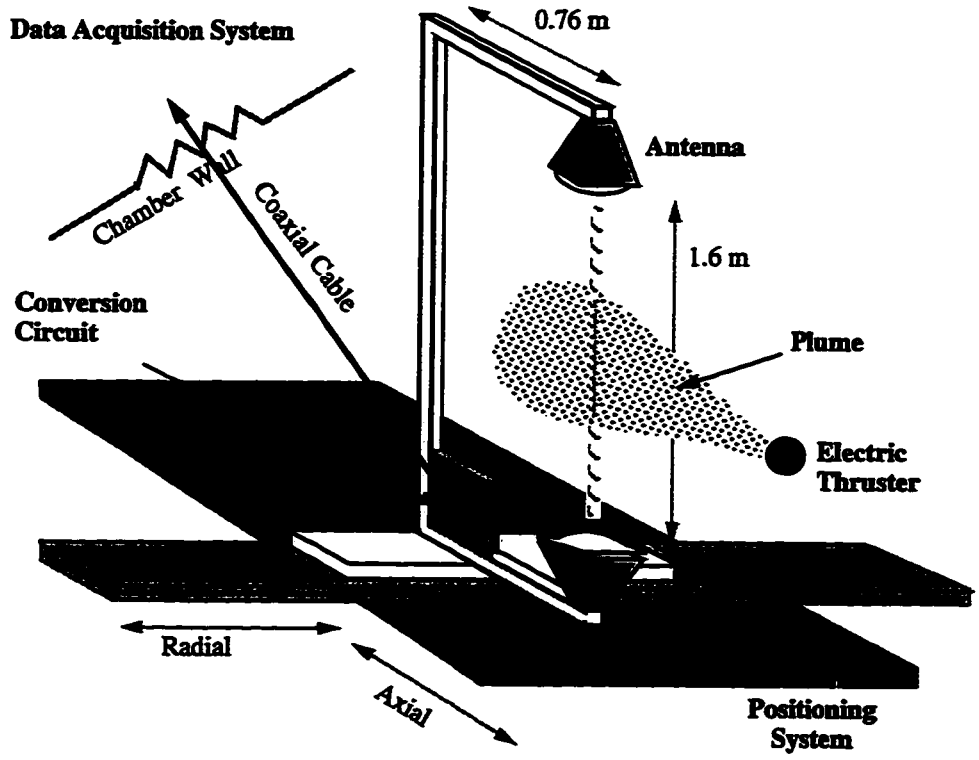

Figure C.1. Schematic representation of microwave interferometer.

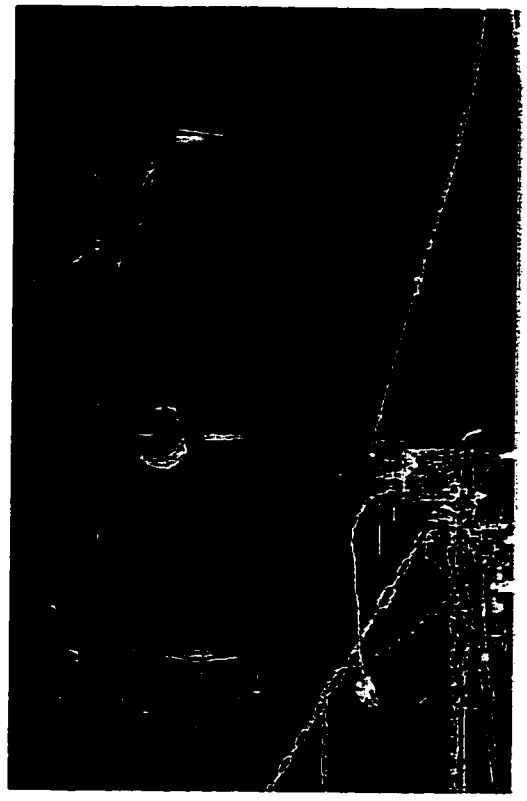

Figure C.2. Photograph of microwave interferometer system.

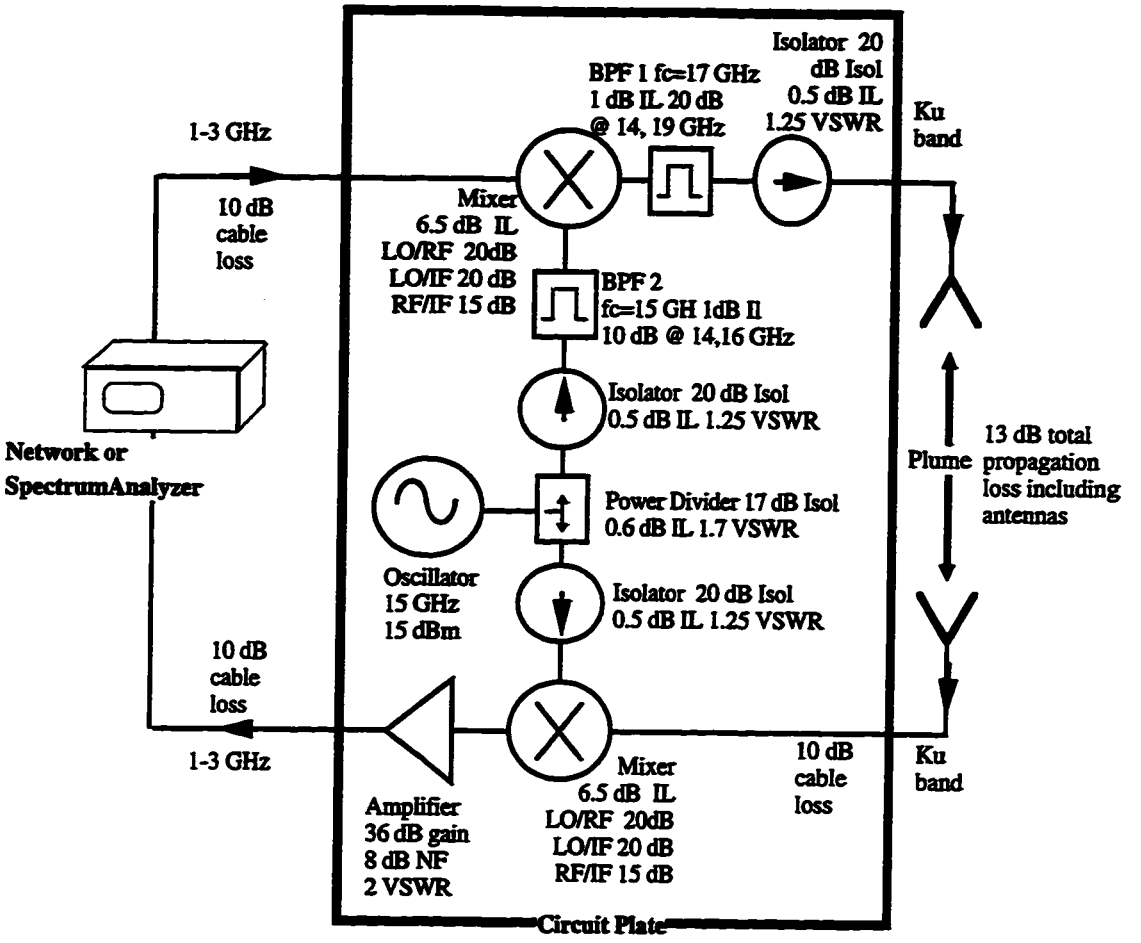

Figure C.3. Circuit diagram for frequency conversion.

Testing and Assembling the System

Testing Prior to Assembly

The microwave system is robust and will work if care is taken with the components; however, a number of the components will break if not handled carefully. As a side note, some components are not fragile, but continual exposure to the thruster plumes degrade their characteristics. In particular the dielectric lens and the coaxial cable will eventually need to be replaced due to degradation by the plume.

In all cases the microwave connectors (SMA's) should be handled carefully. Most are specified to a limited number of connections; therefore, a connector saver (male-female adapter) should be used on the critical connectors that cannot easily be replaced: the flexible coaxial cable connectors, the feed-throughs, and circuit component connectors. Additionally, the connectors should be finger tightened (sometimes the threads do not line up exactly, be aware of this and avoid stripping the threads by forcing the connection) then tightened slightly with a wrench. For microwave level repeatability a torque wrench (the correct one not just any torque wrench) should be used. One component needing special care is the copper hard-line (this is actually considered semi-rigid since it will bend) that attaches to the support structure. The copper coax should not be bent if possible although slight bending is permissible in order to fit it to the structure and make connections. The connectors on the copper coax are particularly susceptible to breaking (twisting off) if they are not connected carefully. Additionally, the circuit components (amplifiers and oscillator) should not be over powered, overheated, or turned on with a step voltage (turn on the voltage gradually). The amplifiers should be powered with 15 V and 90 mA each and the oscillator requires 20 V and 280 mA. The voltages should be stabilized by two voltage regulators. (See the description on operation and testing for more information about powering the microwave circuit.) Turning on the power slowly will also allow observation of the settling of the system signal and provides a good indication of correct system operation.

Prior to assembling the microwave system in the vacuum chamber some of the components can easily be tested and with a little effort the system can be tested as a unit. The primary components that can be tested individually are the coaxial cables, the circuit, and the antennas. Each of the three components can be tested with the HP8753D network analyzer except the antennas (which requires a higher frequency network analyzer; however, the antennas usually do not need to be tested and can be evaluated in the system level testing.

The coaxial cables can be tested and verified to have minimal reflected power (S11 or S22), on the order of ~-40 dB or less. When testing the reflected power, the coaxial cable can be terminated by either hooking both ends of the coaxial cable to the network analyzer or putting a matched load on one end. To test the semi-rigid line, one of the flexible cables should be tested first, then the flexible cable can be used to connect the semi-rigid line to the network analyzer. The semi-rigid line should exhibit losses of 11.6 dB/100 ft at 1 GHz and 62 dB/100 ft at 18 GHz. The flexible cable should exhibit losses of 20 dB/100 ft at 2.5 GHz and 75 dB/100 ft at 18 GHz.

The circuit can be tested as a stand alone unit by connecting the two RF (high frequency) ports together with a section of flexible coaxial cable. In order to know which connectors correspond to which ports in the circuit, the circuit diagram presented earlier in this manual can be compared to the circuit after taking the cover off. The ports should be marked so that the cover does not need to be removed multiple times during installation in the chamber. The two low frequency ports should be connected to the network analyzer. The network analyzer should be set to sweep over the range from 1 to 3 GHz with a power output that will produce a 0 dBm signal at the input to the mixer. The measurement of cable loss and the loss estimates on the circuit can be used to determine appropriate network analyzer power (to be safe, set the network analyzer power to 0 dBm so that the mixer cannot receive more than 0 dBm). A single connection is used to power two voltage regulators which supply power to the oscillator and two amplifiers. The voltage should be gradually turned on to ~22 V and the current should rise to ~500 mA. The current will not rise linearly, but it should reach a saturation value. The current should be monitored closely when first applying voltage to check for a short in the system (it is easy to hook the power up backwards). Also, when applying the power to the circuit, if the current does not rise, the power connections and power cable should be verified for continuity then the voltage regulators should be checked for correct operation (this will probably require taking the

cover off of the circuit). Before powering the circuit, calculate the expected received power (S21 or S12) for the network analyzer.

After verifying the operation of the circuit, the antennas can be tested alone with a high frequency network analyzer or in the total system test. A total system test can be implemented outside the chamber by assembling the microwave components (as discussed in the next section) on the stand that stores the support structure. The total system power and noise level should be verified. The expected power level can be determined by using the measured cable losses, the circuit values in the previous section, and calculated propagation loss (through the Friis transmission formula). If possible the system setup should come as close as possible to the system in the chamber. Differences primarily will be in the flexible coaxial cable and the alignment of the antennas (which will not be as precise outside the chamber).

Assembling the Microwave System in the Vacuum Chamber

All of the components of the microwave system can be easily taken into the chamber except the support structure which requires entry through the large door. The base should be taken into the chamber along with the support structure so that when the experiment is complete the support structure can be removed from the table and kept in the chamber (if the large door is difficult to open at that particular time). Before placing the support structure on the positioning table, verify the operation of the table. Also before placing the support structure on the positioner, one rotary will need to be removed for the test, and the other will need to be removed temporarily. The weight of the microwave system tends to stress the positioner; therefore, re-lubricating the positioner screws might prevent problems with the table during testing. Placing the support structure on the positioner requires at least two people to lift the structure and one to balance the structure while the second person attaches the structure to the positioning table. The support structure is attached to the positioner in two places. The main attachment point is directly to

the top of the radial table where one of the rotaries was attached. The support structure should be positioned as far to one side as possible to make the cross piece connection point as far away as possible (better mechanical support). The lower horizontal piece is attached using two unistrut flat two hole joints and four bolts (not unistrut bolts). The unistrut joints are placed in the slots on the radial table. The bolts are difficult to tighten, but a secure joint is critical to minimize vibration. The second point of attachment is the diagonal cross piece which attaches to the other end of the radial table by a bolt which connects the cross piece and the radial table slot. The second radial table cannot be in position when placing the bolt, but can be returned after the connection is made. Make sure all unistrut bolts on the support structure are tight. Some might have loosened while moving the structure.

After attaching the support structure to the positioning table the microwave system can be assembled on the support structure. Start by attaching the circuit vertically to the support structure. The cover will need to be removed to do this. After attaching the circuit and replacing the cover, attach the antennas to the upper and lower supports. Then connect the hard-line from the circuit to the two antennas using the plastic support loops if possible. Next, attach the flexible microwave cable and power cable to the circuit and the chamber feed-throughs. Currently, the power connection uses a BNC coaxial feed-through. The cables should use strain relief on the support structure and should hang from the cable loop to prevent interference with the table (the table should be moved to different positions to verify that the cable will not be caught by the table). Feed-through on the end cap or the side of the chamber can be used for the microwave connections. Verify the chosen feed-throughs for good microwave characteristics (low losses).

After assembling the microwave system on the support structure, align the antennas so that the apertures line up. A level and a string with a weight on the end should be sufficient to align the two antennas. Accurate alignment is important to maximize the transmitted power since the antennas have narrow beam widths (slight misalignment can

significantly reduce power). Aligning the antennas could require a number of adjustments: modification of the attachment of the diagonal support beam, shimming the antenna at the attachment point to the unistrut, or bending the antenna joint slightly (be careful not to break the joint).

At this point, the microwave system operation should be verified by connecting the network analyzer and power supply to the feed-throughs outside the chamber. Verification can be implemented as described in the last section. In addition, an experiment can be implemented to partially block and fully block the transmission beam to further verify operation. Also, the time domain signal should be examined to verify or identify spurious reflections. All ambient levels should be recorded for comparison with measurement during testing while under vacuum.

The final assembly step is to cover exposed components with graphfoil. This is especially important in the SPT plume to minimize sputtering. The following surfaces should be covered: unistrut support, flexible coaxial cable, circuit box, and the exposed side of the antennas. The front of the antennas (the dielectric lens) should not be covered as this will inhibit transmission. After complete assembly, the positioning system should be calibrated to find the microwave system relative to the thruster.

Implementing the Microwave Interferometer

Using the microwave system to characterize phase (and electron density) requires the use of the microwave system, positioning system, and data acquisition system. The microwave system operation has been discussed. The positioning system is required to move at a constant speed across the entire length of the radial table. (In this implementation, a constant velocity positioning is implemented. Lastly, the data acquisition system needs to record phase from the network analyzer while the system is moving. An alternative implementation to the constant velocity approach would be to move to each position, wait for the vibration to damp, and take data while the system is not moving. The

constant velocity option is implemented due to the length of time required for damping of the oscillations that are produced by starting and stopping.

Before recording plume data a baseline characterization should be completed. A number of measurements should be recorded in order to fully understand the results. Initially, the phase should be recorded at one position to quantify the microwave system phase noise (or amplitude noise). Then the phase should be recorded during multiple radial sweeps at the same speed that will be used in the plume characterization. This will provide the phase noise due to the system vibration. The phase should also be recorded over a long period of time (30 minutes) to quantify the phase drift. In addition to the initial calibration, post experiment calibration should also estimate the phase drift.

After pre-calibration, the plume can be characterized. The system should sweep in planes of constant axial distance from the thruster at a constant velocity (~0.5-1 cm/s). The velocity and acceleration should be chosen to produce sufficiently small increase in the phase noise due to vibration. The vibrations induced by the positioning system will vary depending on the table operation (which could change from day to day). Some method needs to be implemented which will provide the capability to match positions with data points. One method is to mark the start time and end time, assume a constant velocity, and interpolate the data positions from the two end points. A second method is to time stamp the phase data and the positioning data. This method is good in theory, but limitations with LabView prevent effective automation of matching position with data; in particular, time stamping is only accurate ±2 s. A last method would be to communicate between the positioning VI and the data acquisition VI for the network analyzer; however, this method has yet to be implemented. At this time, accurately matching the data with position in post processing is time consuming.

The phase measurements should characterize the plume in a number of planes. After characterization, a basic phase calibration should be done while transmitting through the plume. Phase noise should be determined by taking phase measurements for a few

minutes in one place and then completing multiple sweeps across the same plane to verify the repeatability of the technique. One caution concerning experiment time frame is that over time the circuit tends to heat up. For experiments longer than a few hours, the temperature and operation of the system should be monitored closely.

Part 2: Analysis Guide

The phase shift of a wave is the phase difference between a wave traveling through the plasma and a wave traveling through free space. The phase shift is related to the line integrated electron density of the plasma along the propagation path. The line integrated density is used to find local electron density through the technique of Abel inversion. Then, the inversion integral is implemented through two methods: (1) assuming an analytical expression for the phase shift, and, (2) transformation of the Abel integral using the Hankel and Fourier transforms.

The phase delay difference of two waves relates to the propagation path difference. By reducing the path difference to only the path difference due to the presence of the plasma, the plasma density is directly related to the phase difference through Equation C-5.

$$\Delta\phi = \phi_{vacuum} - \phi_{plasma} = \frac{\omega}{2cn_c}\int_{s_1}^{s_2} n_e(x,z)\partial s \qquad \text{•C-4}$$

The derivation of this equation utilized the phase transformation for a vacuum and a plasma, and it assumes that the electron density is much less than the critical density at 17 GHz.

A single measurement is of phase difference or integrated electron density; however the local electron density is of greater interest. In order to find local density, a series of

spatial measurements as in Figure C.4 are recorded where the final measurement is of free space.

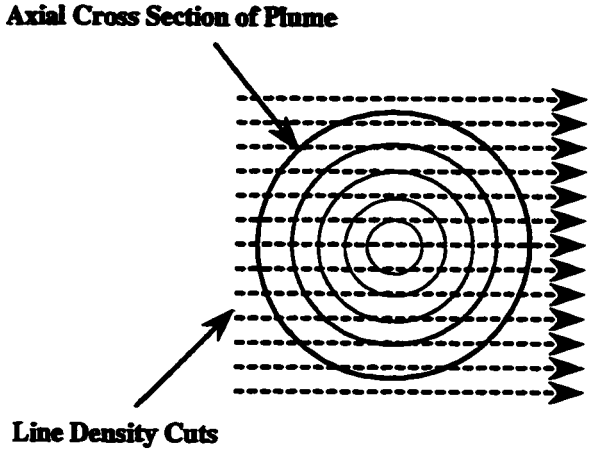

Figure C.4. Schematic of measurement rays for a cross section.

The spatial map of the line integrated density (phase shift), Equation C-5 is mathematically manipulated through Abel analysis into Equation C-6 by assuming radial symmetry.

$$n(r) = -\frac{\lambda n_c}{\pi^2}\int_r^R \left(\frac{\partial\phi(x)/\partial x}{\sqrt{x^2-r^2}}\right)dx \qquad \text{•C-5}$$

The assumption of radial symmetry is well justified in most thrusters. Physically, the integral starts at the edge of the plasma (r=R) where the permittivity of free space is known. The integral incrementally adds the affect of the plasma progressing inward to the desired radius using the incremental change in the phase which is proportional to the density increment.

The implementation of the Abel integral is not straight forward due to the derivative of the data and the pole at the integral end point. Two alternatives are implemented with different advantages. The first implementation which is used for the arcjet measurement,

uses an analytical fit to the raw data that closely matches the trends in the measurements. This option provides an analytical solution; therefore, eliminating any issue with the derivative or pole. This also provides greater flexibility in the measurement if the positioning system cannot move sufficiently out of the plasma. This method is simply implemented by choosing a reasonable functional form for the phase data (such as a Gaussian), and analytically doing the Abel integral to find local density.

The second option which is used for the SPT-100 measurements is to mathematically remove both the derivative and the pole through a Fourier transform and a Hankel transform:

$$n_e(r) = 2\lambda n_c \int_0^{+\infty} qJ_o(2\pi rq) \int_{-\infty}^{+\infty} \phi(x) \exp(-j2\pi xq) dx dq \quad \text{•C-6}$$

This method removes the assumption of a functional form and also provides a convenient step in which to low pass filter the raw data after the Fourier transform; however, this method requires a complete spatial mapping of the phase into a free space region. The computer implementation of the Abel inversion of Equation C-7 is included for reference.

Computer Code for Microwave Interferometry

The following four subroutines which are implemented in MATLAB are the basic algorithm necessary to take phase and position data to find local electron number density. The first subroutine creates a table lookup file for Bessel functions necessary in the Hankel transform. The second subroutine implements the deconvolution of the antenna pattern function, takes the Fourier transform, and applies a filter. The third subroutine uses the data from subroutine 2 and takes only the data from the long side (with respect to the radial axis) of the data set which will be used in the last subroutine. The last subroutine takes the Hankel transform and finds the local electron density for a cross sectional plane of the plume.

```
% this subroutine creates a lookup table for the Bessel function values
% needed in the Hankel transform


clear;

M = 1000;
Mfilterlim = 200;
for n2 = 1:1:M./100
        for n1 = 1:1:100
                n = n1*n2;
                ind = (0:1:Mfilterlim-1).*2*pi./M.*(n-1);

                bessfn(n1,:)=bessel(0,ind);

        end;
        eval (['save bessfiles3/bessval.f' int2str(n2) ' bessfn -ascii -tabs']);
n2

end;
```

```
% this subroutine does the deconvolution, Fourier transform, and low pass filter

trialnum = 0; %input('trialnum ');

for filenum = 1:filenummax
filenum

scale =0.5;

        % load in the phase and radial position pairs in two column format
        % the phase should be for an entire radial sweep

eval(['load phase1/trial' int2str(trialnum) '/phdata' int2str(filenum) ';']);

eval(['pos = (phdata' int2str(filenum) '(:,2)-41.5).*2.54;']);
eval(['data=phdata' int2str(filenum) '(:,1);']);

data = data - min(data);
len =length(data);
buff=zeros(len+99,1);
phase=buff;
phase(50:length(data)+49)=data';

%antenna calibration function

sig= 2.4017212e+00 ;
fnincr=(-14:1:14)*scale;  %row
fn = scale .* exp((-fnincr.^2)./(2*sig.^2))./(sqrt(2*pi)*sig);

columns = length(phase)-length(fn)+1;
rows = length(phase);
fnmat = zeros(columns,rows);
clear tempfnmat;

for count =1:length(phase)
        tempfnmat(count,count:count+length(fn)-1)=fn;
end;

fnmat = tempfnmat(:,length(fn):length(tempfnmat)-length(fn)+1);


% this step does the deconvolution in matrix format
answ = fnmat\abs(phase);


% this step combines the Fourier transmform and the low pass filter

frqansw = fft(answ);
```

```
lenansw = length(answ);
cutoff = .1*scale*lenansw;
buff = zeros(lenansw-cutoff*2,1);
filtansw = frqansw;
filtansw(cutoff:length(buff)+cutoff-1)=buff;
newansw = abs(ifft(filtansw));


[val,valind]=max(newansw);
index = [-valind:1:length(newansw)-valind-1]*scale;

temp=[index' newansw];
eval(['save data/' datestr '/phase2/trial' int2str(trialnum) '/decph' int2str(filenum) '
        temp -ascii -tabs;']);


end;
```

```
% this subroutine assumes that the peak phase is the center of the plume
% then take the phase data for the longer side of the data set (longer radially)
% to use for the hankel transform


trialnum = 0 ; %input('trialnum ');

for filenum = 1:filenummax

eval ([data/' datestr '/phase2/trial' int2str(trialnum) '/decph' int2str(filenum) ';']);

eval (['phdata = decph' int2str(filenum) ';'])

lenind = length(phdata);
[temp,centind] = max(phdata(:,2));

if lenind./2 > centind
        halfdata = phdata(lenind:-1:centind,:);
else
        halfdata = phdata(1:centind,:);
end;

lenhalf = length(halfdata);
phset = zeros(lenhalf*2-1,2);
phset(1:lenhalf,:)=halfdata;
halfdata(:,1)=-halfdata(:,1);
phset(lenhalf:lenhalf*2-1,:)=halfdata(lenhalf:-1:1,:);
```

```
eval (['save  /users/shawno/interferometer/data/' datestr '/phase3/trial'
        int2str(trialnum) '/phset' int2str(filenum) ' phset -ascii -tabs']);


end; % filenum



%subroutine to do Hankel transform and find electron density

trialnum = 0 ; %input('trialnum ');


for filenum = 1:filenummax
M=1000;

text = ['data/' datestr '/phase3/trial' int2str(trialnum) '/phset' int2str(filenum)];
load(text);
eval(['phset = phset' int2str(filenum) ';']);

scale = .5;  %must be same as the deconvolution increment

delx = scale;

f = zeros (1,phset*2);
lendata = length(phset);
f(M-(lendata-1)./2:M+(lendata-1)./2)= phset(:,2);

ft = delx.*fft(f);

ftpos= abs(ft(1:length(ft)./2));
ftincr= (0:1:length(ftpos)-1);

delincr = 1./length(ft)./delx;
const = ftincr.*ftpos.*delincr.^2;

%assume filter no wider than 200th value
%if need more need to recalcuate Bessel values for 1000 point full range
% Do Hankel transform

const = const(1:200);
clear H;

for l2 = 1:1:M./100
        eval (['load bessfiles3/bessval.f' int2str(l2) ]);
        for l1 = 1:1:100
                func = const.*bessval(l1,:);
                %bessel(0,bessind);  can use bessel function in matlab but time
                        %intensive
                H(l1*l2)=sum(func);
        end;
```

```
end;

H=H.*2.*pi;

R=256;
c=1;
b=1;
edge = 100
r= (0:1:edge-1).*delx.*2;

nc = 3.59e12; % critical density in cm-3 for 17 GHz
lambda = 1.76;  %wavelength in cm for 17 GHz
nH= H ./180*lambda*nc;   % electron density in cm-3
pair = [r;nH(1:edge)]';

eval (['save  density/trial' int2str(trialnum) '/dens' int2str(filenum) ' pair  -ascii -
        tabs']);

end;
```

APPENDIX D

COMPUTER CODE FOR RAY TRACING ANALYSIS OF MICROWAVE CHARACTERIZATION

The electromagnetic impact simulations of Chapter 7 have been completed with a ray tracing code written by Matthew Holladay and Christopher Nelson. The ray tracing subroutine are included along with an example electron density function.

Subroutines:	
sweep.m	highest level ray-tracing driver
drv3.m	antenna driver producing output for a single antenna position
trace_2d.m	ray driver producing output for a single ray
steps.m	error function producing error value used by trace_2d to determine the proper step size for the current position in the ray
ne.m	electron density profile calculates the new direction of propagation using Snell's law
direction3.m	vector solution for Snell's law calculates the new direction of propagation using Snell's law
grad.m	gradient numerical approximation of the gradient of a field
dot.m	dot product

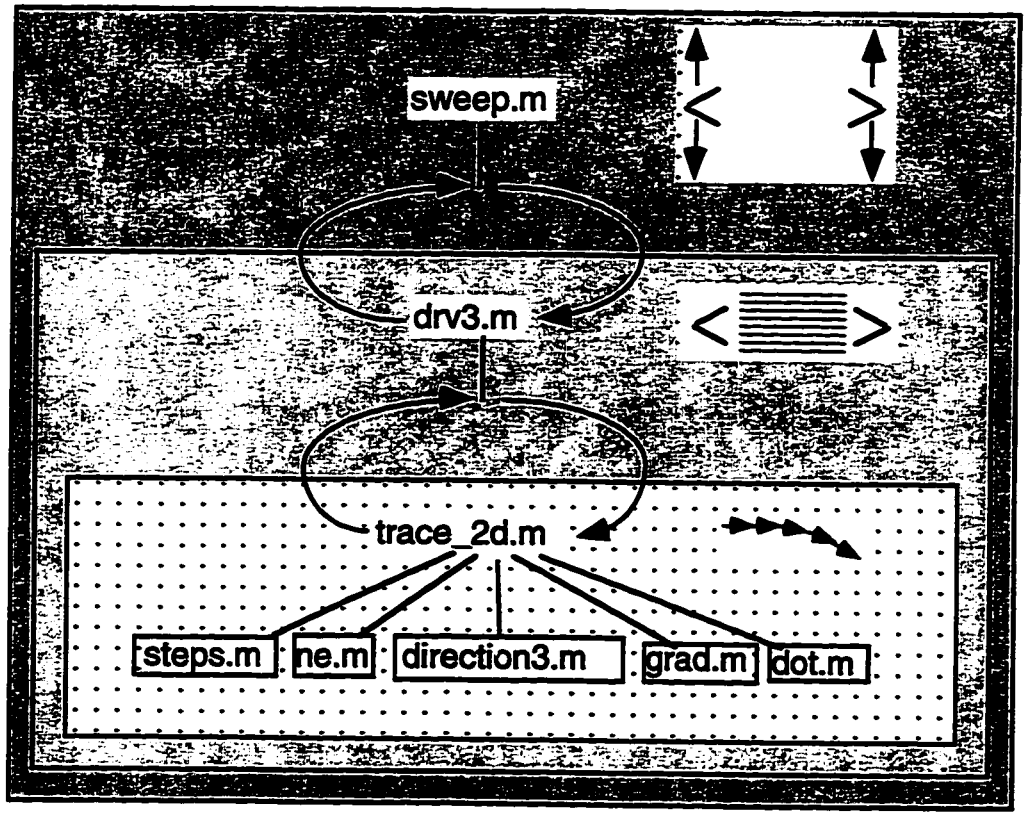

Figure D.1. Flow diagram for ray tracing simulations.

```
%
%              FUNCTION TRACE_2D
%              -----------------
%
% This function performs 2-d ray tracing of an
% electromagnetic wave through a plasma. Note that
% for good results, the wave frequency must be greater
% than the plasma frequency. A single ray is traced
% through the plume and plotted.
%
% SYNTAX: [x,y,phase]=trace_2d(pos,freq)
%
% INPUTS: pos   - The starting position of the ray
%         freq  - Wave frequency (Hz)
%
% OUTPUT: x     - x coordinates along the ray
%         y     - y coordinates along the ray
%         phase - phase shift of the specific ray
%
% NOTICE: The Plume model presently assumes a 162cm x 162cm
%         x-y distribution of electrons. To change this,
%         modify the trace_2d.m file and change xsize
%         and/or ysize to change the x-y size of the model.
%

function [x,y,phase]=trace_2d(pos,freq)

% Constants

w=2*pi*freq;          % Angular wave frequency
step=10;              % step size in cm
c=3.0e8*100;          % speed of light, cm/s
beta=w/c;             % phase constant
phase=0;              % initial phase shift
d=[0,1];              % initial wave direction

xsize=162;
ysize=162;

x=[];
y=[];

d_unit=d/(sqrt(d(1)^2+d(2)^2));

done=0;

% take a step

while done~=1,

 if step < 8
  step=2*step;
 end
```

```
 while steps(step,pos,d_unit,xsize,ysize,w)>.0001
  step=step/2;
 end

 x=[x,pos(1)];
 y=[y,pos(2)];

 ne_old=ne(pos(1),pos(2));
 pos=pos+step*d_unit;
 phase=phase+beta*step;
 ne_new=ne(pos(1),pos(2));

% calculate the normal to the new surface

 n=grad(pos(1),pos(2),step,xsize,ysize,d_unit);
 n_unit=n/(sqrt(n(1)^2+n(2)^2));

% calculate the plasma frequencies

 wp_old2=3.19e9*ne_old;
 wp_new2=3.19e9*ne_new;

% calculate the indexes of refraction

 n_index_old=sqrt(1-wp_old2/(w^2));
 n_index_new=sqrt(1-wp_new2/(w^2));

% calculate the new phase constant

 beta=w/c*sqrt(1-wp_new2/(w^2));

% satisfy snell's law

 theta_old=abs(acos(dot(d_unit,n_unit)));
 if theta_old > pi/2
  theta_old=pi-theta_old;
 end

 theta_new=abs(asin(n_index_old*sin(theta_old)/n_index_new));
 if theta_new > pi/2
  theta_new=pi/2;
 end

  % take the real part of theta_new to avoid a representational
  % error caused when matlab encounters something it thinks is
  % imaginary (eg. theta_calc=0.2100 + 0.0000i)

  theta_new=real(theta_new);

% Determine the new direction of propagation

  d=direction3(d_unit,n_unit,theta_old,theta_new,n_index_old,n_index_new);
  d_unit=d/(sqrt(d(1)^2+d(2)^2));
```

```
% check to see if we are about to go out of range

 test=pos+2*step*d_unit;

 if ((test(1)<1)|(test(2)<1))
  if step < 1
    done=1;
    x=[x,pos(1)];
    y=[y,pos(2)];
  else
    step=step/50;
  end
 elseif ((test(1)>xsize)|(test(2)>ysize))
  if step < 1
    done=1;
    x=[x,pos(1)];
    y=[y,pos(2)];
  else
    step=step/50;
  end
 end

end

phase=phase-w/c*y(length(y));

% Plot the ray
 plot(y,x)
 xlabel ('y in cm')
 ylabel ('x in cm')
 title('Plot of Path Through Plume')
```

```
%
%           FUNCTION SWEEP
%           --------------
%
% This function performs a sweep of gain and phase
% measurements, moving the center of the antenna 1
% cm at a time.
%
% SYNTAX: [gain,phase]=sweep(start,freq)
%
% INPUTS: start - initial center of antenna
%         freq  - wave frequency (Hz)
%
% OUTPUT: gain  - attenuation data
%         phase - phase data
%
% NOTICE: To change either the number of measurements taken
%         (currently 20) or the step size (currently 1cm)
%         edit the sweep.m file and change the appropriate
%         parameters in the _for_ loop.
%

function [gain,phase,xpos]=sweep(start,freq)

xpos=[];
gain=[];
phase=[];

for n=1:20
 center=start+n
 xpos=[xpos, center];
 [ngain,nphase]=drv3(center,freq);
 gain=[gain, ngain]
 phase=[phase, nphase]
end

clf;
plot(xpos,gain);
```

```
%
%                FUNCTION STEPS
%                -------------
%
% Returns the error value associated with a given step size.
% The error value is the difference between the final position
% after two steps of a given step size and four steps of half
% that size.
%
% SYNTAX: value=steps(step,pos,d_unit,xsize,ysize,w)
%
% INPUTS: step  - the current step size
%         pos   - position in plume
%         d_unit - direction vector at the given position
%         xsize  - size of the plume model in x
%         ysize  - size of the plume model in y
%

function value=steps(step,pos,d_unit,xsize,ysize,w)


% TWO STEPS AT FULL STEPSIZE

stepsize=step;
steppos=pos;
dir_unit=d_unit;

for count=1:2,
 ne_old=ne(steppos(1),steppos(2));
 steppos=steppos+stepsize*dir_unit;
 ne_new=ne(steppos(1),steppos(2));

% calculate the normal to the new surface

 n=grad(steppos(1),steppos(2),stepsize,xsize,ysize,dir_unit);
 n_unit=n/(sqrt(n(1)^2+n(2)^2));

% calculate the plasma frequencies

 wp_old2=3.19e9*ne_old;
 wp_new2=3.19e9*ne_new;

% calculate the indexes of refraction

 n_index_old=sqrt(1-wp_old2/(w^2));
 n_index_new=sqrt(1-wp_new2/(w^2));

% satisfy snell's law

 theta_old=abs(acos(dot(dir_unit,n_unit)));
 if theta_old > pi/2
  theta_old=pi-theta_old;
 end
```

```
  theta_new=abs(asin(n_index_old*sin(theta_old)/n_index_new));
  if theta_new > pi/2
   theta_new=pi/2;
  end

   % take the real part of theta_new to avoid a representational
   % error caused when matlab encounters something it thinks is
   % imaginary (eg. theta_calc=0.2100 + 0.0000i)
    theta_new=real(theta_new);

% Determine the new direction of propagation

   d=direction3(d_unit,n_unit,theta_old,theta_new,n_index_old,n_index_new);
   dir_unit=d/(sqrt(d(1)^2+d(2)^2));

end

%%%%%%%%%%%%%%%%%%%%%%%%%%%%%%%%%%%%


% FOUR STEPS AT 1/2 STEP SIZE

stepsize=step/2;
steppos2=pos;
dir_unit2=d_unit;

for count=1:4,
 ne_old=ne(steppos2(1),steppos2(2));
 steppos2=steppos2+stepsize*dir_unit;
 ne_new=ne(steppos2(1),steppos2(2));

% calculate the normal to the new surface

 n=grad(steppos2(1),steppos2(2),stepsize,xsize,ysize,dir_unit2);
 n_unit=n/(sqrt(n(1)^2+n(2)^2));

% calculate the plasma frequencies

 wp_old2=3.19e9*ne_old;
 wp_new2=3.19e9*ne_new;

% calculate the indexes of refraction

 n_index_old=sqrt(1-wp_old2/(w^2));
 n_index_new=sqrt(1-wp_new2/(w^2));

% satisfy snell's law

 theta_old=abs(acos(dot(dir_unit2,n_unit)));
 if theta_old > pi/2
  theta_old=pi-theta_old;
 end

 theta_new=abs(asin(n_index_old*sin(theta_old)/n_index_new));
```

```
 if theta_new > pi/2
  theta_new=pi/2;
 end

  % take the real part of theta_new to avoid a representational
  % error caused when matlab encounters something it thinks is
  % imaginary (eg. theta_calc=0.2100 + 0.0000i)
   theta_new=real(theta_new);

% Determine the new direction of propagation

  d=direction3(d_unit,n_unit,theta_old,theta_new,n_index_old,n_index_new);
  dir_unit2=d/(sqrt(d(1)^2+d(2)^2));

end

%%%%%%%%%%%%%%%%%%%%%%%%%%%%%%%%%%%


% ERROR

aux1=(steppos(1)-steppos2(1))^2;
aux2=(steppos(2)-steppos2(2))^2;
value=sqrt(aux1+aux2);
```

```
%
%            FUNCTION NE
%            ----------
%
% This function creates a functional model of a
% Plasma Plume by using functional distributions to
% calculate electron density.
%
% SYNTAX: density=ne(x_position,y_position)
%
% NOTICE: The Plume model presently assumes a 162cm x 162cm
%       x-y distribution of electrons. The axial position
%       is set at 15 cm (Axial Position 6). To change these
%       parameters, modify the ne.m file and change xsize
%       and/or ysize to change the x-y size of the model and
%       change the parameter x to change the axial position.
%

function density=ne(a,b)

% Define the size of the model

xsize=162;
ysize=162;

% Build the model

C1=4.67e10;
C2=0.019;
C3=1.29e13;
C4=0.0162;
no=.65e14;
n=.65;
lam=37;

x=15;

 y=sqrt((a-xsize/2).^2+(b-ysize/2).^2);

 radxy=sqrt(x.^2+y.^2);
 thetaxy=180/pi*atan(y/x);

func3=C1.*exp(-C2.*(radxy.*sin(thetaxy.*pi/180)).^2)+C3./radxy.^2.*exp(-
C4.*thetaxy);
density1=func3;

%func1=no/(radxy^2*(cos(thetaxy.*pi/180))^2);
%a=lam*(1-cos(thetaxy.*pi/180));
%func2=exp(-(a^n));
%density2=func2*func1;

density=1.1*density1;
```

```
%
%           FUNCTION DRV3
%           -------------
%
% This function handles a single antenna measurement.
% It assumes the antenna is centered at a point on the
% x axis, and computes attenuation and phase data by
% tracing 41 weighted rays. The rays are also plotted.
%
% SYNTAX: [gain,theta]=drv3(center,freq)
%
% INPUTS: center - the center of the antenna on the x axis
%         freq   - wave frequency
%
% OUTPUT: gain   - attenuation data
%         theta  - phase data
%

function [field_received,lindex,frtot,tphase]=ndrv3(center,freq)

clf;
size=20;
sent=41;
step=size/(sent-1);
start=center-size/2;

hold;

% antenna transfer function, fn is the system transfer
% function, pn is the function for a single antenna

% trace each ray, keeping track of the total power incident
% upon the receiver

power_received=0;
field_received=0;
tgain=[];
lindex=[];
tphase=[];
for count=1:sent,
 count
 pos=[start+step*(count-1) 0]
 [x y phase]=trace_2d(pos,freq);
 lastindex=length(x);
 lindex=[lindex,x(lastindex)];
 index1=round( (pos(1)-start) / step ) + 1;
 index2=round( (x(lastindex)-start) / step ) + 1;
 p=1;
 fr=sqrt(p)*exp(-j*phase)
 tphase=[tphase,phase];
 frtot=[frtot,fr];
 field_received=field_received+sqrt(p)*exp(-j*phase);
end
```

```
%
%                FUNCTION GRAD
%                -------------
%
% This function calculates an approximation of the gradient of
% a scalar field at a given point in space.
%
% SYNTAX: n=grad(x,y,step,xsize,ysize,d_unit)
%
% INPUTS: x      - position in x
%         y      - position in y
%         step   - step size for derivative approximation
%         xsize  - size of data set in x
%         ysize  - size of data set in y
%         d_unit - a unit vector to be returned if gradient = 0
%

function n=grad(x,y,step,xsize,ysize,d_unit)

 s=step;

% Calculate the derivative in x

 x2=x+s;
 dx1=(ne(x2,y)-ne(x,y))/s;
 x2=x-s;
 dx2=(ne(x,y)-ne(x2,y))/s;

 dx=(dx1+dx2)/2;

% Calcualte the derivative in y

 y2=y+s;
 dy1=(ne(x,y2)-ne(x,y))/s;
 y2=y-s;
 dy2=(ne(x,y)-ne(x,y2))/s;

 dy=(dy1+dy2)/2;

% If the gradient is exactly zero, return the origional vector.
% Otherwise, return the calculated gradient.
d_unit=[0 1];
if ((dx==0)&(dy==0))
 n=d_unit;
else
 n=[dx dy];
end
```

```
%
%              FUNCTION DIRECTION3
%              -------------------
%
% This function calculates the vector direction of a wave incident
% upon a refractive surface using a modified version of Snell's Law.
% This new direction is returned as d.
%
% SYNTAX: d=direction3(d_unit,n_unit,theta1,theta2,n1,n2)
%
% INPUT:  d_unit - the unit vector in the direction of propagation
%         n_unit - the unit vector normal to the surface of incidence
%         theta1 - incident angle
%         theta2 - transmitted angle
%         n1     - index of refraction for incident wave
%         n2     - index of refraction for transmitted wave
%

function d=direction3(d_unit,n_unit,theta1,theta2,n1,n2)

flag=-1;

% Make sure the normal is pointing away from the direction of
% propagation.

if dot(d_unit,n_unit) <= 0
  n_unit=-n_unit;
end


% For a normally incident wave

if d_unit == n_unit

  d=n_unit;

% For other incident waves

else

  d=(n1/n2)*d_unit+(cos(theta2)-(n1/n2)*cos(theta1))*n_unit;

end
```

```
%
%            FUNCTION DOT
%            ------------
%
% This function calculates the dot product
% of two cartesian vectors.
%
% SYNTAX: c=dot(a,b)
%

function c=dot(a,b)

c=0;

for k=1:length(a),
 c=c+a(k)*b(k);
end
```

APPENDIX E

MANUAL FOR IMPLEMENTATION OF ION ACOUSTIC WAVE DIAGNOSTIC TECHNIQUE

Overview

The implementation of the ion acoustic wave probe is based on the propagation characteristics of an ion acoustic wave that is superimposed on a flowing plasma such as with a stationary plasma thruster. The basic theory and necessary assumptions are reviewed as relevant to electric propulsion. Then an experimental configuration is described including probe, lock-in amplifier, and computer acquisition. A suggested experimental plan is outlined in order to effectively utilize the available information. Finally, a method is outlined for interpreting the experimental results.

Ion Acoustic Wave Basics

In order to apply this technique, a number of conditions must be met. First, the flow velocity needs to be greater than the ion acoustic phase velocity; if this is not the case, the procedure needs to be modified slightly. Second, the electron temperature must be much greater than the ion temperature (2-3 times greater might work with extra care). Third, the collision frequency must be much less than the excitation frequency; in particular, the electron-neutral collisions will significantly damp the wave. Lastly, the plasma properties must be relatively homogeneous over the measurement area; this measurement results in an average value over the propagation region and severe inhomogeneity will distort propagation. After meeting these criteria, the ion acoustic wave characteristics of the amplitude and phase can be interpreted as an ion acoustic wave (following the ion acoustic wave dispersion relation) superimposed on a flowing plasma.

In a plasma moving slower than the wave velocity the wave is expanded (or Doppler shifted) in the direction of the flow and compressed in the direction opposite the flow as in Figure E.1. When the flow velocity is faster than the wave velocity, the wave cannot propagate opposite to the flow and is limited to a propagation zone which is defined by the wave velocity and flow velocity.

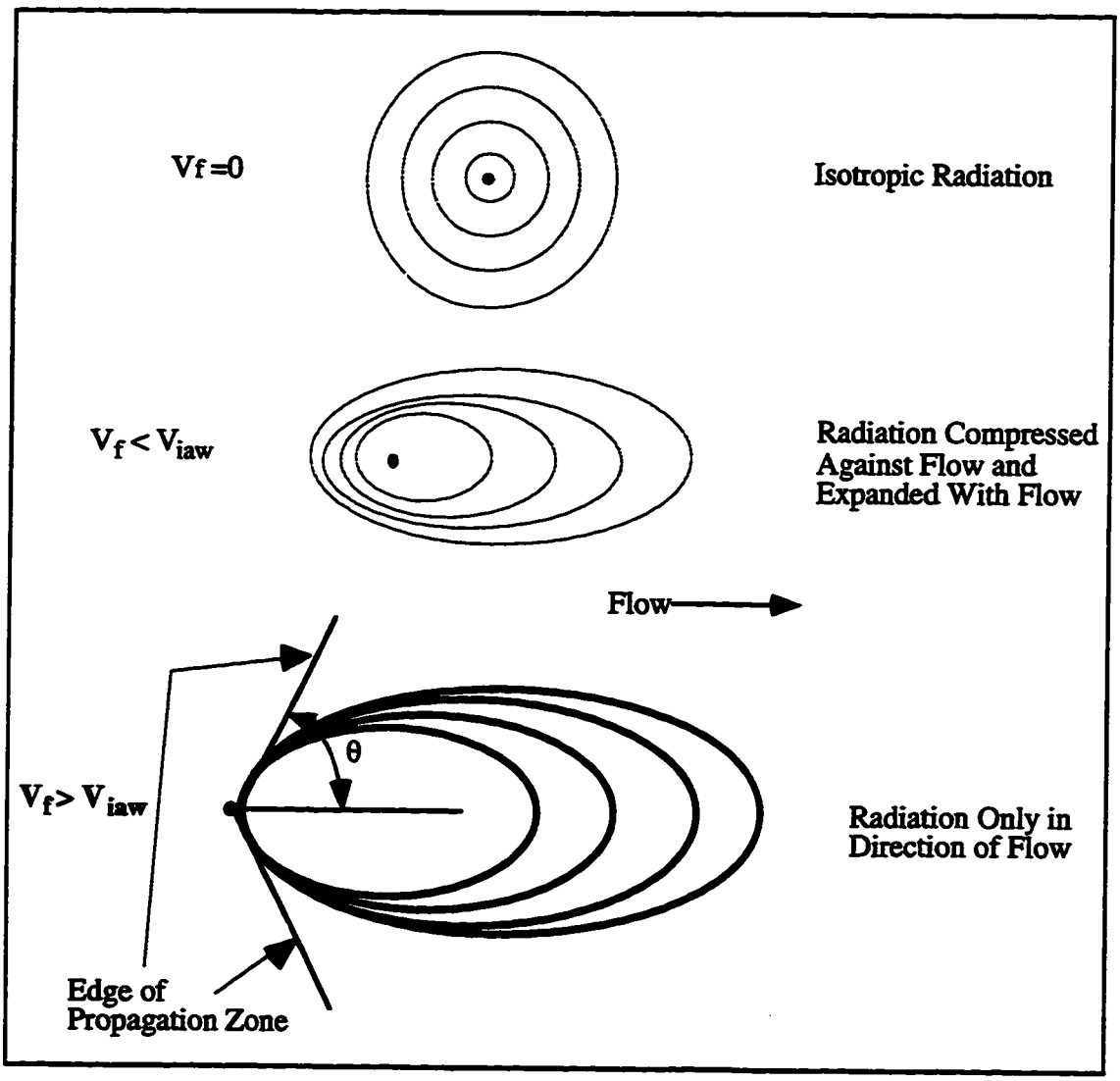

Figure E.1. Schematic representation of ion acoustic wave propagation.

After initial excitation, the wave propagates with the wavenumber which is determined by the vector sum of the ion acoustic wave velocity and the flow velocity. With

this model no propagation occurs opposite the flow. Propagation initiated orthogonal to the flow follows a path determined by the vector sum of the velocities where the angle of this vector defines the theoretical propagation zone of the wave. Lastly, propagation parallel to the flow direction moves with a velocity equal to the sum of the ion acoustic wave velocity and the flow velocity.

The velocities of both the ion acoustic wave and the plasma flow are found by quantifying the propagation along the two limiting directions: orthogonal and parallel to the flow. The wave initiated orthogonal to the flow follows a path that is the boundary of the propagation zone; experimentally determining the propagation zone (θ) defines the ratio of the two velocities through Equation E-1 (Figure E.2). The wave propagating parallel to the flow is defined by the wavenumber and frequency which are directly related to the sum of the velocities through Equation E-2 (Figure E.3). The wave is excited with a known frequency and the wavenumber is determined through a measurement of the wavelength. The two measurements determine the wave velocity and flow velocity.

$$\theta = \tan^{-1}\left(V_{iaw} / V_{flow}\right) \qquad \text{•E-1}$$

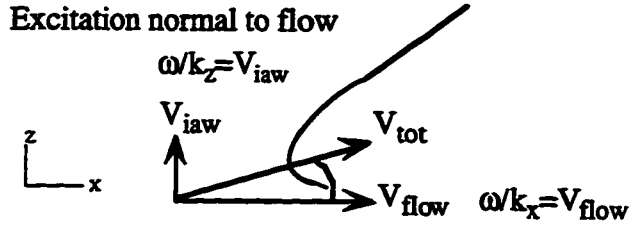

Figure E.2. Velocity vector of the ion acoustic wave normal to the flow.

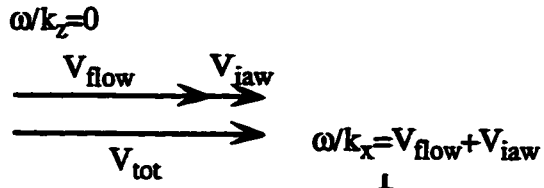

$$f\frac{360^\circ}{\Delta\phi}d = 2\pi\left(V_{flow} + V_{iaw}\right) \qquad \text{•E-2}$$

Figure E.3. Velocity vector of ion acoustic wave parallel to flow.

Using this experimental information, the flow and ion acoustic velocity are easily found:

$$V_{flow} = \frac{360^\circ}{\Delta\phi} df \frac{1}{(1+\tan(\theta))}, \qquad \text{•E-3}$$

$$V_{iaw} = \frac{360^\circ}{\Delta\phi} df \frac{\tan(\theta)}{(1+\tan(\theta))}. \qquad \text{•E-4}$$

The ion acoustic velocity is then related to plasma parameters through the dispersion function:

$$V_{iaw} = \sqrt{\frac{eT_e + 3eT_i}{m_i}}. \qquad \text{•E-5}$$

The velocity provides information concerning the sum of the electron and ion temperature. The analysis to utilize this relation varies depending on the plasma and other available information. One suggested technique is to assume the ion temperature is negligible and utilize the ion acoustic velocity to estimate the electron temperature. Another method utilizes electron temperature obtained from another diagnostic such as a Langmuir probe in addition to the ion acoustic wave velocity to estimate the ion temperature. This second method will only estimate an upper bound to the ion temperature. Further work is necessary to accurately determine ion temperature with this diagnostic.

Experimental Configuration

A tungsten wire probe is suggested which is oriented orthogonal to the flow direction. The probe (Figure E.4) should be between 0.2 mm and 1 mm in diameter and between 0.5 and 1.5 cm long. Larger probes can be used, but wake effects must be assessed, and smaller probes can be used but the signal strength is lower with smaller probes. A ceramic insulator is suggested as in Figure E.4 which is extended approximately 10 cm from a stainless steel metal shield (such as tubing for gas lines). The ceramic should be a ceramic tube with inner diameter approximately that of the tungsten wire outer diameter. Ceramic epoxy can then be used to secure the wire and ceramic tube in the metal shield. The inner conductor of a coaxial cable is crimped to the tungsten wire (soldering will not work with tungsten) and then insulated with Capton tape. The outer shield is connected to the stainless steel tube. The stainless steel tube is for support of the probe assembly, protection of the joint between the probe wire and coaxial cable, and protection of the coaxial cable. Normal coaxial cable can be used but high temperature ratings are suggested; if normal coaxial cable is used, it stiffens over time and should be checked periodically for structural and electrical integrity.

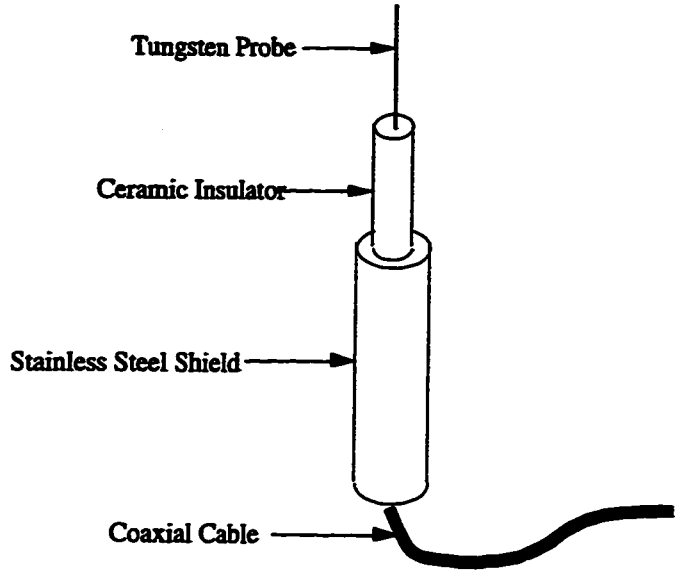

Figure E.4. Probe schematic.

The lock-in amplifier (Stanford Research Systems, SR850) is the key instrument in the ion acoustic wave diagnostic. The instrument provides extremely sensitive detection of a known frequency signal even when the amplitude of the signal is apparently in the noise of the voltage signal (as seen on an oscilloscope). Suggested initial settings for the lock-in amplifier are as follows: first harmonic, 1 s time constant, 18 db/oct filter, maximum reserve, 1 mV sensitivity, ±5 V, and 100 kHz internal reference. The exciter probe is attached directly to the reference signal from the lock-in amplifier and the detector probe is attached to the input port A. Once a particular setup is verified and the ion acoustic wave is measured the settings should be optimized primarily in terms of the time constant and voltage sensitivity. Experiments can also be implemented with a amplifier to increase the amplitude of the excitation signal; however, a precision integrated amplifier should be used so as not to loose the high fidelity of the lock-in amplifier, and the bias voltage should be set so the voltage remains in the ion saturation region.

In order to effectively implement the diagnostic, two LabView VI's are necessary, the table positioning VI and the lock-in amplifier data storing VI. The positioning VI should include the capability to enter an array of points where the data acquisition is to take

place. The two VI's should also have the ability to pause for a certain time period so as to allow the lock-in amplifier to attain an accurate measurement at each position. The programs are ideally synchronized via a direct connection.

Procedural Suggestions

A number of steps are suggested to successfully implement the ion acoustic wave probe. Initially, baseline measurements should include amplitude and phase data sets at the same position and also over a series of positions to determine the noise level and repeatability of the particular experiment. Next an experiment should be completed to determine at what axial distance the near-zone wake effects are minimal. This can experimentally be found by implementing a system such as in Figure E.5 where a stationary probe is placed at a known position and a second probe is moved along the flow axis measuring the amplitude and phase. Example data sets (Figures E.6 and E.7) show that for probe separation farther than 5 cm the signal monotonically decreases in both the amplitude and phase thus indicating minimal interference and wake effects. An initial guess for this distance is 50 to 100 times the probe diameter. A suggested spatial sampling distance is 0.1 to 0.25 cm for the closest measurements and up to 0.75 cm for 15 cm or greater axial separation. This should be sufficiently fine sampling to observe the trends in the measurements (sometimes this is much more than necessary).

After identifying an appropriate far-zone distance to place the nearest detector probe, the experimental setup in Figure E.8 should be constructed in order to provide spatial sampling of the plasma (possibly along axial and radial coordinates as in Figure E.9). Often the first probe can be placed between 5 to 10 cm from the exciter and the second detector can be placed 2-5 cm downstream of the first detector. The position of the second probe should be placed so as to obtain 50 to 200 ° phase shift. Less phase shift would risk significant loss of phase resolution, and higher phase shift would risk missing phase jumps of greater than 360 °. A rotary scan should initially be ±20° and can later be

reduced to ±10°. These estimates are for the SPT and should be modified for different plasma parameters (5 times expected propagation zone angle). The center of the scan should be on the geometric line with the thruster (Figure E.9). In the fringes of the plume the center of the pattern will not exactly match the geometric line, but will indicate the flow direction. The rotary scan should be initially stepped at 0.1° increments particularly near the edge region and the pattern center. Representative data sets are included where Figure E.10 is an amplitude characterization near the center of the plume, Figure E.11 is an amplitude scan at the periphery of the plume, and Figure E.12 is the phase scan of both detectors providing the information necessary to find the phase shift over a given distance, in this case 4.46 cm.

Interpretation of the data is the last step in the diagnostic technique before applying the theoretical equations relating the experimental measurements to the plasma parameters. The two quantities of interest are the propagation zone edge and the phase shift along centerline. The propagation zone edge is determined by identifying a noise level and finding the angle at which the amplitude decreases to the noise level. This discounts the small amplitude at the nulls and is sometimes difficult to accurately assess with low signal and high noise levels, especially in the measurements at the plume periphery where the density is low or close to the thruster where the natural plasma noise is strongest. Half the angle between the two edges can be used as the propagation zone boundary angle. The phase shift should be taken at the center of the propagation zone. This is not always the strongest peak in the amplitude signal. This position is approximately the geometric angle to the thruster for measurements close to the plume center and can often be approximated by half the distance between the two edges. An estimation of the uncertainty in the measurement is determined by using the uncertainty in the measurements of propagation zone and phase shift and propagating the uncertainty through the theoretical equations.

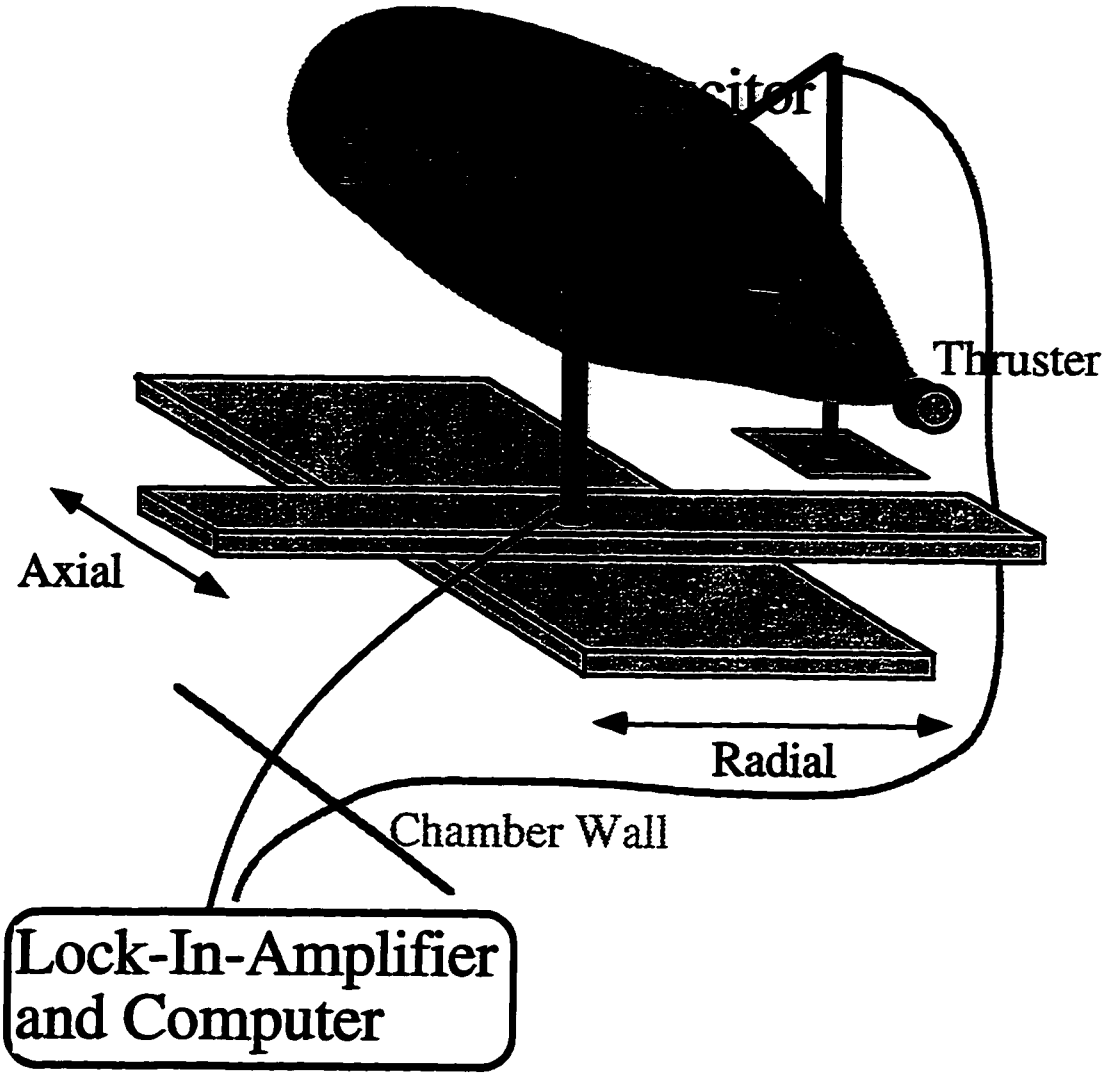

Figure E. 5. Experimental system for evaluating axial and radial variation in ion acoustic wave parameters.

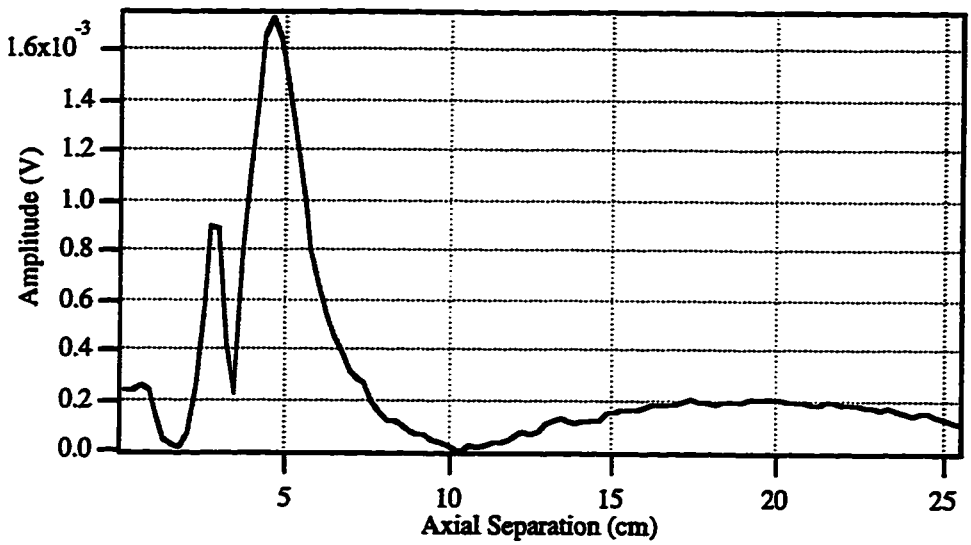

Figure E.6. Representative axial variation of amplitude.

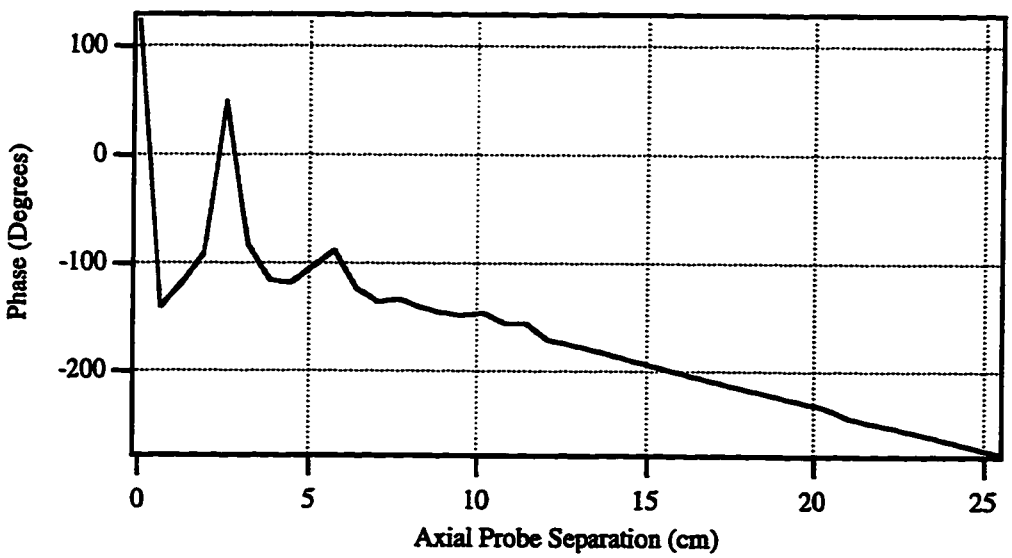

Figure E.7. Representative axial variation of phase.

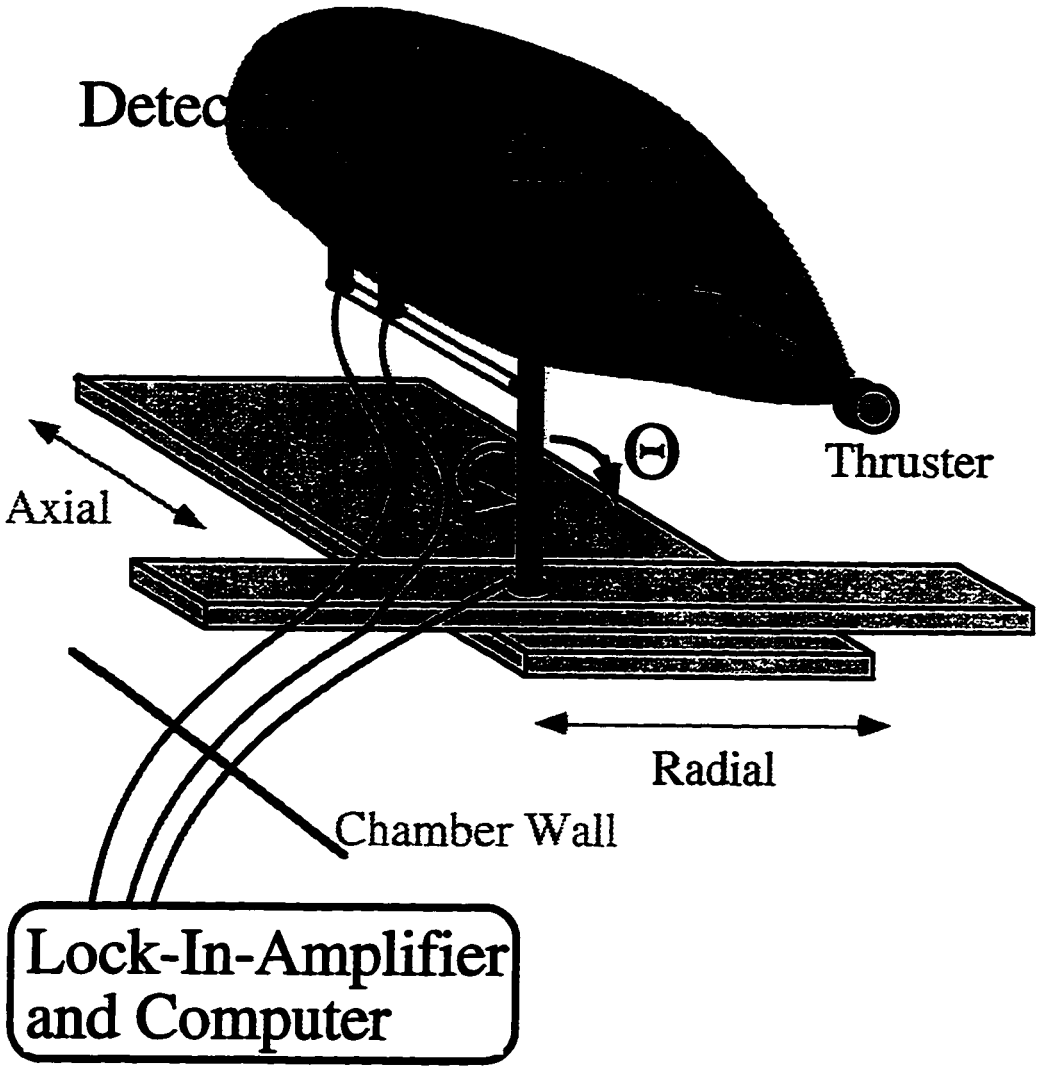

Figure E.8. Experimental system for ion acoustic wave diagnostic to spatially map plasma parameters.

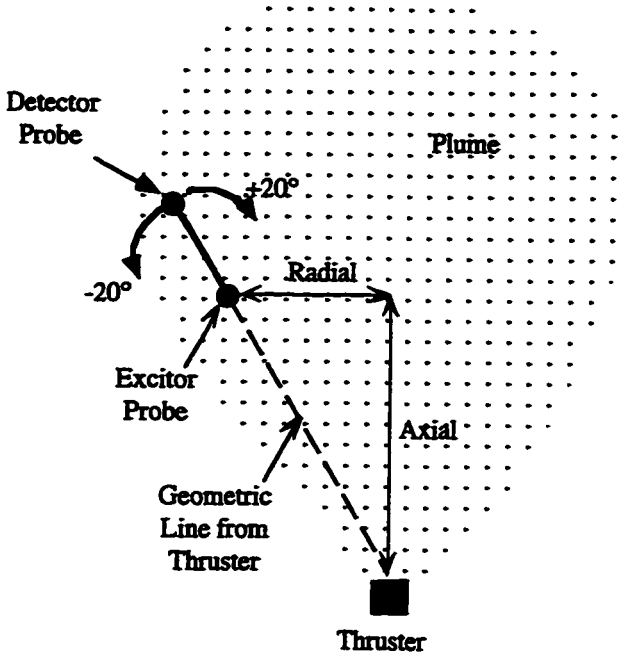

Figure E.9. Guide for measurement coordinate system.

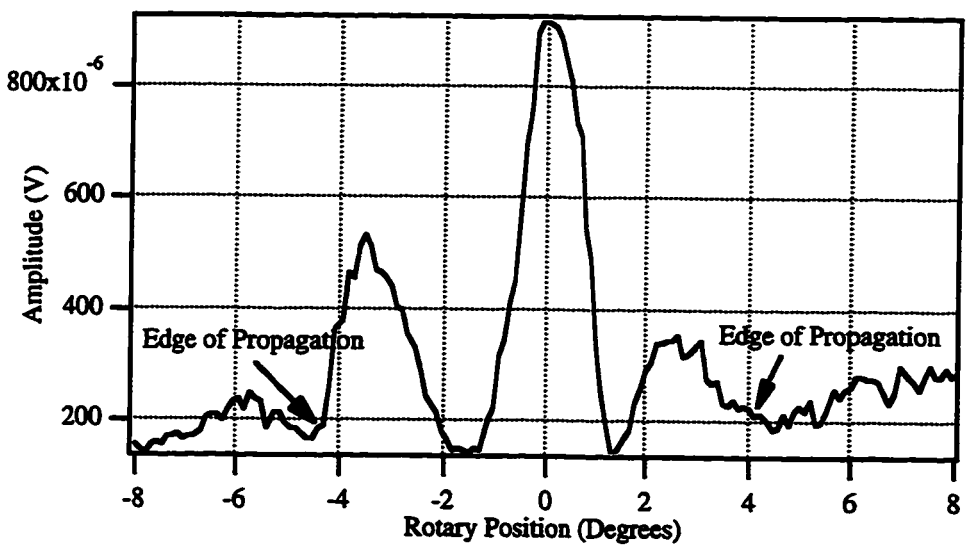

Figure E.10. Example amplitude rotary sweep near plume center.

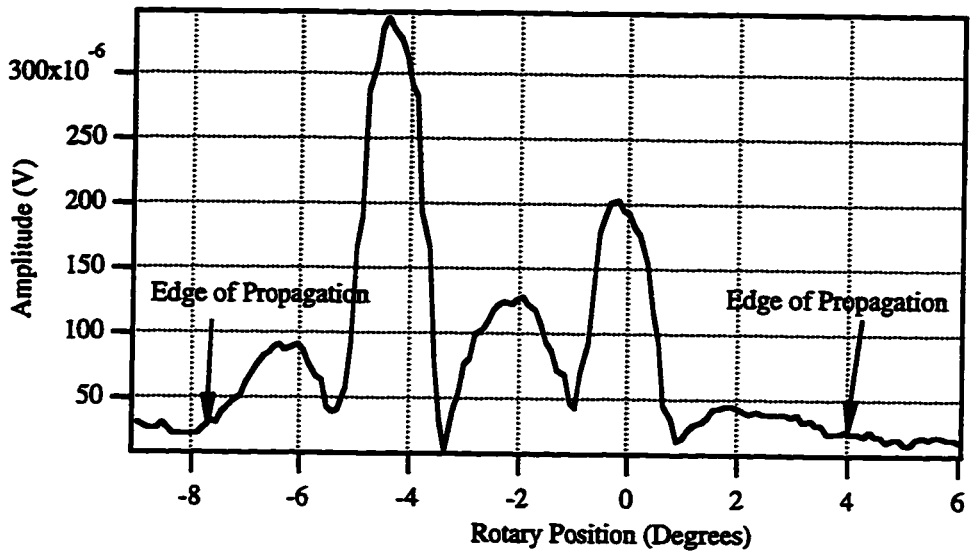

Figure E.11. Example amplitude rotary sweep away from plume center.

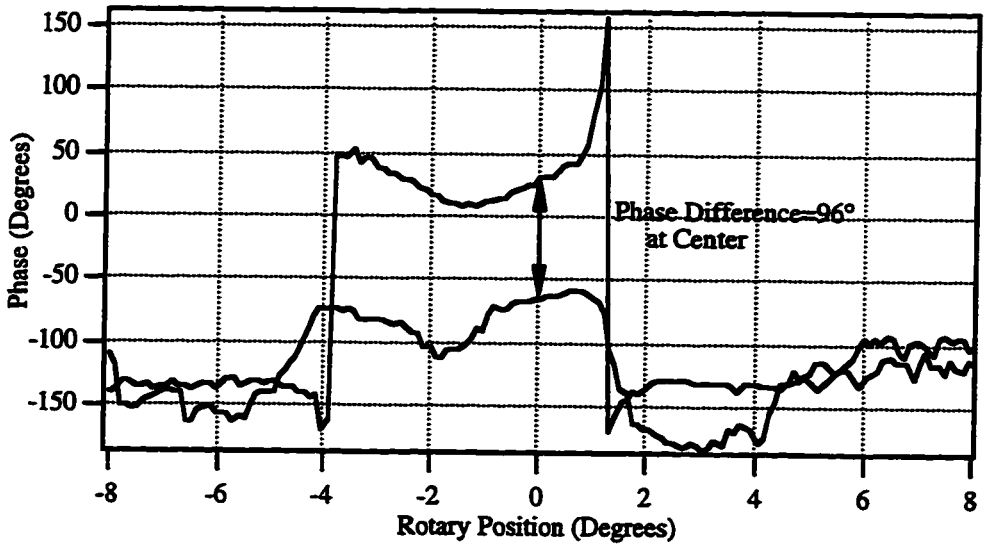

Figure E.12. Example phase comparison rotary sweep.

APPENDIX F

FINDING ION TEMPERATURE THROUGH SCATTERING FROM THE DOPPLER SIGNATURE

Overview

Ion temperature is one plasma parameter that indicates physical processes present in a plasma. The ion temperature is often difficult to measure due to the sometimes low magnitude in comparison to the electron temperature and also the electron to ion mass ratio which is sometimes coupled to the temperatures in the theoretical basis of many diagnostics.

The measurement of ion temperature by analysis of the Doppler spectrum of a scattered wave has undergone theoretical consideration [Dougherty, *et al.* 1960, *et al.* 1963; Moorcroft, 1964; Rosenbluth, *et al.* 1962; Salepter, 1960; Evans, 1969; Booker, *et al.* 1950] and has been used to study the ionosphere [Evans, 1969; Evans 1970; Gordon, *et al.* 1961, Vickrey, *et al.* 1976; Vickrey, 1980] as well as dense laboratory plasmas [Offenberger, *et al.* 1971; Forrest, 1974; Dobele, 1976; Hailer, 1977; Kasparek, *et al.* 1982; Baconnet, *et al.* 1969; Bernard, *et al.* 1971; Kronast, *et al.* 1971; Little, *et al.* 1966]. The ionospheric measurements have used radars operating throughout the range from 30 MHz up to 2 GHz with peak power up to 10 MW and gain up to 120 dB. The systems scatter the signal off of the ionosphere to find not only ion temperature, but electron temperature, and electron density through detailed analysis of the Doppler signature. Dense Laboratory plasmas with electron densities greater than 10^{17} m^{-3} have been analyzed using the Doppler spectrum of a scattered wave. A CO_2 laser, ruby laser, and argon laser have all been used in these experiments, where optical frequencies are necessary due to the higher plasma density.

This work studies the possibility of finding ion temperature using the signal spectrum scattered off a plasma created from an electric thruster. The plasma electron density for electric thrusters is between the low density of the ionosphere and the more dense laboratory plasmas, hence, our choice of a microwave signal to develop the diagnostic for electric propulsion. This diagnostic has the same advantages as the microwave interferometer discussed Chapter 1 to 3. In particular, it is non-intrusive and it does not rely on limited flow and chemical models in the analysis. Using the scattered microwave signal to find ion temperature is new to electric propulsion and could potentially provide a more accurate approach to quantifying this value. The dominant drawback to the technique is the low scattered signal levels and complication of scattering inside the chamber which are discussed in the following sections. Initially the theoretical basis is established, then a possible experimental description is outlined, and finally a discussion addresses practical implementation and possible recommendation for future work.

Theoretical Basis of Ion Temperature Scattering Measurement

The theoretical basis for this diagnostic has been developed in a number of papers [Salpeter, 1960, 1961; Dougherty, 1963; Rosenbluth, *et al.* 1962; Moorcroft, 1964]. A complete derivation of the problem is found in Sheffield [1975] or Hutchinson [1987]. The technique relies on examining the Doppler signal due to the thermal energy distribution of electrons and ions. The electrons are the primary scattering element, but the electrons track the ions due to the need for neutrality at distances greater than a Debye length. Given the intrinsic link between the ions and electron, we can find the ion temperature from the signal scattered from electrons.

The scattered power level from the electrons, as would be expected, is very small. The scattered power spectrum from an incident wave is given by [Sheffield, 1975]:

$$P_s(\bar{r},\omega_s) = P_i r_o^2 L\Omega \left|\hat{s}\times\hat{s}\times\hat{E}_i\right|^2 n_e S \qquad \text{•F-1}$$

where P_s (W/Hz) is the scattered power spectrum, P_i (W) is the power incident on the plasma, r_o is the classical electron radius of 2.82 10^{-15} m, L (m) is the length of the plasma over which the scattering occurs, Ω (Sr) is the solid angle of the plasma viewed by the receiving antenna, $\hat{s}$ is the scattered wave unit vector, $\hat{E}_i$ is the incident electric field unit vector, n_e (m^{-3}) is the electron density, and S is the shape function describing the Doppler signature of the scattered signal. The complete list of equation defining the shape function is found at the end of this appendix.

The shape function, S [Sheffield, 1975; Hutchinson, 1987], depends upon the electron temperature, ion temperature, ion mass, electron number density, and the incident frequency. The area under the curve is determined by the number of scattering sites which is a measure of the electron number density. The width of the spectrum, $2f_D$, is primarily determined by the ion temperature and ion mass while the electron temperature will determine the relative height of the signal at the peaks, Pf_D/Pf_o. The general shape, drawn in Figure F.1, highlights the double -humped feature of the Doppler signature for this situation which is primarily characterized by the total frequency spread and the frequency offset of the peaks. The spectrum is dependent upon many quantities but the double humped nature results from two competing characteristics directly related to the ions: the scattering cross section increases with increasing ion temperature, however the ion number distribution drops off with increasing energy, hence the double-humped signature [Vickrey, 1980].

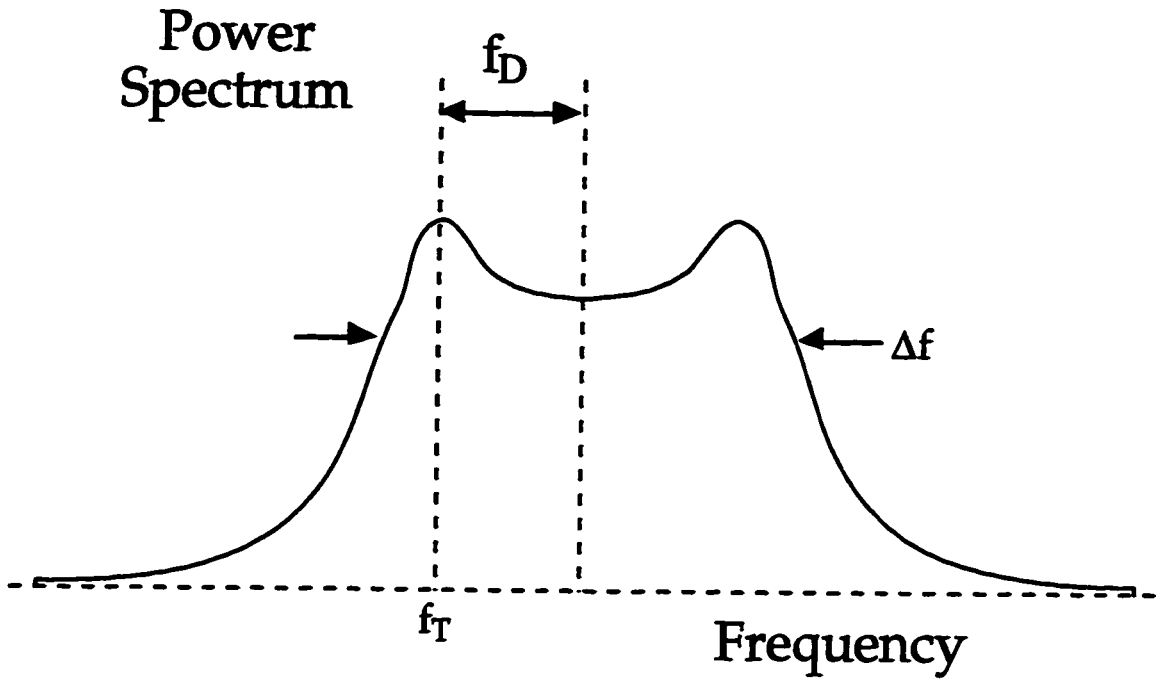

Figure F.1. Shape function for broadening from thermal motion (f_D is the thermal Doppler shift, f_O is the incident frequency).

Experimental Description

For our laboratory situation, Equation F-1 can be evaluated assuming orthogonally directed antennas with 10° beamwidth which are place 2.5 m from the center of the scatter volume. The plasma has typical temperatures of 3 eV for electrons and 0.1 eV for the ions and an average electron density of $2x10^{16}$ m^{-3}. Given the above situation the following parameters define the system: a scattering length of .44 m, orthogonal incident and scattered wave vectors, a solid angle of 0.024 Sr (given the antenna gains and distance to plasma), and a narrow 1 Hz receiver bandwidth The shape function is given by the equations at the end of this appendix and the expected shape distribution is shown in Figure F.2. For the purposes of the scattered power calculation an average value of 10^{-6} is

assumed. These values result in a scattered received power of 208 dB below the incident power.

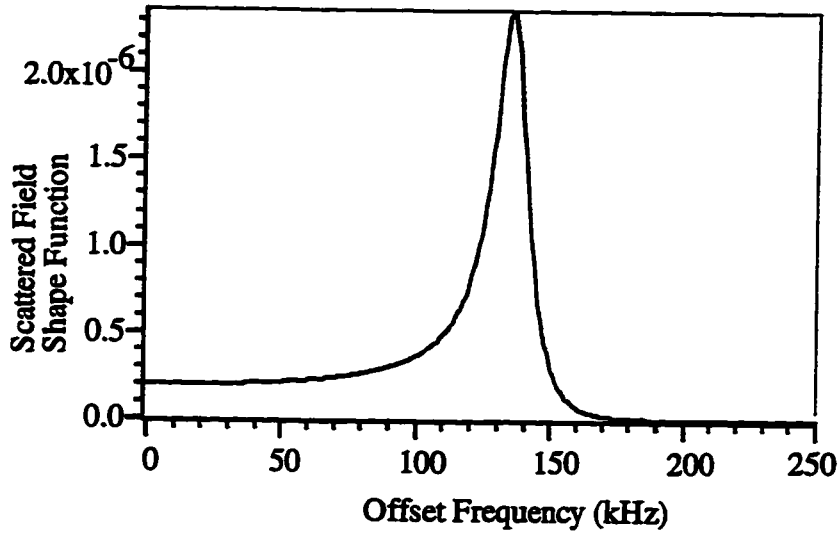

Figure F.2. Predicted frequency distribution calculated from scattering shape function.

All the necessary plasma parameter can be estimated directly from the scattered power spectrum or, for more accurate estimations the electron temperature and electron number density can be done using a Langmuir probe and microwave interferometry. The ion mass and incident frequency are known stimuli. Therefore, by using the functional expressions describing the shape function a measure of the ion temperature can be found through a best fit analysis.

The proposed configuration for this experiment, Figure F.3, is a bistatic scatter configuration using the 15 GHz oscillator as a source, mixing down at the receiver, and detecting the signal with a spectrum analyzer. The signal will be mixed down at the receive antenna to reduce the power loss over the long lines connecting the spectrum analyzer to the receiver.

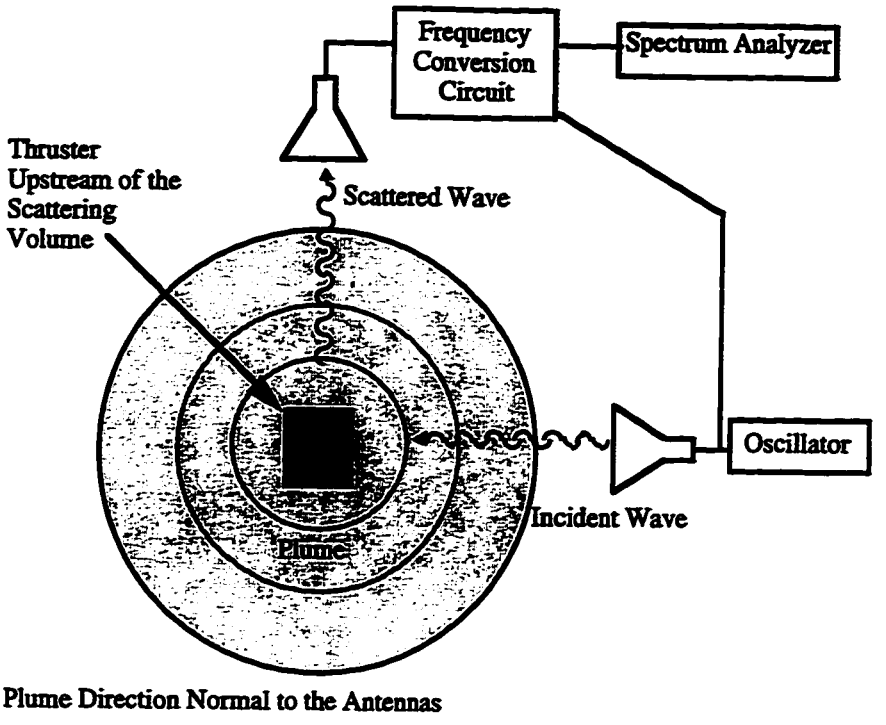

Figure F.3. Schematic of configuration for measurement of ion temperature.

Discussion of Practical Considerations

For electric propulsion measurements in a vacuum chamber, new issues must be addressed not present in either ionospheric or fusion experiments. The primary concern is maintaining the scattered signal above of the noise. The primary sources of interference will be thermal noise, chamber noise, and the direct or indirect carrier signal. In order to increase the detected signal above the thermal noise, amplification up to 10 W is necessary at the transmitter if possible. The thermal noise level is estimated to be at -204 dBW for a receiver bandwidth of 1Hz and a receiver temperature of 300K.

The transmitted signal can be received directly between the antennas or from scattering from metallic surfaces within the chamber. Received power greater than 50 kHz off the carrier is expected to be 210 dB below the transmitted power level or -200 dBW for a 10 W source. Averaging would be essential to clarify the signal due to the small signal to noise ratio with the scattered signal expected to be -198 dBW with a 10 W source. The

most significant issue with the diagnostic technique is the background noise in the vacuum chamber produced from other systems or from leakage of microwave energy from the bistatic system that does not dissipate due to the metallic nature of the chamber. The base noise level of the bistatic system in the chamber is -100 dBm (1 Hz bandwidth) or in this case -30 dBc which is well above the expected level of the received scattered power.

Future implementation of this diagnostic for electric propulsion could explore a number of improvements. First, a high power signal (1 to 10 W or greater) is essential to receive scattered power greater than the thermal noise floor. In order to minimize leakage of the scattered signal, waveguide should be used for all connections, and additionally, the signal should be down converted as near to the transmitter and receivers as feasible. A state-of-the-art phase locked source should be used to minimize spectral noise at the desired offset frequency. Lastly, a non-metallic (Plexiglas) vacuum chamber would minimize the background noise level and reduce the scattered power from the chamber walls.

Basis of Scattering Equations and Shape Function as Related to Plasma Parameters

A rigorous analysis of wave propagation in the plasma is necessary to adequately relate the plasma parameters to the frequency spectrum of a scattered signal. The effect on the frequency spectrum is a low level effect attributed to Doppler broadening. The analysis includes the finite energy distribution of the plasma assuming a Maxwellian distribution centered around the average temperature of the plasma. Both the electron and ion energy distributions are included in the derivation which starts with the Klimontovich equation (F-2), the equation of motion (F-3), and Maxwell's equations (F-4 to F-7) to find the scattered power spectrum. These equations lead to the scattered power (Equation F-8) where the frequency spectrum is defined by a shape function (Equation F-9) which is the fundamental link to the plasma parameters. The shape function is defined by Equations F-10 to F-16.

$$\frac{\partial F_q}{\partial t}+\bar{v}\cdot\frac{\partial F_q}{\partial \bar{r}}+\bar{a}\cdot\frac{\partial F_q}{\partial \bar{v}}=0 \qquad \text{•F-2}$$

$$\bar{a}=\frac{q}{m}\left(\bar{E}+\frac{\bar{v}}{c}\times\bar{B}\right) \qquad \text{•F-3}$$

$$\nabla\bullet\bar{E}=\sum 4\pi q\int F_q\partial\bar{v} \qquad \text{•F-4}$$

$$\nabla\times\bar{E}=-\frac{1}{c}\frac{\partial\bar{B}}{\partial t} \qquad \text{•F-5}$$

$$\nabla\bullet\bar{B}=0 \qquad \text{•F-6}$$

$$\nabla\times B=\frac{1}{c}\frac{\partial\bar{E}}{\partial t}+\sum 4\pi q\int\bar{v}F_q\partial\bar{v} \qquad \text{•F-7}$$

$$P_s(\bar{r},\omega_s)=P_i r_o^2 L\partial\Omega\frac{\partial\omega_s}{2\pi}\left|\hat{s}\times\hat{s}\times\hat{E}_i\right|^2 n_e S(\bar{k},\omega) \qquad \text{•F-8}$$

$$S(\bar{k},\omega)=\frac{2\pi^{1/2}}{ka}\left\{\frac{A_e}{|\varepsilon|^2}+\frac{A_i}{|\varepsilon|^2}\right\} \qquad \text{•F-9}$$

$$A_e=\exp\left(-x_e^2\right)\left[\left(1+\alpha^2 Z\frac{T_e}{T_i}Rw(x_i)\right)^2+\left(\alpha^2 Z\frac{T_e}{T_i}Iw(x_i)\right)\right] \qquad \text{•F-10}$$

$$A_i=Z\left(\frac{m_i T_e}{m_e T_i}\right)^{1/2}\exp\left(-x_i^2\right)\left[\left(\alpha^2 Rw(x_e)\right)^2+\left(\alpha^2 Iw(x_e)\right)\right] \qquad \text{•F-11}$$

$$|\varepsilon|^2=\left\{\left[1+\alpha^2\left(Rw(x_e)+Z\frac{T_e}{T_i}Rw(x_i)\right)\right]^2+\left[\alpha^2 Iw(x_e)+\alpha^2 Z\frac{T_e}{T_i}Iw(x_i)\right]^2\right\} \qquad \text{•F-12}$$

$$x_e=\omega/ka \quad x_i=\omega/kb \quad \alpha=1/k\lambda_D \qquad \text{•F-13}$$

$$a=\left(2\kappa T_e/m_e\right)^{1/2} \quad b=\left(2\kappa T_i/m_i\right)^{1/2} \qquad \text{•F-14}$$

$$Rw(x)=1-2x\exp\left(-x^2\right)\int_0^x\exp\left(p^2\right)dp \qquad \text{•F-15}$$

$$Iw(x)=\pi^{1/2}x\exp\left(-x^2\right) \qquad \text{•F-16}$$

List of Parameter definitions for equations in this appendix:

F_q	Microscopic particle distribution
q	e or Ze, for electrons or ions
e	Electron charge
Z	Ionization number

t	Time
$\bar{v}$	Velocity Vector
$\bar{a}$	Acceleration Vector
$\bar{r}$	Position Vector
me,mi	Mass of an electrons and ions
$\bar{E}$	Electric field
$\bar{B}$	Magnetic Flux
c	Speed of light
Ps	Scattered power
Pi	Incident power
ro	Classical electron radius
L	Length of plasma over which scattering occurs
Ω	Solid angle
ω_s	Radial frequency
$\hat{s}$	Scattered wave direction
ne	Electron density
k	Total wave number, $\lvert k_s - k_i \rvert$
ω	Frequency difference, $\omega_i - \omega_s$
Te, Ti	Thermal temperature of electrons and ions
κ	Boltzmann Constant

BIBLIOGRAPHY

BIBLIOGRAPHY

Absalamov, S. K., V. B. Andreev, T. Colbert, M. Day, V. V. Egorov, R. U. Gnizdor, H. Kaufman, V. Kim, A. I. Korakin, K. N. Kozubsky, U. V. Lebedev, G. A. Popov and V. V. Zhurin, Measurement of Plasma Parameters in the Stationary Plasma Thruster (SPT-100) Plume and its Effect on Spacecraft Components, paper AIAA-92-3156 presented at *28th Joint Propulsion Conference and Exhibit*, Nashville, TN, 1992.

Alexeff, I., W. D. Jones and K. Lonngren, Excitation of Pseudowaves in a Plasma Via a Grid, *Physical Review Letters*, *21*, 878-881, 1968.

Andrews, J. G. and A. J. Shrapnel, Propagation of an Ion Rarefaction Wave from a Growing Sheath, *The Physics of Fluids*, *15*, 2271-2274, 1972.

Ashkenazy, J., Y. Raitses and G. Appelbaum, Investigations of a Laboratory Model Hall Thruster, paper AIAA 95-2673 presented at *31st AIAA/ASME/SAE/ASEE Joint Propulsion Conference and Exhibit*, San Diego, CA, 1995.

Baang, S., C. Domier, N. L. Jr., W. Peebles and T. Rhodes, Spatial Resolution of Microwave/Millimeter-Wave Reflectometry, *Review of Scientific Instruments*, *61*, 3013-3015, 1990.

Baconnet, J., G. Cesari, A. Coudeville and J. Watteau, 90° Laser Light Scattering by a Dense Plasma Focus, *Physics Letters*, *29A*, 19-20, 1969.

Basu, B. and J. Jasperse, Marginal Stability of Ion-Acoustic Waves in a Weakly Collisional Two-Temperature Plasma Without a Current, *Physical Review A*, *38*, 3785-3788, 1988.

Bernard, A., A. Coudeville, J. Garconnet, A. Jolas, J. D. Mascureau and J. Watteau, Forward Laser Scattering by the Plasma Focus During the Neutron Emission, *Physics Letters*, *35A*, 7-8, 1971.

Bernstein, I., J. Hirshfield and J. Jacob, Symmetry Considerations for Grid-Launched Ion-Acoustic Waves, *The Physics of Fluids, 14*, 628-632, 1971.

Bhartia, P. and T. J. Bahl, *Millimeter Wave Engineering and Applications*, Wiley, New York, 1984.

Biasca, R. and J. Wang, Ion Current Collection in Spacecraft Wakes, *Physics of Plasmas, 2*, 280-288, 1995.

Bingham, R., Decay of an Electromagnetic Wave into an Ion-Acoustic Wave and a Langmuir Mode which is Heavily Damped, *Plasma Physics and Controlled Fusion, 26*, 631-639, 1984.

Birkner, B. W., G. Hallock, H. Kim and H. Ling, Arcjet Plasma Plume Effect on a Microwave Reflector Antenna, *Review of Scientific Instruments, 61*, 1990.

Birmingham, T., J. Dawson and C. Oberman, Radiation Processes in Plasmas, *The Physics of Fluids, 8*, 297-307, 1965.

Booker, H. G. and W. E. Gordon, A Theory of Radio Scattering in the Troposphere, *Proceedings of the I.R.E.*, 401-412, 1950.

Bora, D. and P. K. Atrey, Plasma Density Measurement Using a Simple Microwave Technique, *Review of Scientific Instruments, 59*, 2149-2151, 1988.

Bora, D., R. Jayakumar and M. K. Vijayashankar, A Simple Microwave Technique for Plasma Density Measurement Using Frequency Modulation, *Plasma Physics and Controlled Fusion, 26*, 8533-857, 1983.

Born, M. and E. Wolf, *Principles of Optics*, Pergamon Press Book, New York, 1964.

Boyd, I. D., D. R. Beattie and M. A. Cappelli, Chamber Effects on Plume Expansion for a Low-Power Hydrogen Arcjet, paper presented at *AIAA/AIDAA/DGLR/JSASS 23rd International Electric Propulsion Conference*, Seattle, WA, 1993.

Boyle, M. J., Acceleration Processes in the Quasi-Steady Magnetoplasmadynamic Discharge, Princeton University, *Doctoral*, 1974.

Brophy, J., J. Barnett, J. Sankovic and D. Barnhart, Performance of the Stationary Plasma Thruster: SPT-100, paper AIAA 92-3155 presented at *AIAA/SAW/ASME/ASEE 28th Joint Propulsion Conference and Exhibit*, Nashville, TN, 1992.

Bruce, C. and L. Talbot, Cylindrical Electrostatic Probes at Angles of Incidence, *AIAA Journal, 13*, 1236-1237, 1975.

Buckley, R., The Response of a Spherical Plasma Probe to Alternating Potentials, *J. Plasma Physics, 1*, 171-191, 1967.

Bufton, S., R. Burton and H. Krier, Measured Plasma Properties at the Exit Plane of a 1 kW Arcjet, paper AIAA 95-3066 presented at *31st AIAA/ASME/SAE/ASEE Joint Propulsion Conference and Exhibit*, San Diego, CA, 1995.

Burton, R. L., S. G. Del Medico and J. C. Andrews, Application of a Quadruple Probe Technique to MPD Thruster Plume Measurements, *Journal of Propulsion and Power, 9*, 771-777, 1993.

Butler, G., I. Boyd and M. Cappelli, Non-Equilibrium Flow Phenomena in Low Power Hydrogen Arcjets, paper AIAA 95-2819 presented at *31st AIAA/ASME/SAE/ASEE Joint Propulsion Conference and Exhibit*, San Diego, CA, 1995.

Bychenkov, V., J. Myatt, W. Rozmus and V. Tikhonchuk, Ion Acoustic Waves in Plasmas with Collisional Electrons, *Physical Review E, 50*, 5134-5137, 1994.

Carney, L., Evaluation of the Communications Impact of a Low Power Arcjet Thruster, paper 88-3105 presented at *24th Joint Propulsion Conference*, Boston, Massachusetts, 1988.

Carney, L. M. and T. G. Keith, Langmuir Probe Measurements of an Arcjet Exhaust, *Journal of Propulsion, 5*, 287-294, 1989a.

Carney, L. M. and J. M. Sankovic, The Effects of Arcjet Thruster Operating Condition and Constrictor Geometry on the Plasma Plume, paper 89-2723 presented at *25th Joint Propulsion Conference*, Monterey, CA, 1989b.

Cassady, R., W. Hoskins and C. Vaughan, Qualification of a 26 kW Arcjet Flight Propulsion System, paper 95-2505 presented at *31st AIAA/ASME/SAE/ASEE Joint Propulsion Conference and Exhibit*, San Diego, CA, 1995.

Cassady, R. J., P. G. Lichon and D. Q. King, Arcjet Endurance Test Program, *AL-TR-90-069*, Olin Rocket Research Company, Defense Systems Group, 1991.

Cavanagh, E. and B. D. Cook, Numerical Evaluation of Hankel Transforms Via Gaussian-Laguerre Polynomial Expansions, *IEEE Transactions on Acoustics, Speech, and Signal Processing, ASSP-27*, 361-366, 1979.

Cecchi, J. L. and e. al., Lecture Notes for the Course "Production and diagnosis of process plasmas,, Princeton Scientific Consultants, Inc., Princeton, NJ, Nov. 1984.

Chan, C., M. A. Morgan and R. C. Allen, Electron Dynamics in the Near Wake of a Conducting Body, *IEEE Transaction on Plasma Science, PS-14*, 915-924, 1986.

Chen, F., *Introduction to Plasma Physics and Controlled Fusion*, Plenum Press, New York, 1984.

Chen, K., Interaction of a Radiating Source with a Plasma, *Proceedings of IEE, 111*, 1668-1678, 1964.

Chen, T. and L. Schott, Excitation of Ion Acoustic Waves with Probes, *The Physics of Fluids*, May.

Choueiri, E. Y., Characterization of Oscillations in Closed Drift Thrusters, paper 94-3013 presented at *30th AIAA/ASME/SAE/ASEE Joint Propulsion Conference*, Indianapolis, IN, 1994.

Christensen, T. and N. Hershkowitz, Near Field Diffraction Pattern of Ion Acoustic Waves, *The Physics of Fluids*, 1977.

Chung, K. and I. Hutchinson, Kinetic Theory of Ion Collection by Probing Objects in Flowing Strongly Magnetized Plasmas, *Physical Review A, 38*, 4721-4731, 1988.

Chung, P., L. Talbot and K. Touryan, *Electric Probes in Stationary and Flowing Plasmas: Theory and Application*, Springer-Verlag New York Inc., New York, 1975.

Coggiola, E. and A. Soubeyran, Mesothermal Plasma Flow Around a Negatively Wake Side Biased Cylinder, *Journal of Geophysical Research, 96*, 7613-7621, 1991.

Collin, R. W., *Antennas and Radiowave Propagation*, McGraw-Hill Book Company, 1985.

Coutrot, A., J. Bugeat, M. Lyszyk and D. Valentian, SPT M2 Development Status, paper 95-2671 presented at *31st AIAA/ASME/SAE/ASEE Joint Propulsion Conference and Exhibit*, San Diego, CA, 1995.

Crawford, F. and R. Mlodnosky, Langmuir Probe Response to Periodic Waveforms, *Journal of Geophysical Research, 69*, 2765-2773, 1964.

Curran, F. M. and T. W. Haag, Extended Life and Performance Test of a Low-Power Arcjet, *Journal of Spacecraft and Rockets, 29*, 444-452, 1992.

Day, M., N. Maslennikov, T. Randolph and W. Rogers, SPT-100 Subsystem Qualification Status, paper 95-2666 presented at *31st AIAA/ASME/SAE/ASEE Joint Propulsion Conference and Exhibit*, San Diego, CA, 1995.

DeBoer, Electric Probe Measurements in the Plume of the UK-10 Ion Thruster, *SMC-TR-94-28*, Mechanics and Materials Technology Center, Technology Operations, 1994.

Diamant, K., D. Tilley, E. Choueiri, A. Kelly and R. Jahn, MPD Thruster Exhaust Velocity Measurement Using Injected Plasma Waves, paper 91-049 presented at *AIDAA/AIAA/DGLR/ JSASS 22nd International Electric Propulsion Conference*, Viareggio, Italy, 1991.

Dickens, J., Communication Impact of Hall Effect Plasma Thrusters, Texas Tech University, *Doctoral*, 1995.

Dickens, J., J. Mankowski, M. Kristiansen and E. O'Hair, Impact of Hall Thrusters on Communication System Phase Noise, paper 95-2929 presented at *31st*

AIAA/ASME/SAE/ASEE Joint Propulsion Conference and Exhibit, San Diego, CA, 1995a.

Dickens, J. C., M. Kristiansen and E. O'Hair, Plume Model of Hall Effect Plasma Thrusters with Temporal Consideration, paper 95-171 presented at *IEPC*, Moscow, Russia, 1995b.

Doane, J. L., E. Mazzucato and G. L. Schmidt, Plasma Density Measurements Using FM-CW Millimeter Wave Radar Techniques, *Review of Scientific Instruments*, *52*, 12-15, 1981.

Dobele, H. F. and K. Hirsch, Anomalies in Scattered Spectra of a Hydrogen Arc Plasma Irradiated by a Continuous Argon Ion Laser, *Physics Letters*, *56A*, 282-284, 1976.

Domier, C. W., W. A. Peebles and J. N.C. Luhmann, Millimeter-Wave Interferometer for Measuring Plasma Electron Density, *Review of Scientific Instruments*, *59*, 1588-1590, 1988.

Doucet, H. and D. Gresillon, Grid Excitation of Ion Waves at Frequencies Above the Ion Plasma Frequency, *The Physics of Fluids*, *13*, 773-781, 1970.

Dougherty, J. and D. Farley, A Theory of Incoherent Scattering of Radio Waves by a Plasma, *Physical Review*, *259*, 78-99, 1960.

Dougherty, J. P. and J. D.T. Farley, A Theory of Incoherent Scattering of Radio Waves by a Plasma 3. Scattering in a Partly Ionized Gas, *Journal of Geophysical Research*, *68*, 5473-5486, 1963.

Drake, R., M. Goldman and J. DeGroot, Linear Ray-Optics Theory of the Radiation-Driven Ion-Acoustic Decay Instability in Flowing, Inhomogeneous Plasmas, *Physics of Plasmas*, *1*, 2448-2459, 1994.

Dum, C., Strong-Turbulence Theory and the Transition from Landau to Collisional Damping, *Physical Review Letters*, *35*, 947-950, 1975.

Efthimion, P. C., G. Taylor, W. Ernst, M. Goldman, M. McCarthy, H. Anderson and N. C. Luhmann, 1-millimeter Wave Interferometer for the Measurement of Line

Integral Electron Density on TFTR, *Review of Scientific Instruments, 56*, 908-910, 1985.

Epperlein, E., Effect of Electron Collisions on Ion-Acoustic Waves and Heat Flow, *Physics of Plasmas, 1*, 109-115, 1994.

Epperlein, E., R. Short and A. Simon, Damping of ion-acoustic waves in the presence of electron-ion collisions, *Physical review letters, 69*, 1765-1768, 1992.

Erwin, D. A., G. C. Pham-Van-Diep and W. D. Deininger, Laser-Induced Fluorescence Measurements of Flow Velocity in High-Power Arcjet Thruster Plumes, *AIAA Journal, 29*, 1298-1302, 1991.

Evans, D. E., The Effect of Impurities on the Spectrum of Laser Light Scattered by a Plasma, *Plasma Physics, 12*, 573-584, 1970.

Evans, J. V., Theory and Practice of Ionosphere Study by Thomson Scatter Radar, *Proceedings of the IEEE, 57*, 496-530, 1969.

Fessey, J., C. Gowers, C. Hugenholtz and K. Slavin, Plasma Electron Density Measurements from the JET 2 mm Wave Interferometer, *The Journal of Physics E., 20*, 169-174, 1987.

Forrest, M. J. and N. Peacock, Measurement of the Ion Temperature in the Dense Plasma Focus by Laser Beam Scattering, *Plasma Physics, 16*, 489-498, 1974.

Fournier, G. and D. Pigache, Wakes in Collisionless Plasma, *The Physics of Fluids, 18*, 1443-1453, 1975.

Gabl, E. and K. Lonngren, On Grid Launched Linear and Nonlinear Ion-Acoustic Waves-II, *Plasma Physics and Controlled Fusion, 26*, 799-811, 1984.

Gallimore, A., B. Gilchrist, L. King, S. Ohler and A. Ruffin, Plume Characterization of The SPT-100, paper 96-3298 presented at *32nd AIAA/ASME/SAE/ASEE Joint Propulsion Conference*, Lake Buena Vista, FL, 1996.

Gallimore, A. D., M. L. Reichenbacher, C. Marrese, S. W. Kim and J. E. Foster, Preliminary Characterization of a Low Power End-Hall Thruster, paper 94-3012

presented at *30th AIAA/ASMA/SAE/ASEE Joint Propulsion Conference*, Indianapolis, IN, 1994.

Garner, C., J. Brophy, J. Polk and L. Pless, A 5,730-Hr Cyclic Endurance Test of the SPT-100, paper 95-2667 presented at *31st AIAA/ASME/SAE/ASEE Joint Propulsion Conference and Exhibit*, San Diego, CA, 1995.

Garner, C., J. Polk, K. Goodfellow and J. Brophy, Performance Evaluation and Life Testing of the SPT-100, paper 93-091 presented at *23rd International Electric Propulsion Conference*, Seattle, WA, 1993.

Ginzburg, V. L., *The Propagation of Electromagnetic Waves in Plasmas*, Pergamon Press, 1970.

Godard, R., A symmetrical model for cylindrical and spherical collectors in a flowing collisionless plasma, York University, Toronto, Canada, *Doctoral*, 1975.

Godard, R. and J. Berrthelier, Influence of nonuniform surface potential on the measurement of plasma parameters by electrostatic probes, *Journal of Geophysical Research, 94*, 17161-17168, 1989.

Goodfellow, K., Theoretical Investigation of Cathode Operation in High-Power Arcjets, paper 95-3061 presented at *31st AIAA/ASME/SAE/ASEE Joint Propulsion Conference and Exhibit*, San Diego, CA, 1995.

Gopalan, K. and C. S. Chen, Fast Computation of Zero Order Hankel Transform, *Journal of the Franklin Institute, 316*, 317-326, 1983.

Gordon, W. E. and L. M. LaLonde, The Design and Capabilities of an Ionospheric Radar Probe, *IRE Transactions on Antennas and Propagation*, 17-22, 1961.

Gould, R., Excitation of Ion-Acoustic Waves, *Physical Review, 136*, 991-A997, 1964.

Group, T., Local Density Fluctuations Measurements by Microwave Reflectometry on TFR, *Plasma Physics and Controlled Fusion, 27*, 1299-1306, 1985.

Haddad, E., C. Belanger, B. C. Gregory, G. Abel and H. D. Pacher, Spectroscopic Measurements of Tokamak Plasma Ion Temperature Using Doppler Broadening of

Impurity Lines: Correction for Chordal Line-of-Sight Observations, *Journal of Applied Physics, 69*, 1968-1973, 1990.

Hailer, H., Spectrally Resolved Measurements of Collective Scattering from Thermal Plasma Fluctuations using a CW-CO2 Laser, *Physics Letters, 62A*, 419-421, 1977.

Hattori, K., A. Mase, A. Itakura, M. Inutake, S. Miyoshi, K. Uehara, T. Yonekura, H. Nishimura, K. Miyashita and K. Mizuno, Millimeter-Wave Phase-Imaging Interferometer for the GAMMA 10 Tandem Mirror, *Review of Scientific Instruments, 62*, 2857-2861, 1991.

Heald, C. B. and M. A. Wharton, *Plasma Diagnostics With Microwaves*, John Wiley and Sons, Inc., New York, 1965.

Hershkowitz, N., J. Glanz and K. Lonngren, Spherical Ion-Acoustic Solitons, *Plasma Physics, 22*, 583-588, 1979.

Hirshfield, J., J. Jacob and D. Baldwin, Interpretation of Spatially Decaying Ion-Acoustic Waves, *The Physics of Fluids, 14*, 615-627, 1971.

Hong, M. and G. Emmert, Two-Dimensional Fluid Modeling of Time-Dependent Plasma Sheath, *Journal of Vacuum Science Technology B, 12*, 889-896, 1994.

Hopkins, M. B. and W. G. Graham, Langmuir probe techniques for plasma parameter measurements in a medium density discharge, *Review Scientific Instruments, 57*, 2210-2217, 1986.

Hoskins, W. A., A. E. Kull and G. W. Butler, Measurement of Population and Temperature Profiles in an Arcjet Plume, paper 92-3240 presented at *AIAA/SAE/ASME/ASEE 28th Joint Propulsion Conference and Exhibit*, Nashville, TN, 1992.

Howard, J., Novel Scanning Interferometer for Two-Dimensional Plasma Density Measurements, *Review of Scientific Instruments, 61*, 1086-1094, 1990.

Howard, J., E. J. Doyle, G. Reibeiz, J. R.L. Savage, W. A. Peebles and J. N.C. Luhmann, Density Profile Reconstruction from 2-D Interferometric Data on Micromotor Using Novel Tomographic Analysis Techniques, *Review of Scientific Instruments, 59*, 2135-2138, 1988.

Huang, T., L. Chen and A. Hasegawa, Collisional Effects on Ion-Acoustic Waves in a Nonequilibrium Plasma, *The Physics of Fluids, 17*, 1744-1748, 1974.

Hugenholtz, C. A. J. and S. H. Heijnen, Pulse Radar Technique for Reflectometry on Thermonuclear Plasmas, *Review of Scientific Instruments, 62*, 1100-1101, 1991.

Hutchinson, I. H., *Principles of Plasma Diagnostics*, Cambridge University Press, New York, 1987.

Ikezi, H., Y. Kiwamoto, K. Lonngren, C. Burde and H. Hsuan, Ion-Acoustic Wave Response to an Impulse Disturbance, *Plasma Physics, 15*, 1141-1147, 1973.

Ito, T. and Y. Nakamura, Reflection and Excitation of Ion-Acoustic Waves in a Multi-Component Plasma with Negative Ions, *Journal of Plasma Physics, 51*, 185-191, 1994.

Jahns, G. and G. V. Hoven, Low-Frequency Grid Excitation in a Magnetized Plasma Column, *Physical Review A, 5*, 2622-2624, 1972.

Janson, S. W., Microwave Diagnostics for Ion Engines, paper 93-237 presented at *23rd International Electric Propulsion Conference*, Seattle, WA, 1993.

Janson, S. W., Microwave Interferometry for Ion Engines, paper 944-2741 presented at *30th Joint Propulsion Conference*, Indianapolis, IN, 1994a.

Janson, S. W., Microwave Interferometry for Low Density Plasmas, paper 94-2424 presented at *25th Plasmadynamics and Lasers Conference*, Colorado Springs, CO, 1994b.

Jensen, M. and K. Baker, Measuring Ionospheric Electron Density Using the Plasma Frequency Probe, *AIAA Journal, 29*, 91-95, 1992.

Johnson, B. and D. Murphree, Plasma Velocity Determination by Electrostatic Probes, *AIAA Journal, 7*, 2028 - 2010, 1969.

Johnson, H. F., An Improved Method for Computing a Discrete Hankel Transform, *Computer Physics Communications, 43*, 181-202, 1986.

Jones, W. D., *An Introduction to the Linear Theories and Methods of Electrostatic Waves in Plasmas*, Plasma Press, New York, 1985.

Kasparek, W. and E. Holzhauer, CO2-Laser Scattering from Thermal Fluctuations in a Plasma with Two Ion Components, *Physical Review A, 27*, 1737-1740, 1983.

Kaufman, H. R., Technology of Closed-Drift Thrusters, *AIAA Journal, 23*, 78-87, 1985.

Kelly, A. J., A Microwave Probe for Plasma Plumes, *AIAA Journal*, 372-373, 1965.

Kim, H. and H. Ling, High Frequency Electromagnetic Scattering From an Inhomogeneous Dielectric Body By Ray Tracing, paper presented at *IEEE Antennas and Propagation Society Symposium*, Ontario, Canada, 1991.

Kim, S. W., J. E. Foster and A. Gallimore, Very-Near-Field Plume Study of a 1.35 kW SPT-100, paper 96-2972 presented at *32nd AIAA/ASME/SAE/ASEE Joint Propulsion Conference*, Lake Buena Vista, FL, 1996.

Kim, V., T. Colbert, M. Day, V. Egorov, S. Khartov, V. Kozlov, N. Maslennikov, A. Nesterenko and G. Popov, Investigation of the SPT Performance Improvement Possibility, paper 95-2670 presented at *31st AIAA/ASME/SAE/ASEE Joint Propulsion Conference and Exhibit*, San Diego, CA, 1995.

Kinderdijk, H. and J. V. Eck, Comparison of Electron Densities Measured with Langmuir Probes and with Two Different Microwave Devices, *Physica, 59*, 257-284, 1972.

Konemann, B., The Collisionless Flow of Unmagnetized Plasmas Around Bodies, *Journal of Plasma Physics, 20*, 17-30, 1978.

Krall, A. D., B. C. Glancy and H. W. Sandusky, Microwave Interferometry of Shock Waves. I. Unreacting Porous Media, *Journal of Applied Physics, 74*, 6322-6327, 1993.

Kronast, B. and Z. Pietrzyk, Discrepancy Between Electron-Drift Velocities Obtained from the Ion and Electron Features of Light Scattering in a Z-Pinch Plasma, *Physical Review Letters, 26*, 67-69, 1971.

Kumar, H., L. Kumar and J. Verma, Measurements of Plasma Density in Argon Discharge by Langmuir Probe and Microwave Interferometer, *Indian Journal of Pure and Applied Physics, 17*, 316-318, 1979.

Lanquart, J. P., Error Attenuation in Abel Inversion, *Journal of Computational Physics, 47*, 434-443, 1982.

Le Toulouzan, J. N., G. Gouesbet, R. Darrigo and A. Berlemont, Experimental and Theoretical Study of a Low-Pressure Axisymmetric Arcjet, *AIAA Journal, 25*, 30-34, 1987.

Lehecka, T., W. A. Peebles, J. N.C. Luhmann and T. N. Carlstrom, Two-Color Interferometry for Fusion Plasma Diagnostics, *Review of Scientific Instruments, 59*, 1580-1581, 1988.

Ling, H., G. A. Hallock, H. Kim and B. W. Birkner, Near Field Interaction of Microwave Signals with a Bounded Plasma Plume, *Grant No. NCC3-127*, Department of Electrical and Computer Engineering, University of Texas at Austin, 1991a.

Ling, H., H. Kim, G. A. Hallock, B. W. Birkner and A. J. M. Zaman, Effect of an Arcjet Plume on Satellite Reflector Performance, *IEEE Transaction on Antennas and Propagation, 39*, 1412-1419, 1991b.

Little, P. and S. Hamberger, Scattering of Electromagnetic Waves by Electro-Acoustic Plasma Waves, *Nature, 209*, 972-974, 1966.

Lo, Y. T. and S. W. Lee, *Antenna Handbook: Theory, Applications and Design*, Van Nostrand Remhold Company, New York, 1988.

Lonngren, K., M. Khazei, E. Gabl and J. Bulson, On Grid Launched Linear and Nonlinear Ion-Acoustic Waves, *Plasma Physics, 24*, 1483-1489, 1982.

Manzella, D., Stationary Plasma Thruster Ion Velocity Distribution, paper 94-3141 presented at *30th AIAA/ASME/SAE/ASEE Joint Propulsion Conference*, Indianapolis, IN, 1994.

Manzella, D. and J. Sankovic, Hall Thruster Ion Beam Characterization, paper 95-2927 presented at *31st AIAA/ASME/ASEE Joint Propulsion Conference and Exhibit*, San Diego, CA, 1995.

Manzella, D. H., Stationary Plasma Thruster Plume Emissions, paper 93-097 presented at *23rd International Electric Propulsion Conference*, Seattle, WA, 1993.

Marrese, C., A. Gallimore, J. Haas, J. Foster, B. King, S. W. Kim and S. Khartov, An Investigation of Stationary Plasma Thruster Performance with Krypton Propellant, paper 95-2932 presented at *31st AIAA/ASME/SAE/ASEE Joint Propulsion Conference and Exhibit*, San Diego, CA, 1995.

Moorcroft, D. R., On the Determination of Temperature and Ionic Composition by Electron Backscattering from the Ionosphere and Magnetosphere, *Journal of Geophysical Research, 69*, 955-970, 1964.

Morgan, M., C. Chan, D. Cooke and M. Tautz, The Dynamics of Charged Particles in the Near Wake of a Very Negatively Charged Body - Laboratory Experiment and Numerical Simulation, *IEEE Transactions on Plasma Science, 17*, 220-227, 1989.

Muehldorf, E. I., The Phase Center of Horn Antennas, *IEEE Transactions on Antennas and Propagation, AP-18*, 753-760, 1970.

Murakami, M. and K. Nishihara, Sheath Dynamics Induced by Ion-Acoustic Rarefaction Wave, *The Physics of Fluids B, 5*, 3441-3446, 1993.

Myers, R. M. and D. H. Manzella, Stationary Plasma Thruster Plume Characteristics, paper 93-096 presented at *23rd International Electric Propulsion Conference*, Seattle, WA, 1993.

Nakamura, Y. and J. Chutia, Reflection of Ion-Acoustic Waves from Bipolar Potential Structures, *41*, 2, 1989.

Nakamura, Y., T. Ito and K. Koga, Excitation and Reflection of Ion-Acoustic Waves by a Gridded Plate and Metal Disk, *The Journal of Plasma Physics, 49*, 331-339, 1993.

Nakamura, Y., Y. Nomura and K. Lonngren, Near Field and Damping Effects of the Radiation of Ion Acoustic Waves from Antennas, *Radio Science, 14*, 1175-1181, 1979.

Offenberger, A. A. and R. D. Kerr, Collision Dominated Thomson Scattering Measurements Using CO2 Laser Radiation, *Physics Letters, 37 A*, 435-436, 1971.

Oh, D. and D. Hastings, Axisymmetric PIC-DSMC Simulations of SPT Plumes, paper 95-160 presented at *24th International Electric Propulsion Conference*, Moscow, Russia, 1995.

Ohler, S., B. Gilchrist and A. Gallimore, Microwave Plume Measurements of an SPT-100 Using Xenon and a Laboratory Model SPT Using Krypton, paper AIAA 95-2931 presented at *31st AIAA/ASME/SAE/ASEE Joint Propulsion Conference and Exhibit*, San Diego, CA, 1995a.

Ohler, S. G., B. E. Gilchrist and A. D. Gallimore, Non-intrusive electron number density measurements in the plume of a 1 KW arcjet using a modern microwave interferometer, *IEEE Transactions on Plasma Science, 23*, 428-435, 1995b.

Ohler, S. G., A. B. Ruffin, B. E. Gilchrist and A. D. Gallimore, RF Signal Impact Study of an SPT, paper 96-2706 presented at *32nd Joint Propulsion Conference*, Lake Buena Vista, FL, 1996.

Ohnuma, T., Radiation Phenomena of Plasma Waves, *IEEE Transactions on Plasma Science, PS-6*, 464-504, 1978.

Okada, S., Y. Kiso, S. Goto and T. Ishimura, Reduction of the Density Profile of a Field-Reversed Configuration from Detailed Interferometric Measurements, *Journal of Applied Physics, 16*, 4625-3631, 1989.

Okazaki, K., Y. Yamada and Y. Nishida, Fast-Imaging Method of Plasma Density Spatial Distribution by a Microwave Heterodyne Interferometer, *Review of Scientific Instruments, 61*, 1243-1246, 1990.

Overzet, L. and M. Hopkins, Comparison of Electron-Density Measurements Made Using a Langmuir Probe and Microwave Interferometry in the Gaseous Electronics Conference Reference Reactor, *Journal of Applied Physics, 74*, 4323-4330, 1993.

Patterson, M. J., R. S. Robinson, T. D. Schemmel and D. R. Burgess, Experimental Investigation of a Closed-Drift Thruster, paper 85-2060 presented at *AIAA/DGLR/JSASS 18th International Electric Propulsion Conference*, Alexandria, VA, 1985.

Pencil, E. J., Preliminary Far-Field Plume Sputtering of the Stationary Plasma Thruster (SPT-100), paper 93-098 presented at *23rd International Electric Propulsion Conference*, Seattle, WA, 1993.

Pencil, E. J., C. J. Sarmiento, D. A. Lichtin, J. W. Palachefsky and A. L. Bogorad, Low Power Arcjet System Spacecraft Impacts, paper 93-2392 presented at *AIAA/SAE/ASME/ASEE 29th Joint Propulsion Conference and Exhibit*, Monteray, CA, 1993.

Poissant, G. and M. Dudeck, Velocity Profiles in a Rarefied Argon Plasma Stream by Crossed Electrostatic Probes, *Journal of Applied Physics, 58*, 1772-1779, 1985.

Polk, J. and K. Goodfellow, Evaluation of a 30 kW Class Ammonia Arcjet at Power Levels Below 12 kW, *JPL D-8157*, Jet Propulsion Laboratory, California Institute of Technology, 1991.

Popa, G. and M. Oertl, Reflection of an Ion-Acoustic Soliton by a Bipolar Potential Wall Structure, *Physics Letters, 98 A*, 110-112, 1983.

Randall, C., Effect of Ion Collisionality on Ion-Acoustic Waves, *The Physics of Fluids, 25*, 2231-2233, 1982.

Raychaudhuri, S., H. Chang, E. Tsikis and K. Longren, Scattering of Ion-Acoustic Solitons, *Physics of Fluids, 28*, 2125-2129, 1985.

Rhee, M. and M. Lewis, Numerical Simulation of Stationary Plasma Thruster Exhaust Plume, paper 95-2928 presented at *31st AIAA/ASME/SAE/ASEE Joint Propulsion Conference and Exhibit*, San Diego, CA, 1995.

Riehle, M., H. Kurtz and M. Auweter-Kurtz, Investigations of Advanced Medium Power Hydrogen Arcjets, paper 95-2507 presented at *31st AIAA/ASME/SAE/ASEE Joint Propulsion Conference and Exhibit*, San Diego, CA, 1995.

Rizzato, F. and A. Chian, Nonlinear Generation of the Fundamental Radiation in Plasmas: the Influence of Induced Ion-Acoustic and Langmuir Waves, *Journal of Plasma Physics, 48*, 71-84, 1992.

Rosenbluth, M. N. and N. Rostoker, Scattering of Electromagnetic Waves by a Nonequilibrium Plasma, *The Physics of Fluids, 5*, 776-788, 1962.

Salpeter, E. E., Scattering of Radio Waves by Electrons Above the Ionosphere, *Journal of Geophysical Research, 65*, 1851-1852, 1960.

Salpeter, E. E., Effect of the Magnetic Field in Ionospheric Backscatter, *Journal of Geophysical Research, 66*, 982-984, 1961.

Sankovic, J., J. Hamley and T. Haag, Performance Evaluation of the Russian SPT-100 Thruster at NASA LeRC, paper 93-094 presented at *23rd International Electric Propulsion Conference*, Seattle, WA, 1993.

Sankovic, J. M., J. A. Hamley, T. W. Haag, C. J. Sarmiento and F. M. Curran, Hydrogen Arcjet Technology, *NASA Technical Memorandum, 105340*, 1991.

Schott, L., Fluid Dynamic Damping of Ion Acoustic Waves, *The Physics of Fluids, 18*, 645-650, 1975.

Schott, L., Reflection of Ion-Acoustic Waves from an Ion Sheath at a Grid, *Physics of Fluids, 29*, 846-851, 1986.

Schott, L., Double Plasma and Grid Excitation of Sinusoidal Ion Acoustic Waves, *The Physics of Fluids B, 3*, 236-243, 1991a.

Schott, L., Effect of a High-Frequency Field on the Reflection of Ion Acoustic Waves from the Sheath at a Grid, *IEEE Transactions on Plasma Science, 19*, 612-618, 1991b.

Schott, L., Ion-Energy Measurements in a Double Plasma Device, *Canadian Journal of Physics, 70*, 345-351, 1992.

Seanson, D. G., *Plasma Waves*, Academic Press, Boston, 1989.

Segall, S. and D. Koopman, Application of Cylindrical Langmuir Probes to Streaming Plasma Diagnostics, *The Physics of Fluids, 16*, 1149-1156, 1973.

Senbetu, L. and J. Henley, Distribution of Plasma Density and Potential Around a Mesothermal Ionospheric Object, *Journal of Geophysical Research, 94*, 5441-5448, 1989.

Sharma, S. K., Density Profile Determination of Cylindrically Symmetric Nonuniform Plasma Spatial Filtering, *Plasma Physics and Controlled Fusion, 28*, 391-392, 1986.

Sheffield, J., *Plasma Scattering of Electromagnetic Radiation*, Academic Press, Inc., New York, 1975.

Simonet, F., Measurement of Electron Density Profile By Microwave Reflectometry on Tokamaks, *Review of Scientific Instruments, 56*, 664-670, 1985.

Sips, A. C. C., Reflectometry and Transport in Thermonuclear Plasmas in the Joint European Torus, College van Dekanen, *Doctoral*, 1991.

Smith, L. M., Nonstationary Noise Effects in the Abel Inversion, *IEEE Transactions on Information Theory, 34*, 158-161, 1988.

Smith, L. M., D. Keefer and S. I. Sudharsanan, Abel Inversion Using Transform Techniques, *Journal of Quantitative Spectroscopy and Radiative Transfer, 39*, 367-373, 1988.

Soltwisch, H., Microwave Diagnostics, *Transactions of Fusion Technology, 25*, 304-314, 1994.

Spores, R., M. Birkan, R. Cohen and R. Einhorn, The Air Force Electric Propulsion Program, paper 95-2378 presented at *31st AIAA/ASME/SAE/ASEE Joint Propulsion Conference and Exhibit*, San Diego, CA, 1995.

Srivastava, S., G. Morales and J. Maggs, Nonlinear Landau damping of resonantly excited fields in nonuniform plasmas, *Physics of Plasmas, 1*, 567-578, 1994.

Stefant, R., Influence of electron-ion collision on ion acoustic waves, *Research Notes*, 2245-2246, 1971.

Stenzel, R., Microwave Resonator Probe for Localized Density Measurements in Weakly Magnetized Plasmas, *Review of Scientific Instruments, 47*, 603-607, 1976.

Stix, T. H., *Waves in Plasmas*, American Institute of Physics, New York, 1992.

Stone, J. R., NASA Electrothermal Auxiliary Propulsion Technology, paper 86-1703 presented at *AIAA/ASMA/SAE/ASEE 22nd Joint Propulsion Conference*, Huntsville, AL, 1986.

Stone, N., The Plasma Wake of Mesosonic Conducting Bodies., *Journal of Plasma Physics, 25*, 351-371, 1981.

Stone, N., W. Oran and U. Samir, Collisionless Plasma Flow Over a Conducting Sphere, *Planet Space Sciences, 20*, 1787-1790, 1972.

Stone, N., U. Samir and W. Oran, Laboratory Simulation of the Structure of Disturbed Zones Around Bodies in Space, *Journal of Atmospheric and Terrestrial Physics, 36*, 253-260, 1974.

Storm, P. and M. Cappelli, Laser-Induced Fluorescence Measurements Within an Arcjet Thruster Nozzle, paper 95-2381 presented at *31st AIAA/ASME/SAE/ASEE Joint Propulsion Conference and Exhibit*, San Diego, CA, 1995.

Swenson, C. M., An Evaluation of the Plasma Frequency Probe, Utah State University, *Master of Science in Electrical Engineering*, 1989.

Szabo, J. and J. Pollard, A Laboratory-Scale Hall Thruster, paper 95-2926 presented at *31st AIAA/ASME/SAE/ASEE Joint Propulsion Conference and Exhibit*, San Diego, CA, 1995.

Taylor, J., Disturbance of a Rarefield Plasma by a Supersonic Body on the Basis of the Poisson-Vlasov Equations - I, *Planetary Space Sciences, 15*, 155-187, 1967.

Tilley, D. L., A. D. Gallimore, A. J. Kelly and R. G. Jahn, The Adverse Effect of Ion Drift Velocity Perpendicular to a Cylindrical Triple Probe, *Review of Scientific Instruments, 65*, 1994.

Tilley, D. L., A. J. Kelly and R. G. Jahn, The Application of the Triple Probe Method to MPD Thruster Plumes, paper presented at *21st International Electric Propulsion Conference*, Orlando, FL, 1990.

Tsang, L. and J. A. Kong, Application of the Radio-Frequency Interferometry Method to a Stratified Anisotropic Medium, *IEEE Transactions on Antennas and Propagation*, 725-728, 1975.

van Blokland, A. A. E., E. P. Barbian, A. J. H. Donne, A. F. v. d. Grift, T. W. M. Grimbergen, T. Oyevaar, F. C. Schuller, H. F. Tammen, H. W. v. d. Ven, T. F. Vijverberg, F. D. A. d. Winter, G. Bertschinger, A. Cosler and M. Korten, Ion Temperature Measurements in Tokamak Plasmas by Rutherford Scattering, *Review of Scientific Instruments, 63*, 3359-3368, 1992.

Vickrey, J. F., Incoherent Scatter Theory-- An Intuitive Approach, Radio Physics Laboratory, SRI International, 1980.

Vickrey, J. F., W. E. Swartz and D. T. Farley, Incoherent Scatter Measurements of Ion Counterstreaming, *Geophysical Research Letters, 3*, 217-220, 1976.

Wang, E. Y., N. Hershkowitz, T. Intrator and C. Forrest, Techniques for Using Emitting Probes for Potential Measurement in RF Plasmas, *Review of Scientific Instruments, 57*, 2425-2431, 1986.

Watanabe, S., Ion-Acoustic Solitons Excited by a Single Grid, *Journal of Plasma Physics, 14*, 353-364, 1975.

Weibel, E. and M. Tran, Nonlinear Excitation of Acoustic Waves in a Double Plasma Device, *The Physics of Fluids, 19*, 1375-1379, 1976.

Wharton, C. B. and D. M. Slager, Microwave Determination of Plasma Density Profiles, *Journal of Applied Physics, 31*, 428-430, 1960.

Widner, M., I. Alexeff, W. Jones and K. Lonngren, Ion Acoustic Wave Excitation and Ion Sheath Evolution, *The Physics of Fluids, 13*, 2532-2540, 1970.

Wu, H. P. and R. L. McCreery, Observation of Concentration Profiles at Cylindrical Microelectrodes by a Combination of Spatially Resolved Absorption Spectroscopy and the Abel Inversion, *Anal. Chem., 61*, 2347-2352, 1989.

Yamagiwa, Y. and K. Kuriki, Performance of Double-Stage-Discharge Hall Ion Thruster, *Journal of Propulsion, 7*, 65-70, 1991.

Zana, L. M., Langmuir Probe Surveys of an Arcjet Exhaust, paper 87-1950 presented at *AIAA/SAE/ASME/ASEE 23rd Joint Propulsion Conference*, San Diego, CA, 1987.